eman ta zabal zazu
Universidad del País Vasco
Euskal Herriko Unibertsitatea
ZIENTZIA ETA TEKNOLOGIA FAKULTATEA
FACULTAD DE CIENCIA Y TECNOLOGÍA

Advances in MALDI-Imaging Mass Spectrometry to characterize lipid distribution in tissues

Doctoral Thesis

Jone Garate Yeregui

Supervised by:

José Andrés Fernández González

Gabriel Barreda Gómez

2019

Jone Garate was recipient of a predoctoral fellowship from the University of the Basque Country.

This research was supported by the Ministry of Economy and Competitiveness-FEDER (Grant RTC-2015-3693-1) and the Basque Government (Grant KK-2017/00041 and KK-2018/00090)

Special acknowledgement for Basque Biobank and IRBLleida Biobank for the collection of tissue samples and SGIKer.

Introduction and objectives **1**
1.1 Introduction 3
1.2 Scope of the thesis 5
An introduction to Imaging Mass Spectrometry and Lipidomics **7**
2.1 Mass Spectrometry 9
2.2 Imaging Mass Spectrometry (IMS) 9
Ion source 10
Matrix assisted desorption ionization (MALDI) 10
Mass Analyzer 13
Orbitrap 13
2.3 Lipidomics 14
Fatty Acids 16
Glycerophospholipids 17
Sphingolipids 18
Nomenclature 19
Materials and Methods **21**
3.1 Sample preparation for MALDI-IMS 23
3.2 MALDI-IMS analysis 24
3.3 H&E staining 25
3.4 Data processing 25
3.5 Lipids assignment 25
3.6 Statistical analysis 26
High Spatial Resolution IMS for prediction of the cell physiological and pathological state **27**
4.1 Introduction 29
4.2 Objectives 31
4.3 Experimental section 31
Human sample collection 31
Imaging and data analysis 31
4.4 Results and discussion 32
Matrix deposition 32
Laser spot characterization 32
High resolution Imaging Mass Spectrometry 33
Colonocyte differentiation status in healthy epithelium 35
Epithelium dedifferentiation in pathological context 39

Differentiation status in healthy and pathological lamina propria 43
4.5 Conclusions 45
An untargeted lipidomic study: IMS and multivariate analysis to discriminate melanoma from benign melanocytes 49
5.1 Introduction 51
5.2 Tumor Heterogeneity 52
5.3 The nature of the chemical noise 53
5.4 Objectives 54
5.5 Experimental section 54
Lipid standards 54
Lipid standards preparation 55
Imaging and data analysis for lipid standards 55
Human sample collection 55
Imaging and data analysis 56
5.6 Results and discussion 56
Mass spectra of lipid standards: In-source fragmentation pathways 56
MALDI-IMS of sections of nevi 59
Unraveling tumor heterogeneity 62
Design of the study for melanoma prediction 66
Melanocytic Nevi vs. Primary Melanoma 67
Molecular biomarkers for tumor aggressiveness 73
5.7 Conclusions 75
Development of new analytical tools of application in clinical research 79
6.1 Introduction 81
6.2 Objectives 81
6.3 Experimental section 82
Cell lines and culture conditions 82
Isolation of cell membranes 82
Cell membrane microarray development 82
Imaging and data analysis 82
6.4 Results and discussion 83
Inter-experimental reproducibility 83
Lipid fingerprint of cell membranes 85
Biomarker discovery for melanoma 86
Advantage over conventional tissue-directed IMS 89

6.5 Conclusions 90
Lung Cancer: a preliminary study 93
7.1 Introduction 95
7.2 Objectives 95
7.3 Experimental section 96
Human sample collection 96
Imaging and data analysis 96
7.4 Results and discussion 96
Imaging mass spectrometry of lung biopsies 96
Statistical analysis of epithelium 98
7.5 Conclusion 101
Future perspectives 103
8.1 Future perspectives 105
Appendix Chapter 4 I
Appendix Chapter 5 XIII
Appendix Chapter 6 XXIX
Appendix Chapter 7 XXXIII
Abbreviations ..... A

Chapter 1

Introduction and objectives

1.1 Introduction

In the past decades, the "omics" studies have gained momentum thanks in part to the advances in analytical instrumentation. The aim of these studies is the characterization and quantification of different biological molecules in order to fully understand the biology that governs the system (cell, tissue or organism).[1,2] The first emerging field by the end of 20th century was genomics, the study of an organism's genome (the total DNA).[3] The completion of the Human Genome Project[4] in 2002 changed medicine by providing new insight into biological processes that could help with diagnosis of cancer and rare diseases. However, they only provide one piece of the big puzzle, as many diseases were shown to be due to post-translational modifications or processes. Later on, in the 21st century, came the revolution of transcriptomic (the total mRNA) and specially proteomic (the study of all expressed proteins).[5,6] Nevertheless, these three fields all together provide only part of the picture, and therefore, this fact has led to an increasing interest in metabolomics, the exhaustive analysis of low molecular weight molecules (< 1.500 Da).[7] Metabolites, the final step in the "omics cascade", are generated by enzymatic proteins that are expressed by genes transcription. Thereby, the metabolome links genotype with phenotype (Figure 1.1.).

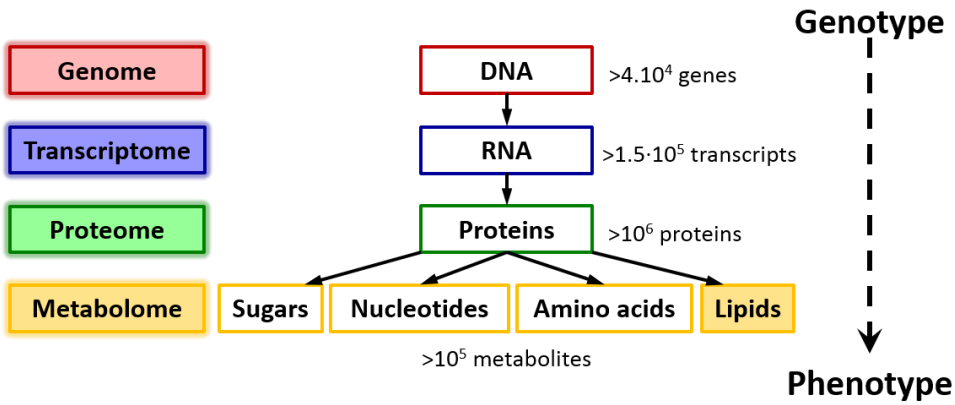

Fig 1.1. Scheme of the omics network. The genotype-phenotype relationship is hierarchically linked by DNA, RNA, protein and metabolites.

Recently lipidomic,[8] a subtype of metabolomics, has emerged as a promising study field, especially in cancer research, providing complexity to the whole picture.

Lipidomics aims to define and quantify lipid classes in different biological systems in order to analyze and understand their specialized task in cells.[8] Lipids play a crucial role in cell, tissue and organ's physiology, as they are the main building blocks of cellular membranes. These biomolecules also act as relevant signaling molecules as well as energy reservoir, regulating key biological processes. Eukaryotic cells invest substantial resources in generating thousands of different lipids.[9] The diversity in headgroups and aliphatic chains allows the existence of ‹1000 different lipid species, providing a wide variety of

properties that can affect the folding, structure and functioning of cell membranes.[10] The specific lipid composition determines the physical and functional characteristics of membranes. Thus, one can expect to observe lipid metabolism disruption in many human diseases.[11]

One of the principal techniques for lipidomic research is Mass Spectrometry (MS), which studies molecules by determining their abundance and the mass-to-charge ratio (m/z) of ions in the gas phase. It was first developed by J.J. Thomson when, like in many great scientific discoveries in history, he was looking for something else. At its origin, mass spectrometry was used in the field of physics to determine the mass of atoms, which contributed to the determination of the existence of stable isotopes of elements. Later, chemists started using it in the petroleum industry to measure the abundance of small hydrocarbons. Great advances boosted MS to new research fields, but it was not until the development of soft ionization techniques that it was introduced to biology, mainly in the omics field.[12]

The development of matrix assisted laser desorption ionization (MALDI)[13,14] and electrospray ionization (ESI)[15] revolutionized the field of mass spectrometry in the 1980s. MALDI was introduced by M. Karas and F. Hillenkamp,[12] and K. Tanaka[13] simultaneously, while ESI was developed by J.B. Fenn.[14] These two techniques changed the way in which biology was studied. Fenn and Tanaka were awarded the Nobel Prize in Chemistry in 2002 for "the development of methods for identification and structure analysis of biological macromolecules".

These advances made MS a unique tool for biological research, however, there was still a vital demand for understanding molecular changes in a spatial context. An old Chinese proverb says "a picture is worth a thousand words". It is in this framework that imaging mass spectrometry (IMS) was developed. IMS originated with secondary ion mass spectrometry (SIMS) over 50 years ago.[16] However, the analysis of biological samples only became possible once soft ionization techniques such as MALDI were introduced.[17,18]

IMS enables the detection and localization of thousands of different molecules in tissue sections in a single experiment. The goal of IMS in biochemistry is to detect the molecular constituents of the tissue, mainly metabolites and proteins, in order to improve the understanding of the connections between genome, phenotype and the biological response in disease. In this regard, IMS has proven to be valuable technique in cancer research, for biomarker discovery, understanding the knowledge of biological processes, as well as disease related classification, among other goals.

However, many questions remain unanswered, pending IMS achieving its full potential. One of the central themes in IMS is if it can provide relevant information to aid medical doctors in clinical decisions like diagnoses, predictions, treatment choice or monitoring. Here we present several modifications and improvements of MALDI-IMS, always aiming to achieve a better description of the changes in the lipidome of cells and tissues in the context of a disease. Thanks to the collaboration with other research groups, we have faced complex analytical problems, each one requiring specific developments to enable MALDI-IMS to answer relevant biological questions.

1.2 Scope of the thesis

For IMS to take off as a powerful technique in clinical application, there are some challenges that need to be acknowledged and overcome. The aim of this thesis is to recognize these bottlenecks and to focus on the development and application of analytical tools to optimize IMS experiments. Each chapter deals with a specific aspect of the MALDI-IMS methodology.

Chapter 4 presents the optimization of the sample preparation for high resolution IMS with a spectrometer equipped with non-optimal optics. It is fundamental in system biology to precisely localize molecules within the tissue with the purpose of understanding mechanistic links between biomolecules and diseases. The study was carried out in collaboration with the group of Dr. Gwendolyn Barceló-Coblijn, Lipids in Human Pathology from Balearic Islands Health Research Institute (Son Espases University Hospital) to analyze changes in the lipidome of colonic biopsies during the differentiation process of colonocytes.

Chapter 5 addresses the challenge of multiple comparative *studies*. In this sense, two main problems will be acknowledged: phenotypic tumor heterogeneity and the need of accurate lipid identification. This research was accomplished with the collaboration of the group of MD. Maria Dolores Boyano from Department of Cell Biology and Histology from Faculty of Medicine and Nursing (University of the Basque Country, UPV/EHU). The final goal was to build a classification model to distinguish nevus (control) from melanoma (disease) by their lipid phenotype.

Chapter 6 introduces the concept of lab-on-a chip. The future of IMS is on developing devices that enable multiple measurements in a single experiment to reduce the sample requirements, improve the reproducibility, reduce cost and increase diagnostic speed and sensitivity. The aim of this chapter was to present as a proof of concept, the tumor prediction capabilities of membranes microarrays based on lipidomic and imaging mass spectrometry. This was carried out in collaboration with Dr. Gabriel Barreda-Gomez and Dr. Egoitz Astigarraga from IMG-Pharma Biotech S.L. and the group of MD. Maria Dolores Boyano.

To conclude, in **chapter 7** we present preliminary results from an attempt to link different diseases and risk factors by the lipid phenotype and their metabolism. This study is now ongoing with the collaboration of the group of Dr. Gwendolyn Barceló-Coblijn.

[1] Kell DB. The virtual human: towards a global system biology of multiscale, distributed biochemical netwrks models. *Lubmb Life*. **2007**. 59: 689-695.

[2] Westerhoff HV, Palsson BO. The evolution of molecular histology into systems biology. *Nature Biotechnol.* **2004**. 22: 1249-1252.

[3] Baltimore D. Our genome unveiled. *Nature*. **2001**. 409: 814-816.

[4] Human Genome Squencing Consortium. Finishing the euchromatic sequence of the human genome. *Nature*. **2004.** 431: 931-945.

[5] Petricoin E, Zoon K, Kohn E, Barrett J, Liotta L. Clinical proteomics: translating benchside promise into bedside reality. *Nat. Rev.* **2002**. 1: 683-695.

[6] Vlahou A, Fountoulakis M. Proteomic approaches in the search for disease biomarkers. *J. Chromatogr. B. Analyt. Technol. Biomed. Life Sci.* **2005**. 814: 11-19.

[7] Nicholson JK, Lindon JC. Systems biology: Metabonomics. *Nature*. **2008**. 455: 1054-1056.

[8] Van Meer G. Cellular lipidomics. *EMBO J*. **2005**. 24: 3159-3165.

[9] Van Meer G, Voelker DR, Feigenson GW. Membrane lipids: where they are and how they behave. *Nat. Rev. Mol. Cell Biol.* **2008**. 8: 112-124.

[10] Laganowsky A, Reading E, Allison TM, Ulmshneider MB, Degiacomi MT, Baldwin AJ, Robinson CV. Membrane proteins bind lipids selectively to modulate their structure and function. *Nature*. **2014**. 510: 172-175.

[11] Wenk MR. The emerging field of lipidomics. *Nat. Rev. Drug Discov*. **2005**. 4: 594-610.

[12] Griffiths J. A brief history of mass spectrometry. *Anal. Chem*. **2008**. 80: 5678-5683.

[13] Karas M, Hillenkamp F. Laser desorption ionization of proteins with molecular masses exceeding 10.000 daltons. *Anal. Chem*. **1988.** 60: 2299-2301.

[14] Tanaka K, Waki H, Ido Y, Akita S, Yoshida Y, Yoshida T. Protein and polymer analyses up to m/z 100.000 by laser ionization time-of flight mass spectrometry. *Rapid Commun. Mass Spectrom*. **1988**. 2: 151.152.

[15] Fenn JB, Mann M, Meng CK, Wong SF, Whitehouse CM. Electrospray ionization for mass spectrometry of large biomolecules. *Science*. **1989**. 246: 64-71.

[16] Castaing R, Slodzian G. Microanalyse oar émission ionique secondaire. *J. Microsc*. **1962.** 1: 395-410.

[17] Spengler B, Hubert M, Kaufmann R. MALDI ion imaging and biological ion imaging with a new scanning UV-laser microprobe. *Proceedings of the 42nd ASMS Conferen on Mass Spectrometry and Allied Topics*. **1994.**

[18] Caprioli RM, Farmer TB, Gile J. Molecular imaging of biological samples: localization of peptides and proteins using MALDI-TOF MS. *Anal. Chem*. **1997**. 69: 4751-4760.

Chapter 2

An introduction to Imaging Mass Spectrometry and Lipidomics

This chapter is dedicated to describing the principle of imaging mass spectrometry, focusing on MALDI-IMS using an Orbitrap as mass analyzer. Furthermore, a brief introduction to lipidomics is provided, as well as lipid classification and structure of the lipid classes studied in this thesis.

2.1 Mass Spectrometry

Mass spectrometry is an analytical technique that enables the identification of chemical species according to their mass-to-charge ratio (m/z).[1] It consists of the ionization of the sample with the conversion of the molecules into gaseous ions, with or without fragmentation, and their characterization by their m/z. As a result, a mass spectrum is generated and displayed as a plot of the relative abundance versus m/z for each ion (Figure 2.1).

Three major components are identified in every mass spectrometer: the ion source, where the ions are generated; the analyzer, where the m/z of the ions are resolved; and the detector, which records the relative abundance of each m/z.

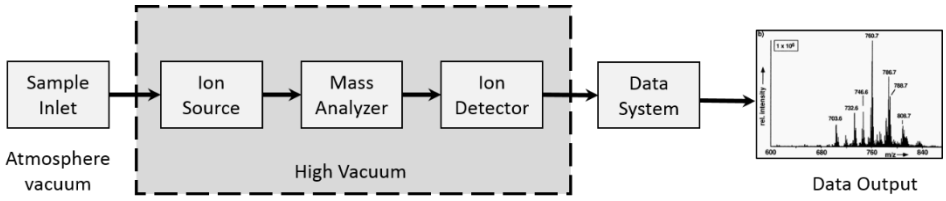

Fig. 2.1. Main components of a mass spectrometer.

It is beyond the scope of this thesis to deal in depth with all aspects related to mass spectrometry and its variation, such as LC-MS or GC-MS. Rather, it is focused on one of the latest and most successful innovation in MS, namely imaging mass spectrometry (IMS). This technique extends the capabilities of mass spectrometry making it a spatially-resolved analysis.

2.2 Imaging Mass Spectrometry (IMS)

IMS enables the detection, identification and spatial localization of different molecules directly from tissue sections.[2,3] In contrast to other imaging techniques, such as immunohistochemistry, it is a label-free and non-invasive approach. It can map hundreds of biomolecules in one experiment on different lengths scale, from sub-cellular to multi-cellular level. In this sense, it looks beyond classical histology.

IMS is a four-step process: sample preparation, desorption and ionization, mass analysis and image acquisition and data processing. All these stages need to be carefully controlled and monitored in order to obtain reproducible and successful images. Among these stages, sample preparation is a key factor to any analytical technique, which will be further discussed in Chapter 4 of this thesis.

Ion source

The three principal ionization methods used in IMS are matrix-assisted laser desorption ionization (MALDI),[4,5,6,7] secondary ion mass spectrometry (SIMS)[8] and desorption electrospray ionization (DESI).[9,10] More recently, improvement of the techniques have led to the development of other ionization techniques, such as laser ablation electrospray ionization (LAESI).[11] The choice of the method has a large impact on the spatial resolution of the experiment, as well as on the biomolecules that can be identified. Table 2.1. summarizes the spatial resolution achievable with each technique, as well as the molecules each technique is more suited for.

Table 2.1. Most common ionization techniques used in imaging mass spectrometry with their main characteristics: need of a previous sample preparation, resolution achievable and most common targeted biomolecules.[12]

	Sample Preparation	Ionization	Spatial resolution	Targeted biomolecules
MALDI	Matrix coating	Laser desorption ionization	3-200 µm	Lipids, peptides, proteins, metabolites
DESI	None	Desorption by solvent droplets and ESI-type ionization	›100 µm	Mostly lipids and metabolites
SIMS	None or matrix/metal coating	Sputtering with a primary ion beam	‹1 µm dynamic mode, ›1 µm static mode	Atoms, small molecular fragment, fatty acids and lipids
LAESI	None	Laser ablation combined with ESI	›200 µm	Lipids, peptides, proteins, metabolites

As MALDI is the ionization source used in this thesis, a brief description of this process is offered below.

Matrix assisted desorption ionization (MALDI)

This soft ionization method is an improvement of laser desorption ionization (LDI).[13] It consists of the co-crystallization of an organic matrix together with the analyte, in order to facilitate its transfer, as ions, into the gas phase, avoiding fragmentation as much as possible. Table 2.2 lists some of the most used matrices for MALDI-IMS in biological samples as well as the targeted analytes.

Table 2.2. Organic molecules of low molecular weight used as matrix in MALDI analysis with the analyte classes for which they are commonly used. [14]

Matrix	Common analytes
2,5-dihydroxybenzoic acid (DHB)	peptides, proteins, lipids, drugs
α-cyano-4-hrydroxycinnamic acid (CHCA)	peptides, proteins, lipids, drugs
3,5-dimethoxy-4-hydroxycinnamic acid (SA, sinapinic acid)	proteins
3-hydroxypicolinic acid (3-HPA)	peptides, oligonucleotides
2,4.dinitrophenylhydrazine (2,4-DNPH)	peptides
4,6-trihydroxyacetophenone (THAP)	lipids, oligonucleotides, drugs
2,6.dihydroxyacetophenone (DHA)	lipids
2-mercaptobezothiazole (MBT)	lipids
1,5-diaminonaphthalene (DAN)	lipids

MALDI-IMS is probably the most widely used imaging mass spectrometry technique. The tissue section is covered with a matrix, an organic molecule of low molecular weight and absorption bands at the wavelength of the laser emission. The role of the matrix crystals generated is to absorb the laser energy, leading to the ablation and ionization of the matrix together with the analyte molecules. Figure 2.2 shows a schematic representation of MALDI desorption and ionization process.

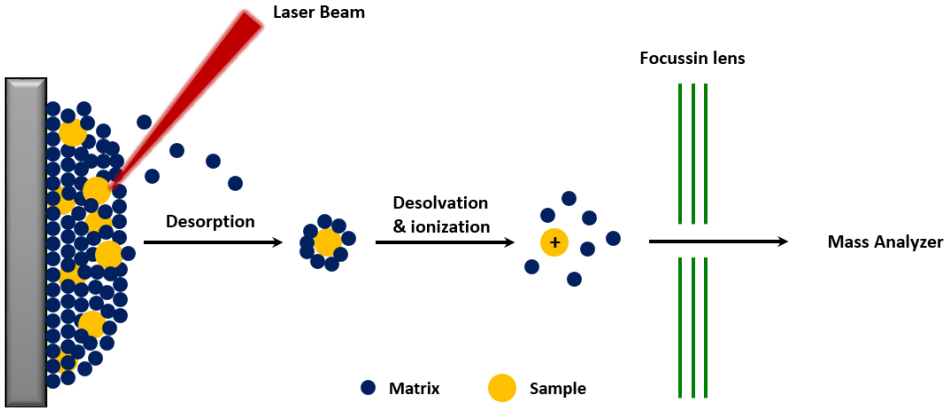

Fig. 2.2. Scheme of the matrix assisted desorption ionization process. A laser beam irradiates the sample-matrix surface. The matrix crystals absorb the energy and vaporize, releasing the analyte into the gas phase as charged ion.

Hence, during a MALDI-IMS experiment, the laser beam is rastered across a selected area of the surface of the tissue with a defined spatial separation between laser pulses. Each point will generate a spectrum with molecular information of that location, providing a new dimension to the experiment: the spatial resolution. This permits the creation of maps of the distribution of all the molecules detected across the area probed. The following steps include statistical analysis to visualize regions of interests (ROI), as well as identification of biomolecules. Figure 2.3. shows an overview of a typical MALDI-IMS experiment.

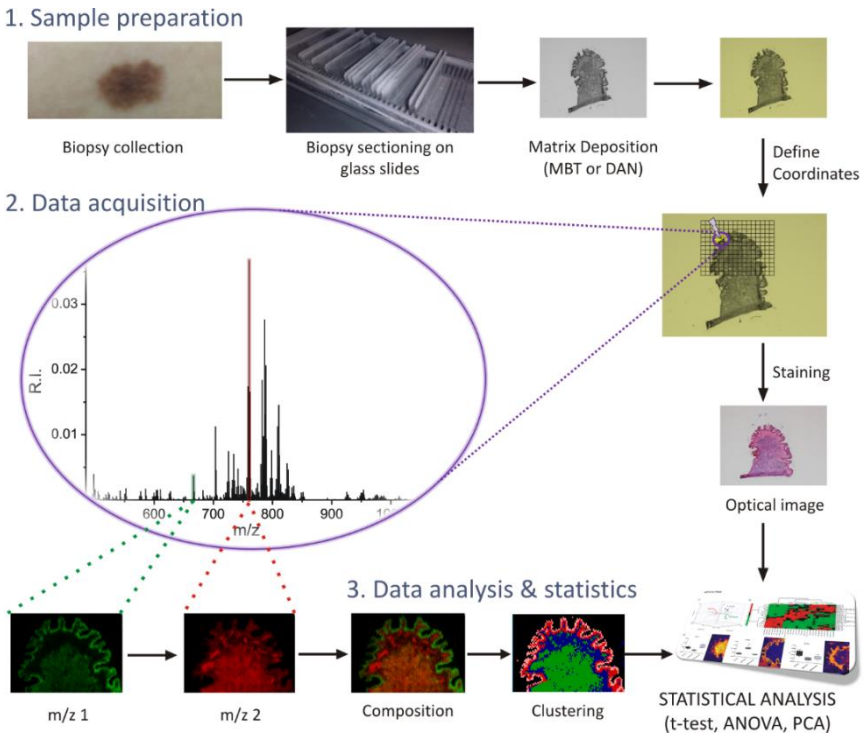

Fig. 2.3. Workflow of a typical MALDI-IMS experiment. Frozen samples are cryo-sectioned and thaw-mounted on glass slides. After the deposition of a thin coat of matrix, a virtual grid is defined, as well as the separation space between laser irradiations. Once the laser rasters the whole area selected, molecular images are reconstructed. Finally, the tissue section is stained and with the optical information and statistical analysis performed over the experiment, regions of interest or patterns are recognized. Further statistical analysis can be used to hunt for biomarkers or to build classification models.

Mass Analyzer

The mass analyzer processes the ions generated in the ion source according to their m/z. There is a variety of mass analyzers, differing in sensitivity, mass resolution and mass accuracy. Table 2.3 summarizes some characteristics for the most common mass analyzers used for MALDI-IMS.

Time-of-flight (TOF)-type analyzers[15] were the first ones to be used for MALDI-IMS,[4] and though it is still popular, the development of Fourier transform ion cyclotron resonance (FT-ICR)[16] and Orbitrap[17] has expanded the selection of analyzers. The main improvement of these devices is their extremely high mass resolving power, especially for small molecules such as lipids. Still, there is room for improvement, mainly regarding acquisition speed.

Table 2.3. Summary of mass analyzers used in imaging mass spectrometry, together with their main characteristics: mass resolving power, mass range, MS/MS capabilities and targeted biomolecules.[14]

Mass analyzer	mass resolving power (m/Δm)	m/z range	pixels/s	Tandem MS capabilities	Application
Linea TOF	10^3	0-10^6	>10	no	peptides/proteins
Reflectron TOF	10^3-10^4	0-10^5	>10	MS^2	drug/metabolites/peptides/lipids
Q-TOF	10^3-10^4	100-6k	>10	MS^2	drug/metabolites/peptides/lipids
Linear ion trap	10^2-10^3	50-3k	1	MS^n	drug/metabolites/peptides/lipids
Triple quadrupole	10^2-10^3	50-5k	>100	MS^2	drug/metabolites/peptides/lipids
FT-Orbitrap	10^4-10^6	50-10k	1	MS^n	drug/metabolites/peptides/lipids
FT-ICR	10^4-10^5	100-10k	1	MS^n	drug/metabolites/peptides/lipids

Orbitrap is the type of mass analyzer used in this thesis, therefore, a brief explanation of how it operates will be given.

Orbitrap

The principal characteristic of Orbitrap and FT-ICR, and what makes them different from the rest of the analyzers, is the way in which the mass-to-charge ratio is determined. Ions are forced to orbit inside a trap, while the frequency of their orbits is registered. Using the Fourier transform, the spectrum of the frequencies is obtained, and from it, the m/z of each ion.

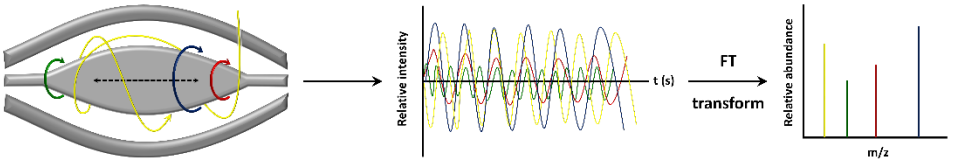

Fig. 2.4. Operation of an Orbitrap FT analyzer. Ions enter tangentially the trap generated by an inner and two outer electrodes and start orbiting around the central electrode with distinct axial frequencies. These frequencies are proportional to the m/z of the ions. The transformation into a mass spectrum is carried out by the Fourier transformation.

Figure 2.4 shows an explanatory scheme of the trajectory that the ions undergo in this type of analyzer. The Orbitrap[17] is composed of three electrodes: an inner spindle electrode surrounded by two outer concave electrodes facing each other. Once ions are injected tangentially into the trap, an electric field is generated between the inner and outer electrodes. Due to this electric field, the ion packet is drawn towards the inner electrode and starts oscillating axially along the electrode at a frequency proportional to $(z/m)^{1/2}$. The image current of the ion motion is detected and processed to convert the data from the frequency domain into m/z values. Longer transient collections produces higher mass resolutions.

2.3 Lipidomics

According to the literature, the term Lipidomics is defined as "the full characterization of lipid molecular species and of their biological roles with respect to expression of proteins involved in lipid metabolism and function, including gene regulation".[18]

Lipids are hydrophobic or amphipathic biomolecules, containing mainly hydrocarbons, which make up the building blocks of the structure and function of living cells.[19] They play several essential roles in cells, including energy storage, structural components of cell membranes, cell signaling and membrane trafficking.[20] The diversity of lipids comes from different and unique chemical structures that are encoded for those different functions.[21]

Lipids are classified into eight major groups, based on their chemical structure: [22] fatty acids, glycerolipids, glycerophospholipids, sphingolipids, sterols, prenols, saccharolipids and polyketides (Table 2.4).

Table 2.4. Lipid categories with their respective abbreviations and major roles that each play in cell biology. [22]

Lipid class	Abbreviation	Main function
Fatty acids	FA	Building blocks for complex lipids
Glycerolipids	GL	Energy storage
Glycerophospholipids	GP	Structural and signaling lipids
Polyketides	PK	Antimicrobial. Precursors for other molecules.
Prenols	PR	Antioxidant. Precursors of vitamins. Cell trafficking
Saccharolipids	SL	Structural
Sphingolipids	SP	Signal transduction and cell recognition
Sterols	ST	Structural and signaling lipids

This thesis is mainly focused on lipid membranes, specially glycerophospholipids and sphingolipids. These are biosynthesized either by *de novo* pathway (Figure 2.5) or remodeling pathway (Lands' cycle)[23] in the endoplasmic reticulum and Golgi. [24]

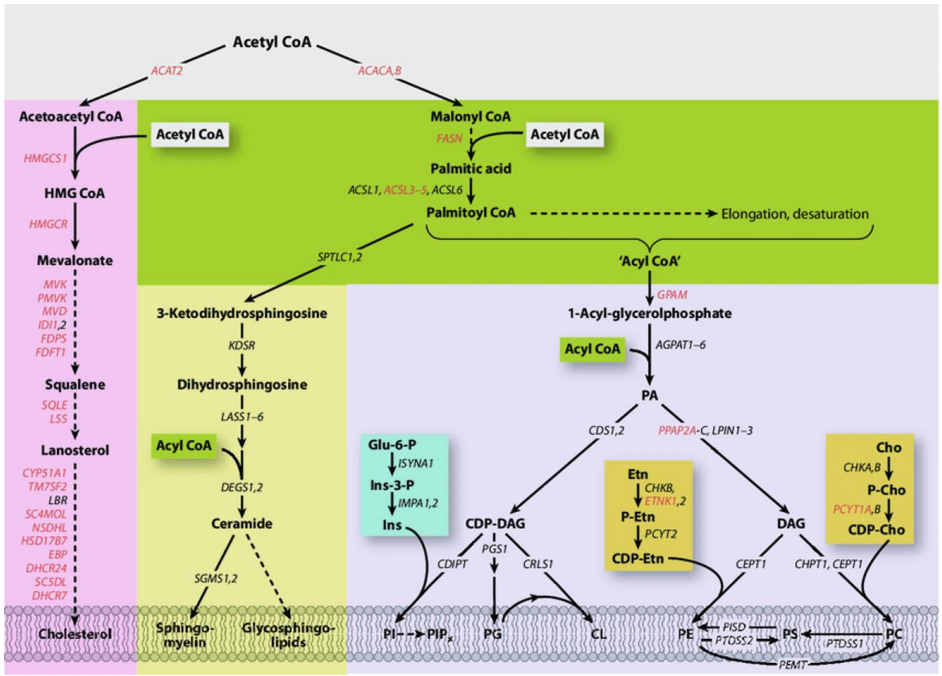

Fig. 2.5. Principal pathways for membrane lipid synthesis in mammals. This is a simplified scheme in which several pathways such as phospholipid turnover and remodeling have been omitted for clarity. [25]

Cell membranes are formed by these polar lipids asymmetrically organized in bilayer structures. The tendency of the hydrophobic part to self-assemble (entropically driven by water), and the propensity of the hydrophilic moieties to interact with aqueous environments and with each other, is the physical basis of the spontaneous formation of membranes, segregating the internal constituents from the external environment. Furthermore, in addition to the barrier function, membrane lipids also provide with the potential for budding, tabulation, fission and fusion, essential characteristics for cell division, reproduction and intracellular membrane trafficking.[26]

Fatty Acids

Fatty acids are the major building blocks of complex lipids. Hence, they are one of the most fundamental lipid classes in biological system. Only traces of free fatty acids are present in free form in tissue cells.

There are 14 subcategories of fatty acids, but the most common FA in nature are composed of a carboxylic acid attached to a long, unbranched and hydrophobic aliphatic-chain that can be saturated or unsaturated. In mammalian cells, the most naturally occurring fatty acids are composed of an even number of carbons (between 14 and 22) with unsaturations that vary from 0 to 6.[27] The degree of unsaturation of FA forming different complex lipids is known to affect membrane fluidity and many biological processes.[28] Examples of some of the most relevant fatty acids are shown in Figure 2.5.

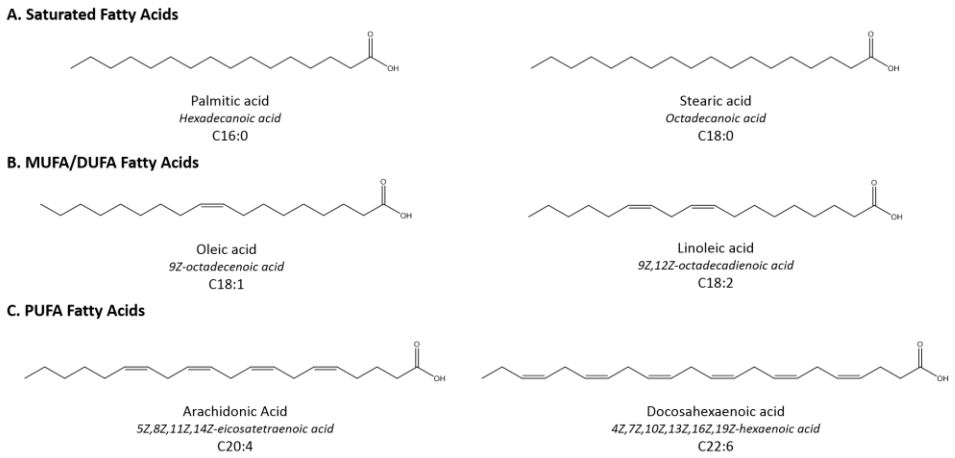

Fig 2.5. Representative examples of most common fatty acids in mammalian cells. **A** – Saturated FA. Palmitic acid (C16:0) and stearic acid (C18:0). **B** – Mono or diunsaturated FA. Oleic acid (C18:1) and Linoleic acid (C18:2). Linoleic acid is an essential lipid, which means that it cannot be synthesized by the body and it has to be ingested in the diet. **C** – Polyunsaturated FA. Arachidonic acid (AA-C20:4) and Docosahexanoic acid (DHA-C22:6). Precursors of molecules mediating inflammatory response and anti-inflammatory molecules, respectively.

Glycerophospholipids

Glycerophospholipids are the most abundant lipids in nature and key components of the lipid bilayer of cells. They consist of a glycerol backbone with fatty acids attached to the sn-1 and sn-2 positions and a hydrophilic head group to sn-3 (Figure 2.6).

Fatty acids vary in length and unsaturation, but normally, saturated acyl chains tend to bond at the sn-1 position, while polyunsaturated and monounsaturated are more often found at the sn-2 position.[29] Furthermore, the fatty acid at the sn-1 position can be linked to the backbone by an acyl, alkyl (ether GPL, plasmanyl) or an alkenyl (vinyl ether GPL, plasmalogen) linkage. On the other hand, the polar head group is made up of a phosphate linked to a head group substituent, such as a choline, ethanolamine or inositol.

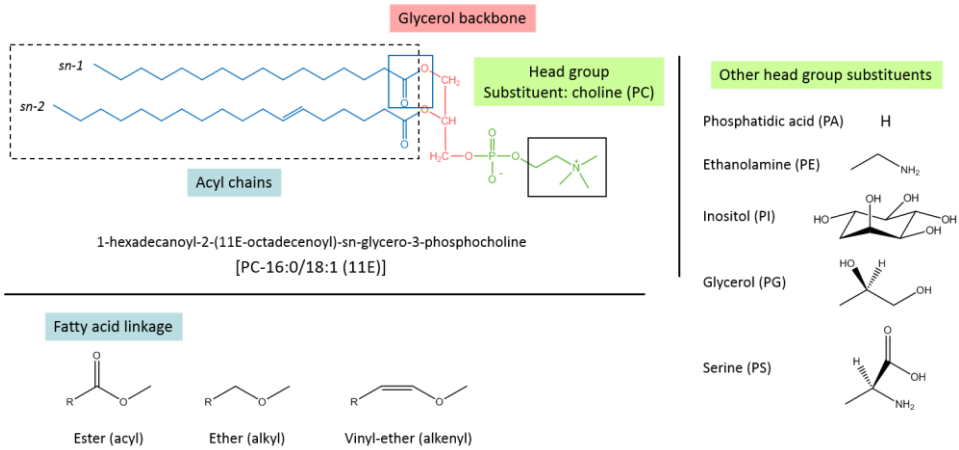

Fig 2.6. Glycerophospholipid structure. A glycerophosphocholine is shown as an example. The base is a glycerol (red) with two fatty acids attached to sn-1 and sn-2 positions (blue) and a head group at sn-3 (green). Depending on the head group substituent, different classes of GP can be formed (right column). Furthermore, the linkage to the fatty acid at sn-1 position can also be an ether or a vinyl ether (below the example), boosting the diversity of lipid species to another level.

Taking into consideration the above, this family of lipids is a very diverse group encoded for various important functions in a cell. The major classes found in mammalian cell membranes include glycerophosphocholines (PC), glycerophosphoethanolamines (PE), glycerophosphoinositols (PI), glycerophosphoglycerols (PG), glycerophosphoserines (PS) and cardiolipins (CL: two PG attached), being PC the most abundant subclass (~50% of glycerophospholipid mass). [30] Furthermore, lysophospholipids can also be produced when phospholipase A2 catalyzes the hydrolysis of the fatty acyl ester bond at the sn-2 position of glycerophospholipids.[31]

In the plasma membrane, PC species are enriched in the non-cytosolic side (external leaflet), whereas PS and PE are enriched in the cytosolic leaflet. Minor lipids such as PI

and PA are predominantly in the cytosolic leaflet, where they participate in cell signaling.[32]

Sphingolipids

Sphingolipids are lipids with relevant roles in signal transduction and cell recognition. They are divided into various classes, but all share a common feature: a sphingoid base as backbone. The main sphingoid bases in mammalian cells are sphingosine and dihydrosphingosine (sphinganine),[33] and they typically consist of 18 carbons. They differ in the presence (or not) of an unsaturation at position 2.

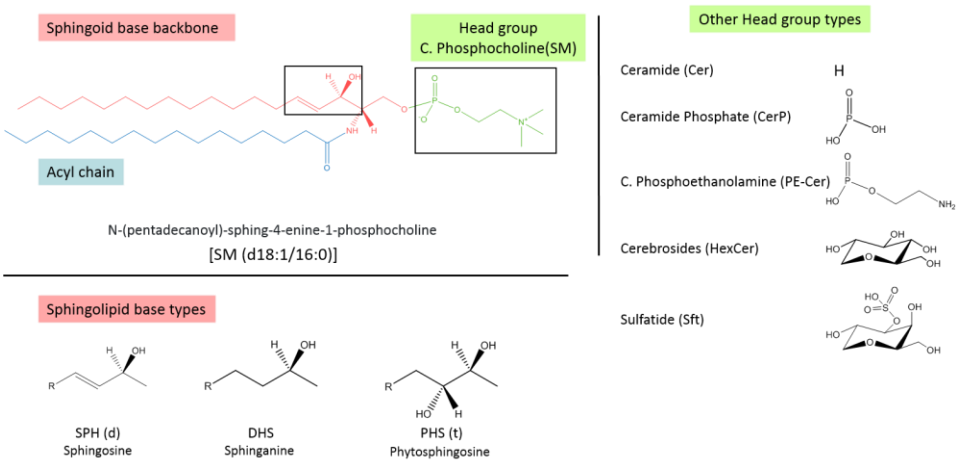

Fig. 5.7. Sphingolipids structure. A sphingomyelin is represented as an example. Sphingolipids consist of a sphingoid backbone (with different type of hydroxylation, see below the example), an N-acyl at sn-2 position and a head group. The head group defines the sphingolipid type, and hence the name (right column).

An amide-linked fatty acid is added at sn-2 position to form ceramide (Cer), the common precursor of the rest of sphingolipids. This structure may be phosphorylated to form ceramide-1-phosphate (CerP) or attached to more complex head groups such as choline, ethanolamine, sugars or even oligosaccharides. In this way, sphingomyelin (SM), ceramide phosphoethanolamine (PE-Cer), cerebrosides (HexCer) or gangliosides are formed, respectively.

SMs, the most abundant sphingolipids in cell membrane, as well as their choline-containing glycerophospolipid analogues, are enriched in the non-cytosolic side of the plasma membrane.[32]

Nomenclature

The nomenclature used in this thesis is as follows:

1. To address the type of lipid, abbreviations (PC, PI, SM, PE…) will be used from now in figures and text.

2. Regarding the ether fatty acid linkage in the case of glycerophospholipids, to the best of our knowledge, it is not possible to distinguish between ether and vinyl-ether even with MS/MS. In order to simplify, only one type will be addressed in this thesis, the most abundant of the two ether bonds. For instance, PE-ether will represent the vinyl-ether (PE-P),[34] as this is the most abundant type in mammalian cells, the so-called plasmalogen; while in the case of PC-ether, we will use PC-O or PE-ether, as this is the most abundant type, although once more, we cannot discard the presence of PC-P.[35]

3. The number of carbons of both fatty acids and the total unsaturations will be summed and the total number will be indicated unless we have data on the precise composition of the two fatty acids. For example, the sphingomyelin in the Figure 5.7 would be SM 34:1.

---

[1] Sparkman, OD. Mass spectrometry desk reference. *Global View Pub.* **2000**. ISBN 0-9660813-2-3.

[2] McDonnell LA, Heeren RMA. Imaging mass spectrometry. *Mass Spectrom. Rev.* **2006**. 26:606-643.

[3] Chughtai K, Heeren RMA. Mass Spectrometric Imaging for Biomedical Tissue Analysis. *Chem. Rev.* **2010**. 110:3237-3277.

[4] Karas M, Hillenkamp F. Laser desorption ionization of proteins with molecular masses exceeding 10.000 daltons. *Anal. Chem.* **1988**. 60:2299-2301.

[5] Tanaka K, Waki H, Ido Y, Akita S, Yoshida Y, Yoshida T. Protein and polymer analyses up to m/z 100.000 by laser ionization time-of flight mass spectrometry. *Rapid Commun Mass Spectrom.* **1988**. 2:151-153

[6] Spengler B, Hubert M, Kaufmann R. MALDI ion imaging and biological ion imaging with a new scanning UV-laser microprobe. *Proceedings of the 42nd ASMS Conference on Mass Spectrometry and Allied Topics.* **1994.**

[7] Caprioli RM, Farmer TB, Gile J. Molecular imaging of biological samples: localization of peptides and proteins using MALDI-TOF MS. *Anal. Chem.* **1997**. 69:4751-4760.

[8] Castaing R, Slodzian G. Microanalyse par émission ionique secondaire. *J. Microsc.* **1962**. 1:395-410.

[9] Takats Z, Wiseman JM, Gologan B, Cooks RG. Mass spectrometry sampling under ambient conditions with desorption electrospray ionization. *Science.* **2004**. 306:471-473.

[10] Ifa DR, Wiseman JM, Qingyu S, Cooks RG. Development of capabilities for imaging mass spectrometry under ambient conditions with desorption electrospray ionization (DESI). *Int. J. Mass Spectrom.* **2007**. 259:8-15.

[11] Nemes P, Vertes A. Laser ablation electrospray ionization for atmospheric pressure, in vivo, and imaging mass spectrometry. *Anal. Chem.* **2007**. 79:8098-8106.

[12] Mascini NE. Mass Spectrometry imaging for the classification of tumor tissue. *PhD Thesis.* **2015**.

[13] Peterson DS. Matix-free methods for laser desorption/ionization mass spectrometry. *Mass Spectrom. Rev.* **2007**. 26: 19-34.

[14] Norris JL, Caprioli RM. Analysis of tissue specimens by matrix-assisted laser desorption/ionization imaging mass spectrometry in biological and clinical research. *Chem. Rev.* **2013**. 113:2309-2342

[15] Stephens WE. A pulsed mass spectrometer with time dispersion. *Phys. Rev.* **1946.** 69:691.

[16] Comisarow MB, Marchall AG. Fourier transform ion cyclotron resonance spectroscopy. *Chem. Phys. Lett.* **1974**. 25:282-283.

[17] Hu Q, Noll RJ, Makarov A, Hardman M, Cooks RG. The Orbitrap: a new mass spectrometer. *J. Mass Spectrom.* **2005**. 40:430-443.

[18] Spener F, Lagarde M, Géloên A, Record M. Editorial: What is lipidomics*? Eur. J. Lipid Sci. Technol.* **2003**. 105:481-482.

[19] Harayama T, Riezman H. Understanding the diversity of membrane lipid composition. *Nat. Rev. Mol. Cell Biol.* **2018**. 19:281-296.

[20] Khalil MB, Hou W, Zhou H, Elisma F, Swayne LA, Blanchard AP, Yao Z, Bennett SAL, Figeys D. Lipidomics era: accomplishments and challenges. *Mass Spectrom. Rev.* **2010**. 29:877-929.

[21] Gross RW, Han X. Lipidomics at the interface of structure and function in system biology. *Chem. Biol.* **2011**. 18: 284-291.

[22] Fahy E, Subramaniam S, Brown HA, Glass CK, Merril Jr. AH, Murphy RC, Raetz CRH, Russell DW, Seyama Y, Shaw W, Shimizu T, Spener F, van Meer G, VanNieuwenhze MS, White SH, Witztum JL, Dennis EA. A comprehensive classification system for lipids. *J. Lipid Res.* **2005**. 46:839-862.

[23] Lands WE, Inoue M, Sugiura Y, Okuyama H. Selective incorporation of polyunsaturated fatty acids into phosphatidylcholine by rat liver microsomes. *J. Biol. Chem.* **1982**. 257: 14968-14972.

[24] Holthuis JC, Menon AK. Lipid landscapes and pipelines in membrane homeostasis. *Nature*. **2014**. 519: 48-57.

[25] Nohturfft A, Zhang SC. Coordination of lipid metabolism in membrane biogenesis. *Annu. Rev. Cell Dev. Biol.* **2009**. 24: 539-566.

[26] Van Meer G, Voelker DR, Feigenson GF. Membrane lipids: where they are and how they behave. *Nat. Rev. Mol. Cell Biol.* **2008**. 9: 112-124.

[27] Bond LM, Miyazaki M, O'Neill LM, Ding F, Ntambi JM. Fatty acid desaturation and elongation in mammals. *Biochemistry of Lipids, Lipoproteins and Membranes*. **2016**. 6th Edition: 185-208

[28] Spector AA, Yorek MA. Membrane lipid composition and cellular function. *J. Lipid Res.* **1985.** 26: 1015-1035.

[29] Yamashita A, Hayashi Y, Nemoto-Sasaki Y, Ito M, Oka S, Tanikawa T, Waku K, Sugiura T. Acyltransferases and transacylases that determine the fatty acid composition of glycerolipids and the metabolism of bioactive lipid mediators in mammalian cells and model organisms. *Prog. Lipid Res.* **2014**. 53: 18-81.

[30] Van Meer G. Cellular lipidomics. *EMBO J.* **2005**. 21: 3159.3165.

[31] Yamashita A, Hayashi Y, Nemoto-Sasaki Y, Ito M, Oka S, Tanikawa T, Waku K, Sugiura T. Acyltransferases and transacylases that determine the fatty acid composition of glycerolipids and the metabolism of bioactive lipid mediators in mammalian cells and model organisms. *Prog. Lipid Res.* **2014**. 53:18-81.

[32] Ingólfsson HI, Melo MN, van Eerden FJ, Arnarez C, Lopez CA, Wassenaar TA, Periole X, de Vried AH, Tieleman DP, Marrink SJ. *J. Am. Chem. Soc.* **2014**. 136: 14554-14559.

[33] Futerman AH. Sphingolipids. *Biochemistry of Lipids, Lipoproteins and Membranes*. **2016**. 6th Edition: 297-326.

[34] Braverman NE, Moser AB. Functions of plasmalogen lipids in health and disease. *Biochim. Biophys Acta*. **2012**. 1822: 1442-1452.

[35] Magnusson CD, Haraldsson GG. *Ether lipids*. Chem. Phys. Lipids. **2011.** 164: 315-340.

Chapter 3

Materials and Methods

This chapter is dedicated to a comprehensive description of sample preparation, experimental settings as well as data analysis. Further annotations or specific analysis methods will be described in following chapters.

3.1 Sample preparation for MALDI-IMS

Sample preparation is a decisive step for a successful imaging experiment. The key is to choose the appropriate matrix that enhances the sensitivity towards specific molecules, as well as to produce an optimal matrix deposition.

The choice of matrices were 2-mercaptobenzothiazole (MBT, Sigma-Aldrich Chemie, Steinheim, Germany)[1] for positive-ion mode and 1,5-diaminonaphthalene (DAN, Sigma-Aldrich Chemie, Dteinheim, Germany)[2] for negative-ion mode. Both matrices were previously shown to be particularly efficient for lipid analysis, enabling the detection of a wide variety of lipid classes with low background, high-resolution, as well as with the high stability needed for long acquisition hours.

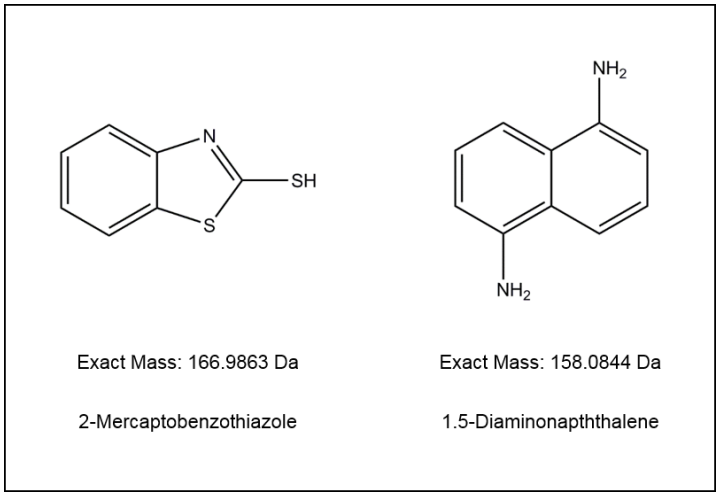

Fig. 2.1. Structure of the matrices used in this thesis.

The other factor is the deposition method. The organic compound can be applied to the sample by robotic spotting or spraying (automated or manual), but we chose to deposit it by sublimation, to avoid the use of any solvent that could perturb the nature of the sample by migration of biomolecules.[3,4]

During the process, the matrix was placed inside a sublimator chamber (Ace Glass™ 8023), while the glass slide with the tissue was fixed to a cold finger inverted just above the matrix. The separation between the sample and the organic compound was less than 1 cm. Once the system was connected to a vacuum pump (with pressure ~10^{-1} mbar) and the heating system reached the temperature desired, the cold finger was filled with ice and water and the whole system was placed on top of the heating plate. Thus, the matrix sublimes and condenses on the surface of the cold sample generating a thin layer of small crystals.

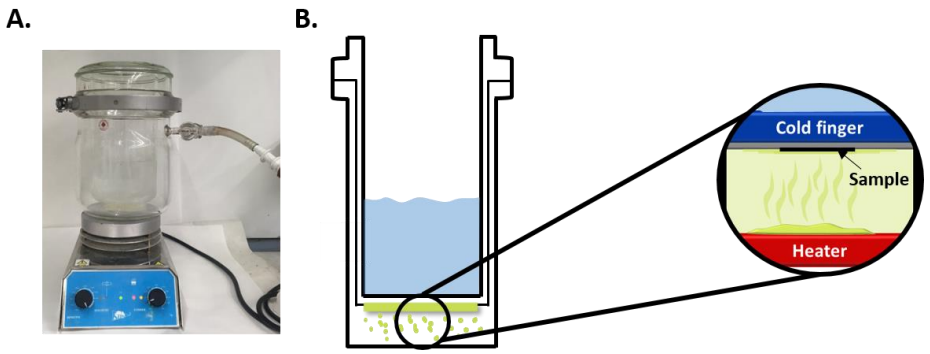

Fig. 2.2. A – Image of the glass sublimator used in this thesis. **B** – The process of sublimation.

This technique was controlled by regulating the heating time and temperature, stopping once the desired thickness was reached.

The optimum matrix quantity as well as the temperature and time needed will be described in Chapter 4.

3.2 MALDI-IMS analysis

MALDI-IMS analyses were performed using a MALDI-LTQ-Orbitrap XL (ThermoFisher).[5] The spectrometer was operated in Orbitrap mode. Data were acquired with a mass resolution of 30.000 and 60.000 at m/z=400 Da in the scanning range of 550-1200 for negative-ion mode and 480-1100 for positive-ion mode. Two microscans of 10 laser shots were recorded for each pixel. Further specific parameters for each study, such as laser energy and raster size used, will be reported in following chapters.

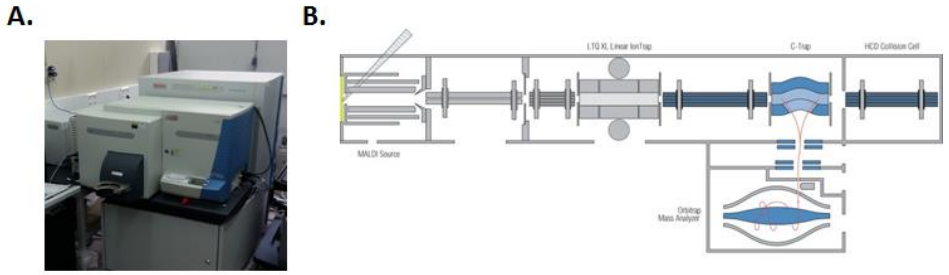

Fig 2.1. A – Image of MALDI-LTQ-Orbitrap XL used for the acquisition of data in this thesis. **B** – Schematic diagram representing the components of the instrument.

3.3 H&E staining

After an imaging experiment finishes, the tissue section was washed off the matrix for a post hematoxylin and eosin (Sigma-Aldrich, Madrid, Spain) staining protocol.

Briefly, the matrix was removed from the surface of the sections by immersion of the glass slide in a 70% ethanol solution for approximately 1 min. After a hydration process of the sections in a graded ethanol series to water, glass slides were immersed, first in hematoxylin for 5 min and then in eosin for 2 min. This was followed by a dehydration process in graded ethanol starting with water and up to 100% ethanol before clearing it with citrosol and mounting it with DPX. Hematoxylin stained nucleic acid with a deep blue-purple color (nuclei), and eosins stained proteins nonspecifically with pink (cytoplasm and extracellular matrix).

3.4 Data processing

Spectra were analyzed using dedicated software (MSIAnalyst, NorayBioinformatics S.L and in-house programs in Matlab (MathWorks, Natick, USA). The spectra were subjected to peak selection using the *Simple Peak Finding* (SPF) method.[6] A detection value of 0.02 was used for experiments recorded at 60.000 mass resolution, and 0.04 for those at 30.000. The pre-processing process continues with the reduction of the size of the data by eliminating all the peaks whose intensity was lower than the 0.5% of the strongest peak on each spectrum, and subsequently, spectra were aligned using the Xiong method[7] assuming a maximum misalignment of 0.02 amu (mass resolution = 60.000) or 0.04 amu (mass resolution = 30.000). Finally, the spectra were normalized using a total ion current algorithm (TIC). During graphical representation, no interpolation or smoothing algorithm or any de-noising procedure was used, always trying to maintain the original features of the data.

3.5 Lipids assignment

Lipid assignment was based upon comparison between the experimental m/z and the species in the software's database (›33,000 lipid species and their adducts), and those in the LIPID MAPS database (www.lipidmaps.org). Mass accuracy was always better than 9 ppm and it was typically better than 3 ppm in the individual spectra. In this type of analysis, mass accuracy depends to some extent on the peaks' intensity and thus, higher intensity m/z values have a better mass accuracy.

3.6 Statistical analysis

Only reproducible lipid species were used in multiple comparative studies to minimize the inter-patient variability. For that, the 80% rule was applied, meaning that if the standard deviation of a specie was above the set threshold of 80% of its average value, it was considered not reproducible within a group and it was removed from the analysis. This was performed with the idea of obtaining the reproducible lipid profiles of the groups.

To group together ions with high correlation, and to represent the original IMS data in a more visual format for further analysis, the well-known *k-means*[8,9] and an in-house programmed clustering algorithm were used. This latter algorithm will be better described in Chapter 5.

Data are presented as means ± S.E.M. Statistical analyses used in each study are described in each chapter, but in all instances p values ‹ 0.05 were considered statistically significant.

---

[1] Astigarraga E, Barreda-Gomez G, Lombardero L, Fresnedo O, Castano F, Giralt MT, Ochoa B, Rodriguez-Puertas R, Fernandez JA. Profiling and imaging of lipids on brain and liver tissue by matrix-assisted laser desorption/ionization mass spectrometry ursing 2-mercaptobenzothiazole as a matrix. *Anal. Chem.* **2008**. 80:9105-9114

[2] Thomas A, Charbonneau JL, Fournaise E, Chaurand P. Sublimation of new matrix candidates for high spatial resolution imaging mass spectrometry of lipids: enhanced information in both positive and negative polarities after 1,5-diaminonapthalene deposition. *Anal. Chem.* **2012**. 84:2048-2054

[3] Hankin JA, Barkley RM, Murphy RC. Sublimation as a method of matrix application for mass spectrometric imaging. *J. Am. Soc. Mass Spectrom.* **2007**. 18:1646-1652

[4] Murphy RC, Hankin JA, Barkley RM, Zemski Berry KA. MALDI imaging of lipids after matrix sublimation/deposition. *Biochim. Biophys. Acta*. **2011**. 1811:970-975

[5] Strupat K, Kovtoun V, Bui H, Viner R, Stafford G, Horning S. MALDI produced ions inspected with a linear ion trap-orbitrap hybrid mass analyzer. *J. Am. Soc. Mass Spectrom.* **2009**. 20: 1451-1463.

[6] Coombes KR, Fritsche HA Jr, Clarke C, Chen JN, Baggerly KA, Morris JS, Xiao LC, Hung MC, Kuerer HM. Quality control and peak finding for proteomics data collected from nipple aspirate fluid by surface-enhanced laser desorption and ionization. *Clin. Chem.* **2013**. 49(10):1615-1623.

[7] Xiong X, De la Torre F. Supervised descent method and its application to face alignment. *IEEE Computer Society Conference on Computer Vision and Pattern Recognition*. **2013**.

[8] McCombie G, Staab D, Stoeckli M, Knochenmuss R. Spatial and spectral correlations in MALDI mass spectrometry images by clustering and multivariate analysis. *Anal. Chem.* **2005**. 77:6118-6124.

[9] Jones EA, Deininger SO, Hogendoorn PCW, Deelder AM, McDonnell LA. Imaging mass spectrometry statistical analysis. *J. Proteomics*. **2012**. 75: 4962-4989.

Chapter 4

High Spatial Resolution IMS for prediction of the cell physiological and pathological state

Recent advances in mass spectrometry have boosted the interest to describe complete lipidomes in diverse of pathological contexts, with the aim of identifying lipid biomarkers for diagnosis or treatment monitoring. However, the biopsies used for this purpose usually contain different cell types. To fully understand the mechanistic link between a potential lipid biomarker and a disease, it is necessary to precisely locate the lipid species within the tissue, as well as to discriminate its cell-type origin. Thus, the next frontier is to achieve the maximum resolution possible to obtain cellular (or even subcellular) information.

In this chapter we present an optimized methodology to reach the highest resolution possible with a spectrometer equipped with non-optimal optics.

The study we present here was conducted over sections from biopsies of human colon mucosa. We demonstrate, with solid evidences, that the images of the lipid fingerprint at cellular resolution can be used to precisely predict the physiological and pathological status of a cell, reinforcing the translational impact of high-resolution IMS techniques.

The data presented here have been published in part in:

1. **Garate J**, Fernández R, Lage S, Bestard-Escalas J, Lopez DH, Reigada R, Khorrami S, Ginard D, Reyes J, Amengual I, Barceló-Coblijn G, Fernández JA. Imaging mass spectrometry increased resolution using 2-mercaptobenzothiazole and 2,5-diaminonapthalene matrices: application to lipid distribution in human colon. *Anal. Bioanal. Chem.* **2015**. 407: 4697-4708.

2. Bestard-Escalas J, **Garate J**, Maimó-Barceló A, Fernández R, Lopez DH, Lage S, Reigada R, Khorrami S, Ginard D, Reyes J, Amengual I, Fernández JA, Barceló-Coblijn G. Lipid fingerprint image accurately conveys human colon cell pathophysiologic state: a solid candidate as biomarker. *Biochim. Biophys. Acta.* **2016.** 1861: 1942-1950.

3. Lopez DH, Bestard-Escalas J, **Garate J**, Maimó-Barceló A, Fernández R, Reigada R, Khorrami S, Ginard D, Okazaki T, Fernández JA, Barceló-Coblijn G. Tissue-selective alteration of ethanolamine plasmalogen metabolism in dedifferentiated colon mucosa. *Biochim. Biophys. Acta Mol. Cell Biol. Lipids.* **2018.** 1863: 928-938.

4.1 Introduction

Since the publication of the first images showing distribution of biomolecules from tissue sections,[1,2,3,4,5] there has been a continuous improvement of the technique that has led to the emergence of the latest generation of mass spectrometers. These are equipped with state-of-the-art MALDI sources and analyzers that yield outstanding spatial and mass resolutions. Even so, it is still possible to achieve cellular resolution with not-that-old spectrometers without any optical modification.

Spatial resolution in MALDI-IMS depends on several factors, the most important being the laser spot size and sample preparation, and more to the point the choice of the optimal matrix substance and its correct application to the sample.[6]

The first step for a successful experiment is the characterization of the laser beam. The laser spot diameter is often referred to as the highest resolution achievable by the spectrometer. Even so, a number of high-resolution images were reported in the literature with step size smaller than the diameter of the beam. This was achieved by oversampling.[7,8,9]

In an oversampling-type acquisition, the whole area covered with the first laser spot is probed and contributes to the signal intensity (Figure 4.1). To record the second spot, the sample is displaced a distance smaller than the diameter of the laser beam, and only the area with fresh sample and matrix contributes to the signal of the second pixel. This area is further reduced in the following rows (Figure 4.1). This method succeeded in improving the resolution up to 5-10 µm/pixel without any optical changes, and in principle, even better resolutions could be achieved, but then, the signal-to-noise (s/n) ratio starts playing a limiting role. Certainly, the laser spot size (or area covered with matrix in this case) is not the limiting factor for the spatial resolution. As the area ablated by the laser becomes smaller, instrument sensitivity is compromised and just the most abundant species in the tissue are detected. Thus, to reach the maximum resolution allowed by the equipment, the best matrix available for analyzing the molecules of interest (lipids, proteins, drugs etc.) must be used.

Hence, the other critical parameter for good quality mass-spectral images with high spatial resolution is sample preparation: choosing the correct matrix and its deposition. Experimental parameters should be optimized for each application, taking considerable care in every stage of this step. 1,5-diaminonapthalene (DAN) has already demonstrated to be particularly efficient for lipid analysis in negative-ion mode. So, it is necessary to create a uniform thin film of small crystals of DAN, with optimal amount of matrix per area unit for oversampling. Therefore, solvent-free deposition methods are advisable,[10,11,12] as they ensure the smallest crystal possible without any migration or perturbation of the original composition of the tissue. So far, matrix sublimation seems to yield the best results.[13,14]

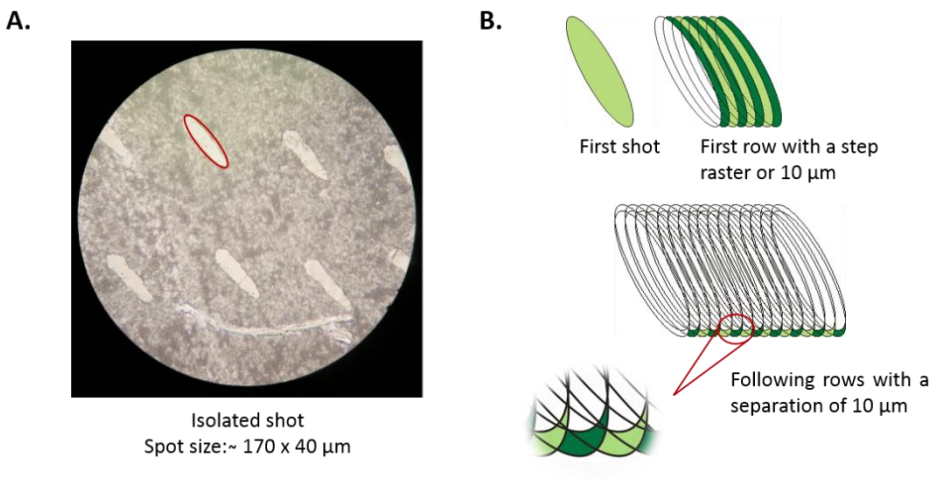

Fig. 4.1. A – Micrography of the laser trace in 1,5-diaminonapthalene. **B** – A scheme explaining the oversampling method. Only green-shaded areas contribute to the signal.

The system chosen for the optimization of the sample preparation was human colon mucosa biopsies. Colon crypt's architecture provides the perfect structure to visualize the improvement in spatial resolution.

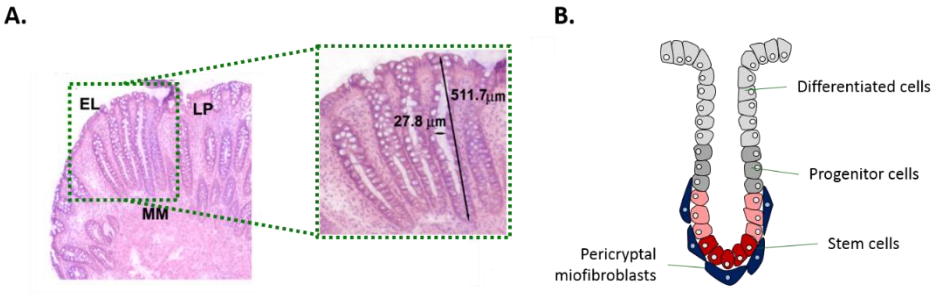

Fig. 4.2. A – Histological sections of a human colon biopsy stained with H&E showing the three types of basic tissues present in the colon mucosa: epithelial layer (EL), the lamina propria (LP), and the muscularis mucosae (MM). **B** – Schematic representation of a colon crypt and its cell types depending on the position (adapted from A. Humphries et al. *Nat. Rev. Cancer.* **2008**. 8: 415-424)

The colon is the last segment of the digestive system. The functional unit of the colon is the colonic crypt, invaginations of the epithelium through the conjunctive tissue, named lamina propria (Figure 4.2). These crypts are made up of a single sheet of columnar epithelial cells (colonocytes) arranged in a strict spatial display: stem cells are found at the base of the unit, which proliferate into young epithelial cells that end up differentiating into mature enterocytes before exiting the crypts.[15] This cell renewal mechanism makes the colon the perfect system, once the methodology for high resolution IMS is optimized, to

explore how sensitive the cell lipidome is to the cell differentiation processes, providing further understanding of the biological process.

4.2 Objectives

The goal of this chapter is to demonstrate that with an adequate sample preparation, it is feasible to achieve cellular resolution, even with a mass spectrometer equipped with a MALDI source that uses a non-so optimal large laser spot. This will allow us to carry out the first study on the changes in the lipidome of the colon, which will permit us to unravel the possible relationship between the maturation process of the colonocytes and the lipid metabolism.

4.3 Experimental section

Human sample collection

The sample collection was approved by the Ethics Research Committee of the Balearic Islands. Written informant consent was obtained from each patient. In total, four healthy patients, four patients with adenomatous polyps (AD) and three with carcinoma were used in this study.

Endoscopic biopsies were immediately snapped frozen in liquid nitrogen and saved at -80ºC until sample preparation. Sections of 10 µm thick sections were cut using a cryostat and placed on glass slides.

This was carried out by the group Lipids in Human Pathology Balearic Islands Health Research Institute (Son Espases University Hospital).

Imaging and data analysis

First, three pixel sizes were tested over a colonic tissue from a healthy patient: 5, 10 and 25 µm. Data was acquired at a mass resolution of 30.000 FWHM at m/z = 400, and with a laser energy between 30-60 µJ/pulse. The rest of the MALDI-IMS parameters used are described in Materials and Methods (chapter 3), as well as the detailed information regarding data analysis. Staining with H&E (Sigma Aldrich Química, Madrid, Spain) was carried out for all biopsies once MALDI-IMS experiments were completed and matrix was removed. Data was handled with MSI Analyst (NorayBioinformatics S.L, Derio, Bizkaia) for *k-means* clustering and image reconstruction with the parameters described in Chapter 2. Statistical results were analyzed by unpaired Student's t-tests and p values < 0.05 were considered statistically significant.

4.4 Results and discussion

Matrix deposition

DAN was used as matrix for negative-ion mode, as previously described in Chapter 3. The amount of matrix deposited over the section was a compromise between obtaining a uniform, thin enough layer so the matrix peaks did not interfere with the detection of lipids and with the optimal amount required for a successful oversampling. Furthermore, the matrix deposited need to be enough to enable the several hours that experiments lasts.

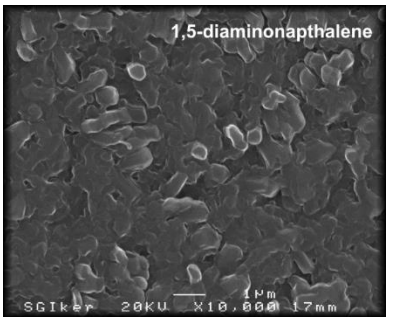

Fig 4.3. SEM image of DAN crystals

The optimal amount of DAN deposited for adequate performance of oversampling was ~ 0.15 mg/cm^2, with an average size of crystals 1-3 µm. Figure 4.3. shows SEM images of DAN deposition on top of a glass slide. This was achieved by depositing the matrix at a temperature of 123ºC for 8 min.

MBT was also optimized for positive-ion mode high resolution IMS. The optimal parameters for deposition, as well as the crystal size may be found in Appendix (Figure A.4.1).

Laser spot characterization

The MALDI source used in this work is equipped with a N_2 laser and a very simple optical arrangement, consisting of two mirrors and a single focusing lens of f = 125 mm.[16] The nitrogen laser uses an electrical discharge to excite the active medium (N_2) and the lack of optical resonator, produces a low spatial coherence non Gaussian beam. So, the laser spot presents a complicated energy distribution, which in addition, changes during the laser lifetime.

The trace left by a laser shot on a microscope slide covered with DAN is shown in Figure 4.1. The laser spot can be approximated to an ellipsoid of ~ 170 x 40 µm, although the energy distribution inside the spot is not homogenous.

A sketch of the oversampling is summarized in Figure 4.1.B, which illustrates the area cleared by a single laser shot (the green ellipsoid), the area probed by the rest of the shots in the first row, and the area probed by each shot in subsequent rows, which is the final pixel size (zoomed in the last section).

High resolution Imaging Mass Spectrometry

Figure 4.4. shows a comparison between the optical image of a healthy colon section and the distribution of some representative lipids obtained by IMS in negative-ion mode (Figure A.4.2 for positive-ion mode). The images are the composition of three scans, at 5, 10 and 25 µm pixels. It shows a rich and unique composition for each type of tissue, and the lipids detected (mainly PI, PS, PG, PE and SM) seem to be tissue-specific, which enables a good recognition of the tissue anatomy.

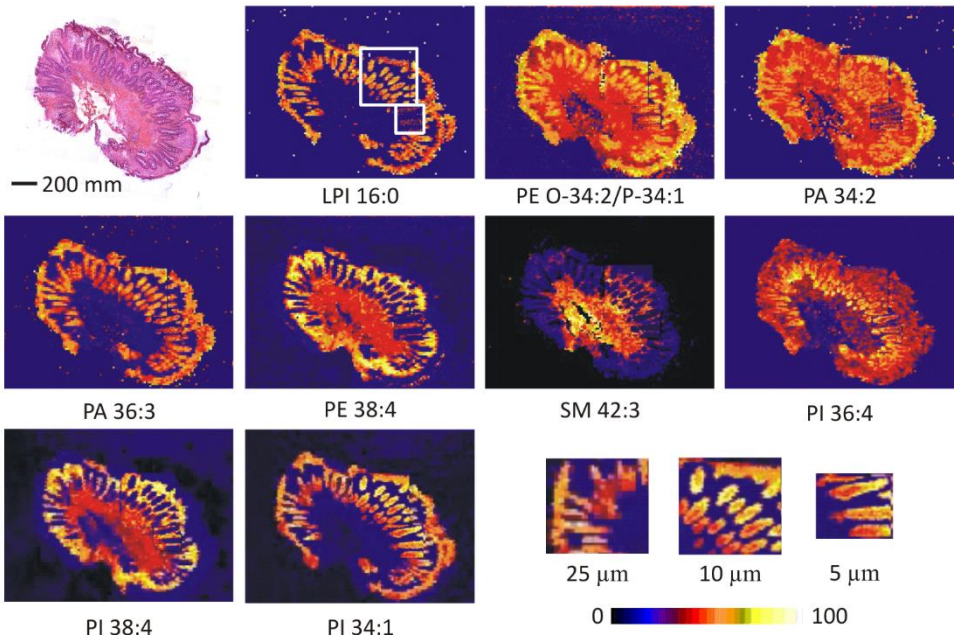

Fig 4.4. Comparison of the optical image of a human colon tissue section stained with H&E and the distribution of some selected lipid species detected in negative-ion mode. The large and small white squares highlight the areas scanned at 10 and 5 µm, respectively. The last three images at the bottom right are a detail of the distribution of PI 34:1 recorded at 25, 10 and 5 µm.

The three pictures at the bottom-right corner show a detail of the distribution of $[PI\ 34:1 - H]^-$ (m/z 835.528) over part of the area scanned at 25, 10 and 5 µm/pixel. Clearly, there is an increase in resolution as the pixel size decreases, which is not only due to a larger density of pixels in the image, but also to a real resolution increase. For example, the cavity inside the crypt, which cannot be distinguished at 25 µm, becomes apparent in the image recorded at 10 µm and it is clearly defined in the image at 5 µm.

It is worth mentioning that arachidonic acid (FA 20:4, AA) containing species, Figure 4.4, PE 38:4 and PI 38:4 for example, are substantially more concentrated in lamina propria compared to epithelium. This could be due to the AA proinflammatory capacity and the

physiological inflammatory level associated to the cells located in the lamina propria of a healthy colon.[17]

The importance of the resolution is further reinforced in the statistical analysis (Figure 4.5). Application of the *k-means* algorithm over the spectra recorded at 25 µm correctly identified the existence of muscularis mucosae (light green), lamina propria (yellow), and the crypts (light blue). Still, crypt boundaries often overlap, while they are perfectly distinguishable in the region scanned at 10 µm. Furthermore, the *k-means* algorithm also found differences between cells at the bottom of the crypts (purple areas) and those close to the upper part (the luminal side of the crypt). This stands out in the area scanned at 5 µm. The algorithm not only was able to group the spectra into clusters that closely follow the tissue anatomy, but it even showed additional divisions. Six different clusters were found in the tissue. Clusters 1, 4 and 5 correspond to different areas of the lamina propria. One of them, cluster 4, follows the crypts contour. This could represent the subepithelial telocytes, cells whose relevant role in maintaining cell support and integrity to stem cells for differentiation process, has been described in the literature.[18] The other two clusters (Cl1 and 5) may be reflecting the cell diversity existing in the lamina propria: fibroblast, myofibroblast, pericytes, etc.[19] Cluster 3 corresponds to the crypt cavity filled with colonic mucin, and surrounding it, there is a cluster (Cl6) that matches with the walls of the crypt, formed by a single line of colonocytes. It is worth noting that the algorithm found an additional cluster that embraces the border between the colonocytes and the lamina propria, and the bottom of a crypt, which is barely visible in the optical image (marked with a green circle).Taking into account that colonocytes are highly polarized cells, this cluster (Cl2) may mark the nuclei, which are usually located at the bottom of the cells. This means that there is a difference in the lipid composition between that side of the cell and the other end. Therefore, this result implies that using a 5 µm step size, allows us to achieve (a modest) subcellular resolution.

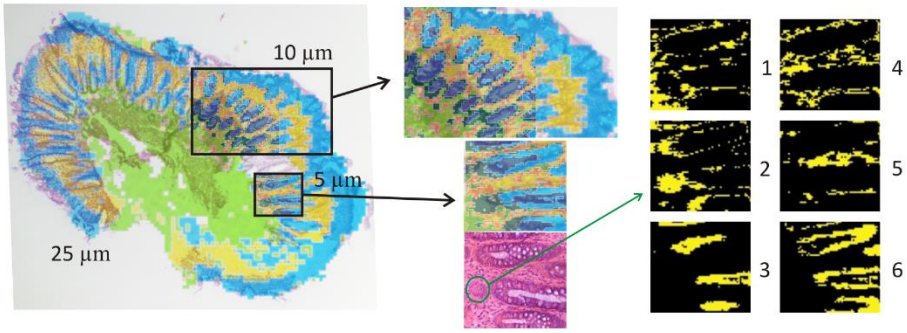

Fig. 4.5. An overlay of the statistical analysis (*k-means*) over the optical image of the section. The different colors (blue, green, yellow, dark blue, dark green and pink) correspond to different types of cells found by the algorithm.

This improvement in resolution enabled us to analyze the changes in the lipidome occurring throughout the crypt and detect the differences between crypt and lamina propria, two juxtaposed tissues. Taking into account that colonocytes fall within the size

range of 20-30 µm, and that in order to get the whole picture of the tissue at a cellular level a quite large area need to be scanned, 10 µm step size will be used for the rest of the study.

Colonocyte differentiation status in healthy epithelium

Four healthy colonic biopsies were scanned, and in order to perform an inter-experiment study, *k-means* statistical analysis was carried out. In the epithelial layer, two lipid clusters were consistently formed, anatomically located at the upper (luminal – light blue color) and lower (basal – dark blue) parts of the crypt (Figure 4.6.). In fact, images obtained at this resolution readily convey the presence of gradients in lipid composition along the colon crypt (Figure 4.6). Furthermore, another cluster was formed within the epithelial tissue (green), which may indicate the differential lipid signature of the nuclei. As previously described, colonocytes are highly polarized cells with the nuclei located at the bottom of the cells, the outermost part of the crypt. However, this would require further validation that is out of the scope of this thesis.

Even though a wide variety of lipid classes were detected, the gradients observed were mostly in phospholipids. This led us to investigate thoroughly the evolution of the phospholipidome in this structure.

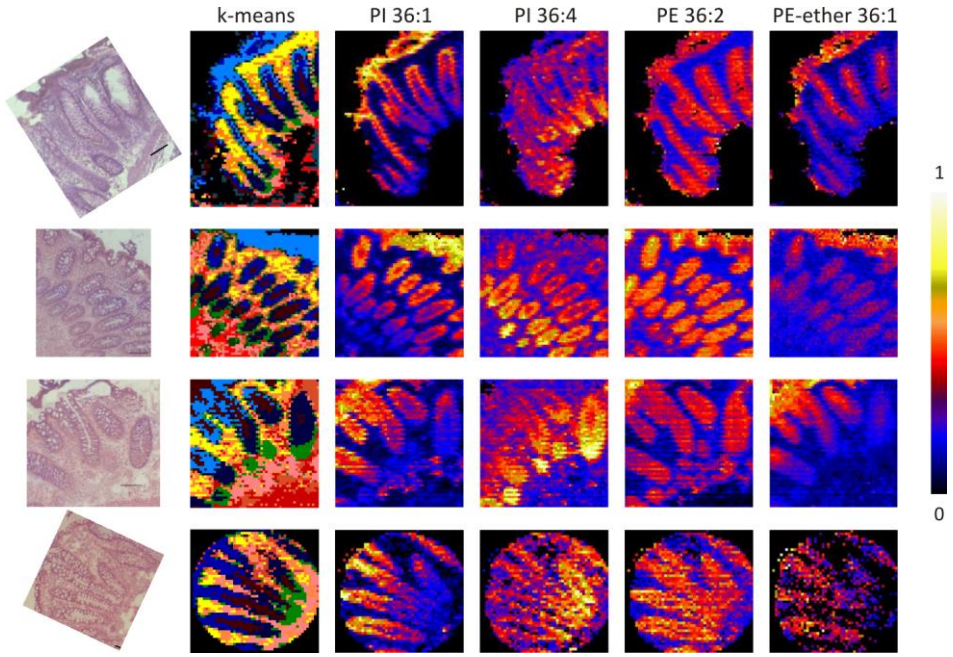

Fig. 4.6. First column: hematoxylin and eosin staining of colonoscopy biopsies included in the study; second column: *k-means* clustering analysis for pattern recognition; and the rest of columns show the distribution of some of the lipids displaying a gradient in intensity.

For this purpose, the approach used was to evaluate, pixel-by-pixel, the changes occurring along a path depicted from the bottom to the top of the crypt (Figure 4.7.A). Once all the spectra were extracted, the strategy was to analyze the data from each family

of glycerophospholipids separately, normalizing the species to the total sum of each subclass. Thus, as an example, Figure 4.7.B shows the variation on the relative amount of PI 36:1 along the crypts from different samples, which can be averaged and described by a straight line with high correlation coefficient (R^2 = 0.97) (Figure 4.7.C).

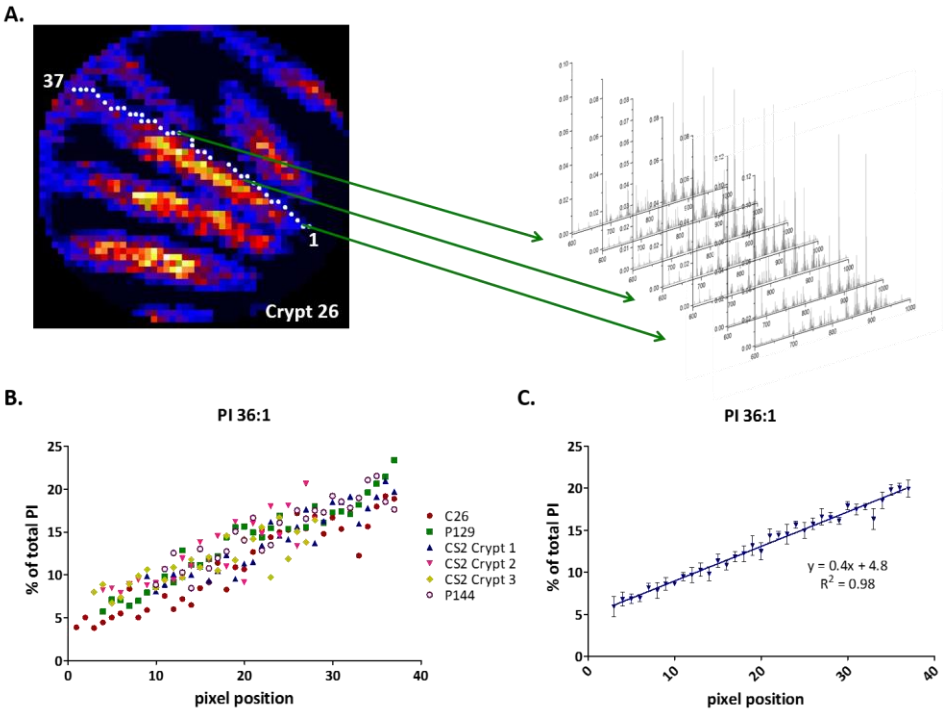

Fig. 4.7. **A** – An example MALDI-IMS image showing the path drawn to analyze, pixel-by-pixel, the changes in the lipidome along the crypt, and representative MS spectra associated to different pixels. **B** – The changes in PI 36:1 normalized to the total PI along the crypt from different samples. **C** – The average distribution of PI 36:1 (n = 6) with a linear fit.

Among all the lipid species detected, the relative intensity (RI) of 15 the phospholipids showed a clear correlation with the pixel position along the crypt, following either a linear or a logarithmic behavior (showing very high correlation coefficients, Tables A.4.1 and A.4.2). Strikingly, these species, felt into three well-defined lipid categories tightly involved in cell signaling: PI species, PE-ether and arachidonic acid-containing species (AA, 20:4n-6).

About 98.5% of PI species displayed changes in the epithelium that correlated with the position of the pixel along the crypt. Interestingly, all AA-species followed a logarithmic decrease (PI 38:4, 36:4, 38:5 and 40:4; R^2 = 0.96, 0.94, 0.64 and 0.89, respectively, Figure 4.8). Specially, PI 38:4 was the specie experiencing the largest change, from 70 to 20% of total PI, which is somehow unexpected, as this lipid is by far the most abundant PI in mammals.[20] Conversely, species containing monounsaturated and/or diunsaturated fatty

acids (MUFA/DUFA) increased linearly (PI 34:1, 34:2, 36:1 and 36:2; R^2 = 0.89, 0.76, 0.98 and 0.94, respectively).

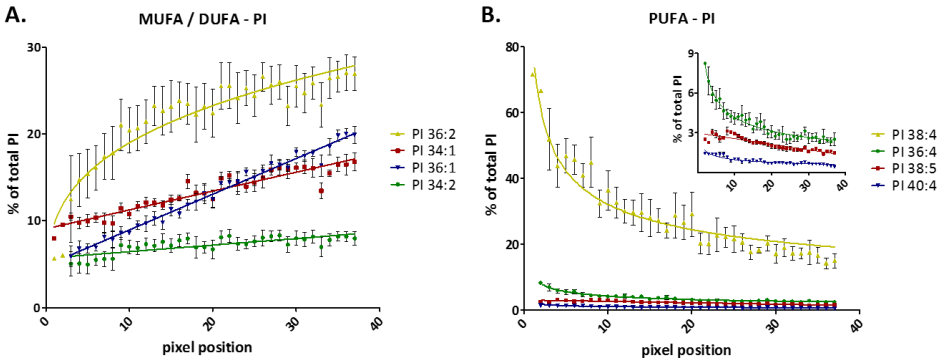

Fig 4.8. Fitted curve showing changes in PI species according to the distance of the pixel to the base of the crypt. **A** - MUFA/DUFA-containing species. **B** - AA-containing species. Values represent the average of the percentage of each specie with respect to the total of PI from six different crypts.

Remarkably, the increase in the sum of MUFA/DUFA mirrored precisely the decrease in AA-containing PIs, indicating that the turnover of these PI species is a highly synchronized event during colonocyte differentiation and that they are extremely sensitive to the developmental state of the cell (Figure 4.9).

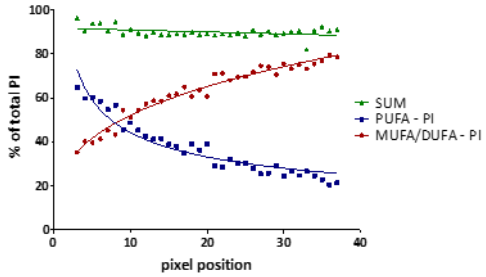

Fig. 4.9. Fitted curve of the sum of MUFA/DUFA and PUFA species that show a monotonal variation along the crypt, and sum of PUFA + MUFA/DUFA-containing species. (n=6)

PE-ether (vinyl ether subclass) species behave identically to PI species, Figure 4.10. Approx. 75 % of total PE-ether (34:1, 36:1, 36:4, 38:4 and 40:4) followed logarithmic laws with high correlation coefficients, R^2= 0.70, 0.82, 0.91, 0.75 and 0.84, respectively (Table A.4.1 and A.4.2). As in the case of PIs, the negative gradient in AA-containing species mirrored the increase in MUFA/DUFA-containing species (Figure 4.10).

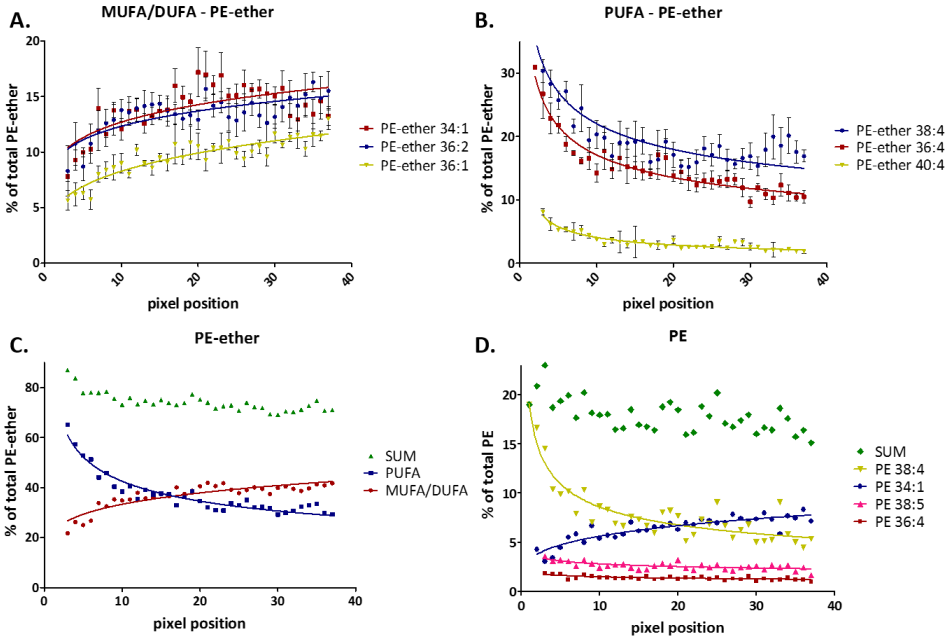

Fig. 4.10. Fitted curves showing changes in PE-ether and PE along the crypts. **A** - Different MUFA/DUFA-containing PE-ether showing an increase in concentration from the bottom to the luminal side of the crypt. **B** - AA-containing PE-ether species displaying a decrease in their expression. **C** - Sum of PUFA-containing and non PUFA-containing species and the sum of both. The decrease on one of them mirrors the increase of the other set of species. **D** - The few PE species exhibiting a change in their concentration along the crypts. Please note that they only account for ~20% of total PE, while in the case of PE-ether is ~75% (**C**).

However, the correlation between concentration and position along the crypt appeared not to be exclusive for PI and PE-ether, as AA-containing PE and PC also showed a logarithmic decrease (Table A.4.1 and .4.2). Thus, changes in PE 38:4 and 34:1 also correlated with the position along the crypt (R^2=0.79 and 0.80, respectively) and, although with lower R^2 values, some additional AA-containing species also showed a logarithmic decrease: PE 38:5 and 36:4, R^2=0.46 and 0.42 respectively, Figure 4.10.D.

Nevertheless, the most remarkable result was the stable values obtained for the most abundant PE species. In contrast to their ether analogues, the abundance of ~ 70% of them remained constant along the crypt, while 75% of PE-ether display changes in distribution, Figure 4.10.C-D. Considering that PE, together with PC, which behave similar to PE, are the major phospholipid classes in mammalian cells, the results suggest that these species could be playing an important role in cell integrity, as the cell maintains constant their values, regardless of its differentiation stage.

Altogether, it is clear that colonocytes strictly regulate their lipid composition concomitant to the differentiation process, modifying some species, while constraining the concentration of others within narrow limits.

These results were further confirmed using immunofluorescence (IF) techniques. Whether changes in the lipidome were accompanied with changes in protein expression was tested, focusing on enzymes involved in the turnover of the lipid species showing a gradient in distribution. This was carried out by our collaborators from Lipid in Human Pathology from Hospital Son Espases (Balearic Island).[21] The hypothesis is that this specificity in PI and PE-ether replacement could be achieved through coordinated regulation of phospholipase A_2 and acyltransferase activity. These enzymes account for the re/insertion of the fatty acid moiety into phospholipids via acylation reactions. Although the current knowledge on this large family of enzymes is still limited, the evidence points to their existence, and to a high selectivity for both, the lipid head group and the fatty acid at sn-2 position.[22]

It is a remarkable fact, the distinctive impact cell differentiation has on ethanolamine diacyl- and ether-lipids, indicating that despite the close metabolic relationship between them,[23] the precise composition at species level may be differently regulated. Yet, the literature is scarce in this regard.

Epithelium dedifferentiation in pathological context

To further test the relationship between a highly regulated lipidome and the differentiation process, we verified whether this regular lipid arrangement was altered in a pathological context, by analyzing human colon adenomatous (AD) polyps, the most common colon lesions. AD polyps are an abnormal growth of tissue with the potential for transformation into invasive carcinoma[24, 25, 26]. They have two basic features: dysregulated proliferation and the failure to fully differentiate. We were particularly interested in AD polyps because, unlike in neoplastic lesions, it is still possible to obtain structures clearly reminding colon crypts, despite the absence of a regular structure. Thus, it was still possible to analyze the changes in the lipid expression along the AD epithelium, pixel-by-pixel.

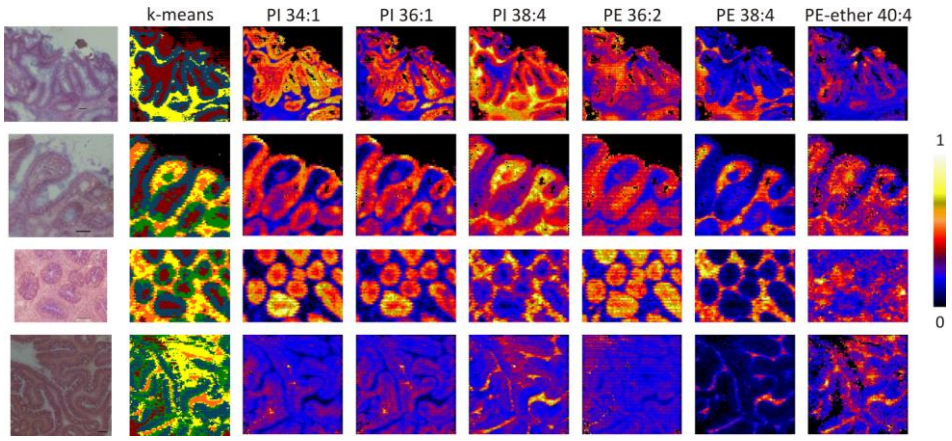

Fig. 4.11. First column: H&E staining of Adenomatous colonic crypts; second column: *k-means* segmentation analysis for pattern recognition; and the rest of columns show the distribution of some of the lipids.

MALDI-MS images readily showed that the strict distribution of lipid species was indeed greatly disturbed in AD, Figure 4.11. Thus, PI 38:4 and 36:1 values, two of the PI species showing the most prominent changes in concentration along the crypt in healthy mucosa, presented a rather constant concentration along the AD crypt, exhibiting variations along the AD epithelium of ±15% of their average value, Figure 4.12. The variations in concentration with the position in the crypt previously observed for most of the PE-ether species (36:1, 36:2, 36:4, 38:4) were also absent, indicating that PE-ether and PI metabolism were deregulated in AD epithelium.

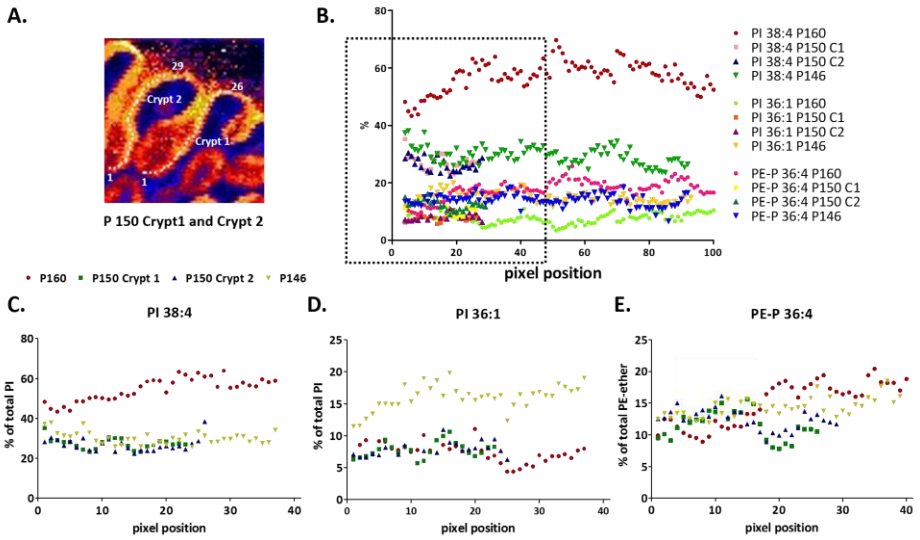

Fig. 4.12. A – Selected MALDI-IMS image of an adenomatous biopsy showing the paths drawn to analyze, pixel by pixel, the changes in lipid composition. **B** – Distribution of PI 38:4, PI 36:1 and PE-ether 36:4 along different crypts from different AD biopsies. The changes observed in healthy epithelium are lost. **C–E** – Distribution of those three lipids, which are some of the most regulated species in healthy epithelium, zoomed for a better visualization. (n=4)

Unlike in healthy epithelium, and in agreement with the dedifferentiation process, in most cases only one epithelial cluster surfaced during *k-means* segmentation of IMS experiments on adenoma (Fig 4.11. blue cluster) and carcinoma sections (Figure A.4.3). The average spectra obtained for healthy basal, healthy apical, AD and carcinoma were statistically compared using Student's t-test, Figure 4.13.

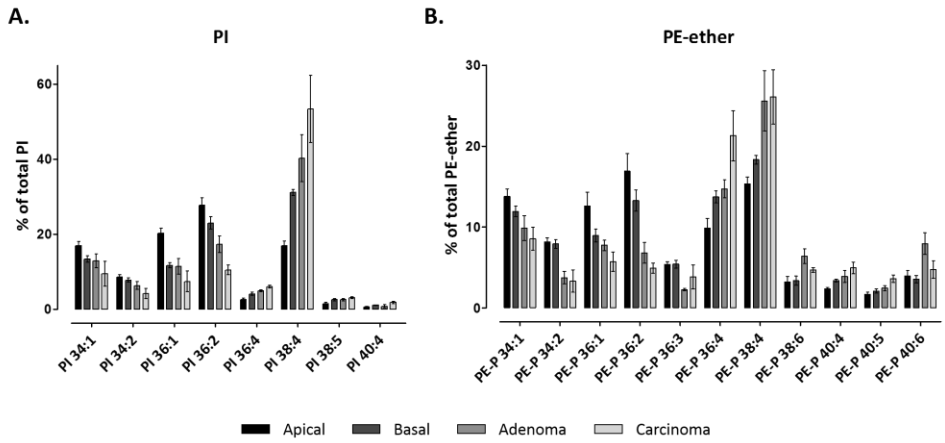

Fig 4.13. Bar diagrams comparing the changes in PI (**A**) and PE-ether (**B**) composition in healthy apical, healthy basal, adenomatous polyps and carcinoma epithelial segments previously established by *k-means*. Only species showing statistical differences are shown, together with the symbols that indicate significance in Table 4.1. Statistical significance was assessed using Student's t-test (p value < 0.05). Values are expressed as mean ± SEM (n=4 in healthy and AD clusters and n=3 in carcinoma).

The large error bars in Figure 4.13 may be in part due to the human origin of the samples. Furthermore, the groups of study were not anatomically homogenous, except for the controls. Thus, within the AD polyp group, adenomas differed in the degree of dysplasia while the carcinoma group included biopsies at different stages of the disease. Still, a clear trend is evident, showing a tendency from apical to basal to AD, and carcinoma samples exhibiting the most differentiated lipid composition compared to healthy apical tissue.

The results exhibited profound differences, especially in PE-ether species as the comparison with AD clusters showed a robust increase from approx. 50% to 72% in long chain PUFA-containing species (36:4, 38:4, 38:6, 40:6) , and a decrease from 50% to 28% in non-PUFA containing species (34:2, 36:1, 36:2, 36:3), Figure 4.13., Table 4.1 and Table A.4.3). These changes were even more notable in carcinoma epithelium, all pointing in the same direction, except for 38:6 and 40:6, which decreased in carcinoma compared to adenoma. Thus, total PUFA-containing species increased up to 77%, whereas non-PUFA species decreased to 23% of total plasmalogen species in carcinomatous epithelium. Comparing adenoma with carcinoma, the most relevant change was the 60% increase in PE-ether 36:4.

Consistently, this increase in AA-containing species and the parallel decrease in mono and/or diunsaturated species was also observed for epithelial PI, especially in carcinomatous epithelium, since adenoma is quite similar to basal epithelium in non-PUFA containing species (34:1, 34:2, 36:1).

The similarity between basal and AD clusters is also reinforced in the analysis of PE species (Table A.4.3 and A.4.4), leading to a scenario in which AD epithelium resembles

somehow the undifferentiated colonocytes and stem cells, highlighting the undifferentiated nature of cells undergoing a tumorigenic process.

Table 4.1. PI and PE-ether lipids statistically different at least in one of the multiple comparisons made. These results were assessed according to the Student's t-test. * $p < 0.05$; ** $p < 0.01$; *** $p < 0.005$; **** $p < 0.001$

		Apical vs Basal	Apical vs AD	Apical vs Carcinoma	Basal vs AD	Basal vs Carcinoma	AD vs Carcinoma
PI	34:1	*					
	34:2			*		*	
	36:1	**	*	**			
	36:2		*	**		**	*
	36:4	*	**	**		*	*
	38:4	****	*	**		*	
	38:5	*	*	**			
	40:4			**		*	
PE-ether	P 34:1			*			
	P 34:2		**	*	**	*	
	P 36:1		*	*			
	P 36:2		**	**	*	**	
	P 36:3		***		***		
	P 36:4	*	*	*		*	*
	P 38:4	*	*	*		*	
	P 38:6		*		*		
	P 40:4	**		**			
	P 40:5			*		*	*
	P 40:6		*		*		

It is worth stressing that the exchange of PUFA-MUFA species along the crypt is especially interesting for PI and PE-ether, phospholipids with the highest content in AA-species, and the fact that, these AA-species are also increased in AD and carcinoma, points altogether to a critical role of AA metabolism in both, colonocyte division and differentiation. According to our results, the higher the division rate, the larger the amount of esterified AA found (differentiated cell < stem cell < adenoma < carcinoma). Thus, it is tempting to speculate that one of the early events during the colonocyte dedifferentiation process involves or leads to the loss of the control over the substitution of AA-species by MUFA/DUFA species. Hence, the affected stem cell would acquire certain advantage that would help to expand faster and to occupy the whole cell niche. Eventually, the mutation

would spread within the epithelium contributing to the initiation and progression of the carcinoma.[14, 27]

Differentiation status in healthy and pathological lamina propria

Regarding the connective tissue, the comprehensive analysis of the lipidome along the lamina propria provided evidence of an additional level of complexity in understanding the specific function of membrane lipids. Unlike the epithelial layer, lamina propria contains a complex mixture of cells of different origin. This fact, at least initially, made less likely the presence of a gradient in lipid composition. However, IMS images at 10 µm did expose a lipid gradient (Figure 4.14.) uncovering a quite different scenario compared to epithelium. And specially, the statistical analysis of the clusters reinforced the hypothesis that the lipid composition varies along the lamina propria, with the formation of three clusters: basal (pink color), intermediate (orange) and apical (yellow).

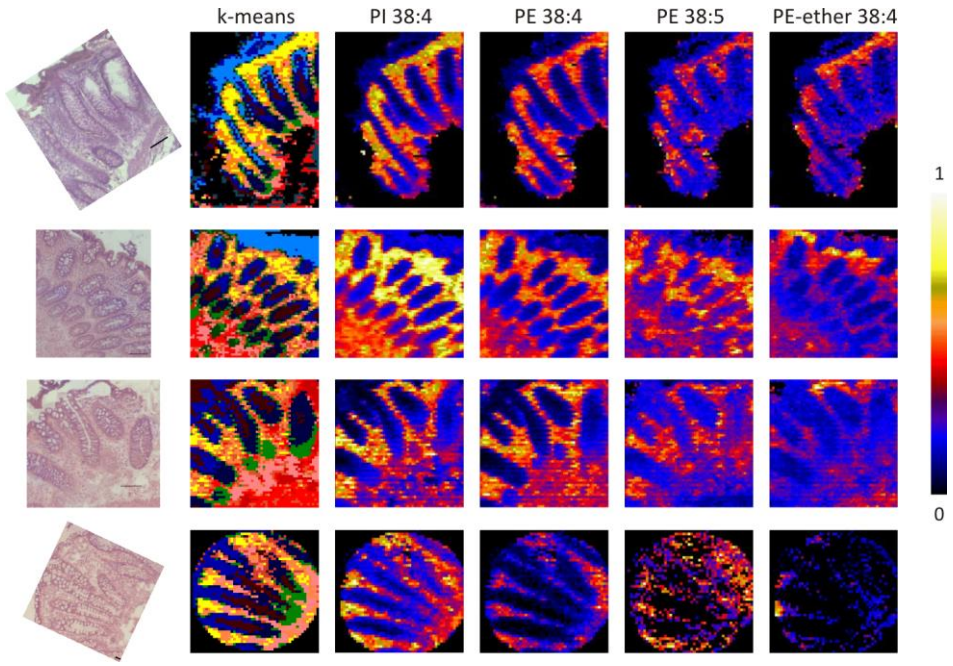

Fig. 4.14. First column: H&E staining of healthy colonic biopsies; second column: *k-means* clustering analysis for pattern recognition; the rest of columns show the distribution of some of the lipids displaying a gradient in intensity in lamina propria.

The most striking observation is that AA-containing phospholipids, especially in the case of PE (and PC in positive-ion mode, Table A.4.5), but also slightly in PI, behave in opposite way from the one observed in the healthy colonic crypt: for example, increasing 38:4 species and decreasing 36:2. Figure 4.15. shows these observations, when the three clusters formed in healthy lamina propria are compared. Thereby, larger quantities of the

pro-inflammatory AA would be available for the cells involved in the immunological response, those located exactly where the gradient of these lipids species reaches the maximum.[16,28] Thus, this clearly indicates the different roles that the same species may play according to the cell context.

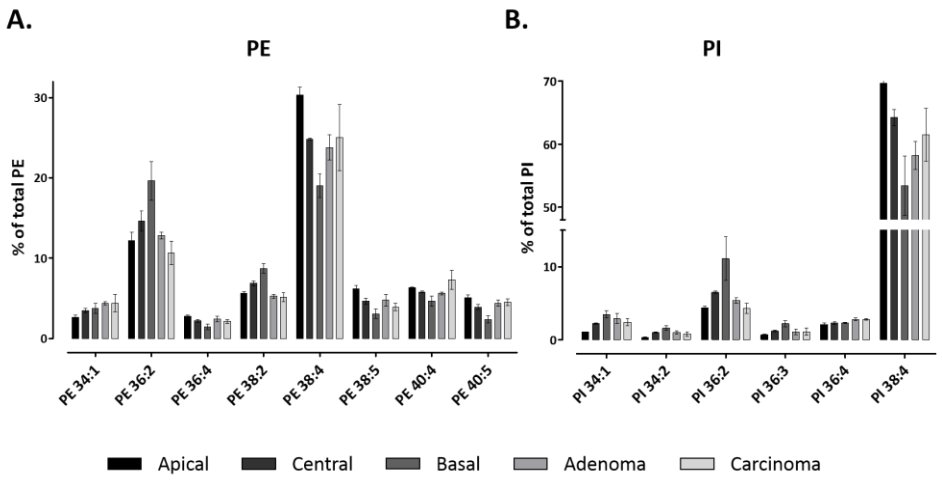

Fig. 4.15. Bar diagrams comparing the lipid species between the three clusters formed in healthy lamina propria, adenomatous LP and carcinoma for PE (**A**) and PI (**B**). Only species significantly different are shown. Statistical significance was assessed using Student's t-test which can be found summarized in Table 4.2 (p value < 0.05). Values are expressed as mean ± SEM (n=4 in healthy and AD clusters and n=3 in carcinoma).

When the three healthy LP clusters are compared with the single LP cluster formed in adenomatous (Figure 4.11. yellow cluster) and cancerous biopsies (Figure A.4.3. yellow cluster), some individual statistical differences were identified, Table 4.2 and Table A.4.6, although they were clearly less pronounced than those observed in the epithelium. The most relevant difference was the decrease in AA-containing species compared to the epithelium, Figure 4.15, points to profound differences in how cells handle the same lipid species, for example PI 38:4.

Table 4.2. PE and PI lipid species that are, statistically different, at least in one of the multiple comparisons made. These results were analyzed by the Student's t-test. * p › 0.05; ** p › 0.01; *** p › 0.005. (Ap: Apical; B: Basal; M: Center; AD: Adenoma; and C: Carcinoma). Only species statistically different are shown. For the average phospholipid composition for each cluster, see Table A.4.5.

		Ap vs B	Ap vs M	Apl vs AD	Apl vs C	B vs M	B vs AD	B vs C	M vs AD	Ml vs C
PE	34:1			**					*	
	36:2	*					*	*		
	36:4	*								
	38:2	**	*				**	*	**	
	38:4	**	**	*		*				
	38:5	*	*		*					
	40:4		*	*						
	40:5	**				*	*	*		
PI	34:1	**	***							
	34:2	**	**	*						
	36:2		**							*
	36:3	*	**							
	36:4			*	*			**		
	38:4	*	*	**						

In contrast to the similarities found between the basal zone and adenoma in epithelium, results from lamina propria point in opposite direction. On this occasion, adenomatous and cancerous connective tissue resemble somehow the upper zone in healthy lamina propria, exactly where more pro-inflammatory cells are located.

4.5 Conclusions

The first goal of this study was the development of a methodology for a successful high resolution IMS analysis with a commercial mass spectrometer equipped with a large laser spot. We demonstrate that with a meticulous procedure, using the right matrices and the correct deposition protocol, 10 µm, or even 5 µm of lateral resolution can be achieved, despite the strongly elliptical laser spot (170 µm x 40 µm).

This increase in resolution allowed us to clearly identify the lipids in the different tissue types present in a colon biopsy. In particular, we demonstrate that the lipid composition of the three main tissues (epithelium, lamina propria and muscularis mucosae) is unique and distinguishable. Interestingly, the statistical analysis that was performed over the images

also found differences between the upper and the bottom part of the crypts and lamina propria. These results emphasize the importance that lipids have in cell physiology, urging us to investigate the changes occurring in the lipidome along these two tissue types.

The study of over several healthy colonic biopsies showed that the abundance of some specific lipids is exquisitely regulated according to the cell type and to cell physiological stage. The description using a mathematical equation of the lipid distribution along the crypt implies that, based merely on its lipid signature, it is possible to predict and assess the pathophysiological status of a single cell embedded in a tissue. Additionally, while in the epithelium, lipid composition changed in an orchestrated manner according to their differentiation state, in lamina propria, it concurred with its characteristic gradient in inflammation. In both cases, AA-containing species were the lipids displaying the most tightly controlled distribution patterns. Yet, the most striking observation was that these species established an inverse gradient. This demonstrates how different two juxtaposed tissues may handle the same lipid specie, cautioning about potential misleading conclusions obtained when composition analysis is performed in tissue homogenates by LC-MS or when not enough spatial resolution is achieved by IMS.

In conclusion, these results strongly reinforce the translational impact that both lipid fingerprint and IMS techniques might have on clinical research.

---

[1] Spengler B, Hubert M, Kaufmann R. MALDI ion imagingand biological ion imaging with a new scanning UV-laser microprobe. *Proceedings of the 42nd ASMS Conference on Mass Spectrometru and Allied Topics*. **1994**.

[2] Caprioli RM, Farmer TB, Gile J. Molecular imaging of biological samples: localization of peptides and proteins using MALDI-TOF MS. *Anal. Chem*. **1997**. 69:4751-4760.

[3] Stoecki M, Farmer TB, Caprioli RM. Automated mass spectrometry imaging with a matrix-assisted laser desorption ionization time-of-flight instrument. *J. AM. SOC. Mass Spectrom*. **1999.** 10:67-71.

[4] Todd PJ, Schaaff TG, Chaurand P, Caprioli RM. Organic ion imaging of biological tissue with secondary ion mass spectrometry and matrix-assisted laser desorption/ionization. *J. Mass Spectrom*. **2001**. 36:355-369

[5] Stoeckli M, Chaurand P, Hallahan DE, Caprioli RM. Imaging mass spectrometry: a new technology for the analysis of protein expression in mammalian tisues. *Nat. Med*. **2001**. 7:493-496.

[6] Dreisewerd K. Recent methodological advances in MALDI mass spectrometry. *Anal. Bional. Chem*. **2014**. 406:2261-2278.

[7] Murphy RC, Hankin JA, Barkley RM. Imaging of lipid species by MALDI mass spectrometry. *J. Lipid Res*. **2009**. 50:S317-S322.

[8] Spraggins J, Caprioli RM, High-speed MALDI-TOF imaging mass spectrometry: rapid ion image acquisition and considerations for next generation instrumentation. *J. Am. Soc. Mass Spectrom*. **2011**. 22:1022-1031.

[9] Jurchen JC, Rubakhin SS, Sweedler JV. MALDI-MS imaging of features smaller than the size of the laser beam. *J. Am. Soc. Mass Spectrom*. **2005**. 16:1654-1659.

[10] Puolitaival SM, Burnum KE, Cornett DS, Caprioli RM. Solvent-free matrix dry-coating for MALDI imaging of phospholipids. *J. Am. Soc. Mass Spectrom*. **2007**. 18:1646-1652.

[11] Goodwin RJA, Scullion P, MacIntyre L, Watson DG, Pitt AR. Use of a solvent-free dry matrix coating for quantitative matrix-assisted laser desorption ionization imaging of 4-bromophenyl-1,4-diazabicyclo(3.2.2)nonane-4-carboxylate in rat brain and quantitative analysis of the drug from laser microdissected tissue regions. *Anal. Chem*. **2010**. 82:3868-3873.

[12] Trimpin S, Herath TN, Inutan ED, Wager-Miller J, Kowalski P, Claude E, Walker JM, Mackie K. Automated solvent-free matrix deposition for tissue imaging by mass spectrometry. *Anal. Chem*. **2010**. 82:359-367.

[13] Hankin JA, Barkley RM, Murphy RC. Sublimation as a method of matrix application for mass spectrometric imaging. *J. Am. Soc. Mass Spectrom.* **2007**. 18:1646-1652.

[14] Thomas A, Charbonneau JL, Fournaise E, Chaurand P. Sublimation of new matrix candidates for high spatial resolution imaging mass spectrometry of lipids: enhanced information in both positive and negative polarities after 1,5-diaminonapthalene deposition. *Anal. Chem.* **2012.** 84:2048-2054.

[15] Humphries A, Wright NA. Colonic crypt organization and tumorigenesis. *Nat. Rec. Cancer.* **2008**. 8:415-424.

[16] Strupat K, Kovtoun V, Bui H, Viner R, Stafford G, Horning S. MALDI produced ions inspected with a linear ion trap-orbitrap hybrid mass analyzer. *J. Am. Soc. Mass Spectrom.* **2009**. 20:1451-1463

[17] Riddell R, Jain D. Small and large bowel structure: developmental and mechanical disorders. *Gastrointestinal Pathology and its Clinicals Implications, vol. 2.* **2014**. 267-283.

[18] Shoshkes-Carmel M, Wang YJ, Wangensteen KJ, Tóth B, Kondo A, Massassa EE, Itzkovitz S, Kaestmer KH. Subepithelial telocytes are an important source of Wnts that supports intestinal crypts. *Nature.* **2018**. 557:242-246

[19] Powell DW, Pinchuk IV, Saada JI, Chen X, Mifflin RC. Mesenchymal cells of the intestinal lamina propria. *Annu. Rev. Phyiol.* **2011**. 73:213-237.

[20] D'Souza K, Epand RM. Enrichment of phosphatidylinositols with specific acyl chains. *Biochim. Biophys. Acta.* **2016**. 1838:1501-1508.

[21] Bestard-Escalas J, Garate J, Maimo-Barcelo A, Fernandez R, Lopez DH, Lage S, Reigada R, Khorrami S, Ginard D, Reyes J, Amengual I, Fernandez JA, Barcelo-Coblijn G. Lipid fingerprint image accurately conveys human colon cell pahophysiologic state: a solid candidate as biomarker. *Biochim. Biophys. Acta.* **2016**. 186: 1942-1950.

[22] Yamashita A, Hayashi Y, Nemoto-Sasaki Y, Ito M, Oka S, Tanikawa T, Waku K, Sugiura T. Acyltransferases and transacylases that determine the fatty acid composition of glycerolipids and the metabolism of bioactive lipid mediators in mammalian cells and model organisms. *Prog. Lipid Res.* **2014**. 53:18-81.

[23] Dorninger F, Brodde A, Braverman NE, Moser AB, Just WW, Forss-Petter S, Brugger B, Berger J. Homeostasis of phospholipids – the level of phosphatidylethanolamine tightly adapts to changes in thanolamine plasmalogens. *Biochim. Biophys. Acta.* **2015**. 1851:117-128.

[24] Fearon ER, Vogelstein B. A genetic model for colorectal tumorigenesis. *Cell.* **1990**. 61:759-767.

[25] Snover DC. Update on the serrated pathway to colorectal carcinoma. *Hum. Pathol.* **2011**. 42:1-10.

[26] Levine JS, Ahnen DJ. Clinical practice. Adenomatous polyps of the colon. *New Engl. J. Med.* **2006.** 355:2551-2557.

[27] Barker N. Adult intestinal stem cells: critical drivers of epithelial homeostasis and regeneration. *Nat. Rev. Mol. Cell Biol.* **2014**. 15:19-33.

[28] O'Leary AD, Sweeney EC. Lymphoglandular complexes of the colon: structure and distribution. *Hystopathology.* **1986**. 10:267-283.

Chapter 5

An untargeted lipidomic study: IMS and multivariate analysis to discriminate melanoma from benign melanocytes

It is clear from the previous chapter that IMS enables localization of hundreds of biomolecules simultaneously, making it an attractive technique in biological system research. Still, the main goal of this young technique is its translation to clinical research, mostly to oncology, pathology and diagnostic. In recent years, technological and methodological improvements have aided to clinical acceptance of IMS. Still, there are some challenges to be solved for the technique to achieve its full potential, particularly with respect to spatial resolution, data management and analysis of multiple comparative studies.

This chapter addresses the comparison between multiple experiments with the final goal of early melanoma detection. Performing such comparison is a challenging and delicate process that is hampered by the large heterogeneity of the tissue and the huge amount of data generated in each experiment, making interpretation and analysis complex.

The data presented here have been published in part in:

1. **Garate J**, Lage S, Fernández R, Velasco V, Abad B, Asumendi A, Gardeazabal J, Arroyo-Berdugo Y, Rodríguez MA, Artola JL, Zabalza I, Ochoa B, Fernández JA, Boyano MD. Imaging mass spectrometry-based lipidomic approach to classification of architectural features in nevi. *J. Invest. Dermatol.* **2019**. Accepted, in press.

2. **Garate J**, Lage S, Martin-Saiz L, Perez-Valle A, Ochoa B, Boyano MD, Fernández R, Fernández JA. Influence of lipid fragmentation in the data analysis of imaging mass spectrometry experiments. Submitted to *Anal. Chem.*

5.1 Introduction

Melanoma is one of the most aggressive forms of cancer. Cancerous growth develops when melanocytes, the melanin producing cells in the skin, begin to multiply rapidly and form malignant tumors (Figure 5.1).[1] Its incidence has been increasing in white population in the past two decades due to large exposure to UV radiation, one of the main risk factors in melanoma.

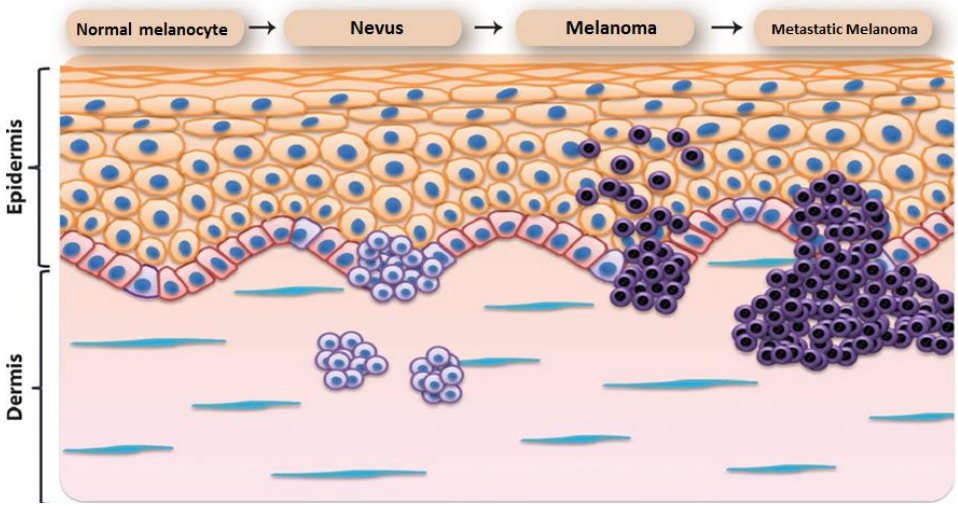

Fig. 5.1. Progression of melanoma from controlled melanocytes to metastatic melanoma in the skin. Under normal conditions, melanocytes are located amongst the basal layer of the epidermis, lodged between keratinocytes, which control the proliferation and differentiation of melanocytes. Due to the mutation of certain genes, melanocytes evade the control exerted by keratinocytes, and proliferate and spread forming moles (nevi). These moles are generally benign, but they may eventually undergo transformation processes and progress towards the formation of melanoma. (Adapted with permission from He Liu et al. *Sci. Transl. Med.* **2013**. 5)

Cutaneous melanocytic lesions represent a collection of heterogeneous entities, ranging from completely benign melanocytic nevi, which are common and have a negligible risk of progressing, to malignant and invasive melanomas, which have the potential to metastasize (Figure 5.1). Achieving a correct diagnosis of these conditions is by no means an easy task, owing to their large variability.[2] There are commonly accepted landmarks that dermatologists use to visually distinguish malignant melanomas from benign nevi. However, such characteristics are sometimes also present in benign skin lesions, leading to erroneous diagnosis.[3] Moreover, the intra- and inter-observer reproducibility among pathologist in the evaluation of challenging melanocytic neoplasm is considered to be poor.[4,5,6] Classic histopathological examination remains the gold standard to diagnose clinically ambiguous lesions,[4] although attempts have been made to introduce more objective alternatives, such as immunohistochemistry (IHC). This technique produces useful additional information regarding the presence of key proteins

that may help the pathologist reach a diagnosis. However, in the same way that hematoxylin and eosin (H&E) histology is limited by subjective interpretations of visual images, the failure to standardize essential steps of the IHC protocols (such as tissue pretreatment, reagents, detection methods and interpretation) restricts its use as a routine technique.[5] Furthermore, IHC is usually limited to the simultaneous visualization of only one or two proteins.[7] Nevertheless, it must be recognized that most melanocytic tumors are readily categorized as benign or malignant using traditional methods.

MALDI-IMS provides the opportunity to adopt a molecular approach to the diagnosis of these entities, due to its ability to map the distribution of large populations of biomolecules. We have previously described in Chapter 4 that the lipid composition of cells can vary with the differentiation process and disease state, signaling the beginning of malignancy. This enables the discovery of biomarkers for diagnostic purposes, for prognosis purposes, or to predict the response to therapy.

In this context, data analysis is an important and challenging part of MSI comparative studies.[8,9] In order to classify high-dimensional data, an extensive pre-processing is mandatory, also for a successful biomarker discovery with predictive power between healthy and diseases. It is also worth mentioning that, for this purpose, a simple statistically significant difference is not sufficient, but rather a more sophisticated multivariate analysis is required to build classification models.[8] Thus, the choice for data analysis and pre-processing steps depends on the type and number of samples.

Two of the major challenges in pre-processing, tumor heterogeneity and chemical noise of artifacts, will be addressed in this chapter during the process of creation of a classification model for nevi and melanoma: tumor heterogeneity and chemical noise or artifacts.

5.2 Tumor Heterogeneity

Cancerous cells are biologically heterogeneous, differing in their genomes, transcriptomes and proteomes, as well as in their metabolism and proliferative and metastatic potential.[10] Thus, the mix of different tumor cells with different phenotypic features within a tumor from a patient is named intratumor heterogeneity (ITH). Moreover, tumors from the same patient may also differ in their molecular features. This level of variability is known as intertumor intrapatient heterogeneity. The last level of heterogeneity is the interpatient variability, which deals with a given tumor type from different individuals.[11] A graphical description of these variabilities can be found in Figure 5.2.

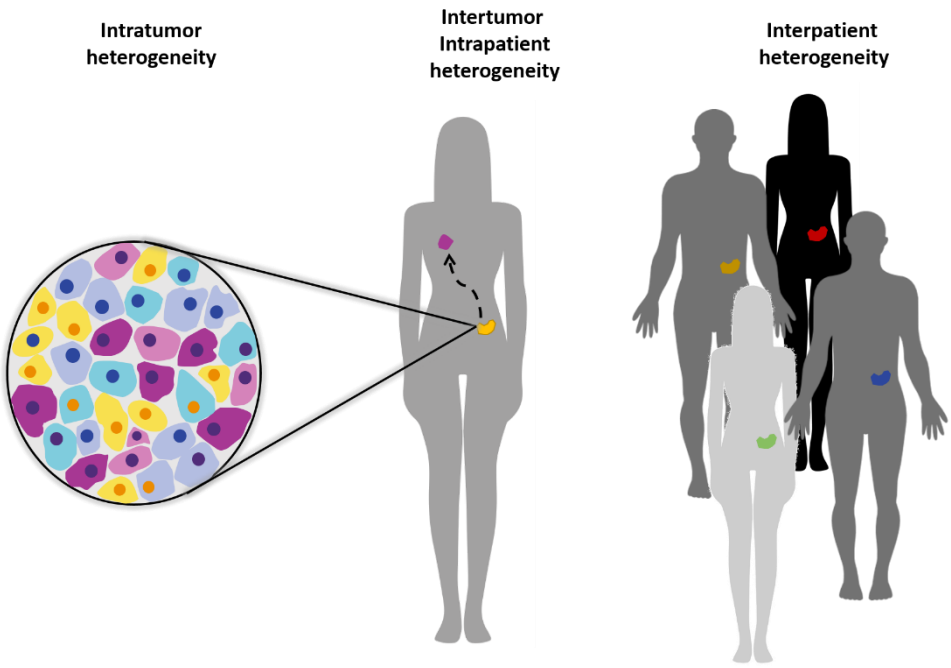

Fig. 5.2. Schematic representation of intertumor and intratumor heterogeneity.

In addition to this complexity, tumor cells are surrounded by stroma, which consists of different cell types, such as fibroblasts, macrophages and immune cells, responsible for the immune response. All this together constitute the tumor microenvironment, taking the heterogeneity of the tumor to a more complex level.

The main advantage of investigating ITH by MALDI-IMS is the possibility of finding cell populations with unique phenotypes that are indistinguishable at microscopic level.[12] These subpopulations could be relevant in tumor progression, as well as in determining the disease outcome.[13] Hence, characterization of tumors becomes fundamental to have a better picture of the tissue landscape in order to understand cancer development.

5.3 The nature of the chemical noise

The other big challenge in multiple comparison cancer studies by MALDI-IMS has been, and is still today, the massive and variable data that is generated in each experiment. In order to overcome the imbalance of the data between samples, it is primordial to reduce the influence of the so-called chemical noise. This chemical noise is produced during the desorption and ionization process, and it is due to the interference from matrix, impurities and fragmentation.

The mass spectrum obtained at each pixel contains the peaks of the target molecules, mixed with a broad collection of adducts and fragments, as well as matrix peaks and impurities. All those undesired signals, apart from complicating the detection of the target species and their correct identification, introduce a statistical noise that strongly perturbs data analysis and in some cases, completely blurs further analysis. Therefore, elimination of those unnecessary peaks, or de-noising of the spectrum, with an accurate identification is crucial.

Here we deal with the difficult task of lipid identification directly from the tissue. This is a problem that was previously reported in a series of pioneering works on MALDI-IMS.[14, 15, 16] However, it is not an easy task, due to the abundance and variety of lipid species, their numerous fragmentation pathways and their tendency to form a significant number of adducts, hampering the accurate identification of some lipid species.

5.4 Objectives

This chapter is divided in three parts.

1. We will explore the fragmentation pathways of 13 lipid classes using lipid standards first, and real samples later, for a comprehensive identification. For this purpose, nevi sections will be used and we will evaluate the bias that the fragments introduce in the statistical analysis of MALDI-IMS experimental data.

2. Melanoma is one of the most aggressive, complex and heterogeneous cancer with several distinct phenotypic and molecular features. The second objective of this chapter is to study this heterogeneity in melanoma and nevi sections.

3. To conclude, and taking into account the first two steps, we will determine lipid features that distinguish melanocytes (nevi) and malignant melanoma (melanoma) to build a classification model. We will use mass spectrometry and multivariate analysis to classify melanoma, validating the use of lipid profiles for this task.

5.5 Experimental section

Lipid standards

As glycerophospholipids and sphingolipids are relevant not only as important constituents of cell membranes, but also due to their involvement in cell signaling processes and may be regarded as disease markers, we will deal exclusively with these classes. Table 5.1 summarizes the 13 lipid standards used in this study.

Table 5.1. Lipid standards used to characterize the different ionization these lipids undergo.

Phospholipid standards		Sphingolipid standards	
Specie	*Mass*	*Specie*	*Mass*
PA 18:1/18:1	700.5043	Cer d18:1/18:0	565.5434
PC 16:0/18:1	759.5778	CerP d18:1/16:0	617.4784
PC P-18:0/18:1	771.6142	GM3 18:0/18:0	1182.7601
PE 16:0/18:1	717.5309	HexCer 18:1/18:0	727.5962
PE P- 18:0/18:1	729.5672	SM d18:1/12:0	646.5050
PG 18:0/18:0	778.5724	SFT d18:1/12:0	723.4591
PI 16:0/18:1	836.5415		
PS 16:0/16:0	735.5050		

Lipid standards preparation

Lipid standards (Avanti Polar Lipids, Alabaster, AL, US) were diluted with methanol to a concentration of 1mg/ml. To reproduce the tissue ionic environment, these standards were mixed with phosphate buffered saline (PBS, 1:10). To simulate the conditions of preparation in a MALDI imaging experiment, the standard:PBS mixtures were spotted on a glass slide and left to dry prior to matrix deposition. Full description of matrix sublimation can be found in the Materials and Methods (Chapter 3).

Imaging and data analysis for lipid standards

Data was acquired emulating the protocol used for tissue sections: scanning a representative area with a step size of 25 µm and a mass resolution of 100.000 FWHM at m/z = 400, with a laser energy between 20-30 µJ/pulse. The rest of the MALDI-IMS parameters were set as described in materials and methods, Chapter 3. The spectra of lipid standards were analyzed using Xcalibur 2.0 (ThermoFisher).

Human sample collection

39 patients were enrolled in this study. The sample collection was specifically approved by the Euskadi Ethics Committee. Biopsies were obtained at the Department of Dermatology at Cruces University Hospital, Galdakao-Usansolo Hospital and IRBLleida Biobank.

Biopsies were immediately snapped frozen in liquid nitrogen and stored at -80°C until sample preparation. Sections of 15 µm thickness were prepared in a cryostat and placed on glass slides.

Imaging and data analysis

A detailed description of sample preparation can be found in Chapter 3 and the optimal amount of matrix for the instrument used is described in Chapter 4.

Data was acquired only in negative-ion mode with 25 µm spatial resolution and mass resolution of 60.000 FWHM at m/z = 400, and a laser energy of 20-30 µJ/pulse. The rest of the MALDI-IMS parameters used are described on Materials and methods (Chapter 3). Staining with H&E (Sigma Aldrich Química, Madrid, Spain) was carried out for all biopsies once MALDI-IMS experiments were completed and matrix removed.

Data analysis was carried out with in-house made softwares built in Matlab (MathWorks, Natick, USA) using captation parameters described in Chapter 3. For clustering, a *k-means* and an in-house algorithm were used (see description in Results section). IBM SPSS Statistics for Windows (Version 23.0; IBM, Chicago, IL, USA) was used for Levene's test, one-way ANOVA and Bonferroni/Games-Howell post multiple comparison. Levene's test determines the homogeneity of the variables (H_0 = groups have equivalent variances) in order to choose the correct post hoc method: Bonferroni if Levene's $p \geq 0.05$ and Games-Howell if Levene's $p \leq 0.05$. In all instances, p values < 0.05 were considered statistically significant. Correlation coefficients were calculated in Matlab. Orange (Bioingormatics Lab, University of Ljubljana, Slovenia)[17] was used for PCA, development of classification model with different algorithms and for their external validation.

5.6 Results and discussion

Mass spectra of lipid standards: In-source fragmentation pathways

Figures 5.3 and 5.4 show the spectra obtained for glycerophospholipid standards analyzed by MALDI-IMS. It is well known that lipids tend to form different adducts, especially in positive-ion mode, with Na^+ and K^+. However, there are many other adduct sources that may not be as evident. Adducts can come from in-source fragmentation. Despite the soft ionization characteristic of MALDI, lipids are labile molecules that fragment easily, even at low laser fluence.

Almost all glycerophospholipids tend to fragment into PA-isobaric species by the total loss of the headgroup. This fragmentation pathway is noticeable in the case of PE, PE-ether, PS species and especially in PC species and their ether analogues. It is also remarkable that, although PC and PC-ether are positively charged lipid subclasses, they are still detectable in negative-ion mode by losing one methyl group instead of a proton, as in the case of the other species.

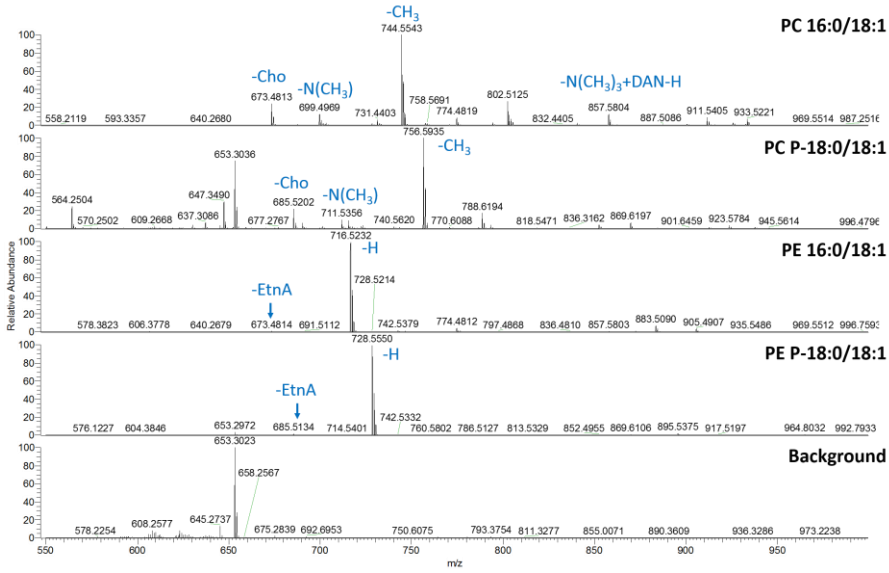

Fig 5.3. Spectra obtained from glycerophospholipid standards in negative-ion mode. Even thought the most intense m/z are $-CH_3$ and –H for PC/PC-ether and PE/PE-ether, respectively, there are other ionization modes due to prompt fragmentation. The loss of the head group substituent resulting in the respective PA is especially intense. EtnA: ethanolamine. Cho: choline.

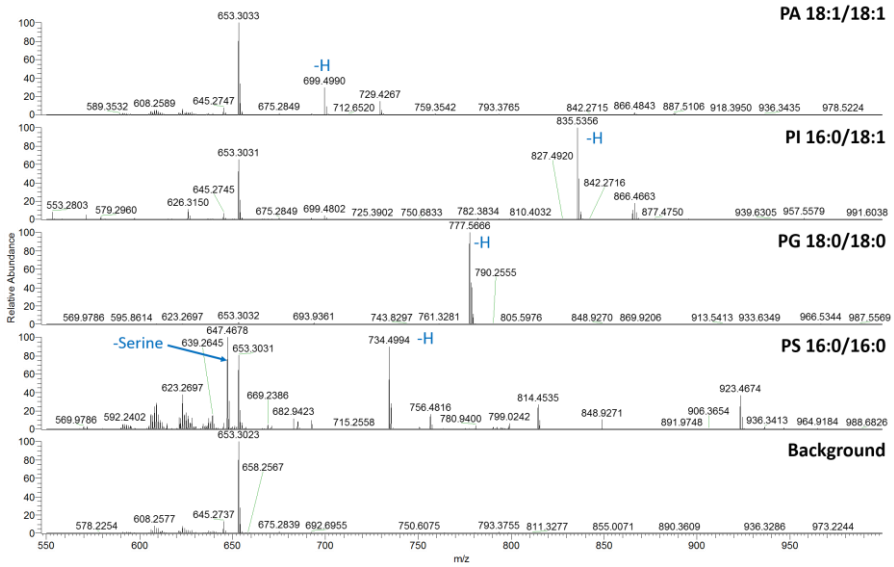

Fig 5.4. Spectra obtained from glycerophospholipid standards in negative-ion mode. The most intense adduct for almost all four lipids is –H. In the case of PS, in addition to the loss of –H, the loss of the head group substituent is also remarkably intense, leading to its detection as PA.

Similar conclusions were reached in the case of sphingolipids, which behave similarly to glycerophospholipids. HexCer and, remarkably, SM loss the headgroup and were also detected as the corresponding Cer, the most basic sphingolipid, and CerP, respectively (Figure 5.5.). Spectrum from the ganglioside standard can be seen in Figure A.5.1. GM3 presents several fragmentation routes whose by-products may be incorrectly taken as Cer, HexCer (the loss of sialic acid and a hexose) and LacCer species (the loss of sialic acid).

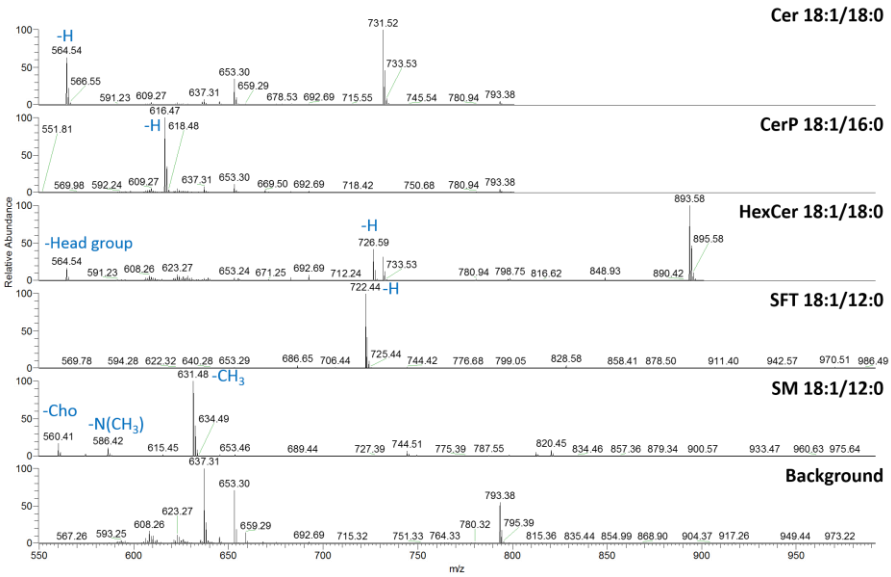

Fig 5.5. Spectra obtained from sphingolipid standards in negative-ion mode. The most intense adduct for most of them is –H, except in the case of SM, which is $-CH_3$. While SM also loses the choline generating a CerP, in the case of HexCer, the loss of the whole head group forms the respective ceramide. No fragment interference were detected for CerP and SFT.

Therefore, there are some lipids that may interference with the detection of others as it can be seen in Figure 5.6 schema. Many fragments may be incorrectly assigned as PA, Cer or CerP species, or may lay in the same mass channel of other species, spoiling their distribution images and thus, making those mass channels unreliable for the analysis. For example, the major adduct for PC 34:1 is due to the loss of the methyl group at 744.5543, which overlaps with PE 36:1 $-H^-$ in tissue samples. This PC/PE interference will need further MS/MS and MS^3 experiments to confirm the presence of both or only one of them.[18]

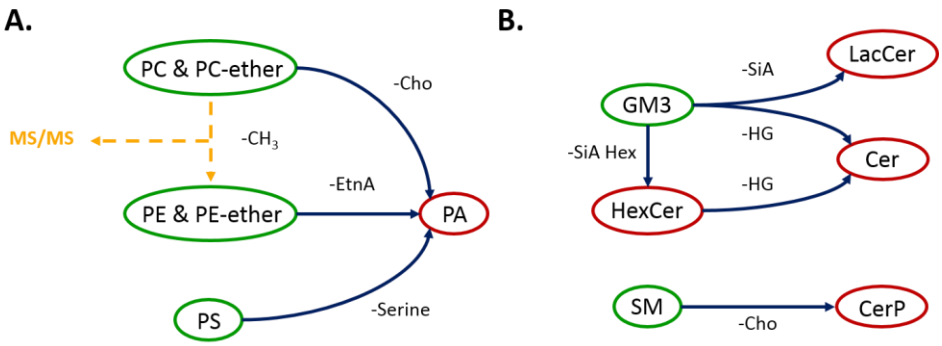

Fig. 5.6. Different interferences found between lipid standards analyzed in negative-ion mode. Only those species that interfere the most are represented. **A** – Phospholipids **B** – Sphingolipids. Straight blue line means direct interaction, while dashed orange line refers to indirect interaction.

All these interferences from prompt fragments and matrix adducts introduce chemical noise into the statistical analysis making it difficult. In order to test the statistical complications that these peaks could induce, we analyzed seven nevi sections.

MALDI-IMS of sections of nevi

Figure 5.7.A shows a comparison between the distribution of three representative lipids along a section of a nevus biopsy. The images clearly showed that while PI 38:5 was preferentially detected in melanocytes, PI 34:1 was more abundant in epidermis, and SM d42:3 was almost exclusively found in the dermis. These maps demonstrated that each lipid specie presented a characteristic distribution. Thus, we could expect that each histological region would have a unique lipid fingerprint, that is different enough to distinguish and classify them, independently of the experiment.

Comparison between the optical images and the corresponding segmentation results of six additional samples is shown in Figure 5.7.B-G. When a supervised *k-means* segmentation algorithm was applied independently over different nevi experiments, three clusters were consistently formed, mimicking the histological areas: epidermis (red), dermis (blue) and melanocytes (green). In some sections, even more clusters were established, which correspond to stratum corneum (pink) or collagen-rich areas (yellow).

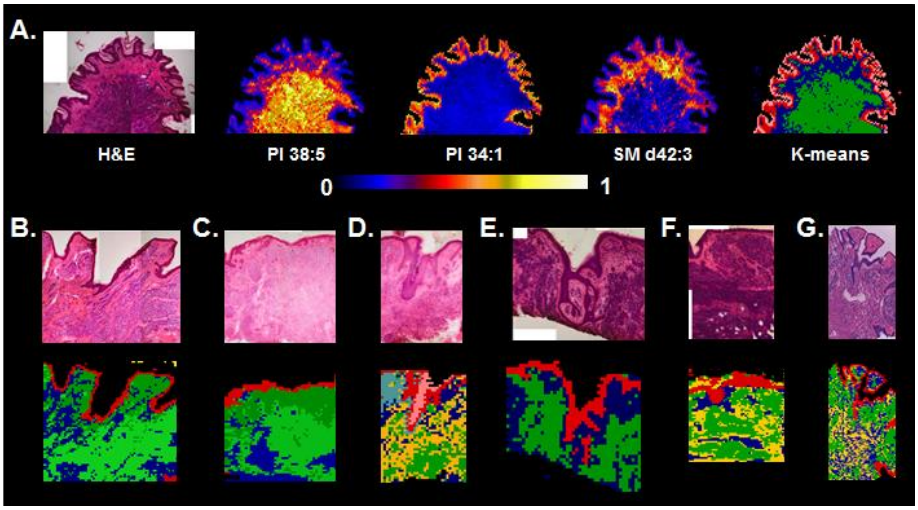

Fig. 5.7. Comparison between the histologic and molecular images of nevi. **A** – H&E optical image of a nevus; expression of three representative lipids over the same section using the color scale below, and segmentation analysis of the lipid fingerprint at each pixel (*k-means*). The algorithm automatically detected four histologic areas: stratum corneum (pink), epidermis (red), dermis (blue) and melanocytes (green). **B-G** – Comparison between H&E optical images of six sections of nevus and the corresponding image of the segmentation analysis (*k-means*) of the lipid fingerprint. Images were recorded in negative-ion mode at a pixel size of 25 µm.

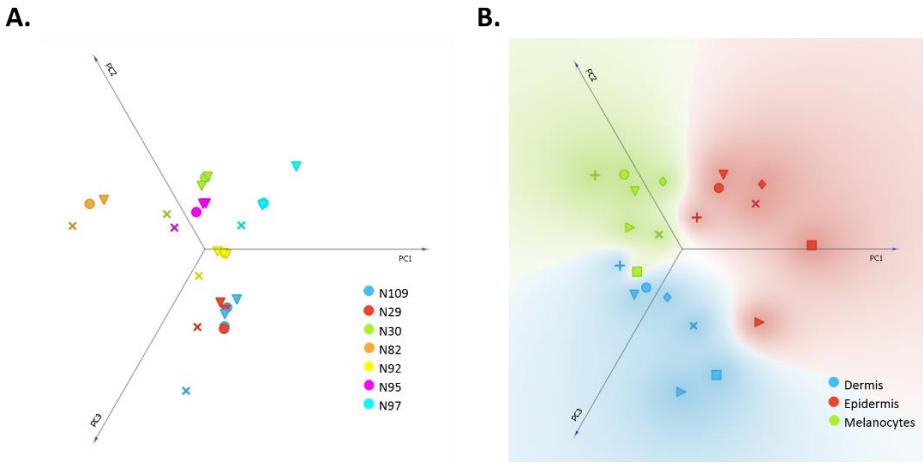

Fig. 5.8. Scores plot of the PCA of the average spectra of each of the three segments found in the tissue sections shown in Figure 5.7. **A** – PCA using all the mass channels as variables. The three ROI of each patient have the same symbol, but the large interexperiment variability do not enable their classification. **B** – Result obtained when filtered mass channels were used. PCA analysis correctly grouped the experiments according to the tissue type, avoiding the interindividual variability. Clusters from epidermis are in red, dermis in blue and melanocytes in green.

Once the spectra and areas obtained from the sections were correctly identified, it was possible to explore the influence that chemical noise filtering has over the final statistical analysis. First, PCA analysis over full spectra was carried out. For this purpose, those m/z that correspond to isotopic distribution and matrix peaks were removed. Figure 5.8.A clearly demonstrates that, when average spectra were used, no separation was achieved. The interexperiment variability was too large, as clusters tend to group according to the experiment rather than by the tissue type. This is due to the statistical noise specified in the previous section, mass channels containing fragments and matrix adducts.

Further demonstration of this hypothesis may be found in Figure 5.8.B, in which, the PCA analysis correctly grouped same tissue types together when only meaningful mass channels were exclusively used after an exhaustive lipid identification (Tables A.5.1 and A5.2 and Figure A.5.2). This lipid assignment was carried out taking into account ionizations and prompt fragmentations described in the previous sections, and eliminating all kinds of interferences, such as PA species, which can come from real PA content in the tissue, or from fragments of the rest of GP. The number of lipid species used for this PCA was 63.

Nevertheless, this last analysis clearly demonstrates that a proper filtering of the data makes interpretation of MALDI-IMS experiments significantly easier. In this way, the only peaks that will be consider for further statistical analysis in this thesis will be the strongest adduct formed for each lipid class (Table 5.2). Peaks that may have contribution from fragments of more complex lipids and in general, any species that cannot be correctly identified will be also removed from the analysis.

Table 5.2. Species and adducts (the strongest ones) that are going to be used in following sections.

Glycerophospholipids			**Sphingolipids**		
Class	Adduct	mass	Class	Adduct	mass
PA	Discard		Cer	Discard	
PE & PE-ether	-H	-1.0073	CerP	Discard	
PC & PC-ether	-CH3	-15.0229	GM3	-H	-1.0073
PG	-H	-1.0073	HexCer	Discard	
PI	-H	-1.0073	SM	-CH3	-15.0229
PS	-H	-1.0073	SFT	-H	-1.0073

Unraveling tumor heterogeneity

In the previous section, a histology-guided approach was taken cluster identification. The purpose was to extract the spectra from the main three tissue types present in nevi sections in order to test the influence of chemical noise in statistical analysis. But melanoma is a highly heterogeneous tissue and this makes direct comparison of samples very difficult, since most sections contain a variable number of cell types. Therefore, a histology-independent analysis is recommended for exploration of melanoma.

Unsupervised analysis methods, such as hierarchical clustering, are used to group the pixels according to their spectral similarity, to reveal patterns in the data. The segmentation maps generated in this way, can describe expected or unexpected structures within the tissue.

Tissue sections from two nevi and two primary melanomas were analyzed using MALDI-IMS lipid profiling in negative ion-mode, and a divisive hierarchical clustering algorithm (DHCA) was applied to the experiment on each of the four tissues individually, in order to extract the patterns for each tissue. The algorithm used in this analysis is an in-house variation of a common hierarchical clustering algorithm. It employs RankCompete[19] (DHCA-RC) as splitting algorithm, using the two pixels with the lowest correlation as starting point. In successive stages, the algorithm selects the positions with the lowest correlation in each group and repeats the separation. The result is visualized as segmentation maps, where each pixel is assigned to a cluster based on the degree of correlation and are colored.

To ensure that no molecular information is lost on the process, first, an overestimate of the number of clusters will be set. This will allow us to identify molecularly different but histologically undistinguishable zones in the tissue. In this sense, Figure 5.9 shows different DHCA-RC levels for one of the primary melanoma, ranging from 4 to 300 clusters. The segmentation maps are represented following the scale bar shown in the figure with two coloring options: clusters from the top are colored with a cluster separation of 1 on the colorbar, while in the ones from below, 1 – correlation is used to assign colors to the clusters. In this way, clusters with more similar lipid profiles receive colors that are closer in the scale.

It is clear that with higher level of clustering, new unexpected areas are revealed, Figure 5.9. The most striking example can be seen in the three melanoma nodules located at the upper side of the tissue, where the algorithm revealed sub-regions within expert-defined tumor areas.

While, even with a cluster level as small as 4, malignant melanocytes are already separated in two, with a higher level such as 15, these three nodules are divided in four different areas (dark blue, blue-purple, dark pink and white clusters, Figure 5.9. A). Additionally, a new cluster (pink color) appears surrounding one of those nodules (dark pink nodule). This could represent the outermost area of the tumor, which is normally a more vascularized area with higher invasive potential.

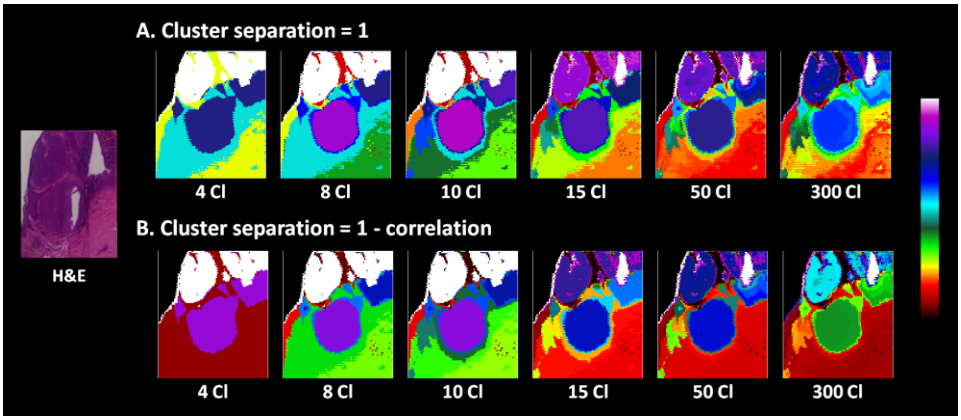

Fig. 5.9. Comparison between the optical images of H&E staining and the divisive hierarchical clustering of a melanoma section in order to retrieve expected or unexpected features of the tissue. This algorithm starts dividing from the two most different pixels using Rank Compete. Two options for visualization are represented with a colorbar. **A** – When separation between cluster is 1. **B** – the separation between clusters is 1-correlation. Thus, clusters that are alike will be closer on the colorbar and therefore, even with clustering levels of 300, the segmentation map captures better the real differences.

The algorithm also separated a thin cluster (dark blue, Figure 5.9.A. 15Cl, better seen in Figure 5.9.B 15Cl in light blue) forming a ring around the bottom nodule (blue-purple) that, after the staining of the tissue, seemed to represent infiltrated cells like macrophages and lymphocytes.

Furthermore, looking at connective tissue, there is also a higher level of separation than expected. However, when clustering results are represented with a cluster separation of 1-correlation between groups, this heterogeneity is less pronounced (Figure 5.9 B). This kind of representation helps to visualize better the real differences, with clusters with more similar lipid fingerprint receiving colors that are closer in the colorbar, and hence hiding artificial clusters. This is the case of the connective tissue in the lower part of the area scanned, which even with 300Cl, the whole zone is reddish and looks like a single cluster.

Another example of tumor heterogeneity is shown in Figure A.5.3. These findings reinforce the importance of molecular information. Moreover, this variability within the tissue is not only limited to tumors, but the algorithm also revealed more clusters than expected when an unsupervised analysis was performed even in nevi sections, Figure 5.10. For example, when the number of clusters was set to four, epidermis stood out as a separate, well-defined cluster. When these maps were compared with the post-MALDI-IMS H&E stained image, it became clear that what the algorithm marked as epidermis, was not entirely homogenous. For instance, the cluster included a crusted area, which was segregated from epidermis when the cluster level was increased. As for the rest, nothing is clear. Close examination of the stained image reveals that the upper zone is full of melanocytes, which are not well defined on segmentation maps. This suggests an unexpected intra-variability within the tissue when the clustering level was increased.

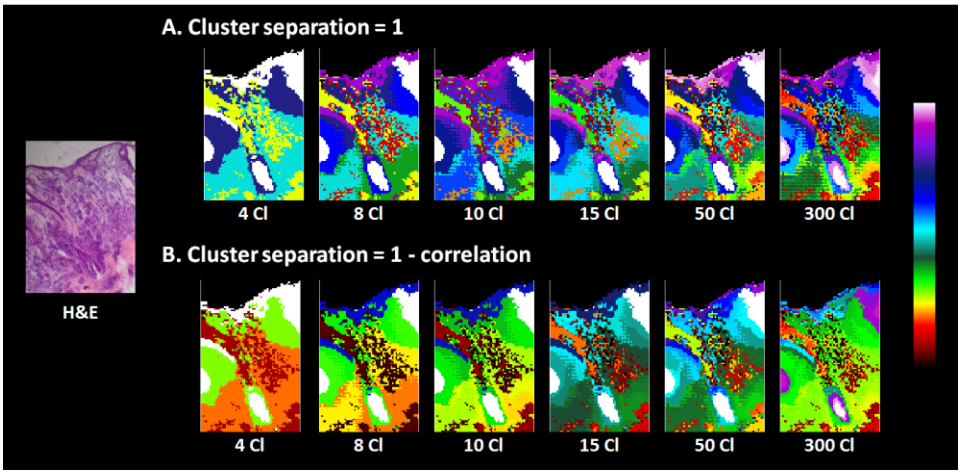

Fig. 5.10. Comparison between the optical images of H&E stained and the divisive hierarchical clustering of a nevus section in order to test the optimum clustering level that reproduces the histology of the tissue. **A** - When separation between cluster is 1. **B** – The separation between clusters is 1-correlation. These segmentation maps demonstrated that more unexpected clusters than those expected from a typical nevus (epidermis, dermis and melanocytes) were obtained.

The lipid phenotype of melanocytic nevi has been poorly studied before and thus, the heterogeneity observed using MALDI-IMS does not have a clear origin. An explanation to such heterogeneity could come from the difference in density between melanocytes and dermis, collagen, or other types of cells present in dermis, but also from metabolic differences among the cells that are not visible in the optical images.

The best segmentation level for capturing the histology of the tissue was achieved when clustering level was set to 300 clusters and 1- correlation was used to color the maps. However, for interpretation of the data and for further statistical analysis, this number is non-viable. Determination of the correct number of clusters is a relevant but challenging step in MALDI-IMS experiments.[20,21] There has been several studies tackling this problem and diverse methods have been proposed, such as Dunn index,[22] Akaike Information Criterion[20] or scree plot method,[23] among others. To the best of our knowledge, a common method has not yet been established.

Here we propose the use of an additional heuristic approach for the determination of the final number of clusters that better represent the tissue heterogeneity and it will be used in all subsequent analysis. This protocol consists of several steps:

1. Peaks from average spectra will be identified following the guidelines described in the first section of this chapter. Thus, only m/z with unequivocal assignment will be used for clusterization in order to avoid introduction of statistical noise. This lipid assignment will be done per-patient.

2. DHCA-RC will be performed over the experiment only with peaks selected in the first step.

3. To facilitate the statistical analysis and standardize the process, we will set the clustering level to 15 for all experiments.

4. Clusters suggested by the algorithm will be verified by examining the correlation between them. The threshold used to group different clusters in one is 95% of the minimum correlation.

The resulting segmentation process ranging from 4 to 300 clusters, using only those peaks that have been identified, can be found in Figure A.5.4. The analysis was slightly improved compared to those in Figures 5.9 and 5.10, although there were no drastic changes.

The first 15 clusters were selected and their degree of correlation was computed. Figure 5.11 shows an example of the table of correlation coefficients for a tumor section (panel A) and for a nevus section (panel B). Colors from above and right side of the matrix represent the grouping of clusters. For example, in the first example, Cl1, Cl2, Cl4-Cl6 (blue) showed high degree of correlation and therefore, they were merged in a single cluster. The colors from the correlation matrix and segmentation maps are not related.

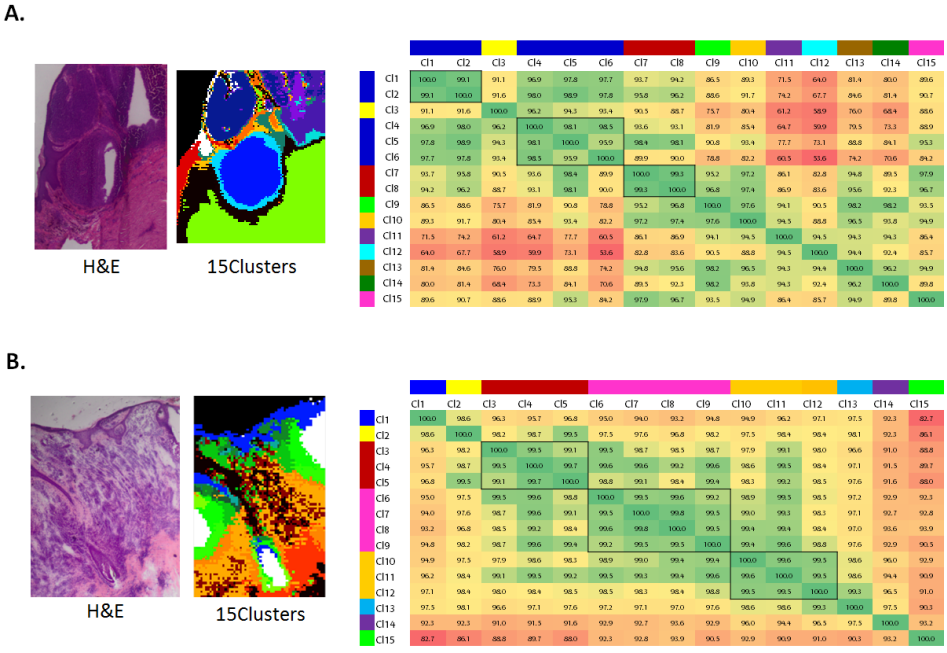

Fig. 5.11. Correlation matrix calculated for the selected clusters from DHCA-RC segmentation process for **A** - melanoma and **B** - nevus. The standard cluster number chosen to highlight the relationship between them has been 15. Thus, taking into account the threshold of 95% of the minimum correlation established, 10 different clusters have been retrieved in the case of the primary melanoma, and 8 Cl for the nevus.

Normally, the correlation between clusters is significantly high within a tissue, due to the similarities between different histological regions, making the determination of the optimal number of clusters a hard task, reinforcing the need to establish a standard threshold of 95% to consider a cluster different enough. Still, sometimes it can be confusing, but this is one of the flaws of working with human tissue, the high variability. The number of clusters established for the primary melanoma shown in Figure 5.11 was 10, while in the case of the melanocytic nevus, it was 8. Separate images of the distribution of each cluster for both experiments can be found in appendix (Figures A.5.5 and A.5.6), as well as results from another example of nevus and primary melanoma mentioned above (Figures A.5.7 and A.5.8).

Design of the study for melanoma prediction

The cohort of the study consisted of 15 nevi sections and 17 primary melanomas. Taking into account that the samples were obtained from two independent tissue banks, and in order to avoid a sampling bias, the whole cohort was randomly split in training and validation datasets.

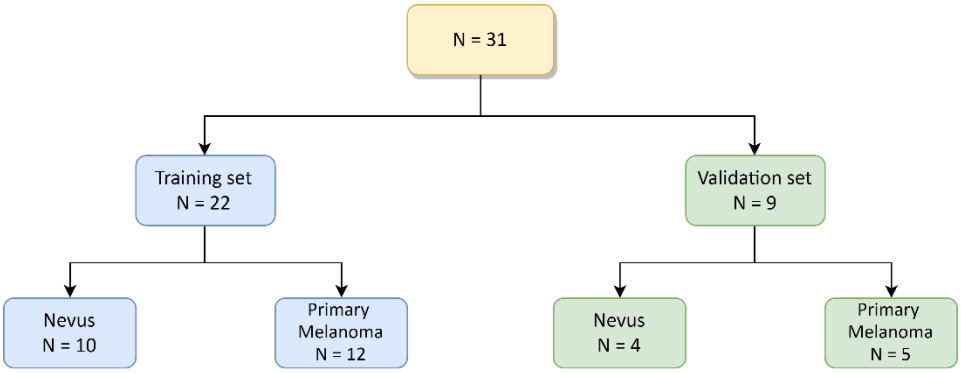

Fig. 5.12. Diagram depicting the sample distribution into training and validation sets for the development of the classification model by machine learning algorithms.

Figure 5.12 graphically depicts the division of the samples for primary melanoma prediction in a binary classification model. A summary of the patient samples randomly assigned for each data set, as well as the number of clusters selected for each patient following the guidelines described in the previous section, may be found in Table A.5.3. When the optimal cluster number was not clear, an over-estimation was done in order to maintain the spectra free of any influence from delimiting areas and to avoid undesirable feature merging.

Melanocytic Nevi vs. Primary Melanoma.

For the supervised analysis, clusters need first to be assigned to a group of study. As previously described, melanoma is a highly heterogenous cancer, and even nevi sections differ from patient to patient. But there are some specific features present in all samples that were used for model development.

An initial unsupervised clustering of the whole nevi training dataset using the clusters selected as different-enough and a PCA revealed three tendencies (Figure 5.13.A). Comparing the PCA results and images from clustering, we deduced that those three groups depicted the three common tissues present in all nevi (epidermis, dermis and melanocytes). Clusters located at the ends of those groups in the PCA were extracted for each patient. All the remaining clusters that felt in the middle of the analysis were excluded for model development, including special cases such as collagen-rich areas, folded tissue, damaged areas... Thus, a new PCA was run only with reproducible species in order to avoid interpatient variability (Figure 5.13.B). The three main tissues, as seen previously in Figure 5.8, are different-enough to distribute separately in the PCA. Still, it is interesting the presence of the epidermis of two nevi from the same patient (example from one of them in Figure 5.13.C) located intermixed with the melanocytes. This could suggest some sort of melanocytic infiltration within the epidermis. It is also noteworthy that, as Figure 5.1 illustrates, melanocytes, under normal condition, are located amongst the basal layer of epidermis, lodged between keratinocytes for proliferation and differentiation control. However, this would need to be confirmed by an expert pathologist, and in order to avoid any noise this could generate, these two clusters were removed for the development of the model.

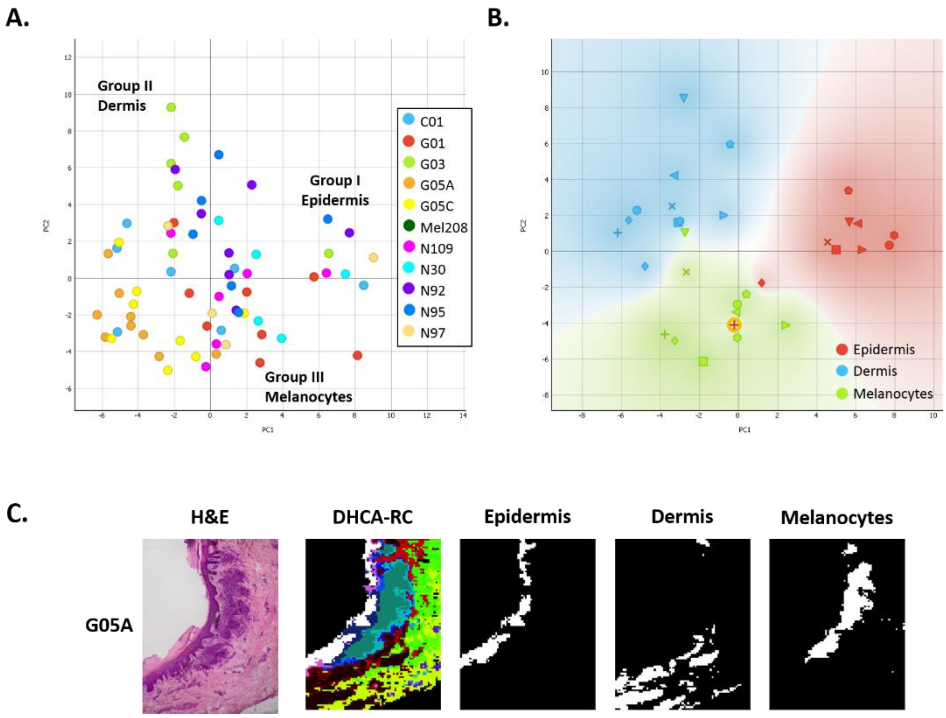

Fig. 5.13. A - PCA analysis of all clusters selected for all nevi of the training data set. Each color represents a different nevus. The analysis was performed with reproducible lipids in order to minimize inter-patient variability. The results suggest a slight trend to group together clusters from different patient. **B** - After comparison of the PCA with the clustering results and H&E stained images, three main tissues were extracted and another PCA was performed. There was a clear separation between epidermis, dermis and melanocytes implying distinct lipid fingerprints. **C** - Comparison between the optical images of H&E stained, the DHCA-RC clustering image and the corresponding clusters named as epidermis, dermis and melanocytes. The epidermis of this nevus (G05A) together with that of another nevus from the same patient (G05C) are located within the melanocytes class in the PCA in panel B (marked in orange), probably because it is infiltrated of melanocytes.

Figure A.5.9 displays some examples of nevi sections. For each section, the H&E optical image were compared with the corresponding DHCA-RC image and PCA results from Figure 5.13.A, and clusters corresponding to epidermis, dermis and melanocytes were extracted. Likewise, Figure 5.14 illustrates the results of a similar analysis as done for nevus, but over the whole training dataset from primary melanoma, using the final clusters determined by the protocol described above, with the aim of selecting the common features present in all samples. Only reproducible inter-patient variables were used. PCA analysis shows that all melanoma samples presented an elongated distribution throughout PC2. This systematic pattern of the points could indicate the presence, specially, of two different tissues. When comparing the clusters from the outermost part of the PCA with the clustering and H&E stained images, they were designated as malignant melanocytes (Clusters located at the left side of PC1 in Figure 5.14.A) and stromal tissue

(right side of the PC1 in Figure 5.14.A). It is worth mentioning that more areas were present in some samples, as lymphocytes, macrophages or inflamed tissue for instance. However, due to reduced number of samples for these cases, no clear grouping was observed and no further statistical analysis was viable.

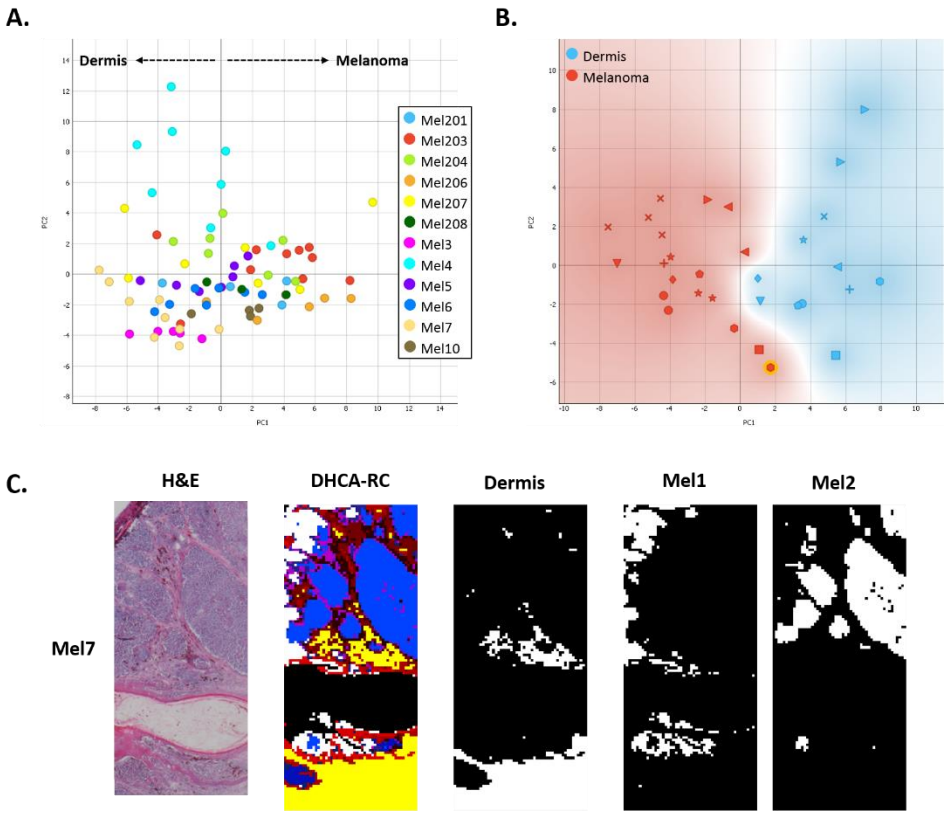

Fig. 5.14. A - PCA analysis of all clusters selected for all primary melanoma of the training data set. Each color represents a different patient. The analysis was performed with reproducible lipids in order to minimize inter-patient variability. The results suggest a slight trend to arrange clusters from different patients. **B** – After comparison of the PCA with the clustering results and H&E stained images, two main tissues were extracted and another PCA was performed. There was a clear separation between melanoma and dermis, implying distinct lipid molecular features. **C** – Comparison between the optical images of H&E stained, the DHCA-RC clustering image and the corresponding clusters named as melanoma (Mel) and dermis. Mel 2 tend to locate closer to stromal clusters than to melanoma, which is surprising looking at the histological image and the cluster image.

It is surprising that in the example shown in Figure 5.14.B-C, the most well defined cluster for melanoma (Mel2), locates closer to Dermis clusters on the PCA analysis than to the rest of melanomas. This could be due to the influence of the immune response of the surrounding macrophages and lymphocytes, or other histologically non-detectable reason. Figure A.5.10. shows some examples of primary melanoma, with the cluster

selected as malignant melanocytes (melanoma) and dermis after contrasting PCA results with the corresponding DHCA-RC and H&E stained images.

Prior to addressing the final goal, the five main tissues defined in our samples were analyzed with a final PCA to explore existence of additional patterns (Figure 5.15). Clusters from each tissue type tend to arrange together, indicating distinct lipid molecular signatures. Moreover, the analysis revealed tumor-specific differences, gathering all tissue types from nevi on one side of the analysis, and melanoma specific clusters on the other.

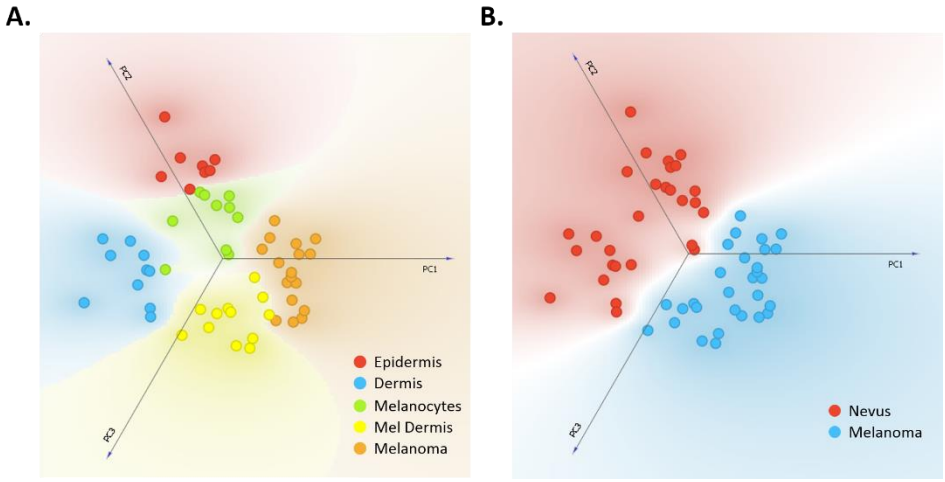

Fig. 5.15. Unsupervised multivariate analysis over the whole training dataset with the reproducible lipid species in order to avoid inter-patient variability. **A** – PCA results imply that each tissue type has a consistent lipid profile, different enough to show a separate trend in spite of some overlapping. **B** -Same analysis but colored by the type of sample (nevus or melanoma) to demonstrate that the clusters tend to group with respect to the origin of the samples, no matter if there are different types of tissue. Nevus and melanoma could be successfully differentiated.

Taking into account these results, two types of classification models were developed for tumor prediction: a two-class design including all clusters from primary melanoma as one group (Primary Melanoma) and the three tissues from nevi sections as Nevus, and a five-class classification model. Thus, Figure A.5.11 shows the final schematic distribution of samples for training and validation sets.

In order to remove irrelevant lipids that can only introduce noise in the process of model fitting, significant lipids were determined by a one-way ANOVA with post hoc correction. The results of the analysis are not shown to preserve the identity of the possible biomarkers to apply for patent.

Molecular classification was generated using four different models: Logistic Regression, Naïve Bayes, Random Forest and Support Vector Machine (SVM). Each model selects and weights different combinations of variables that contribute to classify the samples. Nevertheless, the data was trained to build two-class and five-class classification

models using 10-fold internal cross-validation with all algorithms. The training dataset was divided in 10 subsets using nine to train the model and the remaining subset for testing. The procedure was repeated nine more times, each time using a different subset for testing, resulting in an overall agreement of 100%-99% for the binary model Figure A.5.12. On the other hand, the multi-class model showed a lower classification accuracy, but still acceptable. This reinforced the result from PCA, that no matter how different tissues are within a sample, the differences are higher for control vs melanoma.

The statistical models were then applied for external validation with a separate set of samples. Clustering results were compared to H&E stained images, and clusters from the main tissues were extracted and imported into the analysis. The classifier models showed an agreement between 85-90% when the multi-class comparison was performed, Figure 5.16. On the other hand, almost all binary classification models yielded a 100% performance. Two of the best performing algorithms were Naïve Bayes and SVM. Confusion matrix for multi-class classification by Naïve Bayes demonstrated that it was able to correctly classify all tissues from nevi samples and that the wrong recognition was from melanoma clusters. The misclassifications were some of the melanoma and melanoma related stroma clusters, which can be visualized in the PCA from Figure 5.16. A with bold symbols. Still, PCA results reinforce that the distinct lipid profile of the tissues described in the training set are still consistent with this dataset.

Finally, it is worth mentioning that a particular lipid stood out as biomarker to discriminate all nevi clusters from melanoma-related clusters in a classification tree shown in Figure 5.16.G, L.S 12 looks characteristic of nevus sample no matter the tissue types, being excluding between nevus and melanoma.

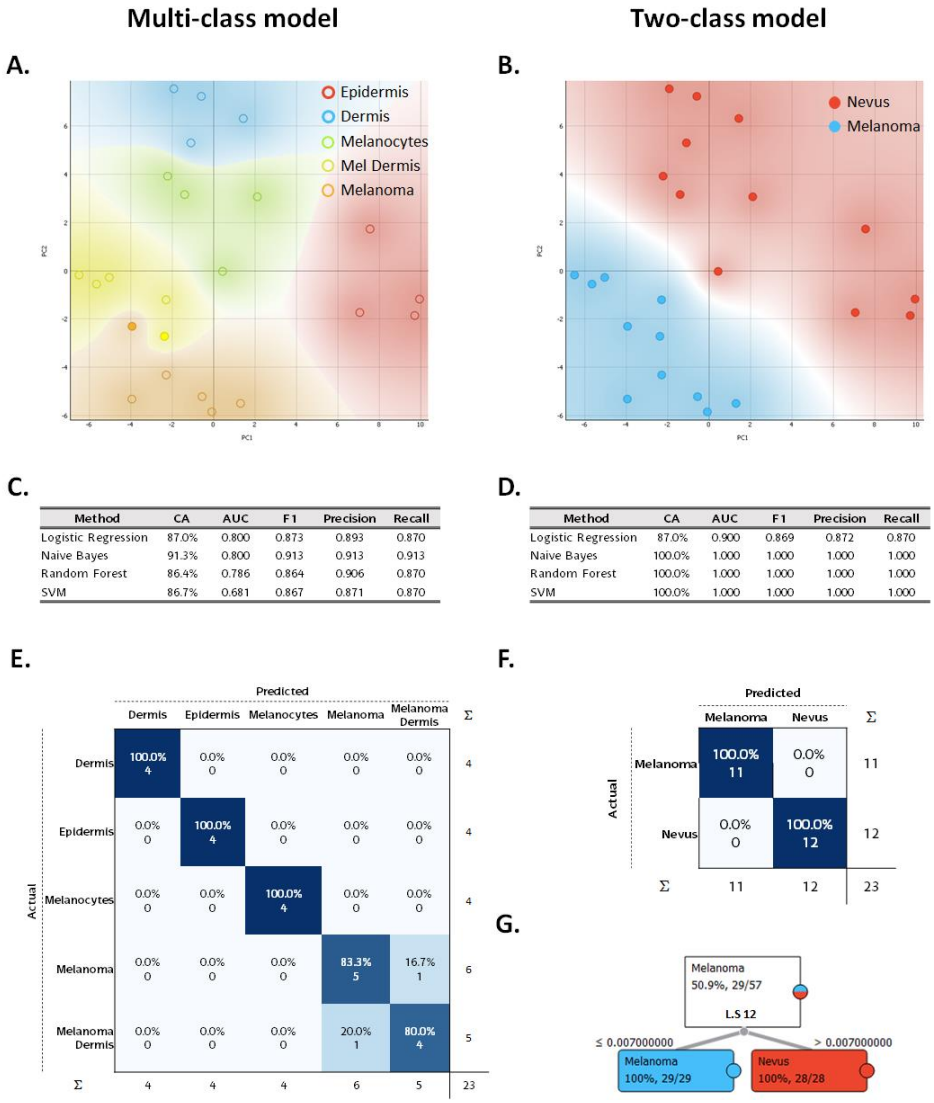

Method	CA	AUC	F1	Precision	Recall
Logistic Regression	87.0%	0.800	0.873	0.893	0.870
Naive Bayes	91.3%	0.800	0.913	0.913	0.913
Random Forest	86.4%	0.786	0.864	0.906	0.870
SVM	86.7%	0.681	0.867	0.871	0.870

Method	CA	AUC	F1	Precision	Recall
Logistic Regression	87.0%	0.900	0.869	0.872	0.870
Naive Bayes	100.0%	1.000	1.000	1.000	1.000
Random Forest	100.0%	1.000	1.000	1.000	1.000
SVM	100.0%	1.000	1.000	1.000	1.000

Fig. 5.16. External validation performance for the four classification models. PCA of the validation dataset showing a noticeable overlap between some of the scores when a multi-class approach was taken (**A**), whilst there was a complete separation between nevus and melanoma clusters despite the tissue type (**B**). **C and D** – Summary of the models' performance for five-class and two-class classifications, respectively. Recognition capability can be seen in the CA column (classification accuracy). **E** – Confusion matrix showing multi-class classification results by Naïve Bayes (91.3% overall correct assignment). **F** – Confusion matrix for nevus vs melanoma for the Naïve Bayes model (100% overall correct assignment). **G** – Classification tree showing one of the variables with highest weight in classification between nevus clusters and all melanoma related clusters with the training dataset: L.S 12. L.S: lipid specie

Molecular biomarkers for tumor aggressiveness.

Additionally, a histology-directed approach was used to determine lipid markers of tumor aggression. The same workflow as in nevi and primary melanoma sections was used for metastatic melanoma. First, lipids were identified in the spectra of each of the eight new samples of metastatic tissue, and with these selected species, DHCA-RC clustering was performed over the images. Correlations between clusters were also calculated to select the optimal clustering level using the histological H&E stained images for comparison. Spectra from metastatic melanoma were extracted and directly compared to those of melanocytes and melanoma clusters used in the previous section for statistical prediction. Figure A.5.13 shows examples of three metastatic melanoma.

PCA from Figure 5.17.A revealed statistically distinct regions and that the three groups were successfully differentiated based on their lipid profile. To determine individual lipids that correlate with this separation between melanocytes, primary melanoma and metastasis, one-way ANOVA with multiple comparison was carried out. Due to patentability of the biomarker panel, statistical results are not shown.

Venn diagram in Figure 5.17.B represents the number of significantly different lipids found in the three possible comparisons. Some lipids were altered in more than one comparison suggesting a specificity toward one of the groups. Thus, 19 lipids are particularly altered in melanocytes compared to both melanoma groups, Figure 5.17.C (marked with a green bar). On the other hand, species marked with the blue bar in Figure 5.17.C are the seven lipids that are specifically unregulated in primary melanoma. Interestingly, only one specie, L.S 26, was noticeably selective for the presence of metastasis, as it was overexpressed compared to primary and benign melanocytes. No lipid was found to be significantly altered for the three conditions, which would have marked tumor progression. Still, results from some lipids, such as L.S 6 from Figure 5.17.C, suggest that there may be some kind of progression tendency. A substantial increment of the sample size may help obtaining more accurate results.

The drastic decrease of almost all SM species is remarkable in both types of melanoma. Moreover, and conversely to what we have seen in colonic mucosa and what has been described in the literature, it is singular the downregulation of PUFA phospholipids accompanied by the rise of unsaturated and mono and di-unsaturated phospholipids.

As a last note, the scatter of the points in the score plot of the PCA suggest heterogeneity within the groups. But this is something we expected in advance due to the large subtypes of primary melanoma, metastatic and nevus used in the analysis. Not all nevi sections were intradermal, and not all primary melanoma were nodular to give an example. Further research would need to include different subtypes in the analysis highly increasing the number of samples.

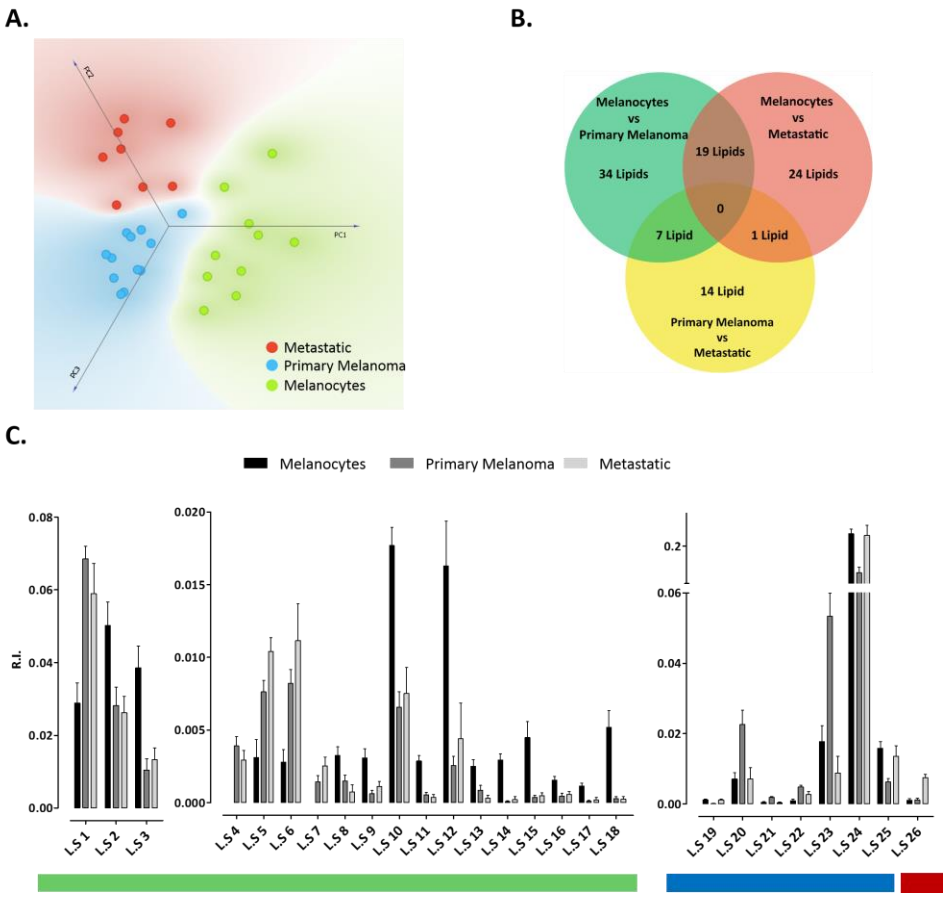

Fig 5.17. A - PCA separating benign melanocytes (green, n=10) from primary melanoma (blue, n=12) and metastatic melanoma (red, n=8). **B** - Venn diagram showing the number of significant lipids found in multiple comparisons. There are some lipids that are altered in more than one comparison suggesting a specificity toward one of the groups. The complete results from one-way ANOVA analysis with post hoc are not shown due to patent procedures. **C** - Bar charts of the lipids that are explicitly altered in one of the three group. Thus, the 19 lipids marked with the green bar were in higher or lower abundance in melanocytes than in both melanoma types. The seven lipids marked with the blue bar, in contrary, are distinctively overexpressed or underexpressed in primary melanoma, whilst L.S 26 is the only lipid in higher abundance compared to both, benign melanocytes and primary melanoma. Values are expressed as mean ± SEM (n=10 in melanocytes, n=12 in primary melanoma and n=8 in metastatic). L.S: lipid specie.

5.7 Conclusions

In this chapter, we have presented a systematic methodology to deal with a difficult case: identification of the lipid signature that distinguish melanocytes from primary melanoma and metastasis.

In the first part of the chapter we demonstrated that proper handling of the data and reduction of the species to only those that have a solid assignment substantially improved the statistical analysis. The large amount of lipid interferences found may perturb, not only the statistical analysis, but also the biologically-relevant conclusions. For instance, PA are, not only the intermediate metabolite in the synthesis of all membrane glycerophsopholipids,[24] but they also are important signaling lipids, especially in the central nervous system.[25,26] However, the results presented here showed that all glycerophospholipids tend to fragment into PA-isobaric species in-source by the loss of the totality of the headgroup. Hence, such lipid class must not be included in the analysis, since conclusions associated to changes in PA abundance may not be 100% sure to be due to PA metabolism alteration. In order to identify a PA specie unequivocally and avoid interferences, prior to MS, chromatographic separation would be required and only those species confirmed by LC-MS should be taken into account during on-tissue lipid identification. Cer and CerP species would require the same approach and identification of HexCer and LacCer species demand the confirmation of the absence of ganglioside species that may interfere with their detection.

Another approach for the detection and identification of biomolecules which have contribution from other species and were removed from the analysis of this chapter would be to optimize the protocol for a targeted lipid class. For example, derivatization has been widely used in mass spectrometry for the detection and identification of small molecules like prostaglandins.[27] Other possibility could be to block fragmentation pathways by derivatization.

Another challenge tackled in this thesis was the heterogeneity of the tissue. The heterogeneity of melanoma has been previously described in literature,[1] but this was the first description, to the best of our knowledge, of lipid phenotype. While colon tissue presented a very uniform composition along patients, nevus and melanoma presented a rich diversity, probably due to the direct exposition to the environmental conditions and to differences depending on the location along the body. Intra-tumor heterogeneity is a vivid problem of molecular oncology that could be addressed by MALDI-IMS.

The methodology described was a simple approach to distinguish different main tissues within nevi sections and melanoma. But heterogeneity of tissue sub-areas can be hidden behind the predominant main tissues. Therefore, and over clustering was performed and then, looking at the correlation between clusters, the optimal cluster numbers representing the diversity within each tissue was selected. Due to the small sample size for relevant regions found in samples, such as lymphocytes or macrophages, they were left out of the analysis. But there are still many interesting aspects to study in the metabolism of tissue diversity which require an increment in the cohort: how

macrophages and lymphocytes affect the delimiting areas, the invasive nature of the outermost melanoma cells, the presence of more or less adipocytes and collagen...

The classification model built yielded outstanding results, especially when all main tissues from nevi were grouped and compared to melanoma and melanoma related stroma clusters. The next step would be to test the model with blind samples. For that study, the protocol would be the methodology described in this chapter: first, identification of lipids from average spectum, and then DHCA-RC clustering over each experiment with only selected peaks. Once the optimal cluster number is selected, the last part would be importation of the spectra from those clusters into the classification model to predict only with the lipid profile used to build the model. Despite that clusters from nevus and melanoma are completely different, it is important to first study the variability of the tissue within each sample separately, not to miss tiny regions that could be hidden by the main tissue if this heterogeneity is not taken into account, areas or cells that could be starting a malignant process would be unnoticed.

Lastly, for future work, it would be interesting to introduce to the cohort enough samples from different types of nevi and melanoma, to try to understand the differences between them, and to predict the role of lipids in different outcomes that they may have. For example, one type of nevus, in which IMS for protein analysis has shown its predictive potential, is Spitz nevus.[28] For pathologist it is sometimes difficult to distinguish between benign and Spitzoid malignant melanoma. Therefore, it would be attractive to introduce this kind of nevi into the study.

In summary, the results show the potential of MALDI-IMS as a tool to study heterogeneity of tissues and to use it in [29]cancer research for tumor detection.

---

[1] Liu H, He Z, von Rütte T, Yousefi S, Hunger RE, Simon HU. Down-regulation of autophagy-related protein 5 (ATG5) contributes to the pathogenesis of early-stage cutaneous melanoma. *Sci. Transl. Med.* **2013.** 5.

[2] Brenn T. Pitfalls in the evaluation of melanocytic lesions. *Histopathology.* **2012**. 60:690-705.

[3] Tsao H, Olazagasti JM, Cordoro KM, Brewer JD, Taylor C, Bordeaus JS, Chren MM, Sober AJ, Tegeler C, Bhushan R, Begolka WS. Early detection of melanoma: reviewing the ABCDEs. *J. Am. Acad. Dermatol.* **2015**. 72:717-723.

[4] Nobre AB, Pineiro-Maceira J, Luiz RR. Analysis of interobserver reproducibility in grading histological patterns of dysplastic nevi. An. Bras. *Dermatol.* **2013**. 88:23-31.

[5] Braun RP, Gutowicz-Krusin D, Rabinovitz H, Cognetta A, Hofmann-Wellenholf R, Ahlgrimm-Siess V, Polsky D, Oliviero M, Kolm I, Googe P, King R, Prieto VG, French L, Marghoob A, Mihm M. Agreement of dermopathologists in the evaluation of clinically difficult melanocytic lesions: how golden is the 'gold standard'? *Dermatology.* **2012**. 224:5-8.

[6] Hawryluk EB, Sober AJ, Piris A, Nazarian RM, Hoang MP, Tsao H, Mihm MC, Duncan LM. Histologically challenging melanocytic tumors referred to a tertiary care pigmented leion clinic. *J. Am. Acad. Dermato.* **2012**. 67:727-735.

[7] Farmer ER, Gorin R, Hanna MP. Discordance in the histopathologic diagnosis of melanoma and melanocytic nevi between expert pathologists. *Hum. Pathol.* **1996**. 27:528-531.

[8] Hilario M, Kalousis A, Pellegrini C. Muller M. Processing and classification of protein mass spectra. *Mass Spectrom. Rev.* **2006**. 25:409-449.

[9] Jones EA, Deininger SO, Hogendoorn PCW, Deelder AM, McDonnell LA. Imaging mass spectrometry statistical analysis. *J. Proteom.* **2012**. 75:4962-4989.

[10] Marusyk A, Polyak K. Tumor heterogeneity: causes and consequences. *Biochim. Biophys. Acta.* **2010.** 1805:105-117.

[11] Burrell R, McGranahan N, Bartek J, Swanton C. The causes ond consequences of genetic heterogeneity in cancer evolution. *Nature*. **2013.** 501:338-345.

[12] Wu JM, Halushka MK, Argani P. Intratumoral heterogeneity of HER-2 gene amplification and protein overexpression in breast cancer. *Hum. Pathol.* **2010**. 41:914-917.

[13] Greaves M, Maley CC. Clonal evolution in cancer. *Nature*. **2012**. 481:306-313.

[14] Schiller J, Süss R, Arnhold J, Fuchs B, Lessig J, Muller M, Petkovic M, Spalteholz H, Zschörnig O, Arnold K. Matrix-assisted laser desorption and ionization time-of-flight (MALDI-TOF) mass spectrometry in lipid and phospholipid research. *Pro. Lipid Res.* **2004**. 43: 449-488.

[15] Fuchs B, Süss R, Schiller J. An update of MALDI-TOF mass spectrometry in lipid research. *Prog. Lipid Res.* **2010**. 49: 450-475.

[16] Jackson SN, Muller L, Roux A, Oktem B, Moskovets E, Doroshenko VM, Woods AS. AP-MALDI mass spectrometry imaging of gangliosides using 2,6-dihydroxyacetophenone. *J. Am. Soc. Mass Spectrom.* **2018**. 29: 1463-1472.

[17] Demsar J, Curk T, Erjavec A, Gorup C, Hocevar T, Milutinovic M, Mozina M, Polajnar M, Toplak M, Staric A, Stajdohar M, Umek L, Zagar L, Zbontar J, Zitnik M, Zupan B. Orange: data mining toolbox in python. *J. Mach. Learn. Res.* **2013.** 2349-2353.

[18] Fuchs B, Bischoff A, Süss R, Teuber K, Schurenberg M, Suckau D, Schiller J. Phosphatidylcholines and –ethanolamines can be easily mistaken in phospholipid mixtures: a negative ion MALDI-TOF MS study with 9-aminoacridine as matrix and egg yolk as selected example. *Anal. Bioanal. Chem.* **2009**. 395: 2479-2487.

[19] Cao L, Jin X, Yin Z, Del Pozo A, Luo J, Han J, Huang TS. RankCompete: simultaneous ranking and clustering of information networks. *Neurocomputing*. **2012**. 95: 98-104.

[20] Hanselmann M, Kirchner M, Renard BY, Amstalden ER, Glunde K, Heeren RMA, Hamprecht AF. Concise representation of mass spectrometry images by probabilistic latent semantic analysis. *Anal. Chem.* **2008**. 80:9649-9658.

[21] Race AM, Steven RT, Palmer AD, Styles IB, Bunch J. Memory efficient principal component analysis for the dimensionality reduction of large mass spectrometry imaging data sets. *Anal. Chem.* **2013**. 85:3071-3078.

[22] Widlak P, Mrukwa G, Kalinowska M, Pietrowska M, Chekan M, Wierzgon J, Gawin M, Drazek G, Polanska J. Detection of molecular signatures of oral squamous cell carcinoma and normal epithelium – application of a novel methodology for unsupervised segmentation of imaging mass spectrometry data. *Proteomics*. **2016**. 16:1613-1621.

[23] Jolliffe IT. Principal Component Analysis. *Springer*. **2002**.

[24] Shin JJ, Loewen CJ. Putting the pH into phosphatidic acid signaling. *BMC Biol.* **2011.** 9: 85.

[25] Goto K, Kondo H. Molecular cloning and expression of a 90-kDa diacylglycerol kinase that predominantly localizes in neurons. Proc. Natl. Acad. Sci. USA. 1993. 90: 7598-7602.

[26] Ishisaka M, Hara H. The roles of diacylglycerol kinases in the central nervous system: review of genetic studies in mice. *J. Pharmacol. Sci.* **2014.** 124: 336-343.

[27] Manna JD, Reyzer ML, Latham JC, Weaver CD, Marnett LJ, Caprioli RM. High-throughput quantification of bioactive lipids by MALDI mass spectrometry: application to prostaglandins. *Anal. Chem.* **2011**. 83: 6683-6688.

[28] Lazova R, Seeley EH, Keenan M, Gueorguieva R, Caprioli RM. Imaging mass spectrometry. A new and promising method to differentiate Spitz nevi from Spitzoid malignant melanomas. *Am. J. Dermatopathol.* **2012**. 34: 82-90.

Chapter 6

Development of new analytical tools of application in clinical research

This chapter addresses the need for new analytical devices that could speed large-scale analysis in an automated way using a reduced amount of sample and time.

Here we present a methodology that uses lipidomic profiles determination with imaging mass spectrometry combined with miniaturized arrays to determine lipid profiles of cell membranes. The work carried out in this chapter was done in collaboration with the group of MD Maria Dolores Boyano from Faculty of Medicine and Nursing (UPV/EHU) and IMG Pharma Biotech S.L.

6.1 Introduction

In cancer research, it is essential to develop tools to help with the diagnoses and with the monitoring of antitumoral treatments. In the past years, new strategies for tissue classification have been developed, based mainly on miniaturization,[1] measuring large sample sets under highly similar experimental conditions. They have been widely used in genomics to analyze gene expression in a fast and automated way.

Lately, great efforts have been made to expand this technology to different areas outside of genomics. Novel approaches using MALDI-IMS in combination with miniaturization techniques, such as tissue microarrays, have helped to develop high-throughput, fast and automated analysis, simplifying sample preparation and reducing the total amount of sample required in each analysis. The final goal is to measure hundreds of samples in a single run, avoiding inter- and intra-experimental variation with the consequent time and cost saving.

There exists an extensive literature on implementing the lab-on-a-chip concept in MALDI-IMS, especially with applications in proteomics,[2,3] but to the best of our knowledge, no similar approach has been produced so far in the field of metabolomics, and more precisely for lipid analysis.

6.2 Objectives

The aim of this chapter is to develop the analysis based on tissue membrane microarray combined with MALDI-IMS. As a proof of concept, we present the results obtained with a microarray consisting of membranes from different cell lines for tumor classification and biomarker discovery. Workflow of the procedure can be found in Figure 6.1.

The use of membrane preparations instead of whole cells improves the biomarker identification by reducing the amount of metabolites and proteins that can interfere in the MALDI-IMS analysis. Taking into account that membrane lipids account for ~80% of the total amount of lipids in a cell, the approximation of using membranes instead of whole cells is representative of the physiological and pathological state of the cell. Moreover, the final goal of this technology is its implementation in hospitals, hence, an easy and fast protocol is necessary. The low sample preparation that the isolation of membranes requires compared to, for example, tissue extraction, makes their use attractive.

6.3 Experimental section

Cell lines and culture conditions

Briefly, different melanocytic cells, primary melanomas and cell lines with high metastatic potential were cultured as monolayer with their optimal culture medium with 10% FBS, 2mM glutamine and antibiotics (Table A.6.1). This task was carried out by Arantza Perez-Valle from the group of MD. Maria Dolores Boyano from the Faculty of Medicine and Nursing, University of the Basque Country.

Isolation of cell membranes

Samples were homogenized using a Teflon-glass grinder (Heidolph RZR 2020) in 20 volumes of homogenation buffer (1 mM EGTA, 3 mM $MgCl_2$, and 50 mM Tris-HCL, pH 7.4) supplemented with 250 mM sucrose. The crude homogenate was subjected to a 1000x g for 8 min, and the resultant supernatant was centrifuged again at 18000x g for 15 min (4˚C, Microfuge 22R centrifuge, Beckman Coulter). The pellet was washed in 20 volumes of homogenation buffer using an Ultra-Turrax (T10 basic, IKA) and re-centrifuged under the same conditions. The homogenate aliquots were stored at -80˚C until they were used.

Cell membrane microarray development

Membranes were resuspended in a patented buffer and printed (20 drops per spot, three replicates per sample) onto glass slides using a non-contact microarrayer (Nano_plotter NP 2.1).[4] Microarrays were stored at -20˚C until they were used.

The isolation of cell membranes and their deposition onto glass slides were carried out by Tarson Tolentino-Cortez and Dr. Gabriel Barreda-Gómez from IMG-Pharma Biotech S.L according to patented procedures.

Imaging and data analysis

A detailed description of sample preparation can be found in Chapter 3. Data were acquired in negative-ion mode with 150 µm spatial resolution and a mass resolution of 60.000 FWHM at m/z = 400, and with a laser energy between 20-30 µJ/pulse. The rest of the MALDI-IMS parameters used are described in Chapter 3.

Data analysis was carried out with in-house software built in Matlab (MathWorks, Natick, USA) using captation parameters described in Chapter 3. IBM SPSS Statistics for Windows (Version 23.0; IBM, Chicago, IL, USA) was used for Levene's test, one-way ANOVA and Bonferroni/Games-Howell post multiple comparison. Levene's test determines the homogeneity of the variables (H_0 = groups have equivalent variances) in order to choose the correct post hoc method: Bonferroni if Levene's $p \geq 0.05$ and Games-Howell if Levene's $p \leq 0.05$. In all instances, p values < 0.05 were considered statistically significant. Receiver-

operating characteristic (ROC) curves were calculated using GraphPad Prism (version 5 for Windows, GraphPad Software, La Jolla, CA, USA).

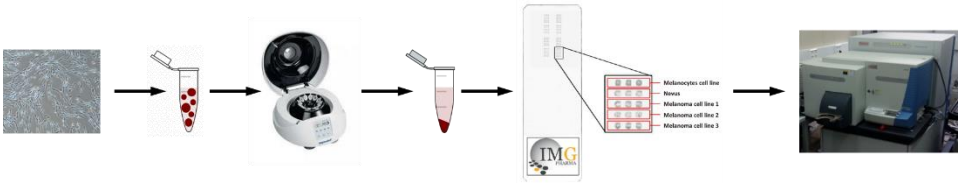

Fig 6.1. Workflow of the methodology used. Cells were cultured and transferred to an eppendorf with homogenation buffer. After several cycles of centrifugation, the pellet with membranes were resuspended in buffer and were printed onto a glass slide with the help of a robot. To conclude, microarrays were measured in convectional MALDI-IMS mode (Figure 2.3 from Chapter 2).

6.4 Results and discussion

Inter-experimental reproducibility

Five replicates of the array containing membranes from different cells (Figure 6.2.A and Figure A.6.1) were scanned in IMS negative-ion mode with a spatial resolution of 150 µm. Despite the small amount of sample deposited, 5-10 nL in each spot, it was enough to record reproducible spectra with good s/n ratio.

In order to explore the reproducibility of the methodology, the five replicates of the array were analyzed in different days. Furthermore, some spots from the same melanocytic cell lines were printed in diverse location of the microchip to test possible intensity fluctuations during experiments.

The five experiments were combined into a single matrix by an in-house developed software and analyzed by the already described DHCA-RC segmentation algorithm. Results demonstrated that the spectra of the replicates of the same cell lines distributed along a given array were homogeneous, so they were classified into the same cluster (red squares in Figure 6.2.B). Moreover, these clusters were consistent across different arrays measured in different days. These results suggest a good intra- and inter-experimental reproducibility.

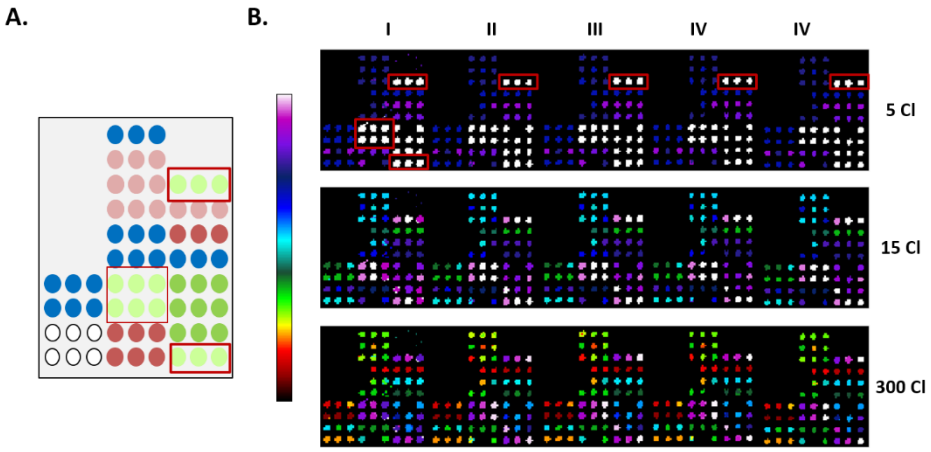

Fig 6.2. A – Scheme of the microarray designed for the study: light green spots represent melanocytic cell lines; dark green, melanocytes extracted and cultured from human nevi; blue spots, primary melanoma cell lines; and red colors represent different cell lines with high metastatic potential: maroon spots are metastatic in lymph node (MMGL), white spots represent subcutaneous metastasis (MMSN) and light maroon metastatic melanoma in other locations. For better visualization of the microarray, see Figure A.6.1. **B** – DHCA-RC analysis over the whole dataset. Experiments were combined in one matrix and the clustering was performed as if it were a single experiment.

Furthermore, the segmentation maps already suggest a different lipid phenotype between membranes from control and melanoma cell lines. For example, with the clustering level set to 5 Cl, all benign melanocytes grouped in the same cluster (green spots in Figure 6.2.A are in white in Figure 6.2.B), and the rest divided in four different groups. As images were represented using 1-correlation between clusters, the similarity in colors for all melanomas (from blue to purple) suggests a correlation between their spectra. When the clustering level was increased to 15Cl, benign melanocytes started to separate into commercial skin melanocytes (white and pink in Figure 6.2.B) and cells extracted from nevi (dark purple), suggesting the existence of differences in their lipid profile. Nevertheless, looking at the position of the colors in the color scale, they still correlated better than with melanoma spots. On the other hand, no separation was found between membranes of melanoma with different degrees of malignancy. In order to analyze and characterize the differences, spectra were extracted from each spot and further statistical analysis was carried out.

Lipid fingerprint of cell membranes

Average spectra of each cell line were obtained from each microarray, and the species were subjected exhaustive identification following the guidelines described in chapter 5, before being subjected to a PCA analysis. Only reproducible species were included in the analysis in order to eliminate those lipids that could be specific of a single cell line. Groups considered in the study were benign melanocytes, melanocytes extracted and cultured from nevus, primary melanoma cell lines and all metastatic cell lines (only one type of metastasis was included in the analysis, MMGL, due to the low sample size of the rest and their diverse origin).

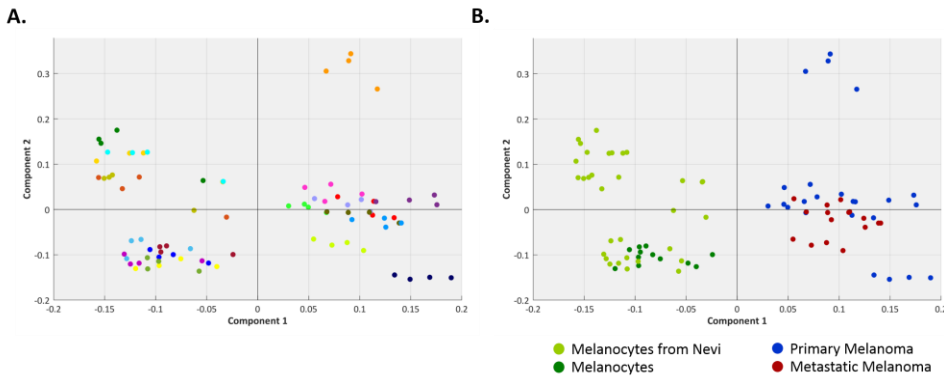

Fig 6.3. PCA analysis with lipid fingerprint extracted from spots of five microarrays**. A** - Each color represents a cell line. Their profiles were reproducible over five different arrays. **B** - Same analysis but highlighting the type of sample. There was a complete separation between melanocytes and all types of melanoma, but no distinction could be made within melanomas. Light green: melanocytes extracted from nevi. Dark green: commercial melanocytes. Blue: commercial primary melanoma. Red: metastatic melanoma.

Figure 6.3 presents the PCA with cells in different colors. Using reproducible lipid fingerprints, the first component was able to segregate primary melanocytic cells and melanocytic cell lines on one side (left side, in green in Figure 6.2.B) and melanoma cells on the other (right, blue and red), but no segregation was observed between primary melanoma and metastatic melanoma membranes. This promising result suggest that classification of a sample as tumor or non-tumor is feasible with this methodology, but a larger sample size would be necessary to build a classification model and validate it.

This analysis also shows the high reproducibility of the arrays throughout different experiments, in which experimental conditions may have suffered slight variations due to different laser energy, or matrix deposition. Taking into account that each spot is a replicate from a cell line (average from arrays measured in different days), the spectrum for each cell line was averaged for further analysis and biomarker discovery. Some studies in the literature use replicates to increase the sample size.[5] However, replicates are valuable for internal control to monitor the performance of the experiment, but not for statistical analysis, as they could introduce biases in the results and in consequence, in

biological conclusions.[6] Thus, the total number of samples for melanocytes is three, melanocytes extracted from nevus eight, primary melanoma six and melanoma with high metastatic potential in lymph node four.

Biomarker discovery for melanoma

In order to determine the molecular species that change with the pathological state of the cell, the lipid fingerprint of melanocyte membranes was compared with those from primary melanoma and membranes from cell lines with high metastatic potential by one-way ANOVA with post hoc correction. First, as usual, the homogeneity of variables was tested with Levene's test, and depending on the results, Bonferroni or Games-Howell was used for multiple comparison. Due to the low commercial melanocytic sample size, and to avoid any inflated false discovery, they were removed from the analysis and only melanocytes from nevi were considered.

The heatmap in Figure 6.4. shows the results from a hierarchical clustergram analysis with the molecular species whose variation was found to be significant (results not shown due to patentability procedures). No statistical differences were observed between primary melanoma and metastatic cell lines, but they were found between melanocytes and metastatic melanoma, and melanocytes and primary melanoma. Bar charts from Figure 6.5.B present these species. It is worth noticing that, for instance L.S 10, although it was not significant for primary melanoma, the bar charts suggest that indeed this specie is overexpressed in primary melanoma compared to melanocytes. Increasing the sample size may help to confirm these results.

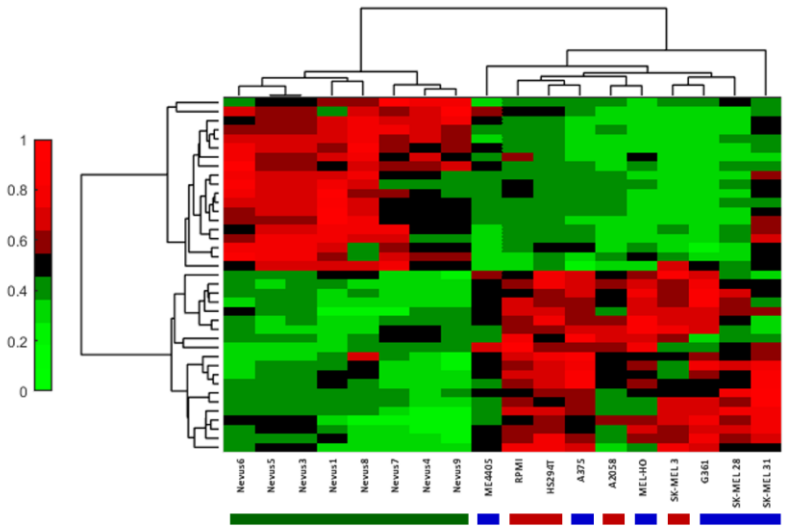

Fig 6.4. Heatmap of statistically different lipids for a better visualization. Hierarchical clustering using these species resulted on the arrangement of melanocytes extracted from nevus on the left side of the dendrogram (green), and melanoma on the right (blue and red). No separation could be achieved between primary and metastatic melanoma.

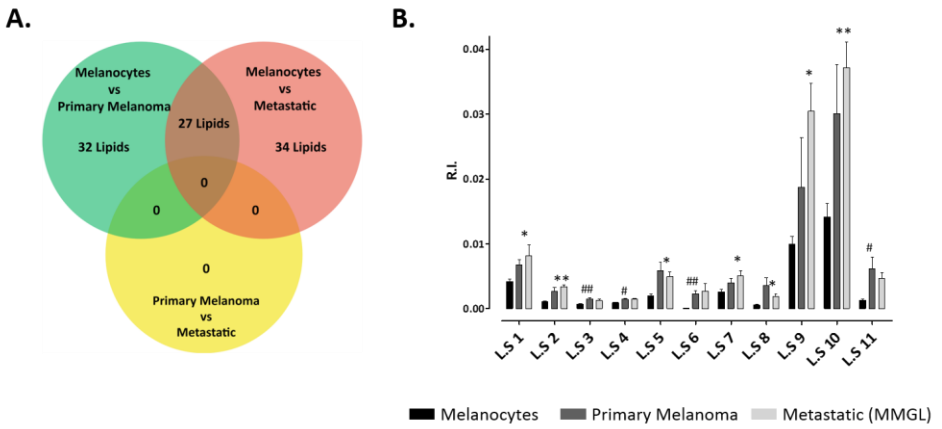

Fig 6.5. A - Number of significant lipids for each comparison. Five lipids were singular to melanocytes vs primary melanoma and seven to melanocytes vs metastatic. **B** - Species that were significant only for primary melanoma or metastatic. * : melanocytes vs metastatic. #: melanocytes vs primary melanoma. L.S: Lipid specie

39 lipid species were found to experience substantial changes among samples. However, not all of them had the same prediction power. In biomarker discovery, it is relevant to find indicators of the disease state with 100% of certainty. Thus, a statistically significant difference between classes is not sufficient, since there may be cases, in which, although the mean of the group is different, overlap between classes exist.[7] As an example, L.S 12 is shown in Figure 6.6.A, in which the values from melanocytes and MMGL (metastatic melanoma) are not completely separated. To test a possible overlap, the correct analysis is the receiver-operating characteristic (ROC). This takes into account true positive and true negatives, and the predictive value of a biomarker is given by the area under the curve of the analysis (AUC). Thus, if AUC value is close to 0.5, the distributions of the values overlap and there is no separation. On the other side, if the value is 1, a complete separation is achieved and this would indicate a possible good biomarker. The ROC curves for L.S 12 values can be found in Figure 6.6.B. While a complete separation was observed for primary melanoma with respect to melanocytes (AUC =1) indicating a possible good biomarker for early signs of melanoma, some of the values from MMGL overlapped with those from melanocytes (AUC = 0.875), suggesting a not so good specificity and sensitivity towards aggressiveness.

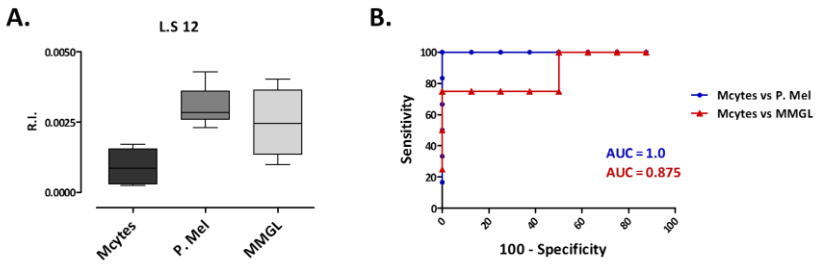

Fig 6.6. A – Box-plot for L.S 12 with whiskers from minimum to maximum observation. Box represents the interquartile range and the horizontal line within the box represents the median**. B** - ROC curve with the respective AUC for primary melanoma (blue) and metastatic (red) with respect to melanocytes. A complete separation was obtained for primary melanoma, while there were some values in metastatic that overlapped with melanocytes. L.S: Lipid specie.

ROC curves with the respective AUC were calculated for the species that one-way ANOVA with post hoc determined as statistically different. From an overall set of 39 lipids marked as relevant, 23 still fulfilled the conditions for good biomarkers, since the distribution has a complete separation in at least one of the comparisons (melanocytes vs primary melanoma or melanocytes vs metastatic). Figure 6.7 presents some examples of a complete separation for both comparisons (A), just between melanocytes and primary melanoma cell lines (B), and metastatic cell lines and melanocytes. It is worth noting that, while there are some lipids with AUC lower than 1, for instance the example in Figure 6.6.A when melanocytes are compared to metastatic melanoma, increasing the sample size may reinforce the differences.

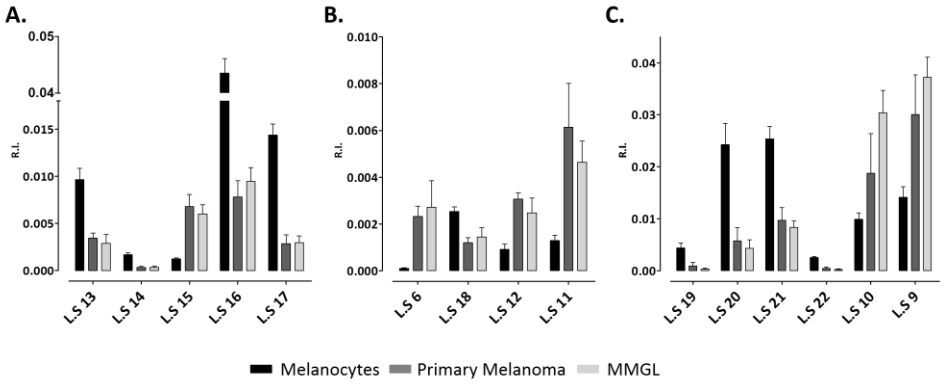

Fig 6.7. Results from ROC analysis. **A** - Complete separation for both melanoma types. **B** - Complete separation of primary melanoma with respect to melanocytes. **C** - Lipids whose values completely segregated metastatic from melanocytic cell membranes. L.S: Lipid specie

Advantage over conventional tissue-directed IMS

A different number of species were found significant comparing the results obtained in membranes of cell lines with those from human biopsies. Due to the different microenvironment of the samples, some of the changes in species differed considerably. While in cell cultures, cells are controlled, with the right amount of cultured medium with specific nutrients for their growth, in biopsies, cells are "free" to grow as they please. Furthermore, membranes instead of whole cells were spotted in the microarrays. Thus, changes occurring in other regions of the cell are lost, but it may also be possible that previous hidden changes were uncovered with the used of microarrays. Hence, it is normal to expect some differences between tissue and cell lines.

Venn diagrams in Figure 6.8.A-B show the comparison of the results obtained from tissues in Chapter 5 with those from membrane arrays, using one-way ANOVA and multiple comparison. While, as mentioned before, the number of significant species varied between the two sets of experiment, 11 mutual lipid species were found in the case of melanocytes vs primary melanoma, and nine species for melanocytes vs metastatic. Some examples are presented in the Figure 6.8.C for the first comparison, and Figure 6.8.D for the second one. Remarkably, the values correlated well between tissue and cell lines.

One of the main advantages of microarrays over tissue experiments is the time employed to obtain the final results. Here we present quite comparable results, from tissue and microarrays. However, while in the first case, the experiments were measured during several months, almost a year, the second only required one week of analysis. In contrast, there are some aspects to consider when microarrays-based technology is employed. One of the most relevant is the loss of spatial context, and hence, the information about the heterogeneity of the tissue, as well as the loss of real biological microenvironment.

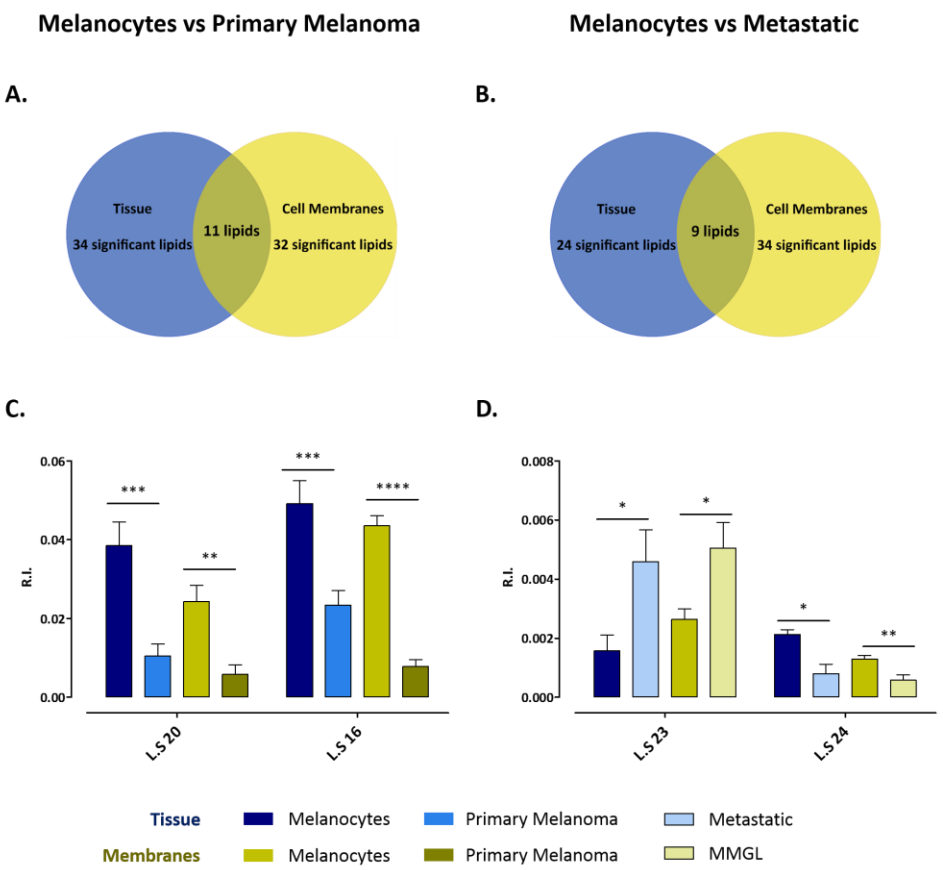

Fig 6.8. Comparison between results from arrays with those obtained directly from tissue. **A** – Number of significant species in tissue and cell membranes to differentiate between melanocytes and primary melanoma. 11 lipids were common to both experiments. **B** – From 24 and 34 significant lipids between melanocytes and metastatic in tissue and cell membranes, respectively, nine were common to both experiments. **C and D** – Some examples of common lipids for both cases.

6.5 Conclusions

We recorded the lipid fingerprint from membranes of several cell lines in an automated and fast methodology to create a lipid profile database as a proof of concept. The lipid phenotypes of the cell membranes were different enough to classify the cells using a simple PCA. This demonstrates the feasibility of using this methodology, which combines microarray technology with mass spectrometry, to build powerful classification models that could yield outstanding results with an appropriate sample size. Thus, this protocol could help in disease diagnosis, prognosis or treatment monitoring.

It is worth mentioning that only cell membranes were used, and not the whole cell or extract, like it is commonly used in LC-MS experiments. Despite that, the membranes were fully functional in the array and various mutual differences were observed with respect to tissue samples. In this way, the use of membranes provides the possibility of combining the results from the lipid analysis with those from enzymatic or radioligand binding studies, with the final goal of unraveling the link between specific lipids and proteins.[4] Moreover, the protocol for sample preparation is simpler than for homogenates and membranes adhere better than cells to glass slides. Furthermore, the intra- and inter-experiment reproducibility of this methodology has been proved, enabling the combined analysis of experiments measured in different days.

Still, there are some challenge that would be interesting to tackle. One of them is quantification. MALDI-IMS is a semi-quantitative technology, and whilst great effort has been made to transform it into a quantitative technique, further developments are required.

In summary, the protocol presented is a miniaturized version of the traditional MALDI-IMS protocol that results in smaller sample and time consumption per analysis, enabling a fast and automated lipidomic analysis for biomarker identification.

---

[1] Djidja MC, Claude E, Snel MF, Francese D, Scriven P, Carolan V, Clench MR. Novel molecular tumour classification using MALDI-mass spectrometry imaging of tissue microarray. 2010. *Anal. Bioanal. Chem.* **2010**. 397: 587-601.

[2] Groseclose MR, Massion PP, Chaurand P, Caprioli RM. High-throughput proteomic analysis of formalin fixed paraffin-embedded tissue microarrays using MALDI imaging mass spectrometru. *Proteomics*. **2008**. 8:3715-3724.

[3] Casadonte R, Caprioli RM. Proteomic analysis of formalin-fixed paraffin-embedded tissue by MALDI imaging mass spectrometry. *Nat. Protoc*. **2011**. 6:1695-1709.

[4] Heber-Chatelain E, Desprez T, Serrat R, Bellocchio L, Soria-Gomez E, Busquets-Garcia A, Pagano-Zottola AC, Delamarre A, Cannich A, Vincent P, Varilh M, Robin LM, Terral G, Garcia-Fernandez MD, Colavita M, Mazier W, Drago F, Puente N, Reguero L, Elezgarai I, Dupuy JW, Cota D, Lopez-Rodriguez ML, Barreda-Gomez G, Massa F, Grandez P, Benard G, Marsicano G. A cannabinoid link between mitochondria and memory. *Nature*. **2016**. 539: 555-559.

[5] Kim HY, Lee H, Kim SH, Jin H, Bae J, Choi AK. Discovery of potential biomarkers in human melanoma cells with different metastatic potential by metabolic and lipidomic profiling. *Sci. Rep.* **2017**. 7: 8864.

[6] Vaux DL, Fidler F, Cumming G. Replicates and repeats. What is the difference and is it significant? *EMBO Rep.* **2012.** 13: 291-296.

[7] Jones EA, Deininger SO, Hogendoorn PCW, Deelder AM, McDonnell LA. Imaging mass spectrometry statistical analysis. *J. Proteomics*. **2012**. 75: 4962-4989.

Chapter 7

Lung Cancer: a preliminary study

Additional samples from different origins were analyzed during this thesis in order to study heterogeneity and multiple comparative study, as well as to try to understand the role lipids play on the development of different disease and explore possible links with different risk factors. One of such system was lung cancer.

The results presented in this chapter are preliminary results from lung biopsies. Further measures and analysis are required to obtain a meaningful sample size.

7.1 Introduction

Human lungs are the primary organ in the respiratory system. It is composed of different types of epithelial cells, as well as pulmonary surfactant. These two major components enable the exchange of gases between blood and air.[1]

Lung cancer is one of the most common cancers, with an estimate of 1.8 million new cases diagnosed per year (13 % of all new cases). It is the leading cause of cancer-related death worldwide, with a 16% of 5-year survival rate.[2] Another common cause of death is Chronic Obstructive Pulmonary Disease (COPD), a progressive and ultimately fatal deterioration of lung function, causing difficulties on breathing. In particular, COPD is characterized by the excessive inflammation and matrix destruction and it is the most common lung disease, even more abundant than lung cancer.[3,4]

The main risk factor for both diseases is tobacco. Despite the well-known health risk of cigarettes, due to the bad habits, smoking is the only major cause of death that is increasing rapidly, especially in developing nations.[5] However, COPD itself is thought to be an independent risk factor for the development of lung cancer, increasing the incidence of lung cancer and lung cancer death.[6,7] Lately, the mechanistic link between these heterogeneous diseases has earned attention, however, still little is known.

Several studies have been reported in literature about the lipidome of healthy lung and lung cancer, in which the decrease of main phospholipids from surfactants was described by LC-MS[8] and lung cancer and healthy lung tissue were characterized by LC-MS and MALDI-IMS.[9,10] However, COPD, and the role lipidome could be playing in this disease has been scarcely investigated,[11] as well as the influence of exposure to tobacco.[12]

Here we examine the potential relationship between tobacco, COPD and lung cancer, focusing on alterations in lipid profiles in lung epithelial cells. These cells are involved in hosts defense and therefore, they are responsible for protection against inhaled particulates, toxic gases and infectious agents.[13,14]

7.2 Objectives

The goal is to study the possibility of using a lipidomic approach combined with MALDI-IMS to investigate and understand the lipid metabolism in healthy lung, COPD and lung cancer and the possible link that may exist between both diseases, as well as with tobacco.

7.3 Experimental section

Human sample collection

Four groups were considered for the study: healthy, healthy smokers, patients with COPD and patients with lung cancer (n = 3 for all groups).

Samples of biopsies were obtained during bronchoscopy (Ethical Committee permission nº IB2270/14 PI) in Son Espases Universitary Hospital (Balearic Island, Spain and were immediately snap frozen in liquid N_2. Ten-micron sections were prepared on glass slides using a cryostat. This part of the study was carried out at Son Espases Universitary Hospital, under supervision of Dr. Gwendolyn Barceló-Coblijn.

Imaging and data analysis

A detailed description of sample preparation can be found in Chapter 3 and information regarding the optimal amount of matrix in Chapter 4. Data was acquired only in negative-ion mode with 25 µm spatial resolution and a mass resolution of 60.000 FWHM at m/z = 400, and with a laser energy of 20-30 µJ/pulse. The rest of the MALDI-IMS parameters used are described on Materials and methods (Chapter 3).

Data handling and analysis was carried out using MSI Analyst (NorayBioinformatics S.L, Derio, Bizkaia) to capture the spectra (parameters in Chapter 3), reconstruct images and clustering analysis. IBM SPSS Statistics for Windows (Version 23.0; IBM, Chicago, IL, USA) was used for Levene's test, one-way ANOVA and Bonferroni/Games-Howell post multiple comparison. Levene's test determines the homogeneity of the variables (H_0 = groups have equivalent variances) in order to choose the correct post hoc method: Bonferroni if Levene's $p \geq 0.05$ and Games-Howell if Levene's $p \leq 0.05$. In all instances, p values < 0.05 were considered statistically significant. Matlab (MathWorks, Natick, USA) was used for PCA analysis and hierarchical clustering dendrogram.

7.4 Results and discussion

Imaging mass spectrometry of lung biopsies

Figure 7.1 shows a comparison between the optical images of lung biopsy sections and the lipid distribution obtained by IMS in negative-ion mode with a spatial resolution of 25 µm. An example from each group analyzed for this thesis is shown: healthy patient, healthy smoker, patient with COPD and patient with tumor. Negative-ion mode enabled the detection of a wide variety of lipids, including PS, PI, PG, PE and SM. Some of them seem to be tissue-specific, like PE 34:1, which seems to be specific of lung epithelium.

When bronchoscopy is performed, the biopsy is extracted with the aid of a tube, however the tissue removed is not always equivalent. Lung is a spongy, air-filled organ with no special anatomy. Biopsies from one patient to another varied considerably, and in the case of our study, these variations increased samples heterogeneity to another level.

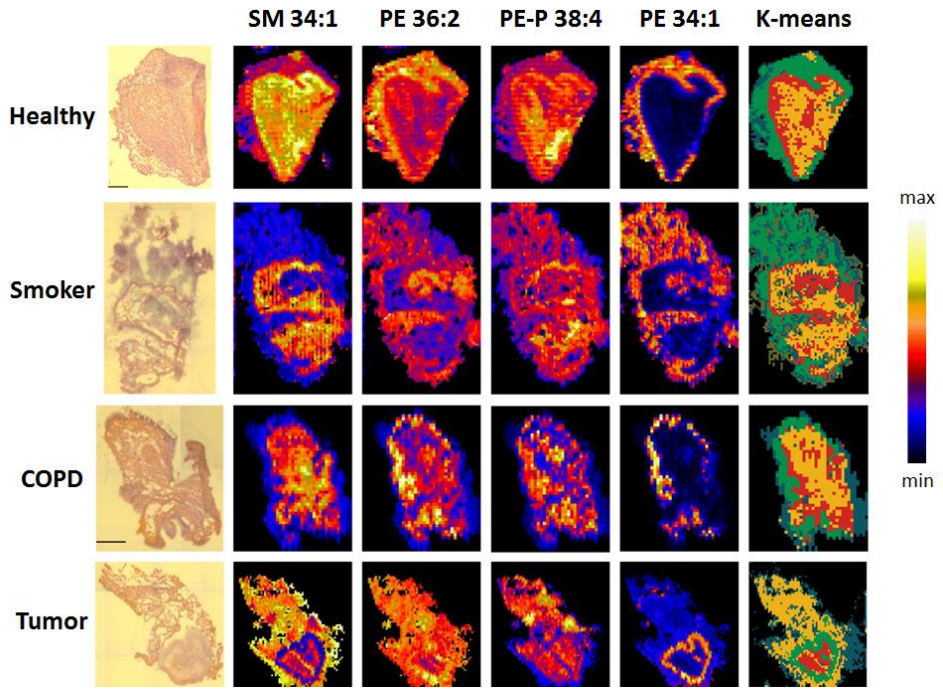

Fig 7.1. Comparison between the optical images of a human lung tissue sections stained with H&E and the distribution of some selected lipid species detected in negative-ion mode. The last column is a *k-means* clustering analysis for pattern recognition, setting the number of clusters to four. An example from each study group is presented: healthy mucosa, healthy smoker, patient with COPD and patient with tumor

Still, with the help of the optical image and *k-means* clustering, epithelial tissue could be identified in all samples (green cluster from segmentation maps in Figure 7.1) to further analyze lipids changes associated to each different condition, as well as to look for possible lipidomic connection between tobacco and both diseases.

Statistical analysis of epithelium

Figure 7.2 presents a PCA analysis of epithelial clusters selected in the Figure 7.1 for healthy, healthy smoker, COPD and lung cancer. The peaks in the spectra were identified with the guidelines from Chapter 5, and only reproducible species were considered during the analysis in order to minimize the interindividual variability. The results suggest that lung cancer presents a unique lipid fingerprint, different enough to allow us to separate those samples from the rest of patients. However, the separated distribution of the three scores in the PCA revealed that these three biopsies present significant differences in lipid expression. Lung cancer is a heterogeneous disease with multiple histological and molecular subtypes.[15] This heterogeneity will need to be considered in future work.

Regarding the rest of the samples, a subtle tendency was observed, grouping together samples according to the type, with COPD located between healthy patients and cancer. However, a further statistical analysis is needed for better separation. Note that the epithelium from healthy smokers are also between COPD and healthy mucosa. This could help us to understand the link between tobacco and diseases.

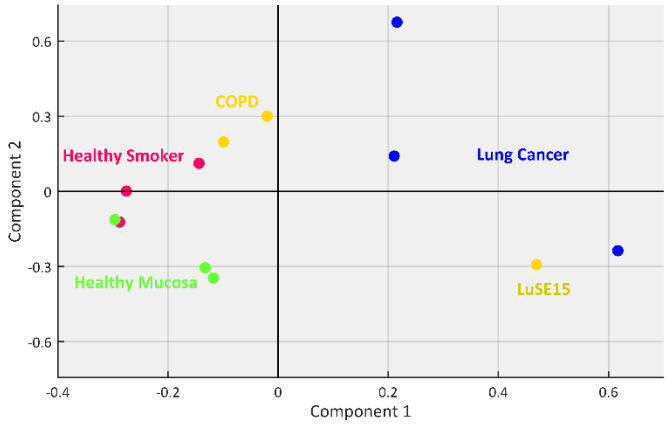

Fig 7.2. PCA analysis of epithelium clusters selected on the first section from healthy patients, healthy smoker, COPD and tumor.

Despite the sample Luse15 (Figure 7.2) was initially diagnosed as COPD, the PCA results showed that the lipidomic of this biopsy section, somehow, resembled lung cancer. Therefore, this sample was removed from the rest of the analysis and the diagnosis will be corroborated with a pathologist.

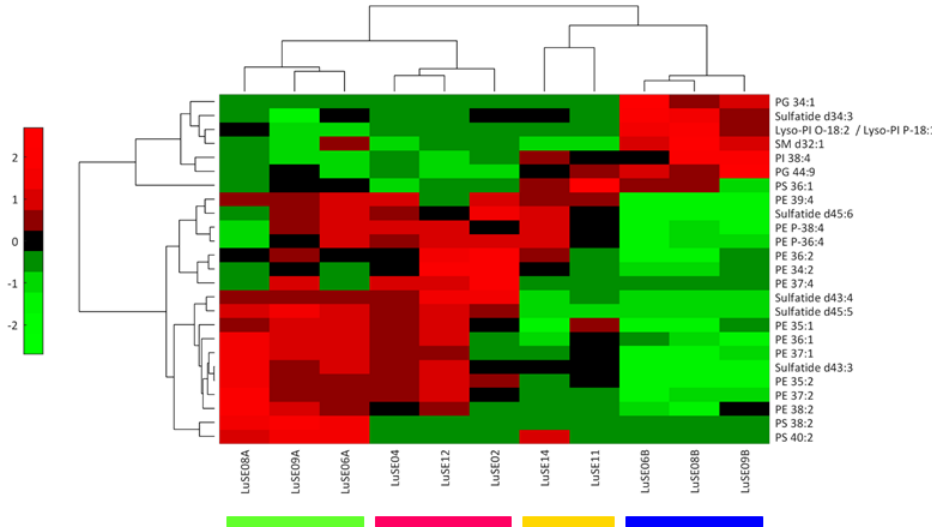

Fig 7.3. Heatmap to present results from one-way ANOVA statistical analysis. Experiments from healthy biopsy sections are marked in green, healthy smokers in pink, while COPD samples are in orange and cancer in blue.

To determine the lipids that are differently expressed in the four groups, a one-way ANOVA with post hoc correction was performed. The results are shown in Table A.7.1. The intensities of lipids that experience statistically significant changes in abundance between types of sample (p-value < 0.05) were plotted on a hierarchical clustergram for better visualization, and a perfect division was obtained (Figure 7.3). Healthy samples are organized on the left side of the heatmap (marked by green for control and pink for healthy smokers), while both diseases, COP (orange) and lung cancer (blue), are arranged on the right side.

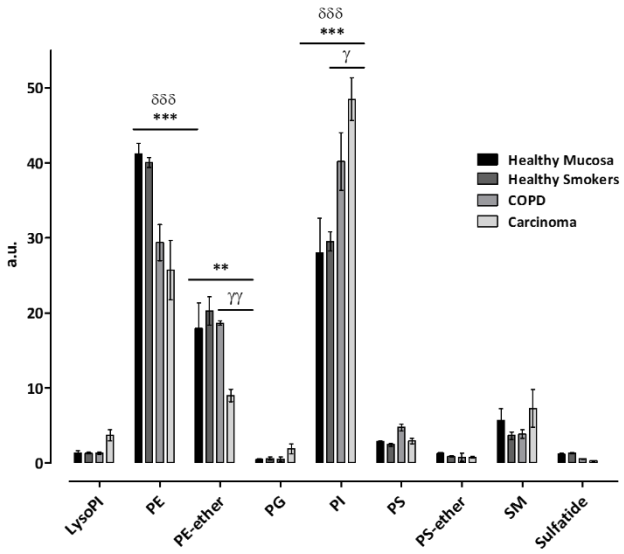

Fig. 7.4. Comparison between relative abundance of different lipid classes detected in negative-ion mode for the four groups. Statistical significance was assessed using one-way ANOVA with multiple comparisons (p value ‹ 0.05). *: healthy mucosa vs. carcinoma. δ: healthy mucosa vs. COPD. γ: healthy smoker vs. COPD. Values are expressed as mean ± SEM (n=3 in healthy mucosa, healthy smoker and lung cancer and n=2 in COPD).

Furthermore, lipid composition of different classes detected in negative-ion mode were also compared between the four groups. Overall, there is a decrease of total amount of PE in both diseases while the total amount of PI increases. Not only there is an increment between healthy and diseases in the total amount of PI, but also between COPD and cancer patients. This tendency on PI species suggests that PI are overexpressed in both diseases, but especially in cancer. Finally, in addition to the reduction of the total amount of PE, there is also a decrease in its alkyl counterpart (PE-ether) in tumor.

With such small sample size, it is not recommended to extract any biological conclusion, but these results suggest that lipidomic combined with mass spectrometry could be a promising approach to study the link between tobacco, COPD and lung cancer, provided that a large-enough collection of samples is available.

7.5 Conclusion

This chapter presented a lipid phenotype characterization of lung biopsies using MALDI-IMS. Clear differences between malignant and non-malignant epithelium were found in this proof of concept, enabling the classification of tumor from healthy or COPD using a simple PCA. But further analysis will be required to be able to differentiate COPD and smoker's epithelium from healthy mucosa. Thus, some possible biomarkers were identified, but no clear biological conclusion could be drawn due to the low sample size.

Further work is currently on going to study the heterogeneity of lung biopsies, and to confirm and validate[16] these preliminary results in order to build a classification model. For these objectives and to draw biological conclusions, it is essential to increase the number of patients in the study.

---

[1] Schneeberger EE in THE LUNG: Scientific foundations. Second Edition. Lippincott - *Raven Phublishers*. **1997**.

[2] Ferlay J, Soerjomataram I, Ervik M, Dikchit R, ESER s, Mathers C, Rebelo M, Parkin DM, Forman D, Bray F. GLOBOCAN 2012: Estimated Cancer Incidence, Mortality and Prevalence Worldwide in 2012. *IARC CancerBase No. 11*. **2014.**

[3] Mannino DM. Epidemiology and global impact of chronic obstructive pulmonary disease. *Semin. Respir. Crit. Care Med.* **2005**. 26: 204-210.

[4] Houghton AM. Mechanistic links between COPD and lung cancer. *Nat. Rev. Cancer.* **2013**. 13: 233-245.

[5] Peto R, Chen ZM, Boreham J. Tobacco-the growing epidemic. *Nat. Med.* **1999**. 5:15-17

[6] Durham AL, Adcock IM. The relationship between COPD and lung cancer. *Lung Cancer.* **2015**. 90: 121-127.

[7] Wasswa-Kintu S, Gan WQ, Man SF, Pare PD, Sin DD. Relationship between reduced forced expiratory volume in one second and the risk of lung cancer: a systematic review and meta-analysis. *Thorax.* **2005**. 60: 570-575.

[8] Eggers LF, Müller J, Marella C, Scholz V, Watz H, Kugler C, Rabe KF, Goldmann T, Schwudke D. Lipidomes of lung cancer and tumour-free lung tissues reveal distinct molecular signatures for cancer differentiation, age, inflammation, and pulmonary emphysema. *Sci. Rep.* **2017**. 7.

[9] Marien E, Meister M, Muley TM Fieuws S, Bordel S, Derua R, Spraggins J, Van de Plas R, Dehairs J, Wouters J, Bagadi M, Dienemann H, Thomas M, Schnabel PA, Caprioli RM, Waelkens E, Swinnen JV. Non-small cell lung cancer is characterized by dramatic changes in phospholipid profiles, *Int. J. Cancer.* **2015**. 137: 1539-1548.

[10] Zemski-Berry KA, Murphy RC, Kosmider B, Mason RJ. Lipidomic characterization and localization of phospholipids in the human lung. *J. Lipid Res.* **2017**. 58: 926-933.

[11] Telenga ED, Hoffmann RF, t´Kindt R, Hoonhorst SJM, Willemse BWM, van Oosterhout AJM, Heikink IH, van den Berge M, Jorge L, Sandra P, Postma DS, Sandra K, ten Hacken NHT. Untargeted lipidomic analysis in chronic obstructive pulmonary disease. *Am. J. Respir. Crit. Care Med.* **2014**. 190:155-164.

[12] de la Monte SM, Tong M, Nunez K, Yalcin E, Kay J, Agarwal AR, Cadenas E. Tobacco smoke-induced alterations in hepatic lipid profiles demonstrated by imaging mass spectrometry. *Mass Spectrom. Purif. Tech.* **2016**. 2: 1000112.

[13] Zhao CZ, Fang XC, Wang D, Tang FD, Wang XD. Involvement of type II pneumocytes in the pathogenesis of chronic obstructive pulmonary disease. *Respir. Med.* **2010**. 104: 1391-1395.

[14] Grainge CL, Dvies DE. Epithelial injury and repair in airways diseases. *Chest.* **2013**. 144: 1906-1912.

[15] Beadsmoore CJ, Screaton NJ. Classification, ataging and prognosis of lunc cancer. *Eur. J. Radiol.* **2003**. 45_ 8-17.

Chapter 8

Future perspectives

8.1 Future perspectives

Recent advances in mass spectrometry have boosted the interest to describe the complete lipidome of different pathological states. IMS is an analytical tool that enables a better comprehension of complex biological system by visualizing metabolites and their spatial arrangement. However, the technique still faces numerous challenges, preventing it from taking off as a powerful technique in clinical application. This thesis deals with some of the obstacles that prevent this tool from find application in clinical research, and specially in cancer research.

The first barrier investigated in **Chapter 4** was the spatial resolution. In order to put IMS on par with other standard optical techniques used in cancer research, it is important to achieve cellular or even sub-cellular resolution, which tests the limits of this technique. We demonstrated that with a meticulous procedure, using the right matrices and the correct deposition protocol, 10 µm, or even 5 µm of lateral resolution can be achieved with a no-so optimal laser spot using oversampling. Still, this methodology requires of a careful sample handling and the optimal instrument conditions. N_2 lasers have a specific lifetime that makes necessary its replacement every other year, if the mass spectrometer is subjected to a heavy duty cycle. Such replacement involves an alteration of the beam profile, as lasers features vary from laser to laser, and even from recharge to recharge, making crucial the characterization process. Moreover, not all types of laser spots are optimal for an oversampling acquisition type. Our experience over the last four years with two different N_2 lasers showed us that it was not always possible to achieve cellular resolution without any optical modification.

In this context, significant progress has been made in spatial resolution, specially with the release of new instrumentation. One of those examples is RapifleX MALDI Tissuetyper from Bruker, the faster spectrometry with high spatial resolution.[1] However, "not all that glitters is gold". Another challenge that has been addressed in **Chapter 5** was metabolites identification. Despite MALDI being a soft ionization technique and due to the labile nature of lipid, we reported the presence of in-source fragmentation, making identification a difficult task. Moreover, the mass resolving power of the analyzer is also a limiting factor for the correct identification. Images reported in the literature with RapifleX are exceptional; however, this instrument uses a TOF-type mass analyzer. The main advantage of this type of analyzer is its speed. They are much faster than magnetic sector mass analyzers; however, they have one main drawback which is the above mentioned limited mass resolving power. Even the latest generation of TOF cannot reach mass resolutions above 10.000 FWHM in the lipid region. This is a major obstacle for the identification of lipids, as the images obtained may come from one molecular specie or from the sum of several of them if the m/z are too close. Hence, the real biological context would be perturbed and the conclusions drawn may differ from the real nature of the tissue.

It is in this framework that our lab is currently working on the improvement of the optical set-up of MALDI-LTQ-Orbitrap described in this thesis. Thus, no matter the dimension and characteristics of the laser beam, our objective is to reach subcellular resolution with an Orbitrap-type analyzer, which yields outstanding mass resolving power, enabling accurate species identification. The idea is, and thanks to the help of the expert

from Laser Facility of SGIKER, to focus the laser beam into a Gaussian-shaped, more concentrated spot with the aid of a set of lenses, and then, with a 20 or 10 μm ceramic pinhole, to filter beam profile. Thus, since only the most intense part of the laser beam is allowed to cross the pinhole, a much smaller but more concentrated spot is achieved, resulting in a loss of signal that is only related to smaller irradiated area, and enabling the recording of outstanding images of lipid distribution

Improvements in technology are essential to push research to the next level, and specially in IMS, to achieve higher resolutions that could battle with conventional optic technologies. Still, progress without giving a biological context makes us question the utility of IMS. From one single experiment the amount of data recorded is immense, and to handle it properly is a difficult task as seen in **Chapter 5.** It is crucial to give biological context to the results in order to, first, understand them and later to use them for diagnostic, monitoring or even to choose the correct therapy. While lipids serve as direct signatures of biochemical activity and are therefore easy to correlate with phenotype, they alone do not explain the complex nature of the cell. We have demonstrated that it is feasible to link lipid changes with certain enzymatic process by immunohistochemical analysis (IHC).[2,3] However, this technique, which is focused primarily on monitoring changes in macromolecules, requires of special antibodies or chemical labeling, limiting the number of molecules analyzed in a single experiment. Moreover, due to the large exposure of the tissue to atmospheric condition, matrix and other external factors, the IHC assay post-MALDI experiment may sometimes be difficult and not always favorably achieved. Hence, our lab is currently engaged in multimodal IMS approach to acquire images from different analytes within the same tissue. The idea is to correlate lipid and protein information from the same region to improve our understanding of different biological processes. In this context, the concept of lab-on-a-chip presented in **Chapter 6** could also help unraveling the link between lipids and protein, combining the results from lipid analysis with those from enzymatic or radioligand binding. The use of membranes microarrays combined with mass spectrometry has proven to be a promising technology, and we are currently working on extending it from cell lines to real biopsies in order to build an accurate classification model for tumor diagnosis as well as prognosis.

In general, IMS is an appealing, powerful, high-throughput technique for biomedical research, but it is important to push it to its limit to earn adepts in clinical applications. It is important to accurately identify molecules to, as seen in **Chapter 4** for example, clearly identify the pathophysiological state of the cell. Another case in which it is relevant to accurately assign lipids is on the identification of malignant cells in a tissue, on the basis of the lipid profile, as done in **Chapter 5**. However, another challenge that IMS must face is the complexity of the whole procedure. Despite the easy sample preparation, and easy experimental set-up, the data analysis, and specially, the pre-processing for the final statistical analysis is still complex as shown in this thesis. Therefore, development of new software that automates the whole process of data processing as well as analysis and interpretation is compulsory for the technique to be, someday, implemented as a routine diagnostic tool in clinics.

[1] Prentice DM, Chumbley CW, Caprioli RM. High-speed MALDI MS/MS imaging mass spectrometry using continuous raster sampling. *J. Mass Spectrom.* **2015**. 50: 703-710.

[2] Bestard-Escalas J, Garate J, Maimó-Barceló A, Fernández R, Lopez DH, Lage S, Reigada R, Khorrami S, Ginard D, Reyes J, Amengual I, Fernández JA, Barceló-Coblijn G. Lipid fingerprint image accurately conveys human colon cell pathophysiologic state: a solid candidate as biomarker. *Biochim. Biophys. Acta.* **2016**. 1861: 1942-1950.

[3] Lopez DH, Bestard-Escalas J, Garate J, Maimó-Barceló A, Fernández R, Reigada R, Khorrami S, Ginard D, Okazaki T, Fernández JA, Barceló-Coblijn G. Tissue-selective alteration of ethanolamine plasmalogen metabolism in dedifferentiated colon mucosa. *Biochim. Biophys. Acta Mol. Cell Biol. Lipids.* **2018**. 1863: 928-938.

eman ta zabal zazu
Universidad del País Vasco
Euskal Herriko Unibertsitatea
ZIENTZIA ETA TEKNOLOGIA FAKULTATEA
FACULTAD DE CIENCIA Y TECNOLOGÍA

Aurrerapenak MALDI-*Imaging* Masa-Espektrometria teknikan: ehunen lipidoak karakterizatzen

Doktorego-Tesia

Jone Garate Veregui

Zuzedariak:

José Andrés Fernández González

Gabriel Barreda Gómez

2019

2015-2019 bitartean Euskal Herriko Unibertsitateko ikertzaileak prestatzeko doktoretza aurreko beka izan dut.

Ikerketa lan hau Espainiako Ekonomia eta Lehiakortasun Ministerioak (RTC-2015-3693-1) eta Eusko Jaurlaritzako Ekonomiaren Garapen eta Lehiakortasun sailak (KK-2017/00041 eta KK-2018/00090) finantziatu zuen.

Aipamen berezia Euskal Biobanku eta IRBLleidako Biobankuari eta, halaber, SGIKerri.

Sarrera orokorra eta helburuak 1

1.1 Sarrera orokorra 3

1.2 Tesiaren helburu nagusiak 5

***Imaging* Masa-Espektrometria eta Lipidomikaren oinarriak 7**

2.1 Masa-Espektrometria 9

2.2 *Imaging* Masa-Espektrometria (IMS) 9

Ionizazio-ganbara 10

Matrix assisted desorption/ionization (MALDI) 10

Masa-analizatzaileak 13

Orbitrap 14

2.3 Lipidomika 15

Gantz-azidoak 17

Glizerofosfolipidoak 18

Esfingolipidoak 19

Nomenklatura 20

Erresoluzio espazial handiko IMS zelulen egoera fisiologikoa eta patologikoa zehazteko 23

4.1 Sarrera 25

4.2 Helburuak 27

4.3 Metodologia 27

Giza kolon biopsien bilketa 27

Imaging eta datuen analisia 27

4.4 Emaitzak eta ezbaida 28

Matrizearen prestaketa 28

Laser-izpiaren karakterizazioa 28

Erresoluzio handiko *Imaging* Masa-Espektrometria 29

Kolonozioten diferentziazioa epitelio osasuntsuan 31

Epitelioaren dediferentziazioa kontestu patologiko batean 36

Diferentziazio prozesua lamina propia osasuntsu eta patologikoetan 41

4.5 Ondorioak 43

Ikerketa klinikoetan erabiltzeko tresna analitiko berrien garapena 47

6.1 Sarrera 49

6.2 Helburuak 49

6.3 Metodologia 50

Zelula-lerro eta beren kultiboen baldintzak 50
Zelula-mintzen isolamendua 50
Zelula-mintzen mikroarraien inpresioa 50
IMS eta datuen analisia 50
6.4 Emaitzak eta eztabaida 51
Erreproduzigarritasuna esperimentuen artean 51
Zelula-mintzen lipido hatz-marka 53
Melanoma adierazi dezaketen biomarkatzaileen bila 54
IMS konbentzionalarekiko abantailak 57
6.5 Ondorioak 59
Zenbait ildo etorkizuneko ikerketei begira 61
8.1 Zenbait ildo etorkizuneko ikerketei begira 63
Eranskina: 4. Kapitulua I
Eranskina: 6. Kapitulua XXXIII
Laburdurak ..... A

1. Kapitulua

Sarrera orokorra eta helburuak

1.1 Sarrera orokorra

Azkeneko hamarkadetan, errendimendu handiko instrumentazio analitikoek izandako aurrerapenei esker ikerketa "omikoek" izugarrizko bultzada izan dute. Ikerketa hauen helburua molekula biologiko ezberdinen karakterizazioa eta kuantifikazioa da, zeluletan, ehunetan edo organismoetan ematen diren prozesu biologiko ezberdinak erabat ulertu ahal izateko.[1,2] XX. Mendearen amaieran sortu zen lehen arloa genomika izan zen, organismo baten genomaren, hots, DNA osoaren azterketa.[3] 2002an Giza Genomaren Proiektuak[4] medikuntza guztiz aldatu zuen, minbiziaren eta gaixotasun arraroen diagnostikorako lagungarri izan daitezkeen prozesu biologikoen ikuspegi berri bat eskainiz. Hala ere, genomika sistema osoaren atal bat besterik ez da, izan ere, gaixotasun asko transkripzioaren ondoren ematen diren aldaketei edo prozesuei esker gertatzen baitira. Geroago, XXI. mendean, transkriptomaren (RNAm osoaren azterketa) eta, bereziki, proteomikaren (adierazitako proteina guztien azterketa) iraultza iritsi zen.[5,6] Hala ere, hiru arlo hauek sistema biologikoak hobeto ezagutzeko aukera eskaini arren, ez dute prozesu biologikoen informazio osoa aditzera ematen, sistema osoa itxiko lukeen arlo baten falta baitzegoen. Honek, metabolomikan gero eta interes handiago izatea sustatu zuen. Metabolomika, pisu molekular baxuko (‹1.500 Da) molekulen (metabolitoak) azterketa sakonean oinarritzen da.[7] Metabolitoak, geneen transkripzioez adierazitako entzima-proteinek sortzen dituzten molekulak dira. Beraz, fenotipoa genotipoarekin erlazionatzen du, 1.1. Irudian ikusi daitekeen bezala, ikerketa omikoek sortzen duten katearen azken mailan kokatzen baitira, sistema osoa itxiz.

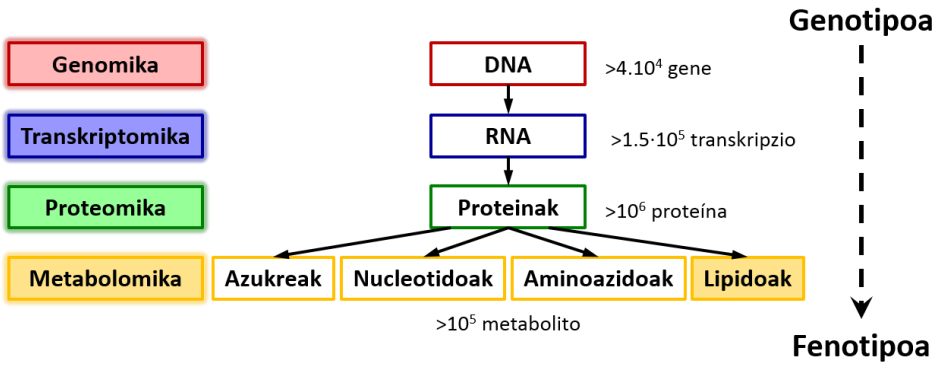

Fig 1.1. Ikerketa omikoak. DNA, RNAm, proteina eta metabolito ezberdinen arteko erlazioak, genotipoa fenotipoarekin lortzen du.

Azken urteotan, lipidomika,[8] metabolomikaren azpi-esparru bat, etorkizun handiko ikerketa-arlo bilakatu da, batez ere minbiziaren ikerketan, konplexutasuna haundituz sistema osoari.

Lipidomikaren helburua, lipidoek zeluletan duten eginkizun edo funtzioa aztertu eta ulertzeko xedearekin, sistema biologiko anitzetan lipido mota ezberdinak zehaztea eta

kuantifikatzea da.[8] Lipidoek berebiziko garrantzia dute zelulen, ehunen eta organoen fisiologian, zelula-mintzen osagai nagusiak baitira. Biomolekula hauek, funtzio estrukturala izateaz gain, funtsezko prozesu biologiko askoren erregulazioan parte hartzen duten seinalizazio molekula garrantzitsuak ere badira. Zelula eukariotoek baliabide ugari erabiltzen dituzte milaka lipido ezberdin sortzeko.[9] Lipido bat osatzeko dauden konbinazio ezberdinek, hala nola kate alifatiko edota talde funtzionalaren dibertsitateak, <1000 lipido espezie ezberdin egotea ahalbidetzen du, aniztasun honek propietate ezberdin ugariz hornitzen duelarik zelula. Mintz bakar bat lipido-espezie ezberdinez osaturik dago, mintz mota bakoitzak lipido konposaketa ezberdina izanez.[10] Normalean organulu guztiek lipido espezie berdinak izaten dituzte, beraien arteko erlazio molarra izanez aldatzen dena. Honela, mintz bakoitzak izango duen ezaugarri fisiko eta funtzionalak, zelula-mintzen tolesturak esaterako, lipido-espezie hauen konposizio zehatzak zehaztuko du. Beraz, patologia askotan lipidoen metabolismoa alteratua egotea espero da.[11]

Lipidomika ikerkuntzan erabiltzen den teknika nagusienetariko bat masa-espektrometria (MS) da, molekulen ugaritasuna eta masa-karga (m/z) erlazioa fase gaseosoan aztertzen dituen teknika. Historiako aurkikuntza zientifiko gehienetan bezala, beste zerbaiten bila ari zela garatu zuen J.J. Thomsonek lehen aldiz teknika hau. Hasieran, soilik fisikaren alorrean erabiltzen zen atomoen masa zehazteko, elementuen isotopo egonkorrak existitzen zirela aurkituz. Geroago, kimikariek petrolioaren industrian erabiltzen hasi ziren hidrokarburo txikien ugaritasuna neurtzeko. Teknika honek izan zituen aurrerapenei esker, masa-espektrometria beste esparru berrietara ere hedatu zen, baina ez zen biologiaren alorrean, eta batez ere, ikerketa "omikoetan" sartu, ionizazio leuneko teknikak garatu arte.[12]

80ko hamarkadan, Matrizeak lagundutako laser bidezko desortzio ionizazioaren (*matrix assisted laser desorption ionization*, MALDI)[13,14] eta elektrospray bidezko ionizazioaren (ESI)[15] garapenek, masa-espektrometriaren arloa irauli zuten. MALDI, M. Karasek eta K. Hillenkampek,[12] eta aldi berean K. Tanakak[13] garatu zuten, eta ESI, aldiz, JB Fennek.[14] Bi teknika hauek goitik behera aldatu zuten biologia aztertzeko era, eta honengatik, 2002an Kimikako Nobel Saria jaso zuten Fenn eta Tanakak, "Makromolekula biologikoen egiturak identifikatzeko eta aztertzeko metodoen garapenagatik".

Aurrerapen horiek masa-espektrometria biologiaren arloan erabiltzeko tresna paregabe bilakatu zuten, baina oraindik ezinbestez gainditu beharreko gabeziak zituen, hala nola molekulak espazioan kokatzeko beharra hauek hobeto ulertzeko. Txinako esaera zaharrak dioen moduan, "irudi batek mila hitzek baino gehiago balio du". Kontestu honetan garatu zen masa-espektrometria bidezko irudikapena deritzon teknika (*imaging mass spectrometry*, IMS). Berez, IMS duela 50 urte baino gehiago bigarren mailako ioien masa-espektrometria bidez sortu zen (*secondary ion mass spectrometry*, SIMS),[16] baina lagin biologikoen analisia ez zen izan posible MALDI gisako ionizazio leuneko teknikak garatu arte.[17,18]

IMS teknikak, ehun biologikoetan dauden ehundaka molekula ezberdin atzematea eta lokalizatzea ahalbidetzen du esperimentu bakar batean. IMS teknikak biokimikaren arloan duen helburu nagusia ehuna osatzen duten espezie molekularrak detektatzea da, batez ere metabolitoak eta proteinak, genomaren eta fenotipoaren arteko erlazioa hobeto

ulertzeko eta patologiaren bat dagoenean, erantzun biologikoa aztertzeko. Minbiziaren ikerketan teknika oso baliagarria dela frogatu da, bai biomarkatzaileak aurkitzeko eta baita minbiziaren prozesu biologikoen ezagutza areagotzeko ere, besteak beste.

Hala ere, IMS teknikak izan lezaken potentzialarekin, oraindik erronka ugarik erantzunik gabe jarraitzen dute. Horietako bat, IMS-k emandako informazioaren baliagarritasuna da, hots, ea medikuen erabaki klinikoetan lagungarri izan daitekeen ala ez, hala nola diagnostikoan, iragarpenetan, tratamenduaren aukeraketan edo hauen monitorizazioan. Tesi honetan, MALDI-IMS teknikaren inguruko hainbat arazo antzeman eta horien hobekuntzak aurkezten dira, beti ere patologiek zelulen eta ehunen lipidometan eragin ditzaketen aldaketak hobeto deskribatzeko xedearekin. Beste ikerketa-talde batzuekin lankidetzan, arazo analitiko konplexuei aurre egin diegu, MALDI-IMS bidez galdera biologiko garrantzitsu ezberdinei erantzun ahal izateko beharrezko aurrerapenak eginez.

1.2 Tesiaren helburu nagusiak

IMS aplikazio klinikoetan teknika boteretsu bilakatu ahal izateko, oraindik zenbait erronka ditu antzeman eta gainditzeko. Tesi honen xedea desafio hauek hautematea eta, baliabide analitikoen bitartez, IMS esperimentuen metodologia optimizatzea da. Kapitulu bakoitzean MALDI-IMS metodologiaren alderdi espezifiko bat izango du hizpide.

4. Kapituluak, optika oso optimoa ez duen masa-espektrometro batez baliatuz, erresoluzio handiko irudiak lortzeko egin beharreko lagin-prestaketaren optimizazioa du helburutzat. Sistemen biologian, ehun biologikoetan egon daitezkeen molekulak zehatz mehatz lokalizatzea funtsezkoa da, biomolekulen eta gaixotasunen artean egon daitzekeen erlazio mekanikoak ulertu ahal izateko. Ikerketa hau, Gwendoyn Barceló-Coblijn doktorea buru den Balear Uharteetako Osasun Ikerketa Insitutuko Lipids in Human Pathology taldearekin elkarlanean burutu zen, giza kolon biopsien kolonozitoek diferentziazio prozesuan jasan ditzaketen lipido aldaketak aztertzeko helburuarekin.

5. kapituluan, konparazio anitzkoitzeko ikerketen erronkari helduko diogu. Ildo honetan, bi arazo nagusiri erreparatuko diegu: tumoreen heterogeneotasuna eta lipidoen identidikazio zehatzaren beharra. Ikerketa hori, Medikuntza eta Erizaintza Fakultateko Zeluen Biologia eta Histologiako Departamentuko MD. Maria Dolores Boyanoren taldearekin lankidetzan burute zen. Azken helburua, lípido profilan oinarrituz, nebus (kontrola) eta melanoma (minbizia) ezberdintzea eta sailkatzea da.

6. Kapituluan, lab-on-a-chip kontzeptua aurkezten da. IMS teknikaren etorkizuna esperimentu bakar batean lagin ugari neurtzea ahalbidetzen duten gailuak eratzea da, esperimentuaren kostua murriztuz, eta abiadura eta diagnostiko-sentsibilitatea areagotuz. Kapitulu honen helburua, kontzeptu-proba gisa, zelula-mintzez osasutako mikroarraiak eta IMS teknika uztartuz, eta egoera fisiologiko desberdinean dauden laginek izan ditzaketen lipido profil ezberdinez baliatuz, minbizi zelulak ezbedintzeko aukera emango digun metodologia optimizatzea da. Lan hau, iMG-Pharma Biotech S.L.-ko Dr.

Gabriel Barreda Gomez eta Dr. Egoitz Astigarraga, eta EHU-ko MD Maria Dolores Boyanoren taldearekin elkarlanean burutu zen.

Amitzeko, **7. Kapituluan**, lipido fenotipoan eta beren metabolismoan oinarrituz, hainbat gaixotasun eta arrisku-faktore erlazionatzeko saiakera baten atariko emaitzak aurkezten dira. Ikerketa hau Dr. Gwendolyn Barceló Coblijn-en taldearkein elkarlanean ari gara ikertzen.

---

[1] Kell DB. The virtual human: towards a global system biology of multiscale, distributed biochemical netwrks models. *Lubmb Life*. **2007**. 59: 689-695.

[2] Westerhoff HV, Palsson BO. The evolution of molecular histology into systems biology. *Nature Biotechnol.* **2004**. 22: 1249-1252.

[3] Baltimore D. Our genome unveiled. *Nature*. **2001**. 409: 814-816.

[4] Human Genome Squencing Consortium. Finishing the euchromatic sequence of the human genome. *Nature*. **2004.** 431: 931-945.

[5] Petricoin E, Zoon K, Kohn E, Barrett J, Liotta L. Clinical proteomics: translating benchside promise into bedside reality. *Nat. Rev.* **2002**. 1: 683-695.

[6] Vlahou A, Fountoulakis M. Proteomic approaches in the search for disease biomarkers. *J. Chromatogr. B. Analyt. Technol. Biomed. Life Sci.* **2005**. 814: 11-19.

[7] Nicholson JK, Lindon JC. Systems biology: Metabonomics. *Nature*. **2008**. 455: 1054-1056.

[8] van Meer G. Cellular lipidomics. *EMBO J.* **2005**. 24: 3159-3165.

[9] van Meer G, Voelker DR, Feigenson GW. Membrane lipids: where they are and how they behave. *Nat. Rev. Mol. Cell Biol.* **2008**. 8: 112-124.

[10] Laganowsky A, Reading E, Allison TM, Ulmshneider MB, Degiacomi MT, Baldwin AJ, Robinson CV. Membrane proteins bind lipids selectively to modulate their structure and function. *Nature*. **2014**. 510: 172-175.

[11] Wenk MR. The emerging field of lipidomics. *Nat. Rev. Drug Discov.* **2005**. 4: 594-610.

[12] Griffiths J. A brief history of mass spectrometry. *Anal. Chem.* **2008**. 80: 5678-5683.

[13] Karas M, Hillenkamp F. Laser desorption ionization of proteins with molecular masses exceeding 10.000 daltons. *Anal. Chem.* **1988.** 60: 2299-2301.

[14] Tanaka K, Waki H, Ido Y, Akita S, Yoshida Y, Yoshida T. Protein and polymer analyses up to m/z 100.000 by laser ionization time-of flight mass spectrometry. *Rapid Commun. Mass Spectrom.* **1988**. 2: 151.152.

[15] Fenn JB, Mann M, Meng CK, Wong SF, Whitehouse CM. Electrospray ionization for mass spectrometry of large biomolecules. *Science*. **1989**. 246: 64-71.

[16] Castaing R, Slodzian G. Microanalyse oar émission ionique secondaire. *J. Microsc.* **1962.** 1: 395-410.

[17] Spengler B, Hubert M, Kaufmann R. MALDI ion imaging and biological ion imaging with a new scanning UV-laser microprobe. *Proceedings of the 42nd ASMS Conferen on Mass Spectrometry and Allied Topics.* **1994.**

[18] Caprioli RM, Farmer TB, Gile J. Molecular imaging of biological samples: localization of peptides and proteins using MALDI-TOF MS. *Anal. Chem.* **1997**. 69: 4751-4760.

2. Kapitulua

Imaging Masa-Espektrometria eta Lipidomikaren oinarriak

Kapitulu honetan masa-espektrometria bidezko irudikapena eta lipidomika era labur batean aurkezten dira. Soilik tesi honetan erabili diren masa-analizatzailea eta ionizazio ganbara azpimarratuko dira eta, halaber, IMS prozesuaren urrats ezberdinak deskribatu. Honetaz gain, lipidoen sailkapen orokorra ere emango da, ikerketa lan honetan aztertutako lipido motak nabarmenduz eta horien egituraren deskribapena ere aurketuz.

2.1 Masa-Espektrometria

Masa-espektrometria, masa/karga erlazioaren (m/z) arabera espezie kimikoak detektatzen dituen teknika analitikoa da.[1] Horretarako, analizatu nahi den lagina gas egoerara ionizatzen da, apurtuz ala apurtu gabe, eta sortutako ioien masaren eta kargaren arteko proportzioa neurtzen da. Emaitza, ugaritasuna m/z-ren aurka irudikaten duen masa-espektroa izango da (2.1. Irudia).

Hiru atal nagusiz osatua dago masa-espektrometroa: ionizazio-ganbara, ioiak sortzen dituen konpartimentua; masa-analizatzailea, sortutako ioiak bereizteko helburua duen ganbara; eta detektagailua, bereizitako ioi horien ugaritasuna eta m/z erlazio neurtzen duen sistema.

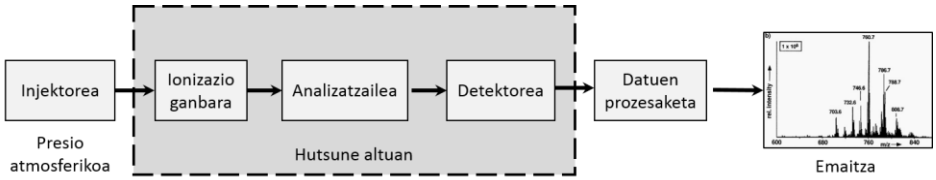

Fig. 2.1. Masa-espektrometro baten atal nagusiak

Tesi honen helburutik haratago doa masa-espektrometriari burruzko alderdi guztiak sakon aztertzea, hala nola, LC-MS edo GC-MS teknikak deskribatzea. Lan hau, masa-espektrometriaren alorrean azken urteotan izan den iraultzarik arrakastatsuenetariko batean oinarritzen da: imaging mass spectrometry edo masa-espektrometria bidezko irudikapena (IMS). Teknika berri honek, masa-espektrometriari espazioan zehar ioiak banatzeko edo lokalizatzeko ahalmena ematen dio, hau da, erresoluzio espaziala.

2.2 *Imaging* Masa-Espektrometria (IMS)

IMS teknikak, ehun biologiko batean egon daitezkeen molekula ezberdinen detekzioa eta identifikazioa ahalbidetzen du, ehunean zehar euren kokapenari buruzko informazioa ere emanaz.[2,3] Beste irudik-teknika batzuekin alderatuta, esate baterako immunohistokimikarekin, aztertu nahi den molekularen aurre-markaketarik behar ez duen teknika garbia eta ez-suntsitzailea da. Ehunka biomolekula kartografiatu ditzake esperimentu bakar batean erresoluzio maila ezberdinetan, erresoluzio zelularretik ikuspegi orokorrago batera. Zentzu honetan, histologia klasikotik haratago doan teknika bat da, informazio ugariz hornitzen gaituelarik.

IMS lau urratseko prozesua da: laginaren prestaketa, desortzio eta ionizazioa, masa-analisia eta irudien erregistroa eta datuen tratamendua. Irudi arrakastatsu eta errepikagarriak eskuratzeko, urrats guzti horiek arretaz kontrolatzea eta monitorizatzea nahitaezkoa da. Fase horien artean, laginaren prestaketa, edozein teknika analitikotan

bezala, funtsezko urrats kritikoa da, tesi honen 4. Kapitulua xehetasunez eztabaidatuko dena.

Ionizazio-ganbara

IMS teknikan erabiltzen diren hiru ionizazio teknika erabilienak matrizeak lagundutako laser desortzio ionizazioa (*matrix-assisted laser desorption ionization*, MALDI),[4,5,6,7] bigarren mailako ioien masa-espektrometria (*secondary ion mass spectrometry*, SIMS)[8] eta elektrospray bidezko desortzio ionizazioa (*desorption electrospray ionization*, DESI)[9,10] dira. Azken urteotan izan diren hobekuntzek, ionizazio-teknika berrien garapena sustatu dute, esaterako, laser bidezko elektrospray bidezko ionizazioa garatuz (*laser ablation electrospray ionization*, LAESI).[11] Ionizazio metodoaren aukeraketak, esperimentuaren erresoluzioan eta, halaber identifikatu ahal diren biomolekulen gainean izugarrizko eragina du. 2.1. Taulan aipatutako ionizazio metodoekin lortu daitezkeen erresoluziorik handienak eta hauekin aztertu daitezkeen biomolekulen informazioa aurkezten da.

2.1. Taula. Masa-espektrometria bidezko irudikapenean erabiltzen diren ionizazio teknika komunenak beren ezaugarri nagusienekin: laginaren aurre-prestaketa behar duten edo ez, printzipioz teknika bakoitzarekin lortu daitekeen erresoluziorik handiena eta ze biomolekulak aztertzeko erabiltzen diren.[12]

	Laginaren prestaketa	Ionizazioa	Erresoluzio espaziala	Aztertutako biomolekulak
MALDI	Matrize geruza	Laser bidezko desortzio/ionizazioa	3-200 µm	Lipidoak, peptidoak, proteinak, metabolitoak
DESI	Ezer	Disolbatzaile tanten bidezko desortzio eta ESI-tipoko ionizazioa	>100 µm	Lipidoak eta metabolitoak
SIMS	Ezer edo matriz/metal geruza	Ioi-izpi primario bidez	<1 µm modu dinamikoan, >1 µm modu estatikoan	Atomo, fragmetu txikiak, gantz-azidoak eta lipidoak
LAESI	Ezer	Laser ablazioa ESIrekin konbinatua	>200 µm	Lipidoak, peptidoak, proteinak, metabolitoak

Tesi honetan erabili den ionizazio metodo MALDI izan da, beraz, soilik honi buruzko azalpena emango da, prozesua modu laburrean deskribatuz.

Matrix assisted desorption/ionization (MALDI)

Ionizazio teknika lehun hau, laser bidezko desortzio ionizazio (*laser desorption ionization*, LDI)[13] metodoaren hobekuntza bat da. Matrize organiko bat analitoarekin batera kristalizatzen da, molekulen transferentzia ioi bezala gas egoerara errazteko,

fragmentazioa ahalik eta gehien sahiestuz. 2.2. Taulan MALDI-IMS esperimentuetan erabiltzen diren matrizerik ohikoenen zerrenda aurkezten da.

2.2. Taula. MALDI esperimentuetan erabltzen diren pisu molekular baxuko molekula organiko ezberdinak eta ze analito motatan erabiltzen diren.

Matrizea	Analitoak
Azido 2,5-dihidroxibentzoikoa (DHB)	peptidoak, proteinak, lipidoak, drugs
Azido α-ziano-4-hridroxizinamikoa (CHCA)	peptidoak, proteinak, lipidoak, drugs
Azido 3,5-dimetoxi-4-hidroxizinamikoa (SA, azido sinapikoa)	proteinak
Azido 3-hidroxipikolinikoa (3-HPA)	peptidoak, oligonukleotidoak
2,4-dinitrofenilhidrazina (2,4-DNPH)	peptidoak
4,6-trihidroxiazetofenona (THAP)	lipidoak, oligonukleotidoak, drugs
2,6-dihidroxiazetofenona (DHA)	lipidoak
2-merkaptobentzotiazola (MBT)	lipidoak
1,5-diaminonaftalenoa (DAN)	lipidoak

MALDI-IMS, masa-espektrometria bidezko irudikapenean erabiltzen den teknikarik erabiliena da. Ehun baten gainazala, laserrak emititzen duen uhin-luzeran absorbatzeko ahalmena duen pixu molekular baxuko molekula organiko batez estaltzen da. Sortutako matrize kristal hauek bitartekari papera egiten dute MALDI prozesuan. Laserrak lagin-matrize nahastea irradiatzen du eta matrize kristalek laserraren energia xurgatzen dute energia analitoei transferituz, euren desortzioa eta ionizazio bermatuz. 2.2. Irudiak, eskematikoki MALDIn ematen den desortzio eta ionizazio prozesuaren azalpena erakusten du.

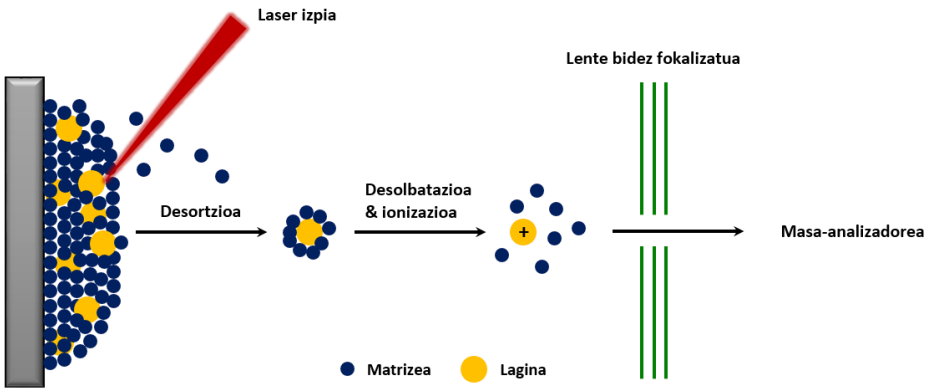

2.2. Irudia. Matrizez lagundutako desortzio ionizazio prozesuaren eskema. Laser-izpi batez lagin-matrize gainazala irradiatzen da. Matrize kristalek energia xurgatzen dute eta lurrundu egiten dira, analitoak kargadun ioi gisa gas egoeran askatuz.

MALDI-IMS esperimentu batean, laser-izpiak, ehunaren gainazalean hautatutako eremu bat, zehaztutako espazio-bereizmen batez ekortuko du *raster* bat eginez. Puntu bakoitzean, kokapen bakoitzaren informazio molekularra izango duen masa-espektro bat lortuko dugu, dimentsio berri bat eskainiz esperimentuei: erresoluzio espaziala. Honek, aztertutako ehunaren eremuan detektatutako biomolekulen banaketa-mapak sortzea ahalbidetzen du. Hurrengo urratsak detektatutako biomolekula horien identifikazioa eta analisi estatistikoen bitartez, interesgarriak izan daitezkeen zonaldeen (*region of interest*, ROI) identifikazioak izango dira. 2.3. Irudian MALDI-IMS esperimentu tipiko baten lan-fluxua ikus daiteke.

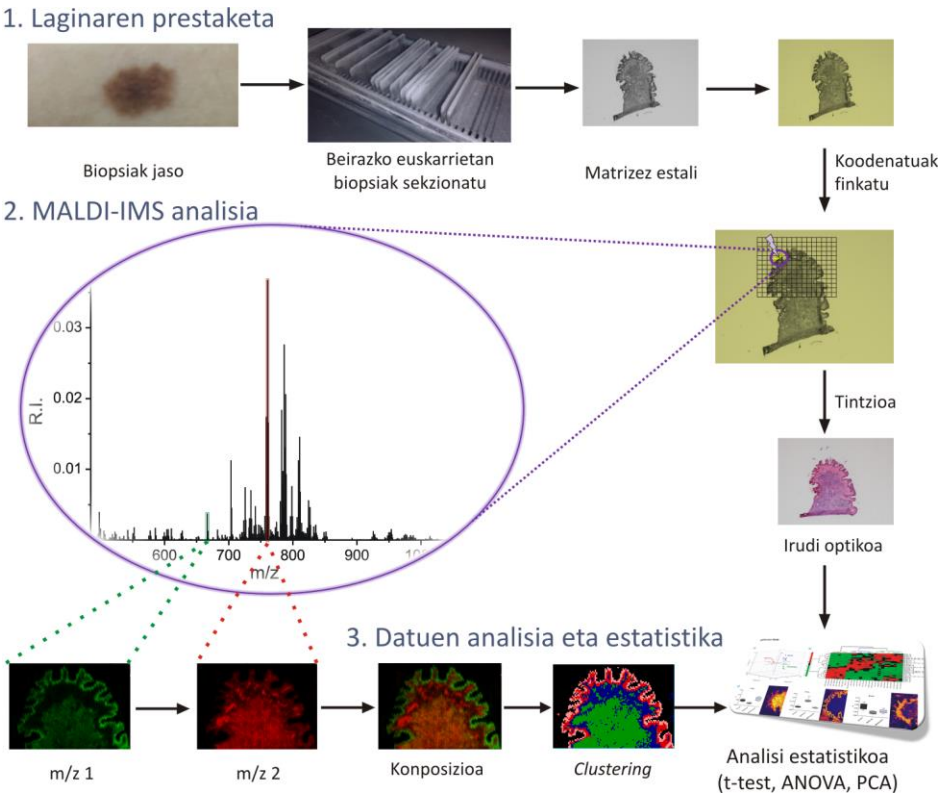

2.3. Irudia. MALDI-IMS esperimentu ohiko baten lan-fluxua. Izoztutako biopsiak kriogenikoki beirazko euskarrietan sekzionatzen dira. Ehunaren gainazala, matrize kristal-geruza mehe batez estali ostean, lauki-sare birtual bat zehazten da, neurtu nahi den eremua eta laser pultsuen arteko distantzia edo erresoluzio espaziala finkatuz. Laserrak hautatutako area osoa neurtu ondoren, irudi molekularrak muntatzen dira eta ehuna hematoxilina-eosina (H&E) bidez tintatzen da. Horrela, detektatutako molekulek ehunean zehar duten banaketa-irudiek helarazitako informazioa erabiliz, analisi estatistikoak burutu daitezke interesgarriak izan daitezkeen eremuak edo patroiak antzemateko (ROI). Analisi estatistiko gehigarriak ere egin daitezke biomarkatzaileak bilatzeko edo sailkapen modeloak eraikitzeko.

Masa-analizatzaileak

Masa-analizatzaileak, ionizazio-ganbaran sortutako ioiak, euren m/z erlazioaren arabera bereizi eta sailkatzen ditu. Gaur egun, sentsibilitate, masa bereizteko ahalmen eta masa-zehaztasun anitzeko analizatzaile ugari daude. 2.2. Taulak MADI-IMS esperimentuetan gehien erabiltzen diren analizadoreen ezaugarri nagusienak laburbiltzen ditu.

Hegaldi-denbora masa-analizatzaileak (Time-of-flight, TOF)[14] izan ziren MALDI-IMS[4] teknikan erabili ziren lehenengo analizadoreak, eta oraindik arrakastatsuak izan arren, Fourier-en eraldaketa erabiliz ziklotroiaren bitartez erresonantzia ionikoko analizadorearen (*Fourier transform ion cyclotron resonance*, FT-ICR)[15] eta Orbitrapen[16] garapenek, IMS esperimentuetan erabiltzeko analizatzailearen aukerak zabaldu dituzte. Teknika hauen aurrerapenik esanguratsuena euren masa bereizteko ahalmen altua da, batez ere molekula txikien kasuan, hala nola, lipidoen kasuan. Hala ere, hobetzeko tartea dago, batez ere espektroen eskuratze abiadurari dagokionez, aurrerapenak izan arren, oraindik TOF eta gainontzeko motatakoak baino mantsoagoak baitira.

2.2. Taula. MALDI-IMS teknikan gehien erabiltzen diren analizatzaileen ezaugarriak laburtzen dituen taula: masa-bereizmen ahalmena, neurtzen duten masa-eremua, MS/MS ahalmena eta aztertzen diren biomolekulak kasu bakoitzean.[17] *Drug* : farmakoa

Analizatzailea	Masa bereizteko ahalmena (m/Δm)	m/z eremua	pixels/s	MS/MS	Aztertutako molekulak
TOF	10^3	0-10^6	>10	ez	peptido eta proteinak
Erreflektroi-TOF	10^3-10^4	0-10^5	>10	MS^2	drug*/metabolitoak/peptidoak/lipidoak
Q-TOF	10^3-10^4	100-6k	>10	MS^2	drug*/metabolitoak/peptidoak/lipidoak
Tranpa opnikoa	10^2-10^3	50-3k	1	MS^n	drug*/metabolitoak/peptidoak/lipidoak
Kuadrupoloa	10^2-10^3	50-5k	>100	MS^2	drug*/metabolitoak/peptidoak/lipidoak
FT-Orbitrap	10^4-10^6	50-10k	1	MS^n	drug*/metabolitoak/peptidoak/lipidoak
FT-ICR	10^4-10^5	100-10k	1	MS^n	drug*/metabolitoak/peptidoak/lipidoak

Ikerketa lan hau burutzeko erabili den masa-analizatzailea Orbitrap motakoa izan zen, eta beraz, bere funtzionamenduaren azalpen orokorrak besterik ez dira emango.

Orbitrap

Gainontzeko analizadoreekiko Orbitrap eta FT-ICR teknikak ezberdin egiten dituen ezaugarri nagusiena m/z zehazteko modua da. Labur, ioiak tranpa baten barruan harrapatu eta orbitatzera behartuak daude, beraien orbita maiztasunak grabatuz. Fourier-en eraldaketa erabiliz, maiztasun horien espektroak lortzen dira, eta hortik, ioi bakoitzaren m/z.

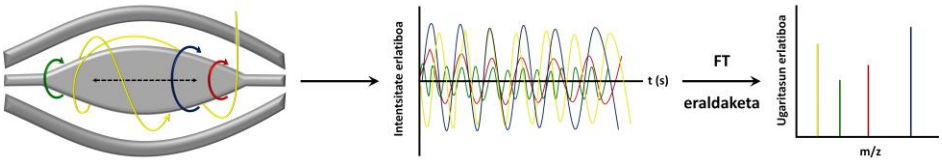

2.4. Irudia. Orbitrap FT analizatzailearen funtzionamendua. Ioiak, barruako elektrodoaren eta honen kanpoaldean dauden beste bi elektrodoren artean sortutako tranpan tangentzialki injektatzen dira, erdiko elektrodoaren inguruan maitztasun axial ezberdinekin orbitatzen hasiz. Maiztasun hauek, ioien m/z erlazioarekiko proportzionalak izango dira. Datu hauetatik, Fourier-en eraldaketa erabiliz, masa-espektroak lortzen dira.

2.4. Irudiak, ioiek masa-analizatzaile honetan jasaten duten ibilbidearen azalpena eskematikoki erakusten du. Orbitrap-a[16] hiru katodoz osatua dago: barneko elektrodo-ardatz bat, eta hau inguratzen duten bi elektrodo konkabo, bata bestearen parean kokaturik daudenak. Behin ionizazio ganberan sortutako ioiak tranpan zeharka injektatzen direnean, eremu elektriko bat sortzen da barruko eta kanpoko bi elektrodoen artean. Eremu elektriko honen ondorioz, ioiak barneko elektrodorantz erakarriak izaten dira eta elektrodo honen ardatzaren baitan, $(z/m)^{1/2}$-rekiko proportzionala den maiztasunarekin orbitatzen hasten dira. Ioien orbitak detektatu eta prozesatu egiten dira, datuak, frekuentzia domeinutik, m/z balioetara eraldatuz Fourier transformazio datu-prozesamendu teknika erabiliz. Masa-bereizmen ahalmena tranparen barruan igarotako denboraren menpekoa da. Horrela, ioiak elektrodoen artean harrapaturik eta orbitatzen denbora luzeagoan egonez gero, masa bereizmen altuagoa lortuko genuke, baino honek, espektroen eskuratze abiaduran eragingo luke, esperimentua luzeago eginez.

2.3 Lipidomika

Literaturan Lipidomika terminoa honela definitzen da: zelula bateko lipido espezie molekularren eta horien funtzio biologikoen karakterazioa da, lipidoen metabolismoan parte hartzen duten proteinen adierazpenarekin eta geneen erregulazioarekin duten erlazioa aztertuz ("*the full characterization of lipid molecular species and of their biological roles with respect to expression of proteins involved in lipid metabolism and function, including gene regulation*").[18]

Lipidoak, nagusiki hidrokarburoz osaturik dauden, eta, zelulen egituraren eta funtzioaren oinarrizko osagaiak diren, biomolekula hidrofobo edo anfipatikoak dira.[19] Hainbat eginkizun ezberdin dituzte, baina garrantzitsuenetariko batzuk, hala nola, erreserba-energia izatea, zelulen mintz-plasmatikoen nahitaezko osagaia izatea, eta seinalizazio zelularrean eta zelulen arteko elkarrekintzetan parte hartzea, dira.[20] Funtzio horiek eta beste batzuk betetzeko kodifikatuak dauden lipido ezberdin anitz daude.[21]

Oso talde heterogeneoa osatzen duten sustantziak dira lipidoak, baina, beren egitura kimikoan oinarrituz, zortzi taldetan banatu daitzeke:[22] gantz-azidoak, glizerolipidoak, glizerofosfolipidoak, esfingolipidoak, esterolak, prenolak, sakarolipidoak eta poliketidoak (2.3. Taula)

2.3. Taula. Lipidoen sailkapena dagokien laburdura eta zeluletan burutzen duten eginkizun nagusienarekin. [22]

Lipido klasea	Laburdura	Funtzio nagusia
Gantz-azidoak	GA	Lipido konplexuen osagai
Glizerolipidoak	GL	Energi-biltegia
Glizerofosfolipidoak	GP	Seinalizazioa eta egitura-lipidoak
Poliketidoak	PK	Antimikrobio. Beste molekulen aintzindari.
Prenolak	PR	Antioxidantea. Bitaminen aitzindari. Zelula garraioa
Sakarolipidoak	SL	Egitura-lipidoak
Esfingolipidoak	SP	Seinaleen transdukcioa eta zelula-ezagutzea
Esterolak	ST	Seinalizazio eta egitura-lipidoak

Tesi hau mintz-lipidoetan oinarritzen da nagusiki, bereziki glizerofosfolipido eta esfingolipidoetan. Hauek, erretikulu endoplasmatikoan eta Golgi aparatuan *de novo* sintesia bidez (2.5 Irudia) edo birmoldaketa prozesu baten (Lands zikloa)[23] bidez ekoitzen dira.[24]

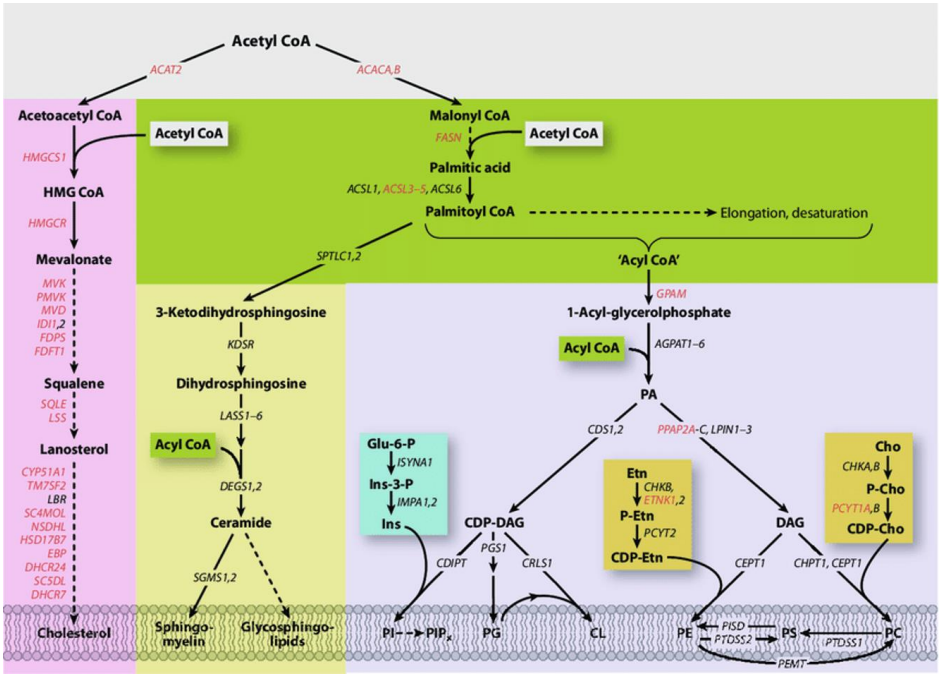

2.5. Irudia. Zelula-mintzetako lipidoak sintetizatzeko bide nagusiak. Argiago ikusteko helburuarekin, sintesiaren eskema sinplifikatu da hainbat bide ez erakutsiz, hala nola birmoldaketa prozesua edota Krebs zikloa.[25]

Zelula-mintza, lipido polar hauek modu asimetrikoak antolaturik dituen geruza bikoitz iragazkorra da. Mintzak, lipidoen alde hidrofoboek, urak modu entropikoan bultzatua, bere burua barrurantz mihiztatzeko duten joera, eta, alde hidrofiloek, ur-ingurunearekin interakzionatzeko duten joeraren ondorioz eratzen dira, kanpoaldea eta barnealdea mugatuz. Gainera, hesi gisa jokatzeaz gain, mintz-lipidoek zatiketa zelularrean, ugalketan eta mintzaren barneko molekulen zirkulaziorako funtsezkoak diren ezaugarriak ere eskaintzen dituzte.[26]

Gantz-azidoak

Gantz-azidoak, gainontzeko lipido konplexuagoen osagai nagusiak dira, eta beraz, zeluletako lipido mota nagusienetarikoa bat izango da. Zeluletan, modu librean soilik trazak aurki daitezke.

14 azpimota egon arren, naturan, gantz-azido ohikoenak, kate alifatiko hidrofobo, luze eta ez-adarkatua, asea edo asegabea izan daitekeena, azido karboxiliko bati lotuak daudenak dira. Normalean, zeluletako gantz-azido gehienak 14 eta 22 arteko karbono kopuru bikoitiaz osatuak daude, 0-6 tarteko asegabetasun mailarekin.[27] Tesi honetan aurrerago ikusiko dugun bezala, asegabetasun mailak sekulako garrantzi du funtzio ezberdinetan, hala nola zelulen diferentziazioan, mintzaren malgutasunean eta prozesu biologiko ezberdinetan.[28] Gantz-azido garrantzitsuenen adibide batzuk 2.6. Irudian ikusi daitezke.

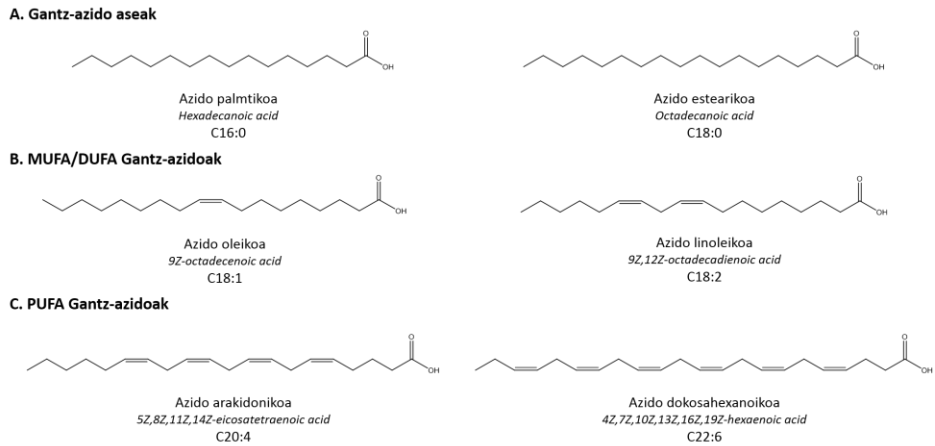

2.6. Irudia. Zeluletako gantz-azido ohikoenen adibide adierazgarriak. **A** - GA aseak. Azido palmitikoa (C16:0) eta azido estearikoa (C18:0). **B** - GA mono edo diinsaturatuak. Azido oleikoa (C18:1) eta azido linoleikoa (C18:2). Azido linoleikoa lipido esentziala da, hots, gorputzak ezin du sintetizatu lipido hau eta beraz dieta bidez hartu behar da. **C** - GA poliasegabea. Azido arakidonikoa (AA – C20:4) eta azido dokosahexanoikoa (DHA - C22:6). Hanturazko erantzunean bitartekari diren molekulen aurrekariak dira. MUFA/DUFA: gantz-azido mono eta diinsaturatuak (*mono unsaturated fatty acid / diunsaturated fatty acid*). PUFA: gantz-azido poliasegabeak (*polyunsaturated fatty acid).*

Glizerofosfolipidoak

Glizerofosfolipidoak, bi gantz-azido, glizerola-eskeletoa eta buru hidrofilo batez osatuta dauden naturako lipidorik ugarienak dira. Gantz-azidoak, glizerolari sn-1 eta sn-2 posizioan batzen zaizkio, eta sn-3 posizioan, talde funtzional bati lotua dagoen fosfatoa kokatzen da (2.7. Irudia).

Gantz-azidoen luzera eta asegabetasun maila ezberdinez osatuak daude GP-ak, baino normalean, gantz-azido asegabeak lehenengo posizioan kokatzen dira, eta monoinsaturatuak eta poliasegabeak sn-2n.[29] Honetaz gain, sn-1 posizioan dagoen gantz-azidoa, glizerolari azil, akil edo alkenil (azken bi hauek GP-eter izena hartuko lukete) lotura bidez batu diezaioke. Azkenik, buru hidrofiloko fosfato terminalean hondar edo talde funtzional ezberdinak lotu daitezke, kolina, serina, etanolamina edo inositola, besteak beste.

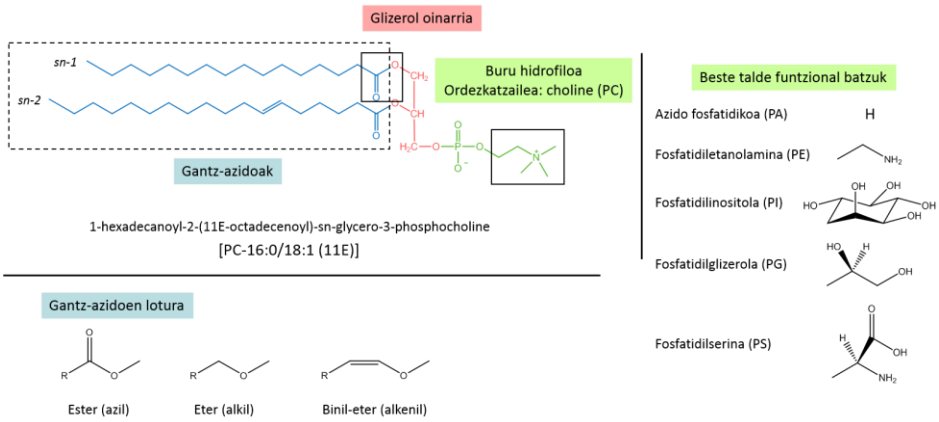

2.7. Irudia. Glizerofosfolipidoen egitura. Adibidez gisa, glizerofosfatidilkolina erakusten da. Hauen oinarrizko egitura glizerol bat da (gorriz markatua), sn-1 eta sn-2 posizioetan bi gantz azidori (kate urdinak) lotua dagoena eta buru hidrofilo bati sn-3n (berdez nabarmendua). Buru hidrofilo honek duen talde ordezkatzailearen arabera, GP ezberdinak osa daitezke (eskuineko zutabea). Honetaz gain, sn-1 posizioan lotzen den gantz-azidoaren eta glizerolaren arteko lortura azil motakoa izateaz gain, alkil edo alkenil motakoa ere izan daiteke, GP espezieen aniztasuna areagotuz (eter lipidoak deritzonak, adibidearen azpialdean).

GP osatzeko dauden aukera ezberdin hauek kontuan izanda, zelulen funtzionamendu egokirako kodifikatuta dauden lipido anitz ezberdinez osatua dago klase hau. Zelula-mintzetan dauden GP azpi-klaseak fosfatidilkolinak (PC), fosfatidiletanolaminak (PE), fosfatidilinositolak (PI), fosfatidilglizerolak (PG), fosfatidilserinak (PS) eta kardiolipinak (CL: PG dimeroa) dira. PC da lipido talderik ugariena zelulatan (glizerofosfolipidoen ~%50), bere funtzio printzipala lipido estrukturala izatea baita.[30] Hauetaz gain, lisofosfolipidoak ere era daitezke A2 fosfolipasa (PLA2) entzimak sn-2 posizioko ester lotura hidrolizatzen duenean.[31]

Mintz plasmatikoan, PC espeziek nagusiki alde ez-zitosolikoan, hau da, kanpoaldeko geruzan lokalizatzen diren moduan, PS eta PE espezieen portzentairik handiena bigeruzaren kapa zitosolikoan kokatzen dira. PI eta PA espezieak ere, nahiz eta aurrekoekin alderatuta kantitate murritzagoan aurkitu mintzetan, zitosolarekin harremanetan dagoen geruzan aurki daitezke nagusiki, bertan seinalizazio zelularrean parte hartzen dutelarik.[32]

Esfingolipidoak

Esfingolipidoak, seinalizazio zelularrean zein zelulen-mintzetan paper garrantzitsuak burutzen dituzten lipidoak, hainbat azpi-klasetan bana daitezke, denek ezaugarri amankomun bat izanik: oinarri gisa esfingoid-base bat izatea. Ugaztunen zeluletan esfingoid-base nagusienak esfingosina eta esfinganina dira,[33] normalean 18 karbonoz osatuak. Bi hauen arteko ezberdintasuna, esfingosinak bigarren posizioan duen asegabetasuna da.

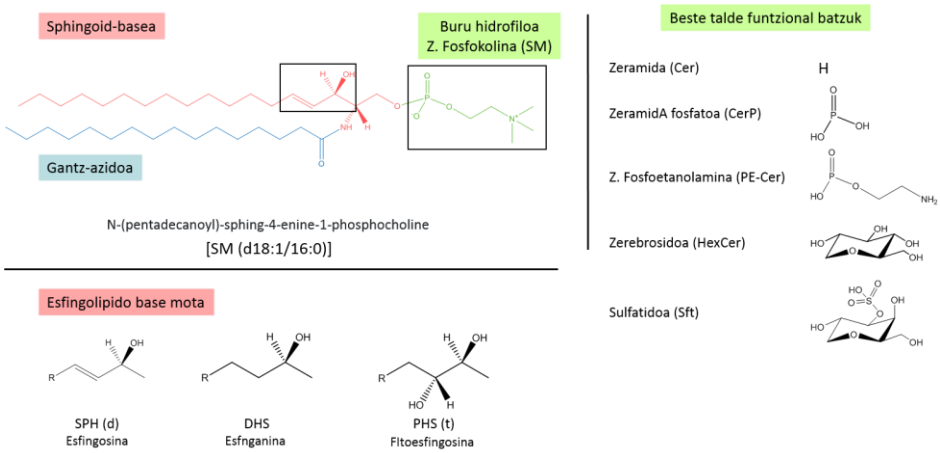

2.8. Irudia. Esfingolipidoen egitura, adibide gisa esfingomielina erakutsiz. Esfingolipidoen egituren oinarria esfingoide-base bat da (hidroxilazio ezberdinak izan ditzakeena, begiratu adibidearen azpialdea), sn-2 posizioan N-azil talde bat duena eta sn-3n buru hidrofiloa. Azken honek esfingolipido tipoa definituko du, eskuinaldean erakusten diren ordezko talde funtzionalekin.

Esfingoid-basearen sn-2 posizioari amida lotura baten bitartez gantz-azido bat lotzen zaionean, zeramidak (Cer) sortzen dira (2.8. Irudia), gainontzeko esfingolipidoen aitzindariak. Estruktura hau fosforilatua izan daiteke zeramida-1-fosfatoa sortuz (CerP), eta hau, aldi berean, kolina, etanolamina edo azukreetara lotu daiteke lipido konplexuagoak sortuz.

Horrela, esfingomielinak (SM), zeramida fosfatidiletanolamina (PE-Cer), zerebrosidoak (HexCer) edo gangliosidoak eratu daitezke, hurrenez hurren.

SMak, zelula-mintzetan aurkitzen diren esfingolipidorik ugarienak, PC espezieekin gertatzen den modura, mintz plasmatikoaren kanpoaldeko geruzan kokatzen dira nagusiki.

Nomenklatura

Tesi honetan espezieak izendatzeko erabiliko den nomenklatura hurrengoa da:

1. Lipido klaseen laburdurak erabiliko dira. Hemendik aurrera, soilik PC, PI, SM PE... erabiliko dira bai testu eta baita irudietan ere.

2. Glizerofosfolipidoetan sortu daitezkeen eterren kasuan, oraindik ez da posible eter eta binil eterraren artean bereiztea, ezta MS/MS teknikak erabilita ere. Beraz, izendapenak eta eztabaidak sinplifikatu nahian, bietatik ugariena den azpimota erabiliko da. Horrela, PE-eterrek binil eterra adieraziko dute (PE-P),[34] plasmalogenoa deiturikoak, hauek baitira bietatik ugarienak zelula eukariotoetan; PC-eterraren kasuan, aldiz, izenak eter azpimotari egingo dio erreferentzia (PC-O).[35] Hala ere, ezin dugu beste motaren presentzia baztertu.

3. Bi gantz-azidoen karbono kopurua eta asegabetasun mailak gehituak izango dira eta zenbaki totalak adieraziko dira. Adibidez, 5.7. Irudiko esfingomielina SM 34:1 izango litzateke.

---

[1] Sparkman, OD. Mass spectrometry desk reference. *Global View Pub.* **2000**. ISBN 0-9660813-2-3.

[2] McDonnell LA, Heeren RMA. Imaging mass spectrometry. *Mass Spectrom. Rev.* **2006**. 26:606-643.

[3] Chughtai K, Heeren RMA. Mass Spectrometric Imaging for Biomedical Tissue Analysis. *Chem. Rev.* **2010**. 110:3237-3277.

[4] Karas M, Hillenkamp F. Laser desorption ionization of proteins with molecular masses exceeding 10.000 daltons. *Anal. Chem.* **1988**. 60:2299-2301.

[5] Tanaka K, Waki H, Ido Y, Akita S, Yoshida Y, Yoshida T. Protein and polymer analyses up to m/z 100.000 by laser ionization time-of flight mass spectrometry. *Rapid Commun Mass Spectrom.* **1988**. 2:151-153

[6] Spengler B, Hubert M, Kaufmann R. MALDI ion imaging and biological ion imaging with a new scanning UV-laser microprobe. *Proceedings of the 42nd ASMS Conference on Mass Spectrometry and Allied Topics.* **1994.**

[7] Caprioli RM, Farmer TB, Gile J. Molecular imaging of biological samples: localization of peptides and proteins using MALDI-TOF MS. *Anal. Chem.* **1997**. 69:4751-4760.

[8] Castaing R, Slodzian G. Microanalyse par émission ionique secondaire. *J. Microsc.* **1962**. 1:395-410.

[9] Takats Z, Wiseman JM, Gologan B, Cooks RG. Mass spectrometry sampling under ambient conditions with desorption electrospray ionization. *Science.* **2004**. 306:471-473.

[10] Ifa DR, Wiseman JM, Qingyu S, Cooks RG. Development of capabilities for imaging mass spectrometry under ambient conditions with desorption electrospray ionization (DESI). *Int. J. Mass Spectrom.* **2007**. 259:8-15.

[11] Nemes P, Vertes A. Laser ablation electrospray ionization for atmospheric pressure, in vivo, and imaging mass spectrometry. *Anal. Chem.* **2007**. 79:8098-8106.

[12] Mascini NE. Mass Spectrometry imaging for the classification of tumor tissue. *PhD Thesis*. **2015**.

[13] Peterson DS. Matix-free methods for laser desorption/ionization mass spectrometry. *Mass Spectrom. Rev.* **2007**. 26: 19-34.

[14] Stephens WE. A pulsed mass spectrometer with time dispersion. *Phys. Rev.* **1946.** 69:691.

[15] Comisarow MB, Marchall AG. Fourier transform ion cyclotron resonance spectroscopy. *Chem. Phys. Lett.* **1974**. 25:282-283.

[16] Hu Q, Noll RJ, Makarov A, Hardman M, Cooks RG. The Orbitrap: a new mass spectrometer. *J. Mass Spectrom.* **2005**. 40:430-443.

[17] Norris JL, Caprioli RM. Analysis of tissue specimens by matrix-assisted laser desorption/ionization imaging mass spectrometry in biological and clinical research. *Chem. Rev.* **2013**. 113:2309-2342

[18] Spener F, Lagarde M, Géloên A, Record M. Editorial: What is lipidomics*? Eur. J. Lipid Sci. Technol.* **2003**. 105:481-482.

[19] Harayama T, Riezman H. Understanding the diversity of membrane lipid composition. *Nat. Rev. Mol. Cell Biol.* **2018**. 19:281-296.

[20] Khalil MB, Hou W, Zhou H, Elisma F, Swayne LA, Blanchard AP, Yao Z, Bennett SAL, Figeys D. Lipidomics era: accomplishments and challenges. *Mass Spectrom. Rev.* **2010**. 29:877-929.

[21] Gross RW, Han X. Lipidomics at the interface of structure and function in system biology. *Chem. Biol.* **2011**. 18: 284-291.

[22] Fahy E, Subramaniam S, Brown HA, Glass CK, Merril Jr. AH, Murphy RC, Raetz CRH, Russell DW, Seyama Y, Shaw W, Shimizu T, Spener F, van Meer G, VanNieuwenhze MS, White SH, Witztum JL, Dennis EA. A comprehensive classification system for lipids. *J. Lipid Res.* **2005**. 46:839-862.

[23] Lands WE, Inoue M, Sugiura Y, Okuyama H. Selective incorporation of polyunsaturated fatty acids into phosphatidylcholine by rat liver microsomes. *J. Biol. Chem.* **1982**. 257: 14968-14972.

[24] Holthuis JC, Menon AK. Lipid landscapes and pipelines in membrane homeostasis. *Nature*. **2014**. 519: 48-57.

[25] Nohturfft A, Zhang SC. Coordination of lipid metabolism in membrane biogenesis. *Annu. Rev. Cell Dev. Biol.* **2009**. 24: 539-566.

[26] van Meer G, Voelker DR, Feigenson GF. Membrane lipids: where they are and how they behave. *Nat. Rev. Mol. Cell Biol.* **2008**. 9: 112-124.

[27] Bond LM, Miyazaki M, O'Neill LM, Ding F, Ntambi JM. Fatty acid desaturation and elongation in mammals. *Biochemistry of Lipids, Lipoproteins and Membranes*. **2016**. 6th Edition: 185-208

[28] Spector AA, Yorek MA. Membrane lipid composition and cellular function. *J. Lipid Res.* **1985.** 26: 1015-1035.

[29] Yamashita A, Hayashi Y, Nemoto-Sasaki Y, Ito M, Oka S, Tanikawa T, Waku K, Sugiura T. Acyltransferases and transacylases that determine the fatty acid composition of glycerolipids and the metabolism of bioactive lipid mediators in mammalian cells and model organisms. *Prog. Lipid Res.* **2014**. 53: 18-81.

[30] Van Meer G. Cellular lipidomics. *EMBO J.* **2005**. 21: 3159.3165.

[31] Yamashita A, Hayashi Y, Nemoto-Sasaki Y, Ito M, Oka S, Tanikawa T, Waku K, Sugiura T. Acyltransferases and transacylases that determine the fatty acid composition of glycerolipids and the metabolism of bioactive lipid mediators in mammalian cells and model organisms. *Prog. Lipid Res.* **2014**. 53:18-81.

[32] Ingólfsson HI, Melo MN, van Eerden FJ, Arnarez C, Lopez CA, Wassenaar TA, Periole X, de Vried AH, Tieleman DP, Marrink SJ. *J. Am. Chem. Soc.* **2014**. 136: 14554-14559.

[33] Futerman AH. Sphingolipids. *Biochemistry of Lipids, Lipoproteins and Membranes*. **2016**. 6th Edition: 297-326.

[34] Braverman NE, Moser AB. Functions of plasmalogen lipids in health and disease. *Biochim. Biophys Acta*. **2012**. 1822: 1442-1452.

[35] Magnusson CD, Haraldsson GG. *Ether lipids*. Chem. Phys. Lipids. **2011.** 164: 315-340.

4. Kapitulua

Erresoluzio espazial handiko IMS zelulen egoera fisiologikoa eta patologikoa zehazteko

Azkeneko urteotan masa-espektrometria alorrean izandako aurrerapenek lipidoma deskribatzeko interesa sustatu dute, batez ere patologia ezberdinetan, diagnostikorako edo tratamenduen monitorizaziorako erabilgarri izan daitezkeen markatzaile lipidikoak identifikatzeko helburuarekin. Helburu hori lortzeko, aztertzen diren laginak biopsiak izan ohi dira, hainbat zelula-mota ezberdinez osatutako sistemak. Markatzaile eta gaixotasun baten arteko erlazioa ulertu ahal izateko, beharrezkoa da lipido espezie ezberdinak ehunean zehaztasunez lokalizatzea, eta, halaber gainontzeko zeluletatik bereiztea. Beraz, gaur egun, IMS arloan helburu nagusienetariko bat ahalik eta erresoluzio espazial handiena lortzea da, informazio zelularra, edo, haratago, azpi-zelularra lortu ahal izateko.

Atal honetan, optika egoki bat ez duen masa-espektrometro batekin, ahalik eta erresoluzio altuena lortu ahal izateko optimizatutako metodologia aurkezten da.

Kapitulu honetan aurkeztutako ikerketa giza koloneko biopsien laginetan burutu da. Lipidoen hatz-marka erabiliz zelula baten egoera fisiologikoa eta patologikoa zehaztasunez iragarri daitekeela frogatuko da, IMS teknikaren garrantzia eta bere baliagarritasuna erakutsiz.

Kapitulu honetan aurkeztutako emaitzak hurrengo artikuluetan argitaratu dira:

1. **Garate J**, Fernández R, Lage S, Bestard-Escalas J, Lopez DH, Reigada R, Khorrami S, Ginard D, Reyes J, Amengual I, Barceló-Coblijn G, Fernández JA. Imaging mass spectrometry increased resolution using 2-mercaptobenzothiazole and 2,5-diaminonapthalene matrices: application to lipid distribution in human colon. *Anal. Bioanal. Chem.* **2015**. 407: 4697-4708.

2. Bestard-Escalas J, **Garate J**, Maimó-Barceló A, Fernández R, Lopez DH, Lage S, Reigada R, Khorrami S, Ginard D, Reyes J, Amengual I, Fernández JA, Barceló-Coblijn G. Lipid fingerprint image accurately conveys human colon cell pathophysiologic state: a solid candidate as biomarker. *Biochim. Biophys. Acta.* **2016.** 1861: 1942-1950.

3. Lopez DH, Bestard-Escalas J, **Garate J**, Maimó-Barceló A, Fernández R, Reigada R, Khorrami S, Ginard D, Okazaki T, Fernández JA, Barceló-Coblijn G. Tissue-selective alteration of ethanolamine plasmalogen metabolism in dedifferentiated colon mucosa. *Biochim. Biophys. Acta Mol. Cell Biol. Lipids.* **2018.** 1863: 928-938.

4.1 Sarrera

Ehun biologikoetan zehar biomolekula ezberdinen kokapenaren edo banaketaren lehen irudiak argitaratu zirenetik,[1,2,3,4,5] etengabeko hobekuntzak izan dira teknika honetan azken generaziok masa-espektrometroak garatuz. Hauek, punta-puntako MALDI ioi-itrurriez eta masa-analizatzailez hornituak daude, erresoluzio espazial eta masa-bereizmen ezin hobeak bermatzen dituztenak. Hala ere, inolako aldaketa optikorik egin gabe, masa-espektrometro "zaharrekin" ere erresoluzio zelularra lortzea posible da oraindik.

MALDI-IMS teknikaren erresoluzio espaziala hainbat faktoreren menpe dago, garrantzitsuenak laserraren izpi-tamaina eta lagin-prestaketa izanik (zehazki, matrizaren aukeraketa eta bere aplikazio metodoaren hautaketak).[6]

Esperimentua arrakastatsua izan dadin, lehenengo urratsa laserraren karakterizazioa izango litzateke. Askotan, laser-izpiaren diametroaren tamaina, espektrometro batek lortu dezakeen erresoluziorik altuena dela esaten da. Hala ere, literaturan hainbat irudi aurkeztu dira laserraren diametroa baino espazio-bereizmen edo *step-size* txikiagoarekin. Hauek, *oversampling* metodoaren bidez lortu ziren.[7,8,9]

Oversampling metodoarekin, matrizez estalita dagoen ehun-gainazala laserrarekin irradiatzean, seinalea, laser-izpiak ablazionatuko duen areatik jasoko da (4.1.B Irudia). Bigarren pixela erregistratzeko, lagina, laserraren diametroa baino txikiago den distantzia batera mugituko da, eta oraindik matrizez estalita geratzen den gainazalak soilik emango du seinalea. Behin lehengo lerroa amaituta, hurrengo lerroetan seinalea emango duen gainazala are eta gehiago murriztuko da finkatutako pixel tamiana lortuz (4.1.B Irudia). Horrela, inolako optika aldaketarik egin gabe, posible da 5-10 µm/pixel-ko erresoluzioak lortzea. Hasiera batean, hau hobetzea egongo legoke, hau da, erresoluzio hobeak lor zitezkeen, baina orduan, seinalea/zarata (s/n) erlazioa txartuko litzateke, laser-izpiaren tamaina ez baita faktore mugatzailea. Tamaina txikitu ahala, tresnaren sentsibilitatea konprometitzen da, ehunean ugarienak diren espezieak soilik detektatuz. Horrenbestez, tresnak baimendutako erresoluzio altuena lortzeko, matrizearen aukeraketa urrats kritiko bat da, aztertu nahi diren molekula bakoitzentzako (lipidoak, proteinak, farmakoak...) ahalik eta matrize onena hautatu behar baita.

Beraz, lagin-prestaketa, edozein metodologia analitikoetan bezala, urrats kritiko eta mugatzailea da. Matrizearen aukeraketa egokia, eta lagina honez estaltzeko metodologia hautaketa bereziki garrantzitsuak dira. Aztertu nahi den lagin mota, edo helburu jakin bat aldatzen den bakoitzean, parametro hauek optimizatu egin beharko dira, kontu haundia izanez urrats bakoitzean. 1,5-diaminonaftalenoa (DAN)-k dagoeneko erakutsi du bere baliagarritasuna lipidoak ionizazio negatiboan detektatzeko orduan. Ehunaren gainazalean ahalik eta kristal tamaina txikienez osatutako geruza mehea bat sortzea beharrezkoa da, *oversampling* metodologia erabiliz, eta beraz, honek behar duen matrize kantitate egokiarekin, analisi arrakastatsua izateko. Kristalik txikienak bermatzen duten deposizio metodoak disolbatzailerik gabekoak izaten dira,[10,11,12] disolbatzaileak sor ditzakeen biomolekulen migrazioak saihesten baitute, ehunaren jatorrizko konposizioa

mantenduz. Orain arte emaitzarik hoberenak lortu dituen metodoa sublimazioa izan da.[13,14]

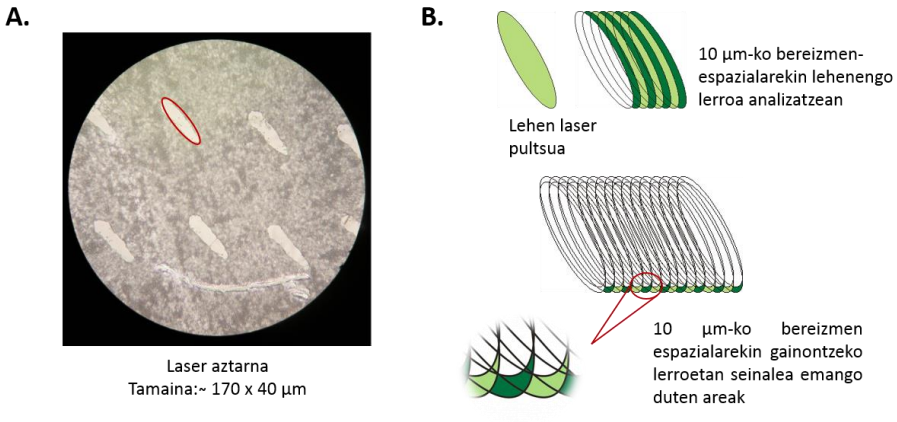

4.1. Irudia. A - 1,5-diaminonaftalenoan laserrak uzten duen aztarnaren SEM argazkia. **B** – Oversampling metodoaren irudikapena. Soilik berdez koloreztatutako zonek emango dute seinalea.

Lagin-prestaketa prozesua optimizatzeko, giza koloneko biopsiak erabili ziren. Ehun mota hau kriptez josia dago, eta arkitektura histologiko berezi hobek erresoluzioaren hobekuntza ikusi eta aztertzea baimenduko digu.

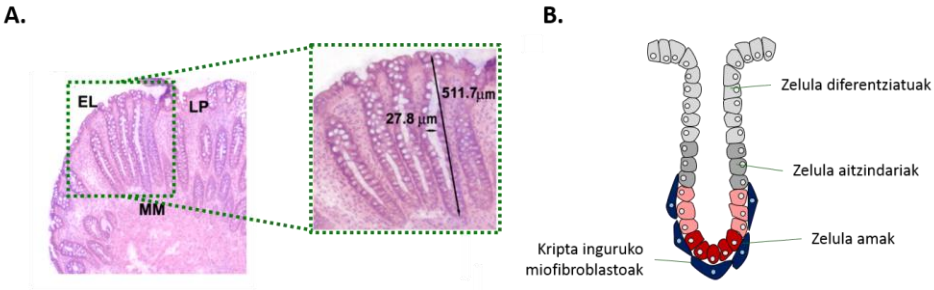

4.2. Irudia. A - Giza kolon biopsia batean dauden hiru ehun mota nagusien histologia H&E-rekin tintatua: epitelioa (EL), lamina propia (LP) eta muskularis mukosa (MM). **B** - Koloneko kripta batean, posizioaren arabera dauden zelula ezberdinen irudikapena (A. Humphries et al. *Nat. Rev. Cancer.* **2008**. 8: 415-124).

Kolona digestio-aparatuko azken zatia da. Bere unitate funtzionalak kriptak dira, epitelioaren inbaginazio zilindrikoak lamina propia (LP) izeneko ehun konektiboan (4.2. Irudia). Kripta hauek, zelula epitelial zilindriko bakunez osatuak daude, banan-banan bata bestearen alboan modu zehatz batean antolatuta: kripta behealdean ama zelulak kokatzen dira, hauek proliferatu egiten dira zelula epitelial aitzindarietan, eta hauek

azkenik kolonozito helduetan diferentziatzen dira kriptatik ezkatatu aurretik.[15] Koloneko kriptan gertatzen den zelula-berritze prozesu honi esker, behin erresoluzio handiko IMS metodologia optimizatzen dugunean, zelula baten lipidoma, diferentziazio-zelularrarekiko nolako zehatza eta sentikorra den aztertzea bermatuko du, prozesu biologiko hau hobeto ulertu ahal izateko.

4.2 Helburuak

Kapitulu honen helburu printzipala, laginaren prestaketa egoki bati esker, eta optikari aldaketarik egin gabe, hain berria ez den masa-espektrometro bat erabiliz, erresoluzio zelularra lortzea da. Horri esker, kolonaren lipidomaren profila eta bertan gertatzen diren aldaketak zehatz-mehatz deskribatu ahal izango ditugu, kolonozitoen diferentziazio prozesua eta lipidoen metabolismoaren arteko erlazioa aztertuz.

4.3 Metodologia

Giza kolon biopsien bilketa

Balear Uharteetako Ikerketa Batzorde Etikoak berariaz onartu zuen laginen bilketa. Paziente bakoitzak bere baimena eman zuen idatziz. Guztira, lau paziente osasuntsu, polipoak zituzten lau paziente (adenoma) eta hiru kartzinomadun paziente erabili ziren ikerketa honetan.

Behin biopsiak jasotakoan, berehala nitrogeno likidoan sartu eta izoztu ziren eta beirazko euskarrietan, 10 µm-ko lodiera zuten sekzioak prestatu ziren.

Lan hau, Balear Uharteetako Osasun Ikerketa Institutuko (Son Espases Unibertsitate Ospitalea) Lipids in Human Pathology taldeko kolaboratzaileek burutu zuten

Imaging eta datuen analisia

Lehenik eta behin, paziente osasuntsu baten biopsiaren ehuna erabiliz, hiru pixel tamaina probatu ziren: 5, 10 eta 25 µm. Datuak m/z = 400-tan 30.000 FWHM-ko masa-bereizmenarekin eta pultsuko 30-60 µJ-ko laser energiarekin jaso ziren. Gainontzeko MALDI-IMS parametroak 3. Kapituluan aurki daitezke. Gainontzeko sekzioak soilik 10 µm-ko espazio-bereizmena erabiliz neurtu ziren. Behin MALDI-IMS esperimentua bukatuta, lagin denak H&E (Sigma Aldrich Química, Madrid, Spain) bidez tintatu ziren. Datuak MSI Analyst (NorayBioinformatics S.L, Derio, Bizkaia) softwarea erabiliz eta 3. Kapituluan aipatutako parametroekin tratatu ziren, bai irudiak sortzeko eta baita *k-means* algoritmoa erabiliz, zatiketa mapak sortzeko (*Clustering*). Emaitza estatistikoak Student-en t proba bidez analizatu ziren (p balioa<0-05).

4.4 Emaitzak eta ezbaida

Matrizearen prestaketa

3. Kapituluan deskribatu den bezala, ionizazio negatiboan ahalik eta lipido gehien detektatu ahal izateko hautatutako matrizea DAN izan zen. Kristal txikiez osatutako geruza mehe eta uniformea lortzeko lain matrize-kantitate jarri behar da, honek eman dezaken seinaleak ahalik eta interferentzia txikienak sor ditzan, baino esperimentuek irauten duten ordu luzeak jasan ahal izateko nahiko kantitate izan behar du. Gainera, *oversampling* metodoa arrakastatsua izan dadin, laserrarekin irradiatutako zona osoaren matrizea guztiz desorbatzea garrantzitsua da, horrela, hurrengo puntuan, soilik matrizez estalita geratuko litzateken azalera txikiagotik lortuko genuke seinalea. Beraz, matrize-kantitatea parametro kritikoa da MALDI-IMS esperimentua arrakastatsua izan dadin.

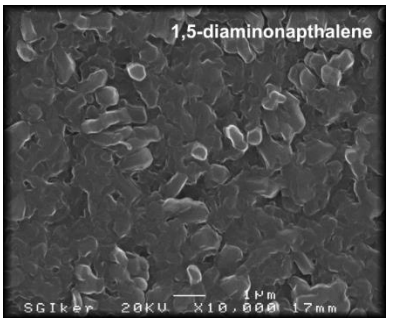

4.3. Irudia. DAN kristalen SEM irudia

Gure masa-espektrometroarekin *oversampling* esperimentu arrakastatsua lortzeko ezarritako DAN kantitate egokiena ~0,15 mg/cm^2 izan zen. Hau, DAN hautsa 123ºC-tan 8 minutuz sublimatuz eskuratu zen. Lortutako kristalak 1-3 µm arteko tamainakoak izan ziren. 4.3. Irudian erakusten den SEM irudian ikusi daitezke kristal hauen tamaina eta forma.

Ionizazio positiborako aukeratutako matrizea MBT izan zen. Honen sublimatze parametroen optimizazioa, eta lortu ziren kristal tamaina eta forma, Figure A.4.1. eranskinean erakusten dira.

Laser-izpiaren karakterizazioa

Lan honetan erabili zen ionizazio-ganbara oso optika sinplea duen N_2-zko laser batez hornituta dago. Sistema optikoa, soilik bi ispilu eta f = 125 mm-ko enfokatze lente batez osatua dago.[16] Nitrogenozko laserrak, deskarga elektriko baten bidez N_2 kitzikatzen du, eta laserraren anplifikazio beharrik gabe, zuzenean emititzen du. Baina honek, laserraren energia-profila askoz ere konplexuagoa izatea dakar, eta ondorioz, ez du laser gehienek izan ohi duten profil Gaussiarra.

4.1.A Irudian, DAN matrizez estalitako laginik gabeko beirazko euskarri huts batean laser pultsuak utzitako aztarna ikusi daiteke. ~170 x 40 µm-ko elipse baten itxura dauka, nahiz eta energiaren distribuzio ez izan homogeneoa.

4.1.B Irudian, 10 µm-ko espazial-bereizmenarekin eginiko *oversampling* metodoaren azalpena aurkezten da. Bertan ikusi daiteke lehenengo laser-izpiak utziko lukeen aztarna (lehenengo elipse berdea), lehenengo lerroko gainontzeko laser pultsuek ablazionatuko luketen azalera, eta azkenik, hurrengo lerroetan ablazionatzeko geldituko litzatekeen azalera (irudiaren azpialdean zoom-a egina) . Azken hau izango litzateke amaierako pixel tamaina, eta beraz, seinalea emango lukeen area.

Erresoluzio handiko *Imaging* Masa-Espektrometria

4.4. Irudian, kolon biopsia osasuntsu baten sekzioaren irudi optikoa eta ionizazio negatiboan, IMS esperimentuen bidez lortutako lipido ezberdinen banaketa-irudiak erakusten dira (ionizazio positiboan lortutakoak eranskineko Figure A.4.2-an ikusi daitezke). Ehunaren irudikapen osoa lortzeko, hiru pixel tamaina (5, 10 eta 25 µm) ezberdina erabilitako esperimentuetatik lortutako emaitzak irudi batean elkartu dira. Emaitzei erreparatuta, kolona lipidoetan oso aberatsa den ehuna dela esan genezake, lipido mota ezberdin ugari detektatutako baitira (PI, PS, PG, PE eta SM). Honetaz gain, lipido espezie molekular horiek sekzioak zehar duten lokalizazio zehatzak ikusita, bakoitza ehun motarekiko oso espezifikoa dela adierazten digu, askok ehunaren histologia zehatz-mehatz jarraitzen baitute.

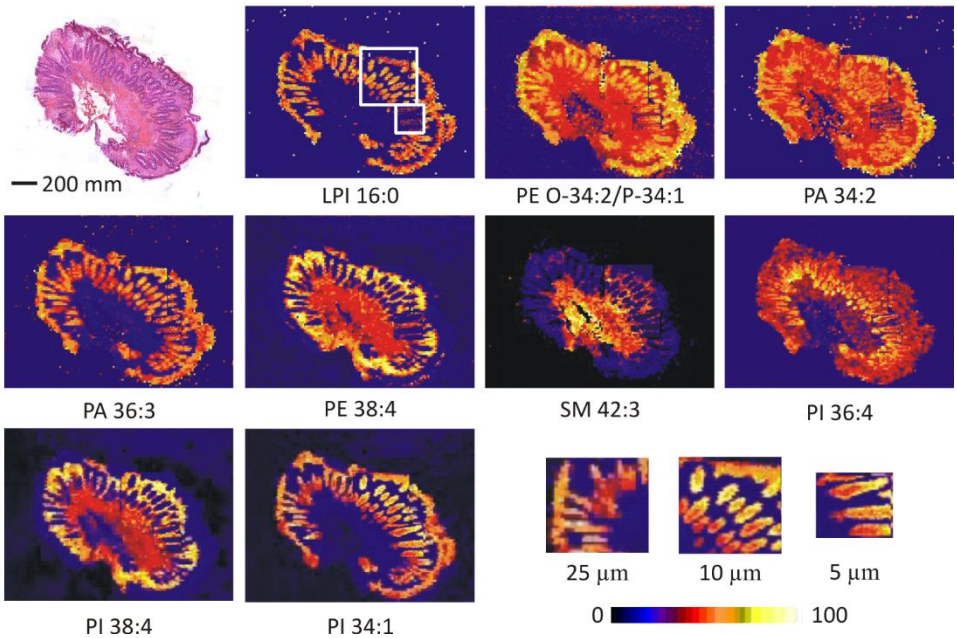

4.4. Irudia. H&Erekin tintatutako giza koloneko sekzio baten irudi optikoa, eta ionizazio negatiboan detektatutako zenbait lipido espezieen banaketa-irudiak ehunean zehar. Lehenengo lipidoaren banaketa-irudian ikusten diren karratu txuri haundi eta txikiak, 10 µm ta 5 µm-tan neurtutako zatiak adierazten dute. Behean eta eskuinean, PI 34:1 lipidoarentzat erresoluzio ezberdinetan lortutako irudiak erakusten dira, erresoluzioaren hobekuntzak ekar dezakeen onura hobeto ikusiarazteko.

4.4. Irudiaren behealdean eta eskubialdean agertzen diren hiru irudiek, [PI 34:1 – H]$^-$ (m/z 835.528) lipidoaren distribuzioa erakusten dute sekzioko zati ezberdinetan 25, 10 eta 5 µm-ko pixel tamainak erabiliz. Garbi dago pixelen tamaina txikitu ahala, irudiek ebazpen hobeagoa dutela. Adibidez, 25 µm-ko erresoluzioan neurtutako zatian bereizten ez diren kripten barneko zuloak, 10 µm-tan nabarmentzen hasten dira, 5 µm-tan eginiko zati txikian argi antzeman daitezkelarik.

Azido arakidonikoz (GA 20:4, AA) osaturik dauden espezieak (4.4 irudia, PE 38:4 eta PI 38:4 hurrenez hurren), epitelioarekin alderatuta, lamina propian gainadierazita daude. Kolon osasuntsu baten lamina propian dauden zelulei ustez dagokien hantura-maila fisiologikoagatik izan daiteke hau, AA hanturan parte hartzen duten molekulen aitzindaria baita.[17]

Irudiei eginiko analisi estatistikoak, erresoluzioak duen garrantzia sustatzen du (4.5 Irudia). 25 µm-n neurtutako esperimentuari *k-means* algoritmoa aplikatzean, honek, kolonean dauden hiru ehun mota nagusiak argi identifikatzen ditu: mucularis mukosa (berde argia), lamina propia (horia) eta kriptak (urdin argia). Hala ere, askotan kripta ertzak gainjarri egiten dira, 10 µm-ko pixel tamainan neurtutako zatia ezin hobeki bereizten direlarik. Honetaz gain, *k-means* algoritmoa kripta bera bitan banatzeko gai izan zen, goialdeko eta behealdeko zelulen artean egon daitezkeen ezberdintasunak nabarmenduz, batez ere, 5 µm-tan neurtutako zatiari erreparatuz gero. Horrela, algoritmoa, anatomia gertutik jarraitzeaz gain, begi bistakoak ez diren ezberdintasunak atzeman eta zatiketa gehiago egiteko gai izan zen. 5 µm-tan eginiko esperimentuan sei pixel-multzo edo kluster ezberdin aurkitu ziren. 1, 4 eta 5 klusterrak lamina propiaren atal ezberdinei dagokien pixel-taldeak dira. Horietako batek, 4. klusterrak, kriptak inguratzen ditu eskuzorro izango balira bezala. Hauek, epitelio azpian kokatzen diren, eta zelula amen sostengu garrantzitsu izateaz gain, diferentziazio prozesuan, zelula ama hauen segurtasuna bermatzen duten telozitoak izan daitezke.[18] Beste bi taldeek lamina propian dagoen zelula-aniztasuna islatzen dute: fibroblastoak, miofibroblastoak, perizitoak...[19] 3. klusterra mukiz beteriko kolon kripten barrunbeari dagokio, eta hau inguratzen duen pixel-multzoa, aldiz, kriptaren pareta izango litzateke, kolonozito lerro bakar batez osatuta. Algoritmoa, kripta eta lamina propiaren artean, telozitoez gain, beste kluster bat banatzeko izan zen, kripta osoa inguratuz, eta batez ere kripta behealdea markatuz (zirkulu urdin batez adierazia). Kontuan izanda kolonozitoak kanporuntz polarizatutako zelulak direla, kluster honek zelula hauen nukleoak adieraz ditzake, normalean zelulen behealdean kokatzen baitira (4.2.B Irudia). Zelularen alde honen eta beste aldearen profil lipidikoa ezberdinak direla iradoki digu, 5 µm-ko espazio-bereizmena erabiliz, erresoluzio azpi-zelular xehea lortu dugula adieraziz.

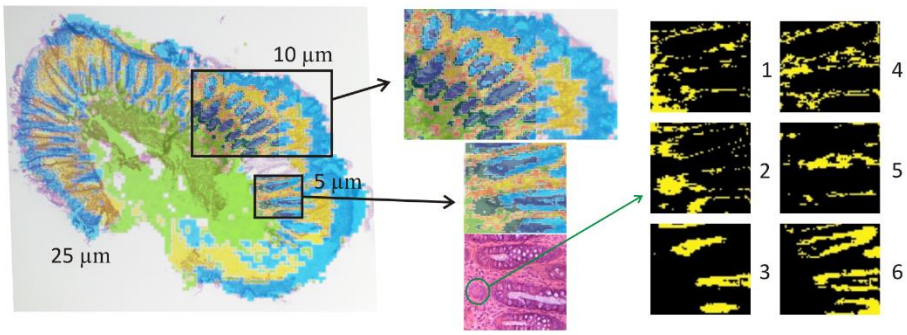

4.5. Irudia. Kolon sekzioan *k-means* algoritmoak sortutako segmentazio mapa eta ehunaren irudi optikoa gainjarriak. Kolore bakoitzak, perfil lipidiko ezberdina izango duen pixel-multzo edo *cluster* bat adierazten du.

Erresoluzioan izandako hobekuntza honek, kriptaren baitan ematen diren aldaketak aztertzea ahalbidetzen digu, eta baita kripta eta lamina propiaren arteko ezberdintasunak ere. Kontuan izanik kolonozitoen tamaina 20-30 µ-koa dela, eta maila zelularrean ehunaren panoramika osoa lortzeko beharrezkoa dela area nahiko handi bat eskaneatzea, 10 µm-ko espazio-bereizmena erabiliko da gainontzeko laginetan.

Kolonozioten diferentziazioa epitelio osasuntsuan

Lau kolon biopsia osasuntsu aztertu ziren, eta esperimentuen artean konparatu ahal izateko, irudiei *k-means* analisi estatistikoa egin zitzaien. Epitelioan bi kluster eratu ziren lagin guztietan, bata kriptaren behealdeati dagokiona (zona basala – urdin iluna) eta bestea goialdeari (zona apikala – urdin argia), 4.6. Irudian bigarren zutabea. Erresoluzio honetan lortutako irudietan ere jadanik sumatu zintezkeen lipido batzuen intentsitateak kriptetan zehar aldatzen zirela (4.6. Irudiko lipidoen banaketa-irudiak). Honetaz gain, epitelioaren nukleoak adieraz zezaketen beste kluster bat ere sortu zen (berdez koloreztatua). Lehen aipatu bezala, kolonozitoak polarizatuak dauden zelula motak dira, hots, nukleoak zelularen behealdean kanporantz begira kokatzen dira. Hala ere, hau konfirmatu ahal izateko, tesi honen helburua ez den froga gehiago egin beharko lirateke.

Lipido klase ugari detektatu arren, sumatutako gradiente gehienak fosfolipidoetan ikusi zirenez, soilik hauen aldaketak kriptetan zehar ikertzeari heldu genion.

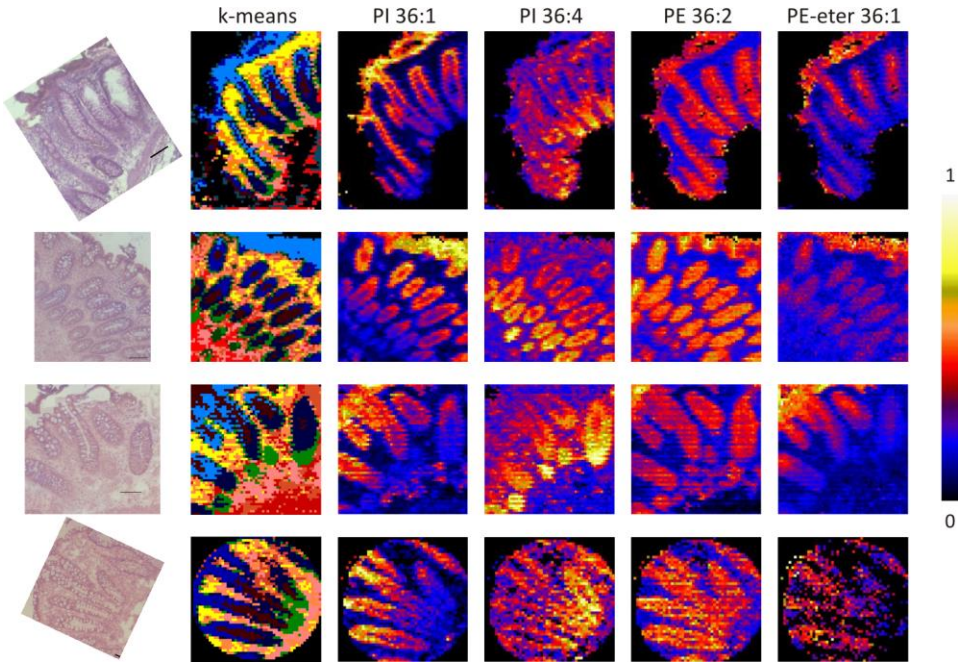

4.6. Irudia Lehenengo zutabea: ikerketa honetan erabilitako biopsien H&E irudi optikoa; bigarren zutabea: Sekzioetan egon daitezkeen ehun mota ezberdinak antzemateko *k-means* bidezko analisi estatistikoa; eta gainontzeko zutabeak kriptan zehar intentsitate aldaketak pairatzen dituzten lipido batzuen banaketa-irudiak.

Aldaketa hauek aztertzeko, kriptaren behealdetik goialderaino, pixel-pixel ibilbide bat markatuz, lipidoetan ematen diren aldaketak behatu ziren (4.7.A. Irudia). Behin pixel guztietako espektroak aterata, glizerofosfolipido azpifamilia bakoitzak banan-banan aztertu ziren, espezie molekularrak azpifamilia bakoitzaren batura totalera normalizatuz. Adibide gisa, 4.7.B Irudian, lagin ezberdinetan PI totalarekiko PI 36:1en portzentaia kriptan zehar nola aldatzen den erakusten da (4.7.B. Irudia), korrelazio-koefiziente altua duen zuzen batekin deskribatu daitekeena (R^2=0.97) (4.7.C Irudia).

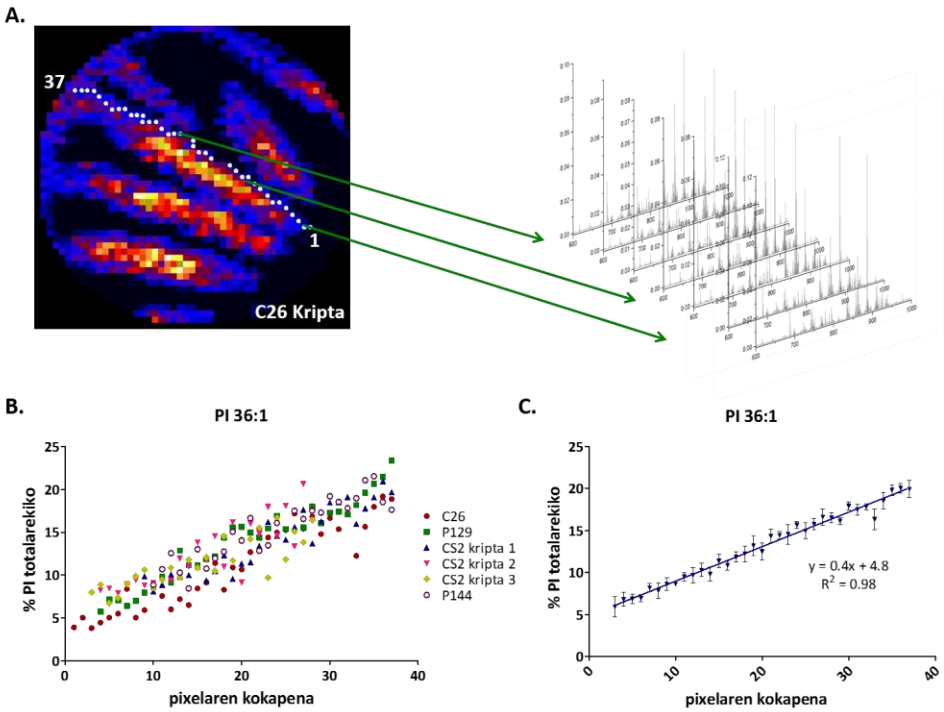

4.7. Irudia **A** - Pixel-pixel lipidoen aldaketak aztertzeko eginiko bidea erakusten duen MALDI-IMS irudi bat, eta pixel bakoitzari dagokion masa-espektroa. **B** - Lagin ezberdinetan PI 36:1 lipidoak, PI totalarekiko, kriptan zehar jasan duen aldaketa. **C** - Zuzen batekin egokitua izan daitekeen PI 36:1 (n = 6) lipidoaren bataz besteko portzentaia pixel posizio bakoitzean.

Detektatutako lipido espezie guztien artean, 15 fosfolipidoen intentsitate-erlatiboa kriptan pixelaren kokapenarekin erlazionatu zitekeen, korrelazio-koefiziente altuko marra zuzen edo portaera logaritmiko batekin deskribatu zitezkeenak (Table A.4.1 eta A.4.2). Espezie horiek seinalizazio zelularrari estuki lotuta dauden hiru lipido kategoriatan bana ditzakegu: PI, PE-eter eta azido arakidonikoa duten espezieen baitan (AA, 20:4n-6).

PI espezieen %98.5ek epitelioan zehar aldaketa pairatu zituzten. Bitxia bada ere, AAz osatuak dauden espezie molekular guztiek kriptan gora igo ahala, euren ehunekoek gutxitze logartimikoa jasan zuten (PI 38:4, PI 36:4, PI 38:5 eta PI 40:4, R^2 = 0.96, 0.94, 0.64 eta 0.89, hurrenez hurren, 4.8. Irudia). PI 38:4, zelula eukariotoetan ugariena den PI espezie molekularra,[20] izan zen, bereziki, aldaketarik handiena pairatu zuen espeziea, PI totalarekiko bere intentsitatea %70etik %20ra gutxituz. Bestalde, gantz-azido monoinsaturatuak eta/edo diinsaturatuak (MUFA/DUFA) dituzten espezieen ehunekoak linealki igo ziren kriptaren zona basaletik apikalera igo heinean (PI 34:1, 34:2, 36:1 eta 36:2, R^2 = 0.89, 0.76, 0.98 eta 0.94, hurrenez hurren).

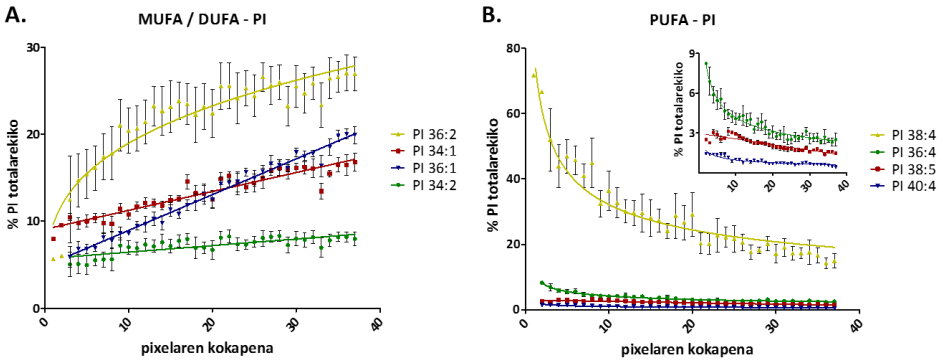

4.8. Irudia. Kriptaren posizioarekiko, PI espezie ezberdinek jasaten dituzten aldaketak. **A** - MUFA/DUFA beren egituran dituzten espezieak. **B** - AA- beren egituran duten espezieak. Portzentaiak, PI totalarekiko sei kripta ezberdinetatik lortutako ehunekoen bataz bestekoak dira.

Harrigarriena, MUFA/DUFA eta PUFA espezieetan ikusitako aldaketak, alderantzi proportzionalak zirela da, kriptaren behealdetik zona apikaleruntz igo ahala, bataren igoera (MUFA/DFA) bestearen jetsieran (PUFA) islatuz, beti ere espezie guzti hauen batura kontaste mantenduz. Honek, espezie hauen artean elkartruke-prozesu sinkronizatu bat egon daitekeela iradoki digu, zelularen egoera fisiologikoarekiko eta diferentziazio prozesuarekiko sentikorra dena (4.9. Irudia)

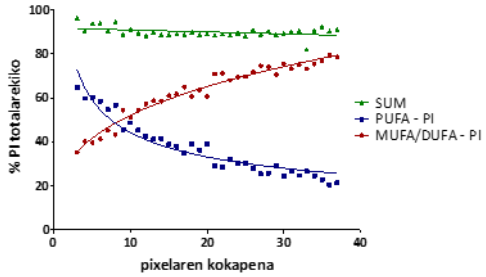

4.9. Irudia. Kriptan posizioarekiko PUFA-PI espezie guztien baturak duen jetsiera MUFA/DUFA-PI espeziek jasaten duten igoeran islatu daiteke, beti era PUFA + MUFA/DUFA konstante mantentzen delarik. (n = 6).

PE-eter lipido klaseari dagokionez, PI espezietan ikusitako portaera bera azaldu zuten, 4.10. Irudia. Nahiz eta aldaketak pairatu zituzten espezieen portzentai total ez izan PIren kasuan bezain altua (%98.2), gutxi gorabehera PE-eter totalaren %75ek, korrelazio-koefiziente altua duten ekuazio logaritmikoekin deskribatu zitekeen euren portaera, PE-eter 34:1, 36:1, 36:4, 38:4 eta 40:4, R^2 = 0.70, 0.82, 0.91, 0.75 eta 0.84, hurrenez hurren (4.10.A-B. Irudia eta eranskinean Table A.4.1 eta A.4.2). Piren kasuan ikusi bezala, kriptan igo ahala, AAz osatutako PE-eter espezieen jetsiera MUFA/DUFA espezieen igoerarekin azaldu zitekeen (4.10.C. Irudia).

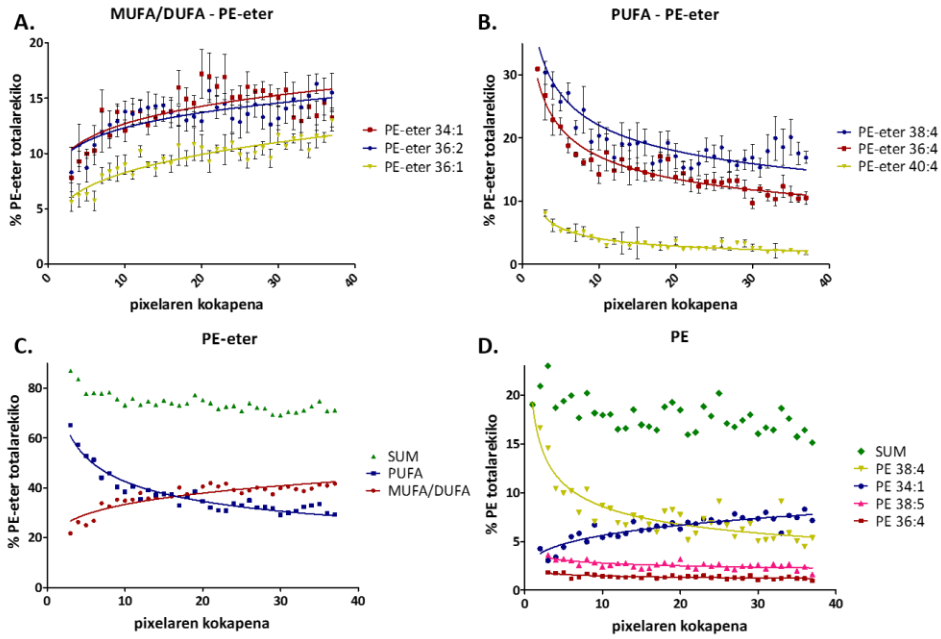

4.10. Irudia. Kriptan zehar PE eta PE-eterr espezieek jasaten ditzutez aldaketak kriptaren posizioarekiko. **A** - MUFA/DUFA duten PE-eter ezberdinen portzentaiaren igoera kriptaren zona baselekiko posizioarekiko. **B** – AA-duten PE-eter espezie ezberdinen jetseira logaritmikoa kripta zehar goruntz igo ahala. **C** – PUFA espezieen baturaren aldaketa, MUFA/DUFA espezienarekin adierazi daiteke, beti ere hauen batura totala gutxi grabehera konstaten mantentzen delarik, ~ %75. **D** – PE klasearen kasuan, soilik, PE totalaren ~ %20ek izan dituzte aldaketak kriptan zehar.

Hala ere, lipido-portzentaien eta kriptan zehar kokapenaren arteko korrelazioak ez ziren PI eta PE-eter klaseetan soilik ikusi, izan ere, AA beren baitan duten PC eta PE espezieek ere gutxitze logaritmikoa erakutsi baitzuten (Table A.4.1 eta A.4.2). PE 38:4 eta 34:1espezieen kasuan posible izan zen aldaketak matematikoki deskribatuak izatea (R^2 = 0.79 eta 0.80 hurrenez hurren), eta, R^2 txikiagoa izan arren, beste AA duten espezie batzuetan ere sumatu zitekeen gutxitze logaritmikoa kriptan zehar: PE 38:5 eta PE 36:4, R^2 = 0.46 eta 0.42 hurrenez hurren, 4.10-D Irudia. Hala ere, PI eta PE-eter espezieekin alderatuta, PC eta PE-n kasuan maila apalagoan eman ziren aldaketak.

Nabarmenena, PE espezie ugarienen balio konstateak izan zen. Euren PE-eter analogoekin alderatuta, PE-eterren kasuan espezieen ~%75ak aldaketan izan zituzten bitartean, PE-n kasuan, soilik ~%20ak izan ziren, gainontzekoak kripaten posizioarekiko konstante mantenduz. PCren kasuan ere portaera bera ikusi zen, eta kontuan izanda PE espezieak, PC espezieekin batera, zeluletan dauden lipidorik ugarienak direla, emaitzek, lipido hauek zelula-osotasunean garrantzi handia izan lezaketela iradoki digu, zelulek, diferentziazio etapa guztietan, hauen balioak konstante mantentzen baitituzte.

Oro har, argi dago kolonozitoek diferentziazio prozesuarekiko beren konposizio lipidikoa zorroztasunez erregulatzen dutela, espezie batzuen kontzentrazioa aldatzen duten heinean, beste batzuena finko mantenduz.

Emaitzak immunofluoreszentzia teknikak (IF) erabiliz balioztatu ziren, lipidoetan ikusitako aldaketak, proteinen adierazpenean egon zintezkeen aldaketekin erlazionatuz. Horretarako, gantz-azidoen elkartrukean (PUFA eta MUFA/DUFA) parte hartu dezaketen entzimei erreparatu genion. Lan hau Son Espases Ospitaleko (Balear Uharteak) Lipid in Human Patoholgy taldeko kolaboratzaileek burutu zuten.[21] Emaitzek, PI eta PE-eter lipido klaseetan ikusitako lipido espezien ordezkapena, A_2 fosfalipasa eta aziltransferasa entzimen aktibitatea bidez erregulatua dagoela iradoki digu. Entzima hauek, gantz-azidoen hidrolisi eta sartze erreakzioak katalizatzen dituzte, eta nahiz eta hauei buruzko infomazioa eskasa izan oraindik, badirudi entzima hauek oso selektiboak direla bai lipidoaren talde funtzionalarekiko eta baita sn-2 posizioan dagoen gantz-azidoarekiko ere.[22]

PE eta PE-eter klaseen arteko harreman-metabolikoa estua izan arren,[23] nabarmentzekoa da diferentziaio zelularrak bi lipido mota hauetan duen eragin ezberdina. Hau, nahiz eta ez egon informazio askorik honi buruz bibliografian, goian aipatutako entzimen selekbtibitatearen ondorio izan daiteke.

Epitelioaren dediferentziazioa kontestu patologiko batean

Diferentziazio prozesuaren eta lipidomaren arteko erlazioa sakonago ikertu ahal izateko, eta egoera patologikoek erregulartasun horri nola eragin diezaioken aztertzeko helburuarekin, koloneko polipo adenomatosoak (AD) analizatu ziren, kolon lesiorik ohikoenak. AD polipoak, kartzinoma inbaditzaile bihurtzeko ahalmena duten ehunaren hazkunde ezohikoak dira.[24, 25, 26]. Bi oinarrizko ezaugarri dituzte: zelulak etengabe bikoizten direla, eta diferentziazioa isilduta dutela. Bereziki interesgarriak dira lesio hauek, neoplasikoetan ez bezala, kasu hauetan posible baita oraindik kriptak gogorarazten gaituen egiturak lortzea, nahiz eta ez izan kripta osasuntsu baten ezaugarri eta morfologia bera. Hala ere, posible izan zen AD-ko epitelioan zehar, pixel-pixel, lipidoen adierazpenean egon zitezkeen aldaketak analizatzea.

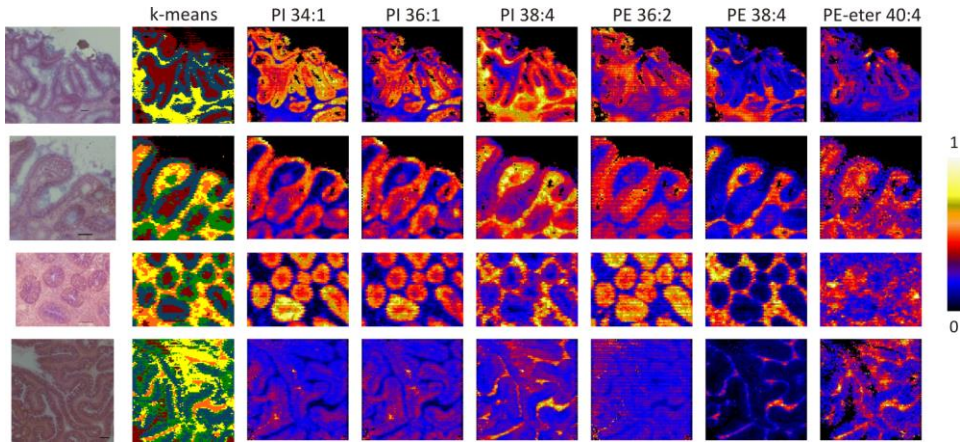

4.11. Irudia. Lehenengo zutabea: H&E bidez tintatutako lau AD kripten irudi optikoa; bigarren zutabea, adenoma hauei dagokien *k-means* segmentazioa; eta gainontzeko zutabeetan lipido jakin batzuen banaketa-irudiak.

MALDI-IMS bidez lortutako banaketa-irudietatik erraz antzeman zitekeen epitelio osasuntsuan ikusitako lipidoen antolaketa erregularra galdu zela polipoetan, 4.11 Irudia. Horrela, PI 38:4 eta 36:1ren portzentaiak, kripta osasuntsuetan zehar aldaketarik nabarmenenak jasan zituzten espezieetako bi, konstantea mantendu ziren polipoetako kriptetan zehar, euren bataz besteko balioek ±%15ko gorabeherak pairatuz, 4.12 Irudia. Halaber, PE-eter espezietan lehen ikusitako aldaketa gehienak (36:1, 36:2, 36:4, 38:4) ere galdu ziren, PE-eter eta PIren metabolismoa guztiz eraldatua dagoela adieraziz.

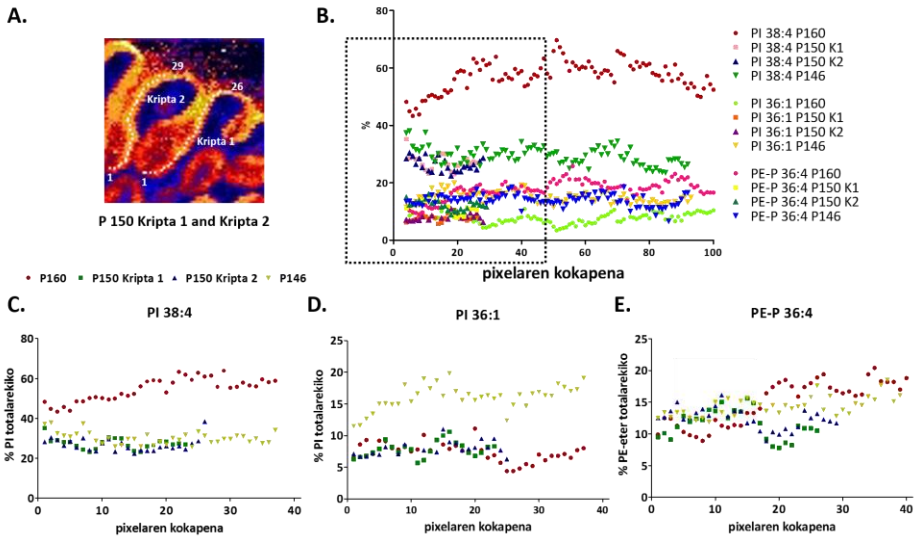

4.12. Irudia. A - Adenoma baten lipidoman eman daitezkeen aldaketak aztertzeko, pixel-pixel, bi kriptetan zehar eginiko bidea markatzen da, aukeratutako pixel horiei dagokien espektroak ateraz. **B** - PI 38:4, PI 36:1 eta PE-eter 36:4-ren portzentaiaren distribuzioa AD lagin ezberdinetako kriptetan zehar. Epitelio osasuntsuetan ikusitako gradiente erregularrak galdu ziren. **C-E** - Aurreko grafikaren zoom-a, hobeto ikusi ahal izateko PI 38:4, PI 36:1 eta PE-eter 36:4 espezie hauen baloreak kriptaren posizioarekiko. (n=4)

Epitelio osasuntsuetan gerta ez bezala, eta adenomak duen diferentziazio prozesuarekin bat eginez, *k-means* algoritmoak AD eta kartzinomako epitelioak soilik kluster batetan banatu zituen MALDI-IMS esperimentu gehienetan (4.11 Irudia, kluster urdina adenomaren kasuan eta eranskineko Figure A.4.3ko kluster urdinak ere kartzinomaren kasuan). Epitelio osasuntsu baten zona basala eta apikala, adenoma eta kartzinomako epitelioekin alderatu ziren Studenten t proba analisiaren bitartez, 4.13 Irudia.

4.13 Irudiko barra-diagramek duten akats-barra luzeak, hein batean, laginen giza jatorriagatik izan daitezke. Kontuan izan behar da lagin taldeak ez zirela anatomikoki homogeneoak izan. Polipoen kasuan, displasia maila ezberdina zuten pazienteak sartu ziren analisian, eta kartzinomaren kasuan berriz, hainbat minbizi-etapetako biopsiak erabili ziren. Hala ere, 4.13 Irudian antzeman daiteke espezieen intentsitateak apikaletik basalerako eta baseltik adenomarako joera dutela (gainadierazi edo azpiadierazi, baina baita beti joera hori mantenduz), kartzinomaren lipidoma izanik apikal zonatik gehien ezberdintzen dena.

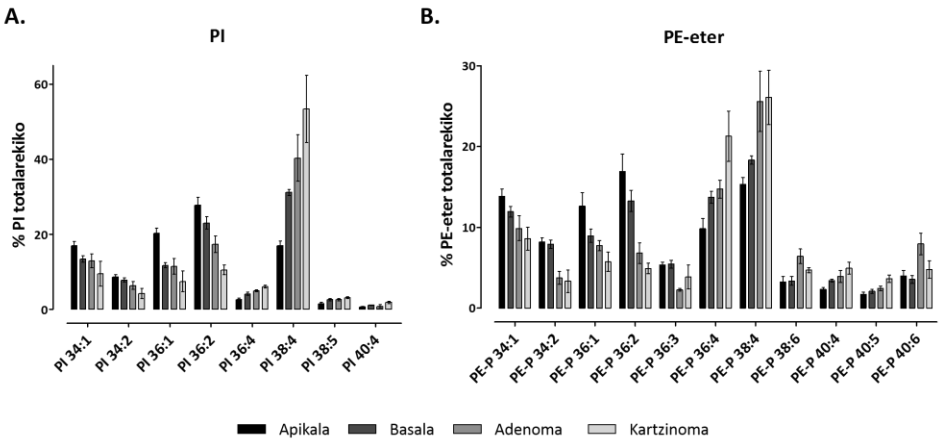

4.13. Irudia. Barra-diagramak, kripta osasuntsuko zona apikala, basala, adenoma eta kartzinomako epitelioen ehunekoak konparatzen dituenak PI (**A**) eta PE-eter (**B**) klaseetan. Soilik estatistikoki ezberdinak diren espezieak erakusten dira, emaitzak 4.1. Taulan aurkeztuz. Esangura estatistikoa Studenten t testa bidez aztertu zen (p balioa < 0.05). Barra-diagrametako balioak pazienteen arteko batezbestekoak ± SEM dira ($n = 4$ kontrola eta AD laginetan, eta $n = 3$ kartzinomaren kasuan).

Emaitzek, ehun osasuntsu eta patologikoen artean ezberdintasun sakonak daudela iradoki ziguten, PE-eter espezieen kasuan batik bat. Izan ere, ADren kasuan, PUFA-PE eter espezieak (36:4, 38:4, 38:6, 40:6) gainadierazita aurkitu ziren kontroleko bi zonekiko, euren kontzentrazio totala %50tik %72ra igoz, 4.13. Irudia eta 4.1. Taua. MUFA/DUFA-PE-eter (34:2, 36:1, 36:2, 36:3) espezieen kasuan, aldiz, euren ehuneko totala %50etik %28ra gutxitu zen, 4.13 Irudia, 4.1 Taula eta eranskineko Table A.4.3. Aldaketa hauek areagotu egin ziren kartzinomako epitelioa kontroleko bi eremuekin alderatzean, espezie horiek AD-n ikusitako joera bera jarraituz, hots, PUFA espezieak oraindik eta giainadierazitagoak egonez (PE-eter totalaren %77 izanez) eta MUFA/DUFA azpiadierazitagoa (PE-eter totalaren %23). PE-eter 38:6 eta 40:6 espezieen kasuak izan ziren joera honen salbuespenak, ADrekin alderatuta hauen portzentaiak jaitsi egin baitziren kartzinoman. Honetaz gain, AD eta kartzinoma arteko beste aldaketarik esanguratsuena PE-eter 36:4 espezieak jasan zuen %60ko igoera izan zen.

PI familiako espezieek ere portaera bera pairatu zuten, hau da, aztertutako bi patologiak kontrolean antzemandako bi eremuekin alderatzean, AA-duten espezieen intentsitate erlatiboak igo ziren heinean, espezie mono edo/eta diinsaturatuen kontzentrazioen jaitsiera ikusi zen, batez ere kartzinomaren kasuan, AD epitelioak eta kontroleko zona basalak nolabaiteko antza erakutsi baitzuten, PUFA ez dituzten espezietan batik bat (34:1, 34:2, 36:1).

4.1. Taula. PI eta PE-eterren portzentaiak Sutudenten t proba bidez alderatu ziren ea estatistikoki esanguratsuak ziren aztertzeko. Horretarako, konparaketa anizkoitzak egin ziren. * p › 0.05; ** p › 0.01; *** p › 0.005. Soilik esanguratsuak diren espezieak erakusten dira. Kluster bakoitzari dagokion fosfolipidoen konposizioa eranskineko Table A.4.5 ikusi daiteke.

		Apikal vs Basal	Apikal vs AD	Apikal vs Kartzinoma	Basal vs AD	Basal vs Kartzinoma	AD vs Kartzinoma
PI	34:1	*					
	34:2			*		*	
	36:1	**	*	**			
	36:2		*	**		**	*
	36:4	*	**	**		*	*
	38:4	****	*	**		*	
	38:5	*	*	**			
	40:4			**		*	
PE-eter	P 34:1			*			
	P 34:2		**	*	**	*	
	P 36:1		*	*			
	P 36:2		**	**	*	**	
	P 36:3		***		***		
	P 36:4	*	*	*		*	*
	P 38:4	*	*	*		*	
	P 38:6		*		*		
	P 40:4	**		**			
	P 40:5			*		*	*
	P 40:6		*		*		

Zona basalaren eta AD-ren arteko antzekotasun hau PE espezietan ere ikusi zen (Eranskineko Table A.4.3 eta A.4.4), AD-k diferentziatu gabeko kolonozitoen eta zelula amen itxura eta portaera dutela iradokiz, eta beraz, tumore-prozesua edo gaiztotze-prozesua jasaten duten zelulen izaera diferentziatu gabea nabarmenduz.

Garrantzitsua da azpimarratzea kriptan zehar ikusitako PUFA eta MUFA espezieen arteko elkartrukea edo ordezkapena, batez ere berezia dela PI eta PE-eterren kasuan, eta hauek AA gehien duten fosfolipidoak izanik, eta ikusita AA duten espezieak AD-n eta kartzinoman ere gainadierazita daudela, honek guztiak, AAaren metabolismoak, bai kolonozitoen banaketan eta baita diferentziazioan ere eginkizun kritikoa duela iradoki digu. Gure emaitzen arabera, zelulek zenbat eta zatiketa tasa handiagoa izan, orduan eta azido arakidoniko esterifikatu gehiago izango dute (zelula diferentziatuak - zona apikala ‹ ama zelula - zona basala ‹ adenoma ‹ kartzinoma). Beraz, kolonozitoen gaiztotze prozesuaren lehenengo urratsean, zelulek PUFA eta MUFA/DUFA-espezieen arteko

elkartrukearen kontrola galduko lukeela hipotetizatu dezakegu. Horrela, gaiztotutako zelula amak azkarrago hedatuko lirateke kripta osoa okupatuz, eta mutazioa epitelioaren baitan barreiatuz, kartzinomaren hasiera eta progresioan lagunduko lukete.[14, 27]

Diferentziazio prozesua lamina propia osasuntsu eta patologikoetan

Ehun konektiboari dagokionez, lamina propian zehar aztertutako lipidomaren analisi zehatzak, mintz-lipidoen funtzio espezifikoa ulertzea pentsa baino lan konplexuago izango dela adierazten du. Epitelioan ez bezala, lamina propian jatorri ezberdineko hainbat zelula mota daude, eta aniztasun honengatik, hasiera batean, epitelioan ikusitako gradienteak ehun honetan ez litzatekela errepikatuko pentsatu genuen. Hala ere, 10 µm-ko pixel tamainarekin lortutako MALDI-IMS irudiek (4.14 Irudia) lipidoek kasu honetan ere antolaketa berezia izan zezaketela iradoki ziguten, epitelioan ikusitakoaren alderantzizkoa hain zuzen ere. *K-means* bidez eginiko segmentazioak ere hipotesia hau indartu zuen ehun mota hau hiru taldetan banatuz: zona basala edo behekoa (arroxa), erdiko zona (laranja) eta zona apikala edo goikoa (horia).

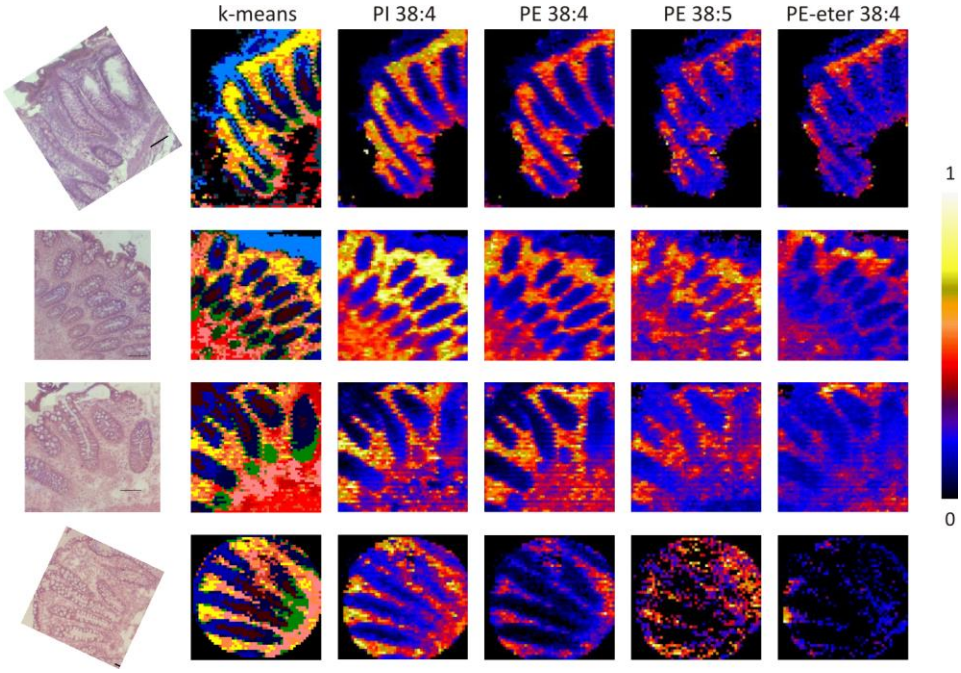

4.14. Irudia. Lehenengo zutabea: H&E bidez tintatutako biopsia osasuntsuak; bigarren zutabea, sekzio hauei dagokien *k-means* segmentazioa; eta gainontzeko zutabeak lamina propioan zehar intentsitatea aldatzen duten lipido jakin batzuen banaketa-irudiak.

Emaitzarik adierazgarriena AA-duten fosfolipidoen portaera epitelioan izandakoaren aurkakoa zela da, batez ere PE espezieen kasuan, baino baita PIn ere, adibidez, 38:4 espeziearen ehunekoa lamina propian gorantz egin ahala igoz, eta 36:2 jaitsiz. 4.15 Irudian ikusi daitezke espezie hauek lamina propia osasuntsu batean duten joera *k-means* analisiak deskribatutako hiru zonaldeak alderatzen direnean. Horrela, immunitate-sisteman parte hartzen duten zelulek, azido arakidoniko molekula prohanturazkoaren kantitate gehiago eskuragarri izango lukete zehazki AA duten espezieen gradienteak maximora iristen diren zonetan.[16,28] Honek, espezie berak, ehun edo zelula motaren arabera, rol ezberdinak izan ditzakela iradoki digu.

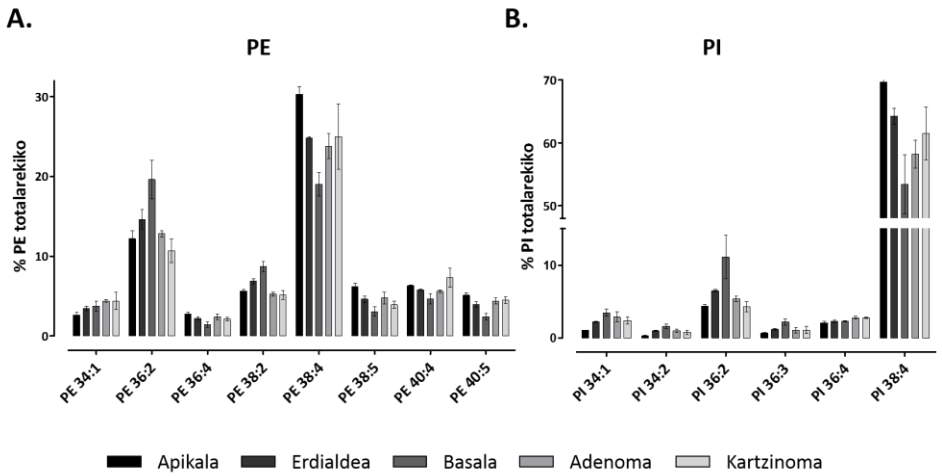

4.15. Irudia. PE (**A**) eta PI (**B**) lipido espezie batzuen ehunekoen barra-diagramak, lamina propio osasuntsu batean sortzen diren hiru klusterrak AD eta kartzinoman sortzen diren kluster bakarrarekin konparatuz. Soilik estatistikoki esanguratsuak diren lipidoak erakusten dira. Esangura estatistikoa Studenten t proba bidez aztertu zen (p balioa < 0.05). Emaitzak 4.2. Taulan ikusi daitezke. Barra-diagrametako balioak pazienteen arteko batezbestekoak ± SEM dira ($n = 4$ kontrola eta AD laginetan, eta $n = 3$ kartzinomaren kasuan).

Lamina propio osasuntsu batean sortutako hiru klusterrak adenoman (4.11. Irudia, kluster horia) eta kartzinoman sortutako kluster bakarrarekin (eranskineko Figure A.4.3, kluster horia) alderatzean, epitelioan baino maila apalagoan izan arren, espezie molekular jakin batzuen adierazpenean ezberdintasunak aurkitu zitezkeen, 4.2. Taula, 4.15. Irudia eta eranskineko Table A.4.6. Ezberdintasunik aipagarriena azido arakidonikoa duten espezieen gutxitzea izan zen (4.15. Irudia), batez ere epitelioarekin alderatzen badugu, zelula bakoitzak lipido jakin batekiko duen portaera, adibidez PI 38:4ekiko, ezberdina dela adieraziz, baita egoera patologikoetan ere.

4.1. Taula. PE eta PI portzentaiak Sutudenten t proba bidez alderatu ziren ea estatistikoki esanguratsuak ziren aztertzeko. Horretarako, konparaketa anizkoitzak egin ziren. * p › 0.05; ** p › 0.01; *** p › 0.005. . * p › 0.05; ** p › 0.01; *** p › 0.005. (Ap: Apical; B: Basal; E: Erdialdea; AD: Adenoma; and K: Kartzinoma). Soilik esanguratsuak diren espezieak erakusten dira. Kluster bakoitzari dagokion fosfolipidoen konposizioa eranskineko Table A.4.5 ikusi daiteke.

		Ap vs B	Ap vs E	Apl vs AD	Apl vs C	B vs E	B vs AD	B vs K	E vs AD	E vs K
PE	34:1			**					*	
	36:2	*					*	*		
	36:4	*								
	38:2	**	*				**	*	**	
	38:4	**	**	*		*				
	38:5	*	*		*					
	40:4		*	*						
	40:5	**				*	*	*		
PI	34:1	**	***							
	34:2	**	**	*						
	36:2		**							*
	36:3	*	**							
	36:4			*	*			**		
	38:4	*	*	**						

Epitelioan aurkitutako zona basalaren eta adenomaren arteko antzekotasunarekin alderatuz, lamina propioan lortutako emaitzek bestelako joera adierazten dute. Kasu honetan, adenomako eta kartzinomako ehun konektiboak, lamina propia osasuntsu baten goiko zonarekiko nolabaiteko antza dutela adierazten dute, zehazki, prohanturazko zelulak kokatzen diren zonari.

4.5 Ondorioak

Ikerketa lan honen lehenengo helburua laser-orban tamaina handia duen masa-espektrometro komertzial bat erabiliz, erresoluzio handiko MALDI-IMS metodologia optimizatzea izan zen. Lagin-prestaketa urratsean kontu handiz ibiliz, eta matrize egokia eta ehunak matrizez estaltzeko metodo aproposa aukeratuz, 10 um edo 5 um-ko erresoluzioak lor zitezkeela frogatu dugu 170 µm x 40 µm-ko tamaina duen laser-izpi eliptiko batekin.

Erresoluzioaren hobekuntzak, koloneko biopsietan egon daitezken ehun-mota ezberdinen lipidoak argi ta garbi identifikatzea eta beren kokapen zehatza lortzea ahalbidetu zuen, hiru ehun mota nagusi horien lipidoma xehatua lortuz (epitelioa, lamina propioa eta muskularis mucosae). Honetaz gain, irudiei eginiko analisi estatistikoari esker, kripta eta lamina propioaren goiko eta beheko aldeen ezberdintasunetaz ohartu ginen, lipidoek zelularen fisiologian izan dezaketen garrantziaren teoria indartuz, eta beraz, bi ehun hauetan zehar ematen diren lipidoen aldaketak ikertzera butzatuz.

Hainbat kolon biopsia osasuntsuetako sekzioetan egindako azterketak, lipido jakin batzuen ugaritasuna zelula motaren eta zelularen fisiologiaren arabera erregulatuta dagoela adierazi zuen. Ikusitako lipido antolaketa bereziak, batik bat kriptan zehar, ekuazio matematikoen bidez deskribatuak izan zintezkeen, honek, lipido profilaz baliatuz, zelula baten egoera fisiopatologikoa iragartzea eta ebaluatzea posible izango litzatekela iradokiz. Gainera, epitelioan aldaketak zelulen diferentziazio prozesuarekin erlazionatuak bazeuden, lamina propioaren kasuan, aldiz, ehun honek berezkoa duen prohanturazko-zelulen gradientearekin bat egin zuen. Hala ere, eta aurkako joera erakutsi arren, bi kasuetan AA-duten espezieak izan ziren lipidorik erregulatuenak. Honela, bata bestearen alboan dauden bi ehun mota desberdinek lipido espezie bera modu ezberdinean maneiatu dezaketela adieraz dezakegu, eta beraz, laginaren konposaketa-lipidikoa LC-MS bidez biopsien homogeneizatuetan eginez gero, edo, IMS-MS bidez behar bezalako erresoluzioa ez bermatuz gero, ondorio engainagarriak lor ditzakegu.

Laburbilduz, emaitza hauek, ikerketa klinikoan, lipido aztarnak eta MALDI-IMS teknikak izan dezaketen aplikagarritasun translazionala sustatzen dute.

[1] Spengler B, Hubert M, Kaufmann R. MALDI ion imagingand biological ion imaging with a new scanning UV-laser microprobe. *Proceedings of the 42nd ASMS Conference on Mass Spectrometru and Allied Topics*. **1994**.

[2] Caprioli RM, Farmer TB, Gile J. Molecular imaging of biological samples: localization of peptides and proteins using MALDI-TOF MS. *Anal. Chem*. **1997**. 69:4751-4760.

[3] Stoecki M, Farmer TB, Caprioli RM. Automated mass spectrometry imaging with a matrix-assisted laser desorption ionization time-of-flight instrument. *J. AM. SOC. Mass Spectrom*. **1999.** 10:67-71.

[4] Todd PJ, Schaaff TG, Chaurand P, Caprioli RM. Organic ion imaging of biological tissue with secondary ion mass spectrometry and matrix-assisted laser desorption/ionization. *J. Mass Spectrom*. **2001**. 36:355-369

[5] Stoeckli M, Chaurand P, Hallahan DE, Caprioli RM. Imaging mass spectrometry: a new technology for the analysis of protein expression in mammalian tisues. *Nat. Med*. **2001**. 7:493-496.

[6] Dreisewerd K. Recent methodological advances in MALDI mass spectrometry. *Anal. Bional. Chem*. **2014**. 406:2261-2278.

[7] Murphy RC, Hankin JA, Barkley RM. Imaging of lipid species by MALDI mass spectrometry. *J. Lipid Res*. **2009**. 50:S317-S322.

[8] Spraggins J, Caprioli RM, High-speed MALDI-TOF imaging mass spectrometry: rapid ion image acquisition and considerations for next generation instrumentation. *J. Am. Soc. Mass Spectrom*. **2011**. 22:1022-1031.

[9] Jurchen JC, Rubakhin SS, Sweedler JV. MALDI-MS imaging of features smaller than the size of the laser beam. *J. Am. Soc. Mass Spectrom*. **2005**. 16:1654-1659.

[10] Puolitaival SM, Burnum KE, Cornett DS, Caprioli RM. Solvent-free matrix dry-coating for MALDI imaging of phospholipids. *J. Am. Soc. Mass Spectrom.* **2007**. 18:1646-1652.

[11] Goodwin RJA, Scullion P, MacIntyre L, Watson DG, Pitt AR. Use of a solvent-free dry matrix coating for quantitative matrix-assisted laser desorption ionization imaging of 4-bromophenyl-1,4-diazabicyclo(3.2.2)nonane-4-carboxylate in rat brain and quantitative analysis of the drug from laser microdissected tissue regions. *Anal. Chem.* **2010**. 82:3868-3873.

[12] Trimpin S, Herath TN, Inutan ED, Wager-Miller J, Kowalski P, Claude E, Walker JM, Mackie K. Automated solvent-free matrix deposition for tissue imaging by mass spectrometry. *Anal. Chem.* **2010**. 82:359-367.

[13] Hankin JA, Barkley RM, Murphy RC. Sublimation as a method of matrix application for mass spectrometric imaging. *J. Am. Soc. Mass Spectrom.* **2007**. 18:1646-1652.

[14] Thomas A, Charbonneau JL, Fournaise E, Chaurand P. Sublimation of new matrix candidates for high spatial resolution imaging mass spectrometry of lipids: enhanced information in both positive and negative polarities after 1,5-diaminonapthalene deposition. *Anal. Chem.* **2012.** 84:2048-2054.

[15] Humphries A, Wright NA. Colonic crypt organization and tumorigenesis. *Nat. Rec. Cancer.* **2008**. 8:415-424.

[16] Strupat K, Kovtoun V, Bui H, Viner R, Stafford G, Horning S. MALDI produced ions inspected with a linear ion trap-orbitrap hybrid mass analyzer. *J. Am. Soc. Mass Spectrom.* **2009**. 20:1451-1463

[17] Riddell R, Jain D. Small and large bowel structure: developmental and mechanical disorders. *Gastrointestinal Pathology and its Clinicals Implications, vol. 2.* **2014**. 267-283.

[18] Shoshkes-Carmel M, Wang YJ, Wangensteen KJ, Tóth B, Kondo A, Massassa EE, Itzkovitz S, Kaestmer KH. Subepithelial telocytes are an important source of Wnts that supports intestinal crypts. *Nature*. **2018**. 557:242-246

[19] Powell DW, Pinchuk IV, Saada JI, Chen X, Mifflin RC. Mesenchymal cells of the intestinal lamina propria. *Annu. Rev. Phyiol.* **2011**. 73:213-237.

[20] D'Souza K, Epand RM. Enrichment of phosphatidylinositols with specific acyl chains. *Biochim. Biophys. Acta*. **2016**. 1838:1501-1508.

[21] Bestard-Escalas J, Garate J, Maimo-Barcelo A, Fernandez R, Lopez DH, Lage S, Reigada R, Khorrami S, Ginard D, Reyes J, Amengual I, Fernandez JA, Barcelo-Coblijn G. Lipid fingerprint image accurately conveys human colon cell pahophysiologic state: a solid candidate as biomarker. *Biochim. Biophys. Acta*. **2016**. 186: 1942-1950.

[22] Yamashita A, Hayashi Y, Nemoto-Sasaki Y, Ito M, Oka S, Tanikawa T, Waku K, Sugiura T. Acyltransferases and transacylases that determine the fatty acid composition of glycerolipids and the metabolism of bioactive lipid mediators in mammalian cells and model organisms. *Prog. Lipid Res.* **2014**. 53:18-81.

[23] Dorninger F, Brodde A, Braverman NE, Moser AB, Just WW, Forss-Petter S, Brugger B, Berger J. Homeostasis of phospholipids – the level of phosphatidylethanolamine tightly adapts to changes in thanolamine plasmalogens. *Biochim. Biophys. Acta*. **2015**. 1851:117-128.

[24] Fearon ER, Vogelstein B. A genetic model for colorectal tumorigenesis. *Cell*. **1990**. 61:759-767.

[25] Snover DC. Update on the serrated pathway to colorectal carcinoma. *Hum. Pathol.* **2011**. 42:1-10.

[26] Levine JS, Ahnen DJ. Clinical practice. Adenomatous polyps of the colon. *New Engl. J. Med.* **2006.** 355:2551-2557.

[27] Barker N. Adult intestinal stem cells: critical drivers of epithelial homeostasis and regeneration. *Nat. Rev. Mol. Cell Biol.* **2014**. 15:19-33.

[28] O'Leary AD, Sweeney EC. Lymphoglandular complexes of the colon: structure and distribution. *Hystopathology*. **1986**. 10:267-283.

6. Kapitulua

Ikerketa klinikoetan erabiltzeko tresna analitiko berrien garapena

Kapitulu honek, aplikazio klinikoetan eskala haundian lagin asko modu automatizatu batean analiza dezaken gailu berrien beharra du hizpide, denbora eta lagin-kantitatea murrizteko helburuarekin.

Zelula-mintzen lipido-profila zehazteko, masa-espektrometria eta mikroarrai miniaturizatuen teknologiak konbinatzen dituen metodologia aurkezten da. Ikerket lan hau EHUko Medikuntza eta Erizaintzako Fakultateko MD. Maria Dolores Boyanoren taldearekin eta IMG Pharma Biotech S.L. enpresarekin elkarlanean burutu zen.

6.1 Sarrera

Minbiziaren ikerketan, gaixotasunen diagnostikorako edota tratamenduaren erantzuna monitorizatzeko lagungarriak diren tresnak garatzea ezinbestekoa da. Azken urteotan, esperimentu-baldintza berean lagin ezberdin ugari neurtu ahal izateko, miniaturizazioan oinarritutako estrategia berriak garatu dira,[1] ehunen sailkapena helburutzat dutenak. Bereziki erabiliak izan dira genomikaren arloan geneen adierazpena era azkar eta automatizatui batean aztertzeko.

Azkeneko urteotan teknologia hau genomikatik haratago zabaltzeko ahalegin handiak egin dira. MALDI-IMS miniaturizazioko teknikekin konbinatzen duten ikuspegi berriek, hala nola ehunen mikroarraiek, errendimendu handiko analisi azkar eta automatizatuak garatzen lagundu dute, lagin-prestaketa sinplifikatuz eta azterketa bakoitzean behar den lagin-kantitatea murriztuz. Honek, ehundaka lagin esperimentu bakar batean neurtzea ahalbidetzen du, egon daitezken inter eta intra-esperimentuen arteko bariabilitateak ekidinez eta denbora eta kostua aurreztuz.

MALDI-IMS teknika erabiliz *lab-on-a-chip* kontzeptua aurkezten duten hainbat lan aurki daitezke bibliografian, batez ere proteinen analisirako,[2,3] baina oraindik ez da honelako metodologiarik metabolomikaren alorrean erabili, eta bereziki lipidomika aztertzeko.

6.2 Helburuak

Kapitulu honen helburua, MALDI-IMS eta ehunen mikroarraietan oinarritzen den metodologia garatzea da. Kontzeptu-froga gisa, zelula-mintzez osaturiko mikroarraien emaitzak aurkezten dira, hauek sailkatzeko eta tumorea marka dezaketen lipidoak identifikatzeko asmoarekin. Erabilitako metodologiaren lan-fluxua 6.1. Irudian aurki daiteke.

Ehun edo zelula osearen ordez zelua-mintzak erabiltzearen arrazoi nagusia analisia oztopatu dezaketen metabolitoen eta proteinen murrizketa da, biomarkatzaileen identifikazioa hobetuz. Mintzetako lipidoek, zelula baten lipido kopuru osoaren ~ %80 adierazten dutela kontuan izanda, zelula osoaren ordez, mitzak soilik erabiltzearen hurbilketa, zelularen egoera fisiologiko eta patalogikoaren adierazgarri izango da. Gainera, teknologia honen azken helburua ospitaleetan ezartzea denez, eta beraz, protokolo erraz eta azkarrak beharrezkoak direnez, mintzen isolamenduak eskatzen dun lagin prestakea motzak gainontzeko erauzketa teknikekiko, aproposa egiten du hauen erabilera.

6.3 Metodologia

Zelula-lerro eta beren kultiboen baldintzak

Labur, melanozito zelula ezberdinak, melanoma primario eta potentizal metastatiko altuko zelula-lerro ezberdinak kultibatu ziren bakoitzari dagokien kultibo medio egokienean 10%FBS, 2mM glutamina eta antibiotikoekin (Eranskineko Table A.6.1). Lan hau Arantza Perez-Valle, Euskal Herriko Unibertsitateko Medikuntza eta Erizaintza Fakultateko MD Maria Dolores Boyanoren taldeko kideak burutu zuen.

Zelula-mintzen isolamendua

Mintzak erauzteko homogeneizazio tanpoia (1 mM EGTA, 3 mM $MgCl_2$, eta 50 mM Tris-HCL, pH 7.4) eta tefloi-kristal homogeneizagailua (Heidolph RZR 2020) erabili ziren. Behin 20 bolumenetan homogeneizatu ondoren, laginak 1000x g 8 minutuz zentrifugatu ziren eta jarraian gainjalkinari beste zentrifugazio ziklo batetik pasa zitzaion, oraingoan 18000x g-tan 15 minutuz (4˚C, Microfuge 22R centrifuge, Beckman Coulter). Lortutako prezipitatuak homogeneizazio tanpoiarekin ikuzi ziren Ultra-Turrax (T10 basic, IKA) bat erabiliz eta berriz ere zentrifugatuak izan ziren aurreko baldintza beretan. Lortutako homogeneizatuak -80˚Ctan gorde ziren mikroarraiak prestatzeko erabiliak izan arte.

Zelula-mintzen mikroarraien inpresioa

Mintzak patentatutako inpresio tanpoi batean bersuspenditu ziren eta mikroarraier robot baten laguntzat (Nano_plotter NP 2.1),[4] beirazko euskarrien gainean inprimatu ziren (20 tanta puntuko, hiru erreplika lagineko). Mikroarrai hauek -20ºC-tan gorde ziren MALDI-IMS esperimentuak egin arte.

Mintzen erauzketa eta beirazko euskarrietan hauen inpresioa IMG-Pharma Biotech S.L. enpresako Dr. Gabriel Barreda-Gómez eta Tarson Tolentino-Cortez kolaboratzaileek burutu zuten.

IMS eta datuen analisia

Lagin-prestaketaren protokoloa 3.Kapituluan irakur daiteke. Datuak soilik ionizazio negatiboa erabiliz neurtu ziren, 150 µm-ko espazio-bereizmena eta m/z = 400-tan 60.000 FWHM-ko masa-bereizmena erabiliz, 20-30 µJ/pultsuko energiarekin. Gainontzeko parametroak 3.Kapituluan aurki daitezke.

Datuak Matlab (MathWorks, Natick, USA) bidez 3.Kapituluan deskribatutako parametroak erabiliz atzeman ziren. Levene-ren testa, faktore bakarreko ANOVA eta Bonferroni/Games-Howell konparaketa anizkoitza burutzeko IBM SPSS Statistics for Windows (Version 23.0; IBM, Chicago, IL, USA) erabili zen. Levene-ren testak datuen homogenotasuna zehazten du (H_0 = taldeek bariantza baliokideak dituzte) post hoc

metodo egokia aukeratzeko: Boferroni Levene-ren p balioa ≥ 0.05 bada eta Gamez-Howell p ≤ 0.05 izanez gero. *Receiver operating characteristic* (ROC) kurbak eta honekin batera emaitza hauen kurba azpiko azalera (*area under the curve*, AUC) GraphPad Prism (version 5 for Windows, GraphPad Software, La Jolla, CA, USA) bidez kalkulatu ziren.

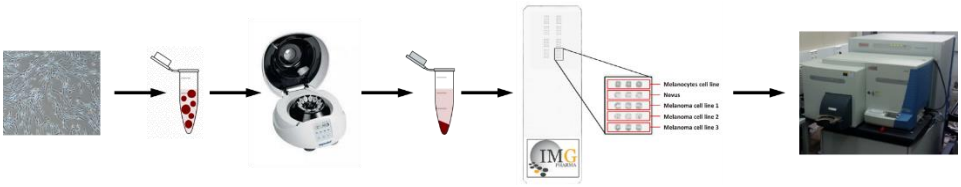

6.1. Irudia. Erabilitako metodologiaren lan-fluxua. Kultiboan hazitako zelulak eppedorfeta transferitu ziren eta homogeneizazio tanpoiarekin zentrifugazio ziklo batzuen ondoren, zelulen mintzak isolatu ziren. Hauek, patentatutako inpresio soluzio batean bersuspenditu ziren eta robot baten laguntzaz, beirazko euskarrietan inprimitu ziren. Bukatzeko, mikroarrai hauek MALDI-IMS bidez neurtu ziren, aurretik beharrezkoa duen lagin prestaketa prozesuarekin (2.3. Irudia, 2. Kapitulua)

6.4 Emaitzak eta eztabaida

Erreproduzigarritasuna esperimentuen artean

Zelula-mintzekin diseinatutako mikroarraiaren bost erreplika neurtu ziren ionizazio negatiboan 150µm-ko erresoluzio espazialarekin (6.2.A Irudia eta eranskineko Figure A.6.1). Mikroarraietan inprimatutako lagin-kantitatea txikia izan arren, 5-10 nL puntu bakoitzean, s/n erlazio oneko espektru erreproduzigarriak lortzeko lain izan zen.

Metodologiaren erreproduzigarritasuna aztertzeko, bost mikroarrai berdin bost egun ezberdinetan neurtu ziren. Horrez gain, esperimentuen baitan gerta zitezkeen intentsitate aldaketak aztertzeko helburuarekin, melanozito zelula-lerroen mintzak txipean zehar kokaleku ezberdinetan inprimatu ziren.

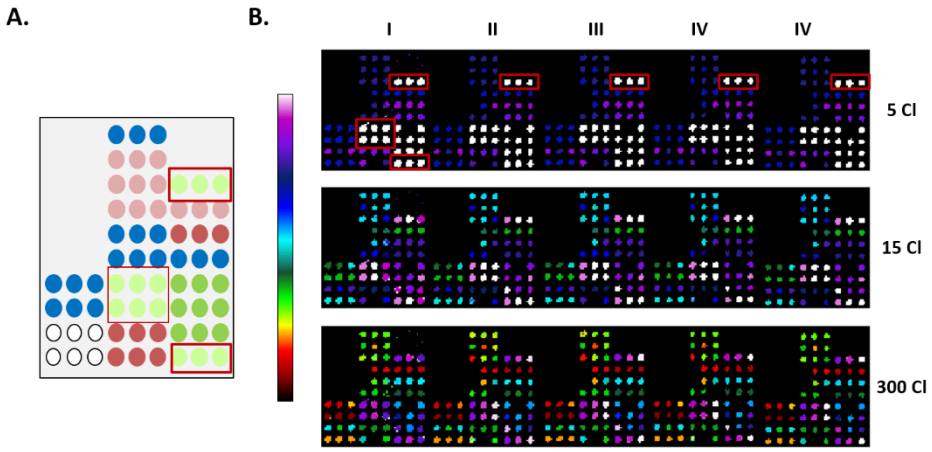

6.2. Irudia. A – Ikerketa lan honetarako diseinatutako mikroarraiaren eskema: puntu berde argiek melanozitoak adierazten dute; berde ilunak, giza *nevus* ezberdinetatik erauzi eta kultibatutako melanozitoak; puntu urdinak, melanoma primarioen zelula-lerroak; eta kolore txuri eta gorrixkek eta zuriek potentzial metastatiko altuko melanoma zelula-lerro ezberdinak adierazten dute: roxek gongoil linfatikoko metastasia (MMGL), zuriak larruazalpeko metastasia (MMSN) eta granateek beste lokalizazio batzuetako metastasia (azala eta zerebrala). Eskema hobeto ikusteko, eranskinean Figure A.6.1-n mikroarraieko puntu bakoitzari dagokion informazioaren aurki daiteke. **B** – DHCA-RC analisia. Neurtutako bost esperimentuak matrize batean konbinatu eta dena esperimentu bat izango balitz bezala aztertu zen, klusterizazioa datu guztiei batera eginez.

Bost esperimentuak matriz bakar batean konbinatu ziren gure ikerketa taldean garatutako algoritmo batez baliatuz, eta dagoeneko 5. Kapituluan deskribatutako DHCA-RC algoritmoa erabili zen segmentazio mapak sortzeko. Emaitzek, mikroarraiean zehar kokaleku ezberdinetak inprimitutako zelula-lerroen mintzen espektroak errepikargarriak zirela erakusten dute, guztiak talde edo kluster berean sailkatuz (karratu gorriz markatua 6.2.B. Irudian). Gainera, sortutako kluster horiek egun ezberdinetan neurtutako mikroarraietan ere mantendu ziren. Honek guztiak, metodologiaren erreproduzigarritasuna egokia izan zela iradoki digu, bai esperimentuen artean, eta baita esperimentu bkoitzean zehar ere.

Honetaz gain, segmentazio mapek, kontroleko zelula-mintzek eta melanoma-mintzek lipido-fenotipo ezberdina eduki lezaketela iradokitzen dute. Esaterako, klusterizazio maila 5Cl-tan ezarriz, melanozito denak talde berean sailkatu ziren (6.2.A. Irudiko puntu berde guztiak zuriz daude 6.2.B. Irudian), eta gainontzeko lagin denak lau talde ezberdinetan, baina inolako klase-joerarik jarraitu gabe. Mapa hau klusterren artean 1 – korrelazioa erabiliz irudikatu zenez, melanoma guztien koloreen antzekotasunak (urdinetik morera kolore-barran) euren espektroen artean korrelazioak egon zitezkeela adierazten du. Klusterizazio maila igotzean, melanozitoak ere banatzen hasi ziren, melanozito zelula-lerro komertzialak alde batetik (zuri eta arroxa 6.2.B. irudian) eta *nevi*-etatik erauzi eta kultibatutako melanozitoak beste aldetik (more iluna), hauen lipido-profiletan ezberdintasunak egon zitezkeela adieraziz. Hala ere, kolore-barran koloreen

posizioa behatuz, euren artean melanomekin baino askoz ere hobe korrelazionatzen dutela esan genezake. Bestalde, ez zen sailkapenik lortu melanomen artean beren gaiztotasunarekiko. Desberdintasunak aztertu eta karakterizatzeko helburuarekin, puntu bakoitzaren espektroa atera zen eta estatistikoki konparatu ziren.

Zelula-mintzen lipido hatz-marka

Mikroarraietik ateratako epektroetako m/z-ak, 5. Kapituluan azaldutako xehetasunak jarraituz identifikatu ziren, eta zelula-lerroen artean egon zitezkeen bariabilitatea ahalik eta gehien ekiditeko, soilik erreproduzibleak ziren lipidoak erabili ziren analisian. Ikerketa lan honetan kontuan hartutako lagin-taldeak melanonizotak, melanoma primarioak, eta MMGL metastasikoak izan ziren (soilik metastasi mota bakarra sartu zen analisian gainontzeko motek ez baitzuten nahiko lagin-tamaina, n).

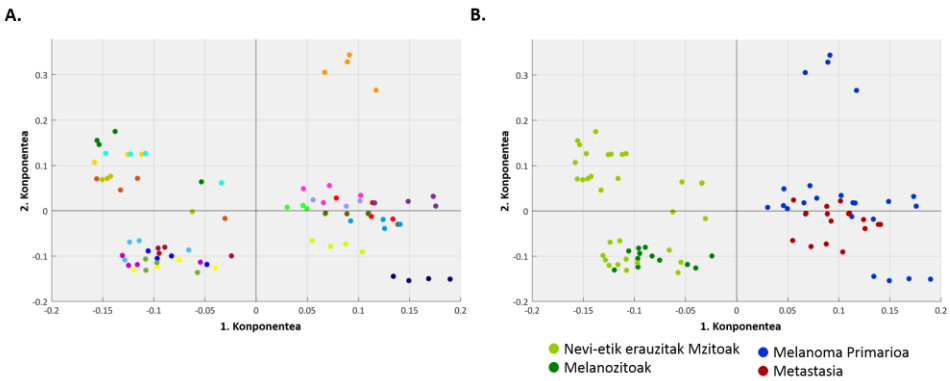

6.3. Irudia. PCA analisia bost mikroarraietatik lortutako lipido profilekin. **A** - Kolore bakoitza zelula-lerro bati dagokio. Lehen ikusi bezala, eta ikusita bost mikroarraietako zelula-lerro bakoitzaren *score*-ak elkartzeko joera zutela, beren lipido hatz-marka erreproduzibleak lortu ziren. **B** - Analisi bera baino zelula-mintzen tipoa markatuz. Melanomen artean euren potentzial metastatikoarekiko banaketarik lortu ez arren, melanozitoak eta melanomak guzti bereiztea posible zen. Berde argia: *nevus*-etik erauzitako melanozito primarioak. Berde iluna: melanozito komertzialak. Urdina: melanoma primarioak. Gorria: potentzial metastatiko handia duten melanomak.

6.3. Irudian PCA analisiaren emaitzak ikus daitezke, zelula bakoitza kolore ezberdinez koloreztatua. Soilik erreproduzibleak ziren espezieak erabili ziren. Lipidoen hatz-marka erabiliz, lehenengo konponentea nahiko zen melanozito zelula-mintz guztiak ezker aldean kokatzeko (berdez koloreztatuak 6.2.B. Irudian) eta melanoma zelula-mintza beste aldean bereizteko (gorriak eta urdinak), baino ez zen ezberdintasunik sumatu primario eta metastasikoen artean, denak nahasturik atera baitziren. Emaitza itxaropentsu honek, metodologia hau erabiliz tumoreen sailkapena bideragarria dela iradokitzen du, baina lagin kopurua nabarmenki handitu beharko litzateke sailkapen ereduak eraiki ahal izateko eta horiek balioztatzeko.

Erabilitako laserraren energia desberdina izanagatik, edo matrizea ezberdin depositatu izanagatik, baldintza esperimentalek jasan dezaketen bariazioak arinak izan arren, emaitza hauek, esperimentu ezberdinen arteko erreproduzigarritasuna handia dela erakusten dute. PCAko *score* bakoitza zelula-lerro baten erreplika dela kontuan hartuta (mikroarrai bakoitzean dauden hiru errepliken batez bestekoa), zelula-lerro bakoitzaren batez besteko espektroa atera zen biomarkatzaileak aurkitzeko helburuarekin. Hainbat ikerketa lan daude erreplikak n berri bat bezala analizatzen dutenak, lagin-tamaina totala handituz.[5] Hala ere, erreplikak oso baliotsuak izan arren barne-kontrola eramateko, hots, esperimentuaren errendimendua monitorizatzeko, ez da egokia analisi estatistikorakoan, emaitzetan sesgoak sor ditzazketelako, eta ondorioz, ondorio biologikoetan eragin ere.[6] Beraz, gure kasuan melanozito lagin-tamaina hiru izango litzake, *nevus*-etik erauzitako melanozitoena zortzi, melanoma primarioena sei eta gongoil linfatikoko metastasiarena lau.

Melanoma adierazi dezaketen biomarkatzaileen bila

Melanozito-mintzen lipido aztarna melanoma primario eta metastasikoarekin alderatu zen post hoc zuzenketa duen faktore bakarreko ANOVA baten bitartez, egoera patologikoarekin aldatzen diren espezie molekularrak zehazteko. Lenengo, Levene-ren testaren bitartez datuen homogenotasuna aztertu zen, eta emandako emaitzaren arabera, Bonferroni edo Games-Howell erabili zen konparaketa anizkoitzak egiteko. Melanozito komertzialen lagin-tamaina txikia zela kontuan izanda, eta emaitza ez puzteko, hots, emaitza faltsuak ahalik eta gehien saihesteko, analisitik kanpo geratu ziren *nevus* ezberdinetatik erauzi eta kultibatutako melanozitoak soilik erabiliz.

Emaitzak patentagarriak izan daitezkeenez, ez dira analisi estatistikoaren emaitzarik aurkeztuko lipido espezieen identitatea babesteko helburuarekin. 6.4. Irudiko *heatmap*-ak, estatistikoki esanguratsuak diren espezie molekularrekin eginiko azterketa hierarkiko baten emaitza aurkezten du. Melanozito eta bi melanoma moten artean ezberdintasunak ikusi arren, melanoma primario eta metastasikoaren artean ez zen estatistikoki ezberdintasunik aurkitu. 6.5.B Irudian esanguratsuak diren lipidoak aurkezten dira. Aipatzekoa da, esaterako L.E. 10 lipidoaren kasuan, melanoma primarioa eta melanozitoaren arteko alderaketak analisiak ez-esanguratsutzat hartu arren, barra-grafikek ezberdintasunak egon daitezkela iradokitzen digutela, lipido honen adierazpena areagotuta baitago melanoma primarioetan. Lagin-tamaina handitzeak emaitza hobeak lortzen lagun dezake.

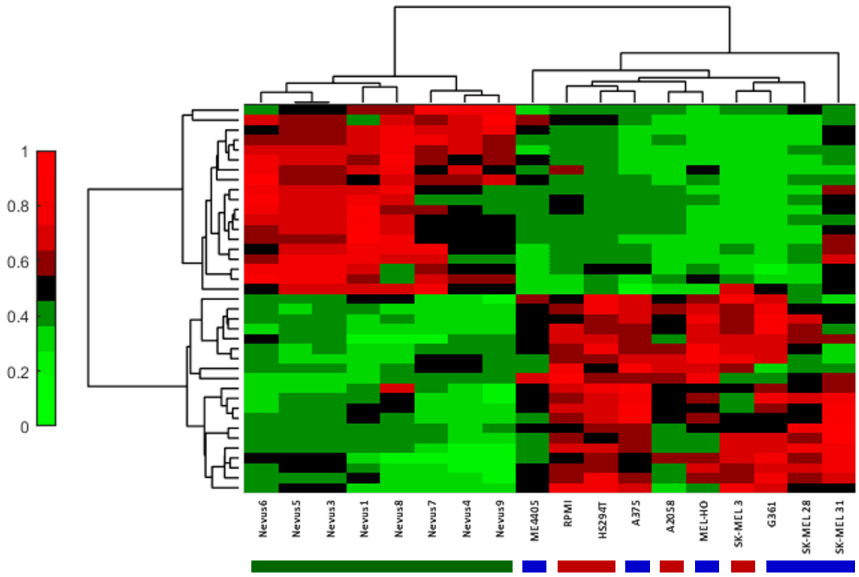

6.4. Irudia. Estatistikoki esanguratsuak diren lipidoak *heatmap* bidez irudikatuak hobeto ikusteko. Esangura faktore bakarreko ANOVA eta konparazio anizkoitzen bitartez (Bonferroni edo Games-Howell) determinatu zen. Datu hauen *klusterizazio* hierarkikoak *nevus*-etik erauzitako melanozitoak dendrogramaren ezkerraldean kokatu zituen (berdeak), eta melanomak eskuinaldean (urdinak eta gorriak), baino ezin izan ziren melanomak beren potentzial metastatikoaren arabera sailkatu.

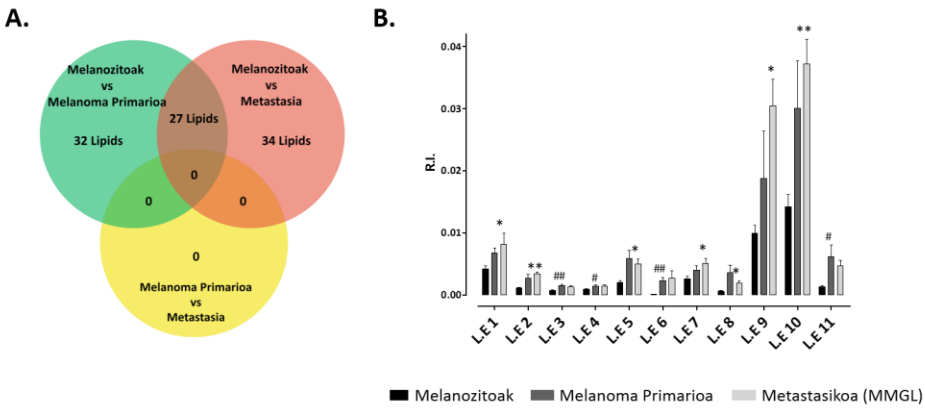

6.5. Irudia A - Estatistikoki esanguratsuak diren lipido-kopurua konparaketa bakoitzarentzako. Zirkulu bakoitzak konparazio bat errepresentatzen du, eta multzo hauek gainjarriak dauden zonaldean adierazten den lipido-zenbakiak, dagokien konparazioen arteko lipido komunen kopurua. Soilik bost lipido zeuden derregulatuak melanozito eta melanoma primarioen arteko konparaketan bakarrik, eta zazpi espezie melanozito eta potentzial metastatiko handia duten melanomen artean. **B** - Espezie horien grafikak. *: melanozitoak vs potentzial metastatiko altuko melanoma. #: melanozitoak vs melanoma primarioa. Gainontzeko lipido esanguratsuak amankomunean zituzten bi konparaketek.

39 lipidok aldaketa garrantzitsuak jasan zituzten. Hala ere, guztiek ez dute iragarpen-ahalmen bera. Biomarkatzaileen aurkikuntzan, garrantzitsua da kontrola eta patologiaren artean ezberdinduko duen markatzaileak %100 ziurtasunarekin iragartzea. Beraz, taldeen artean estatistikoki esanguratsuak direla esatea ez da nahikoa, bi talderen batez bestekoak ezberdinak izan arren, zenbait balio gainjarri daitezkelako. Adibide gisa, melanozito eta melanoma metastasikoaren artean separazio total ez duen L.E. 12 lipidoaren kasua erakusten da 6.6.A Irudian, Egon daitezken balioen gainjartzeak aztertzeko *receiver-operating characteristic* izeneko analisia erabili ohi da (hargailuaren funtzionamenduko ezaugarria, ROC). Honek benetako positiboak (*true positive*) eta benetako negatiboak (*true negative*) kontuan hartzen ditu, eta biomarkatzaile baten predikzio ahalmena kurbaren azpiko azalera (*area under the curve*, AUC) bidez ematen da. Horrela, AUCren balioa 0.5 edo antzekoa bada, bi talderen balioak guztiz gainjarriko lirateke eta ez litzakete egongo bereizketarik. Aldiz, balioa 1ra hurbiltzen bada, bi talde guztiz bereizten direla esango litzateke eta beraz iragarpen-ahalmen egokia, eta baliozko biomarkatzailea dela adieraziko luke. PI 36:4ren ROC kurba, dagokien AUCrekin eginiko bi alderaketentzat 6.6.B Irudian aurkezten da.

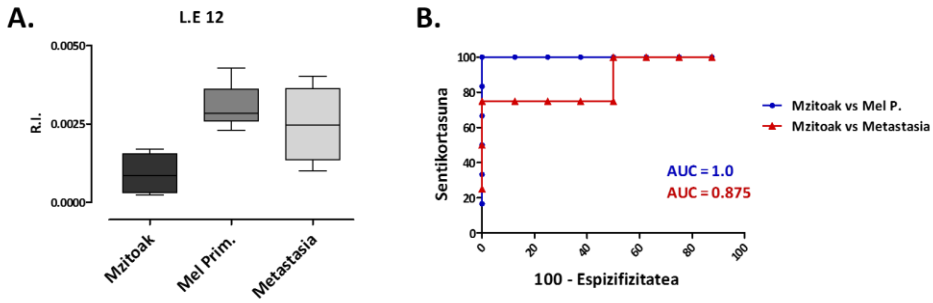

6.6. Irudia. A - PI 36:4 espeziearen kaxa-diagrama hiru kasuetan**.** Kaxen muturrek datuen lehen eta hirugarren kuartilak adierazten dute, barruko marra bertikalak mediana eta biboteek balore minimo eta maximoak adierazten dutelarik. **B** - ROC curbak melanoma primarioak (urdina) eta potentzial metastatiko haundia duten melanoma (gorria) melazonitoekko dagokien AUC balioarekin. Melanoma primarioak guztiz banatzen ziren bitartean, metastasiaren balore batzuk melanozitoenekin gainjarri ziren.

Faktore bakarreko ANOVAk estatitikoki esanguratsutzat eman zituen lipidoen ROC kurbak kalkulatu ziren dagokien AUC-ekin. Emaitzak eranskineko Table A.6.2an aurkitu daitezke. Lehenago aipatutako 39 lipidoetatik, 23 lipidok biomarkatzaile ontzat hartzeko bete beharreko baldintza gainditzen zuten (AUC = 1), gutxienez, eginiko konparaketaren batean (melanozitoak vs melanoma primarioa edo/eta melanozitoak vs metastasikoa). 6.7 Irudiak iragarpen-ahalmena ona duten zenbait lipido aurkezten dira, hots, balioak gainjartzen ez diren espezieak bi melanomentzat melanozitoekiko (A), soilik melanozito eta melanoma primarioaren artean (B) eta soilik melanozito eta metastasiaren artean (C). Nahiz eta lipido batzuen AUC 1 baino txikiago izan, esaterako 6.6.A. Irudiko lipidoa melanozito eta melanoma metastasikoaren arteko alderaketan, lagin-tamaina igotzeak ezberdintasun hauek susta ditzakete.

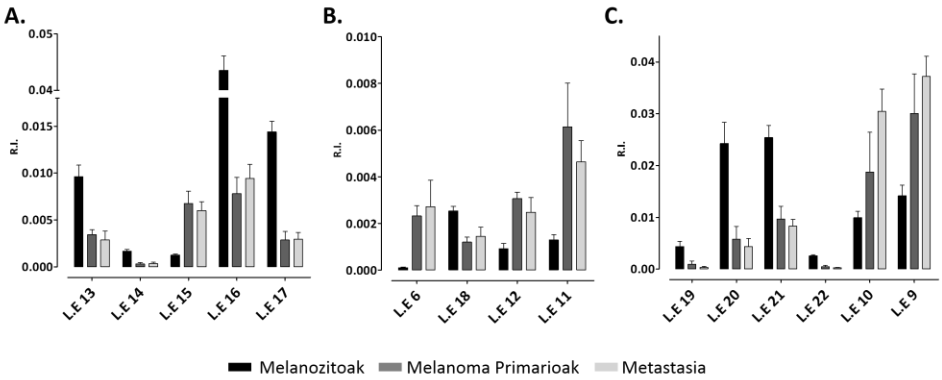

6.7. Irudia. ROC analisiaren emaitzak. **A** - Melanoma guztiak melanozitoetatik guztiz banatzen zituzten lipidoak. **B** - Melanoma primario eta melanozitoen arteko konparaketan esanguratsuak izateaz gain, ROC analisian AUC = 1 zuten lipidoak. **C** - Melanozito eta potentzial metastatiko altuko melanomen arteko balioak gainjartzen ez ziren lipidoak, biomarkatzaile ontzat hartu ditzakegunak.

IMS konbentzionalarekiko abantailak

Estatistikoki esanguratsuak diren lipido kantiate ezberdinak detektatu ziren giza biopsietako ehunetan egindako analisia, zelula-mintzetan egindakoarekin alderatzean. Zenbait aldaketak bat etorri ez arren, baliteke hau laginaren mikroingurune ezberdinagatik izatea. Zelula kultiboetan, zelulak era kontrolatu batean hazten dira, beren hazkuntzarako garrantzitsuak diren nutrienteekin hornituz, eta biopsien kasuan, aldiz, zelulak aske dira, kontrolik gabe nahi bezala hazteko. Gainera, mikrotxip hauetan ezarritako lagina soilik zelula-mintzak izan ziren, ez zelula osoak. Mintz-lipidoak zelula osoko lipidoen ~ %80 izan arren, baliteke zelulako beste zonaldeetan, edo ehunaren mikroingurunean gerta daitezkeen beste aldaketak batzuk galtzea, ezkutuan zeuden beste batzuk azaleratuz. Hau dela eta, logikoa da ehunaren eta zelula-mintzen artean ezberdintasunak espero izatea.

6.6. Irduian, Venn diagraman bitartez, bi metodologia moten arteko konparaketa aurkezten da, hots, ehunean lortutako emaitzen eta zelula-mintzez osatutako mikroarraietan lortutakoen arteko alderaketa. Lehen aipatu bezala, espezie esanguratsuen kopurua bi esperimentu moten artean ezberdina izan arren, 11 lipido esanguratsu komun aurkitu ziren melanozitoen eta melanoma primarioen artean. Melanozito eta potentzial metastatiko zelulen arten bederatzi lipido dira bi metodologiak erabiliz estatistikoki ezberdinak direnak. 6.8.C eta 6.8.D Irudietan bi kasu hauen adibide adierazgarri batzuk aurkezten dira. Aipatzekoa da ehunen eta zelula-mintzen artean lipido hauen balioen korrelazioa.

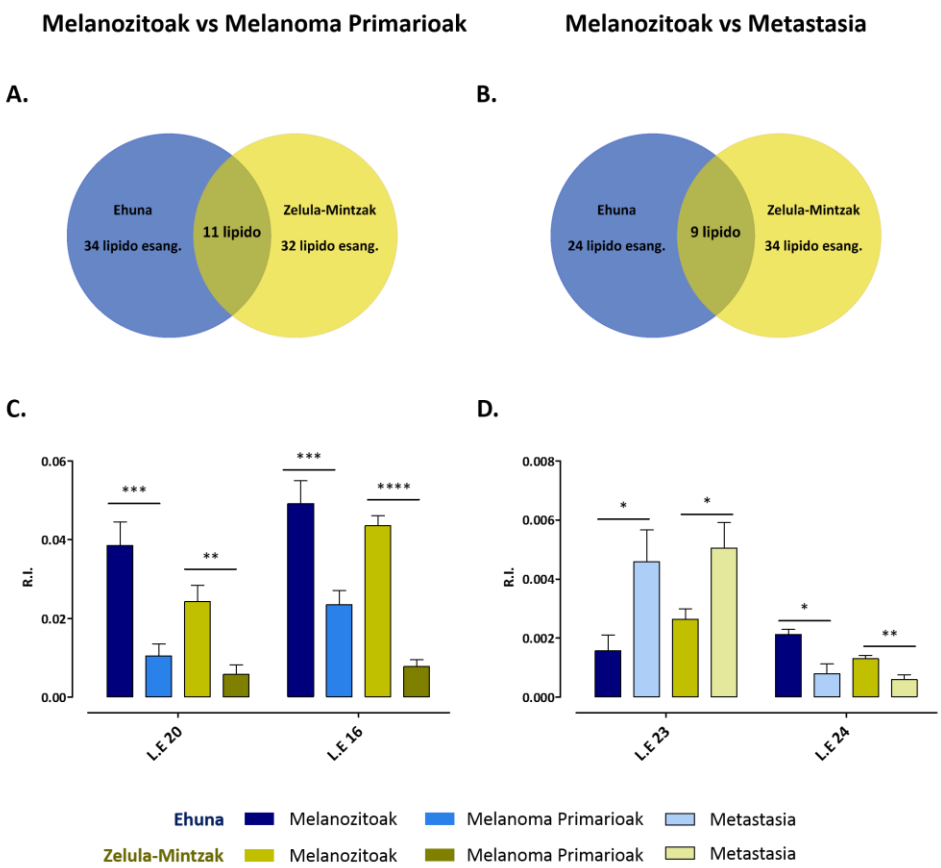

6.8. Irudia. Mikroarraietan eta aurreko kapituluan ehunean lortutako emaitzen arteko konparaketa. **A** - Melanozito eta melanoma primarioen arteko konparaketetan lortutako lipido esanguratsuen kopurua irudikatzen da bai zelula-mintzetan (multzo horia) eta baita ehunetan ere (zirkulu urdina). 11 espezie molekular amankomunean zituzten bi metodoek. **B** - Melanozito eta potentzial metastatiko handia duten melanomen arteko konparaketak mikroarraietan eta ehunean emandako emaitzen alderaketa. 24 eta 34 lipido esangurutsuetatik, hurrenez hurren, bederatzi espezie izan ziren berdinak bi metodologietan. **C eta D** - Bi metodologiekin amankomunean lortutako lipido esanguratsu batzuen barra-grafikak adibide gisa.

Mikrotxipek, ehunean eginiko esperimentuekiko duten abantaila nagusinetariko bat, bukaerako helburura iristeko behar izan den denbora da. Ikerketa lan honetan, bi metodologiekin lortutako emaitzetan ezberdintasunak egon arren, zenbait emaitza amankomun aurkezten dira. Lehenengo kasuan, hots, biopsia ehunak erabilitako esperimentuetan, MALDI-IMS analisiek hainbat hilabete, ia urte bat, iraun zuten bitartean, bigarren kasuan, mintz-mikroarraiak erabiliz, aste batean, pare bat astetan gehienez jota, MALDI-IMS analisia eta hare gehiago, post-analisia ere burutua egon daiteke. Hala ere, mikroarraien teknologian oinarritutako esperimentuak diseinatzean zenbait alderdi kontuan hartu behar dira. Horietako bat informazio espazialaren galera da, eta beraz,

laginak izan dezaken heretogeneitateari buruzko informazioaren falta eta, baita benetako mikroingurunearen biologia ere.

6.5 Ondorioak

Kontzeptu-froga gisa, eta lipido-profilen datu-base bat sortzeko helburuarekin ere, hainbat zelula-mintzen lipido aztarnak metodo automatizatu eta azkar batean lortu genituen. Lortutako zelula-mintzen lipido-fenotipoak PCA sinple batekin euren artean bereiztea ahalbidetzen du. Honek, mikrotxipen teknologia masa-espektrometriarekin konbinatzen duen metodologia erabiliz, eta lagin-tamaina egokia izanez, hots *n* handituz, emaitza bikainak lortuko lituzkeen sailkapen-eredu indartsuak eraikitzeko aukera ahalbidetzen du. Beraz, protokolo honek gaixotasunen diagnostikorako lagundu dezake, eta halaber pronostikorako edo tratamenduaren monitorizazioarako.

Aipatzekoa da LC-MS esperimentuetan ohikoa den ez bezala, soilik zelula-mintzak erabili zirela, eta ez zelula osoa edo zelulen homogeneizatua. Hala ere, mintz hauek guztiz funtzionalak ziren mikroarraietan, eta ehuneko laginekin alderatuta, zenbait ezberdintasun amankomun antzeman ziren. Mintzez osatutako mikroarraien erabilerak MALDI-IMS lipidomikaren analisitik lortutako emaitzak beste teknika batzuekin konbinatzeko aukera ematen digu, hala nola erradioligando edo entsaio entzimatikoekin, lipidoen eta proteinen arteko erlazioa argitzearren.[4] Gainera, ehun edo zelulen homogentauak lortzeko protokoloa baino asko ere prestaketa errazagoa izateaz gain, mintzak zelulak baino hobeto atxikitzen dira beirazko euskarrietara. Metodologiaren erreproduzigarritasuna ere frogatu da, inter- eta intra-esperimentalki, egun ezberdinetan neurtutako esperimentuen arteko analisi konbinatua ahalbidetuz.

Hala ere, metodologia honek oraindik erronka ugari ditu aurre egiteko. Horietako bat, eta interesgarrienetariko bat, kuantifikazioa da. MALDI-IMS teknologia erdi-kuantitatiboa da, eta azkeneko urteotan ahalegin handiak egin diren arren, oraindik kuantifikazioak gai korapilotsu bat izaten jarraitzen du.

Laburbilduz, aurkeztutako protokoloa, MALDI-IMS protokolo tradizionalaren bertsio miniaturizatua da, emaitzak lagin-kantitate txikiagoarekin eta analisirako denbora gutxiagorekin lor daitezkeenak, analisi lipidomiko azkar eta automatizatua ahalbidetuz.

---

[1] Djidja MC, Claude E, Snel MF, Francese D, Scriven P, Carolan V, Clench MR. Novel molecular tumour classification using MALDI-mass spectrometry imaging of tissue microarray. 2010. *Anal. Bioanal. Chem.* **2010**. 397: 587-601.

[2] Groseclose MR, Massion PP, Chaurand P, Caprioli RM. High-throughput proteomic analysis of formalin fixed paraffin-embedded tissue microarrays using MALDI imaging mass spectrometru. *Proteomics*. **2008**. 8:3715-3724.

[3] Casadonte R, Caprioli RM. Proteomic analysis of formalin-fixed paraffin-embedded tissue by MALDI imaging mass spectrometry. *Nat. Protoc*. **2011**. 6:1695-1709.

[4] Heber-Chatelain E, Desprez T, Serrat R, Bellocchio L, Soria-Gomez E, Busquets-Garcia A, Pagano-Zottola AC, Delamarre A, Cannich A, Vincent P, Varilh M, Robin LM, Terral G, Garcia-Fernandez MD, Colavita M, Mazier W, Drago F, Puente N, Reguero L, Elezgarai I, Dupuy JW, Cota D, Lopez-Rodriguez ML, Barreda-Gomez G, Massa F, Grandez P, Benard G, Marsicano G. A cannabinoid link between mitochondria and memory. *Nature*. **2016**. 539: 555-559.

[5] Kim HY, Lee H, Kim SH, Jin H, Bae J, Choi AK. Discovery of potential biomarkers in human melanoma cells with different metastatic potential by metabolic and lipidomic profiling. *Sci. Rep.* **2017**. 7: 8864.

[6] Vaux DL, Fidler F, Cumming G. Replicates and repeats. What is the difference and is it significant? *EMBO Rep.* **2012.** 13: 291-296.

8. Kapitulua

Zenbait ildo etorkizuneko ikerketei begira

8.1 Zenbait ildo etorkizuneko ikerketei begira

Azken urteotan masa-espektroetrian izan diren aurrerapenei esker, patologia ezberdinen lipidomak deskribatzeko interesa sustatu da. IMS, metabolitoen lokalizazioa irudikatuz, sistema biologiko konplexu ezberdinen ezagutza areagotzea bermatzen duen teknika analitikoa da. Hala ere, klinikan erabilgarri izan dadin, oraindik zenbait erronka ditu aurre egiteko. Tesi honek ikerketa klinikoan, eta batez ere minbiziaren ikerketan izan ditzaken oztopo hauetako batzuk ditu hizpide.

4. Kapituluan ikertu den lehen erronka erresoluzio espaziala izan da. IMS minbiziaren ikerkekuntzan erabiltzen diren gainontzeko teknika optiko estandarrekin parekatzeko, garrantzitsua da erresoluzio zelularrak edo azpi-zelularrak lortzea, teknika honek izan ditzaken mugak gaindituz. Protokolo zorrotz batekin, matrize egokia erabiliz eta hau ezartzeko metodo zuzena aukeratuz, 10 µm, edo, areago 5 µm-ko erresoluzio espaziala lortzea posible dela frogatu dugu, optika egokia ez duen masa-espektrometro bat erabiliz *oversampling* metodoaz baliatuz. Hala ere, metodologia honek, laginaren manipulazio oso ongi kontrolatu beharra eta intrumentua baldintzarik onenetan egotea eskatzen du. N_2 laserrek bizidenbora jakin bat izaten dute, eta masa-espektrometroak lan erritmo handiak jasanez gero, laser zaharra berri batez ordezkatu beharko da ia urtero. Ordezkapen hauek laserraren profila aldatu dezakete, laserren ezugarriak laser batetik bestera aldatzen baitira, baita laser bera berriz kargatzean, aldaketa bakoitzean nahitaezko urratsa bilakatuz laserraren karakterizazio. Honetaz gain, laser guztiek ez dituzte izpi ezaugarri egokiak *oversampling* arrakastatsu bat izateko. Azken urteotan bi N_2 laser ezberdinekin izandako esperientziak, optikan inolako modifikaziorik egin gabe erresoluzio zelularra lortzea beti ez dela posible erakutsi digu.

Hori dela eta, eta ikusita informazio zelularra beharrezkoa dela prozesu biologiko asko ulertzeko, erresoluzioaren alorrean sekulako hobekuntzak egin dira intrumento berriak garatuz. Horietako bat Bruker etxearen punta-puntako RapifleX MALDI Tissuetyper da, erresoluzio handiko masa-espektrometro azkarrena.[88] Hala ere, euskal esaera zaharrak dioen bezala, "*urruneko eltzeak urrez, iritsi eta lurrez*". **5. Kapituluan** aztertu den beste oztopo bat metabolitoen identifikazioa izan da. MALDI ionizazio leuneko teknika bada ere, lipidoen izaera labila kontuan izanda, ionizazio-ganbaran lipidoen fragmentazioa gerta daiteke, identifikazioa zailduz. Honetaz gain, masa-analizatzaileen masa bereizteko ahalmena era faktore mugatzailea da identifikazio zehatz eta egoki baterako. RapifleX erabiliz lortutako irudiak apartekoak izan arren, instrumentu hau TOF motako analizatzaile batez hornitua dago. Nahiz eta analizadore hauek merkatuko azkarrenak izan, euren disabantailarik nagusiena duten masa bereizteko ahalmen baxua da. Azken belanauldiko TOF gailuek ere ezin dute 10.000 FWHM-ko baino bereizmen altuagoa lortu lipidoen eremuan. Hau oztopo garrantzitsua da lipidoak identifikatzek orduan; izan ere, lortutako irudiak espezie molekular baten banaketa-irudia izan daiteke edo, bi espezien m/z hurbilegi badaude, bi espezie molekularren batura. Beraz, benetako inguru-biologikoa nahastuta ikusiko litzateke eta ateratako ondorioak ehunaren benetako izaerarekin bat ez etortzea gerta daiteke.

Ildo honetan, gure ikerketa taldea tesi honetan deskribatutako MALDI-LTQ-Orbitrap ekipoaren konfigurazio optikoaren hobekuntzan ari da lanean. Helburua, Orbitrap

analizatzailea duen masa-espektrometro batekin, hots, masa-bereizmen ahalmen altua duen analizadore batekin, edonolakoa izanda laser-izpiaren tamaina eta ezaugarria, erresoluzio zelularra bermatuko duen konfigurazioa garatzea da. Horretarako, eta SGIKEReko Laser Zerbitzuko adituaren laguntzari esker, ideia, laserra perfil gaussiarragoa izango duen puntu kontzentratuago baten enfokatzea da lente multzo bat erabilir, eta ondoren, 20 µm-ko zeramikazko *pinhole* batekin, hau filtratzea. Horrela, soilik laser-izpiaren zatirik energetikoenak zeharkatuko du *pinhole* zuloa, laser-orban kontzentratuago eta txikiagoa lortuz, eta nahiz eta irradiatutako eremua txikiagoaren ondorioz seinalearen intentsitatea apurtxo bat galdu, lipidoen banaketa-irudi bikainak lortzeko aukera ematen du konfigurazio berri honek.

Teknologien hobekuntzak ezinbestekoak dira ikerkuntzan aurrerapenak izateko, eta IMSn, bereziki, teknologia optiko konbentzionalen erabilerarekin parekatu ahal izateko.Hala ere, aurrerapenak testuinguru biologikorik eman gabe zalantzan jartzen du IMS teknikaren erabilgarritasuna klinikan. Esperimentu bakar batetik lortutako datu-kopurua izugarria da, eta behar bezala maneiatzea zaila, **5. kapituluan** ikus dugun bezala. Funtsezkoa da emaitzei behar bezalako garrantzi biologikoa ematea, lehenik eta behin, prozesu biologiko ezberdinak hobeto ulertzeko, eta behin ezagutza lortuta, diagnostikoa egiteko, terapia egokia aukeratzeko edo hauen monitorizazioan laguntza tresna izateko. Lipidoek jarduera biokimikoaren zuzeneko sinadura izan arren, fenotipoarekin korrelazionatzeko errazak, berez, beraiek bakarrik ez dute zelularen izaera konplexua azaltzen. Gure ikerketa taldeak kanpogo kolaboratzaileekin elkarlanean, lipidoen aldaketak prozesu entzimatikekin lotzea posible dela frogatu dugu analisi inmunohistokimiko (IHC) bidez.[89,90] Teknika honek, nagusiki makromolekuletan aldaketak monitorizatzea ahalbidetzen duen teknikak, antigorputz bereziak edo aurre-markatze kimikoa behar ditu, detektatutako molekulen kopurua mugatuz. Gainera, lagin-prestaketa eta MALDI-IMS analisiak, ehuna, presio atmosferikoan eta hutspean egotera beahrtzen du, eta jakinda matrizez estaltzen dela ere, MALDI esperimentuaren ondoren IHC bidezko analisiak egitea delikatua izaten da eta ez beti arrakastatsua. Hori dela eta, gure ikerketa taldea, IMS bidez ehunen ikuspegi multimodalaren baita ari da lanean beste talde batzuekin elkarlanean, analito ezberdinen irudiak lortuz. Ideia, ehun sekzio beran, lipido eta proteinen informazioa espaziala lortzea da, hauen artean egon daiteken erlazioa ulertu ahal izateko eta prozesu biologiko ezberdinen ezagutza hobetzeko helburuarekin. Ildo honetan, **6. Kapituluan** aurkeztutako *lab-on-a-chip* kontzeptua ere lagungarri izan daiteke lipidoen eta proteinen arteko erlazioa argitzeko, lipidoen analisiatik lortutako emaitzak entsegu entzimatikoek edo erradioligandoek emandako emaitzekin alderatuz. Mintz-mikroarraiak eta masa-espektrometria bateratzen dituen protokoloa etorkizun handiko teknologia dela erakutsi da, eta behin diseinua optimizatua dugula, orain benetako pazienteen biopsiekin diseinatutako mintz-mikroarraiak egiten ari gara minbiziaren diagnotikorako eta pronostikorako laungarri izan daitekeen txipak prestatuz.

Orohar, IMS ikerketa biomedikorako teknika erakargarri, boteretsu eta errendimendu handikoa da, baina garrantzitsua da bere mugetik haratago joatea aplikazio klinikoetan erabiltzaileak lortzeko. Garrantzitsua da identifikatutako molekulak prozesu biologikoekin erlazionatzea, **4. Kapituluan** ikusi bezala, zelulen egoera patofisiologikoa adieraz dezakeena. Teknika honek izan dezaken aplikazioa zelula gaiztoak osasuntsuekiko sailkatzea da, **5. Kapitulua** egin bezala. Hala ere, IMS-k duen beste erronka garrantzitsua

prozedura osoaren konplexutasuna da. Lagin-prestaketa eta IMS analisia errazak izan arren, tesi honetan ikusi bezala, datuen prestaketa, aurreprozesaketa eta analisi estatistikoa prozesu korapilotsuak izaten jarraitzen dute. Horregatik, garrantzitsua izango litzateke prozesu guztia automatizatzea bermatuko lukeen softwareak garatzea, egunen batean, diagnostiko tresna arrunt gisa erabiltzeko klinikan.

[88] Prentice DM, Chumbley CW, Caprioli RM. High-speed MALDI MS/MS imaging mass spectrometry using continuous raster sampling. *J. Mass Spectrom.* **2015**. 50: 703-710.

[89] Bestard-Escalas J, Garate J, Maimó-Barceló A, Fernández R, Lopez DH, Lage S, Reigada R, Khorrami S, Ginard D, Reyes J, Amengual I, Fernández JA, Barceló-Coblijn G. Lipid fingerprint image accurately conveys human colon cell pathophysiologic state: a solid candidate as biomarker. *Biochim. Biophys. Acta.* **2016**. 1861: 1942-1950.

[90] Lopez DH, Bestard-Escalas J, Garate J, Maimó-Barceló A, Fernández R, Reigada R, Khorrami S, Ginard D, Okazaki T, Fernández JA, Barceló-Coblijn G. Tissue-selective alteration of ethanolamine plasmalogen metabolism in dedifferentiated colon mucosa. *Biochim. Biophys. Acta Mol. Cell Biol. Lipids.* **2018**. 1863: 928-938.

Appendix Chapter 4

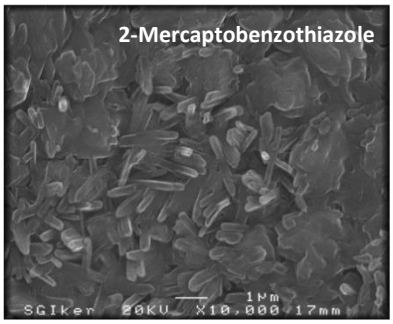

T (°C)	t (min)	mg/cm²	Crystal size (μm)
124	10	~ 0.16	3-5

Fig. A.4.1. SEM images of MBT crystals over a glass slide and optimization of the parameters for its sublimation. The morphology of the crystals is not homogenous and they tend to form aggregates with an average size range of 3-5 μm.

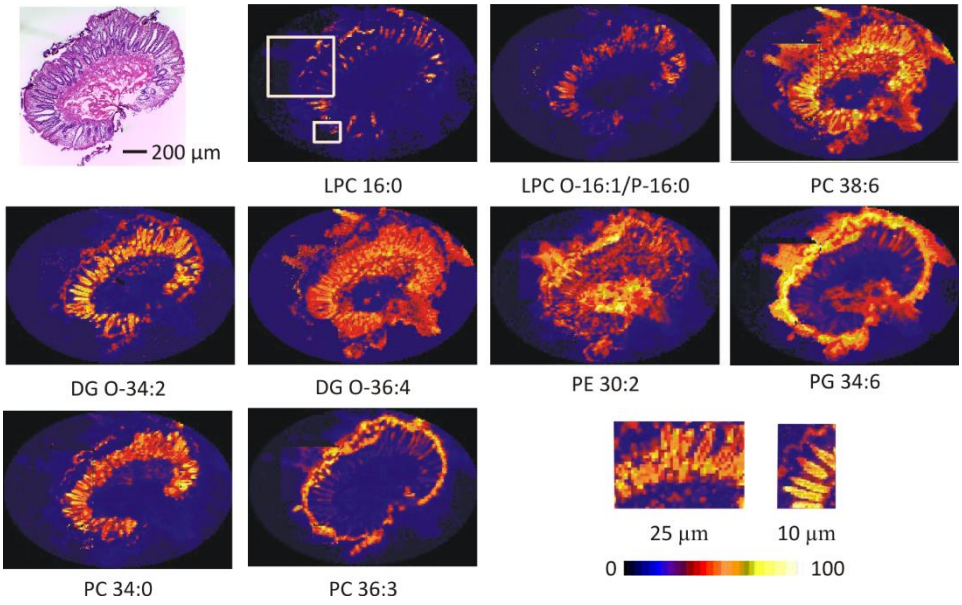

Fig. A.4.2. Comparison of the optical image of a human colon tissue section and the distribution of some selected lipid species detected in positive-ion mode. The large white square highlights the area scanned at 10 μm resolution, while the small square highlights the area scanned at 5 μm pixel size. The rest of the section was scanned at 25 μm. The last two images at the bottom-right are a detail of the distribution of DG O-34:2 + Na^+ recorded at 10 and 25 μm.

Table A.4.1. Lipid species detected in the epithelial layer displaying distribution patterns that correlate with the position along the crypt. Changes in relative intensity (RI) along the crypt were fitted to a linear equation, a polynomial equation of second grade (2nd) or to a logarithmic equation (log). The gradient was considered positive (+) when RI increased from the base of the crypt towards the lumen, and negative if the opposite. Values of the RI are expressed as mean percentage of the total RI for a given lipid class. Results for PC are from positive-ion mode IMS. (n = 6)

Distribution along the crypt					
Lipid class	**Species**	**R^2**	**Fit**	**Gradient**	**RI basal / apical values**
PI	32:1	0.62	Log	+	0.2/0.6
	34:1	0.89	lineal	+	8.0/17.0
	34:2	0.76	Log	+	5.0/8.0
	36:1	0.98	lineal	+	6.0/20.0
	36:2	0.94	Log	+	5.7/27.0
	36:4	0.94	Log	-	8.2/2.5
	38:4	0.97	Log	-	71.6/15.0
	38:5	0.81	lineal	-	2.5/1.5
	40:4	0.82	lineal	-	1.4/0.4
PE-ether	34:1	0.7	Log	+	8.3/14.4
	36:1	0.82	Log	+	5.6/13.0
	36:2	0.63	Log	+	8.3/15.5
	36:4	0.91	Log	-	21.3/9.7
	38:4	0.77	Log	-	28.6/16.1
	40:4	0.84	Log	-	8.1/1.9
PE	34:1	0.8	Log	+	4.3/7.2
	36:4	0.42	lineal	-	1.8/1.0
	38:4	0.79	Log	-	20.0/5.4
	38:5	0.46	lineal	-	3.6/1.6
PC	32:0	0.69	lineal	-	6.5/4.6
	38:2	0.68	lineal	-	0.7/0.4
	38:3	0.68	lineal	-	1.0/0.5
	38:4	0.43	Log	-	2.8/1.1
	38:5	0.26	Log	-	1.1/0.7

Table A.4.2. Lipid species detected in the epithelial layer displaying constant and scattered distribution patterns along the crypt. Values of the RI are expressed as mean percentage of the total RI for a given lipid class. % represents the percentage of variation of the lipid with respect to the mean. Results for PC are from positive-ion mode IMS. (n = 6)

Constant distribution along the crypt				
Lipid class	**Species**	**Mean**	**SD**	**%**
PI	36:3	4.42	0.72	16.2
PE-P	34:2	8.4	0.9	10.7
	36:3	4.8	0.6	12.5
	38:5	8.8	1.5	17.0
	38:6	4.4	0.6	13.6
	40:6	4.7	0.6	12.8
PE	36:1	24.2	1.3	5.5
	36:2	25.4	2.0	7.7
	36:3	8.3	1.3	15.7
	38:2	10.0	0.9	9.1
	38:3	7.3	0.7	9.7
PC	32:1	1.5	0.1	6.7
	34:1	37.2	1.5	4.1
	34:2	16.4	0.6	3.7
	34:3	1.5	0.1	6.7
	36:2	17.1	0.4	2.3
	36:3	10.4	0.7	6.7
Scattered distribution				
Lipid class	**Species**	**Mean**	**SD**	**%**
PI	32:0	0.5	0.1	11.3
	38:6	1.0	0.2	20.7
PE	34:2	2.3	0.3	13.6
	38:1	2.2	0.4	20.4
PC	36:1	4.4	0.5	10.9
	36:4	3.2	0.4	13.3

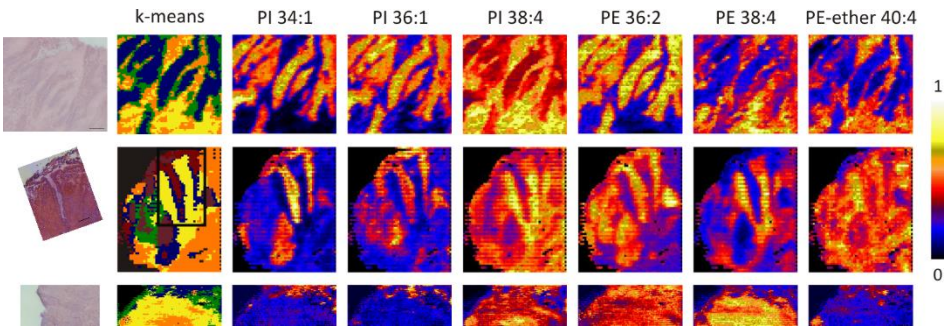

Fig. A.4.3. First column: H&E staining of carcinomatous colonic crypts; second column: *k-means* segmentation analysis for pattern recognition; and the rest of columns show the distribution of some characteristic lipids.

Table A.4.3. Average lipid composition of clusters established by *k-means* analysis in healthy, adenomatous and carcinomatous colon epithelium. Values are expressed as mean ± SEM (n=4 for healthy and adenoma and n=3 for carcinoma). In the case of PC (positive ion mode), only healthy and adenomatous biopsies were measured. nd: not detected

Lipid Specie		Apical	Basal	Adenoma	Carcinoma
PI	34:1	17.0 ± 1.1	13.3 ± 0.9	12.9 ± 1.8	9.5 ± 3.3
	34:2	8.6 ± 0.5	7.8 ± 0.5	6.3 ± 1.1	4.2 ± 1.4
	36:1	20.2 ± 1.5	11.7 ± 0.6	11.4 ± 2.1	7.4 ± 2.7
	36:2	27.8 ± 2.0	23.0 ± 1.7	17.3 ± 2.2	10.4 ± 1.3
	36:3	4.2 ± 0.7	4.8 ± 0.7	3.3 ± 0.6	3.7 ± 1.4
	36:4	2.6 ± 0.4	4.1 ± 0.4	4.9 ± 0.3	6.0 ± 0.3
	38:4	16.9 ± 1.3	31.1 ± 0.8	40.3 ± 6.2	53.4 ± 8.9
	38:5	1.5 ± 0.3	2.5 ± 0.3	2.5 ± 0.3	3.1 ± 0.2
	38:6	0.6 ± 0.2	0.5 ± 0.2	0.4 ± 0.2	nd
	40:4	0.6 ± 0.1	1.0 ± 0.1	0.8 ± 0.4	1.8 ± 0.3
	40:6	0.1 ± 0.1	0.1 ± 0.1	nd	0.6 ± 0.3
PE	34:0	0.6 ± 0.4	1.5 ± 0.5	1.1 ± 0.8	3.3 ± 0.9
	34:1	7.0 ± 0.3	5.6 ± 0.4	5.8 ± 0.4	7.1 ± 1.7
	34:2	2.0 ± 0.2	2.1 ± 0.1	1.5 ± 0.5	1.8 ± 0.7
	36:0	1.9 ± 0.7	1.7 ± 0.6	1.2 ± 0.7	2.7 ± 0.4
	36:1	26.7 ± 1.5	23.6 ± 1.1	30.5 ± 2.8	27.5 ± 4.8
	36:2	25.5 ± 0.8	24.9 ± 0.7	23.3 ± 1.9	15.8 ± 2.2
	36:3	6.5 ± 0.8	7.6 ± 0.5	4.2 ± 0.6	2.9 ± 1.3
	36:4	1.0 ± 0.2	1.3 ± 0.2	1.1 ± 0.2	1.8 ± 0.5
	38:1	1.9 ± 0.7	1.7 ± 0.6	2.5 ± 0.4	3.1 ± 1.0
	38:2	9.7 ± 0.1	9.4 ± 0.2	7.5 ± 0.6	6.8 ± 0.9
	38:3	7.5 ± 0.4	7.8 ± 0.4	6.1 ± 0.9	4.8 ± 1.0
	38:4	5.2 ± 0.4	7.2 ± 0.5	8.1 ± 1.5	12.6 ± 1.4
	38:5	1.8 ± 0.4	2.2 ± 0.4	2.9 ± 0.6	2.8 ± 1.0
	38:6	0.2 ± 0.2	0.3 ± 0.2	0.7 ± 0.2	0.7 ± 0.1
	40:4	0.5 ± 0.2	0.8 ± 0.1	0.9 ± 0.3	1.9 ± 0.2
	40:5	1.5 ± 0.3	1.0 ± 0.4	1.6 ± 0.1	1.5 ± 0.3

PE-ether	P 34:1	13.8 ± 0.9	11.9 ± 0.7	9.9 ± 1.5	8.6 ± 1.4
	P 34:2	8.2 ± 0.5	7.9 ± 0.5	3.7 ± 0.8	3.3 ± 1.4
	P 36:1	12.6 ± 1.7	9.0 ± 0.8	7.7 ± 0.6	5.7 ± 1.2
	P 36:2	16.9 ± 2.2	13.3 ± 1.3	6.8 ± ± 1.3	4.9 ± 0.6
	P 36:3	5.4 ± 0.3	5.4 ± 0.5	2.3 ± 0.2	3.9 ± 1.5
	P 36:4	9.9 ± 1.2	13.7 ± 0.7	14.7 ± 1.1	21.3 ± 3.1
	P 38:4	15.3 ± 0.9	18.3 ± 0.5	25.6 ± 3.7	26.1 ± 3.4
	P 38:5	6.0 ± 0.9	7.4 ± 0.8	7.6 ± 0.5	7.9 ± 0.3
	P 38:6	3.2 ± 0.7	3.4 ± 0.6	6.4 ± 0.9	4.7 ± 0.3
	P 40:4	2.4 ± 0.2	3.4 ± 0.2	3.9 ± 0.7	5.0 ± 0.7
	P 40:5	1.7 ± 0.3	2.1 ± 0.3	2.4 ± 0.3	3.6 ± 0.5
	P 40:6	4.0 ± 0.7	3.6 ± 0.5	8.0 ± 1.3	4.8 ± 1.1
	P 40:7	0.7 ± 0.3	0.6 ± 0.3	0.9 ± 0.3	0.2 ± 0.2
PC	32:0	3.2 ± 0.8	5.9 ± 0.6	3.3 ± 0.3	
	32:1	1.1 ± 0.3	1.4 ± 0.2	0.9 ± 0.1	
	34:0	3.3 ± 0.3	2.4 ± 0.3	4.6 ± 0.3	
	34:1	36.1 ± 1.6	31.9 ± 0.2	47.1 ± 2.5	
	34:2	16.3 ± 2.2	17.4 ± 1.9	14.3 ± 1.2	
	34:3	1.3 ± 0.2	1.5 ± 0.1	0.8 ± 0.1	
	36:0	0.4 ± 0.1	0.2 ± 0.1	0.4 ± 0.1	
	36:1	5.5 ± 0.2	4.5 ± 0.2	5.8 ± 0.7	
	36:2	17.1 ± 0.7	16.5 ± 0.6	12.7 ± 1.3	
	36:3	10.1 ± 1.2	10.8 ± 0.3	5.6 ± 0.6	-
	36:4	2.9 ± 0.3	3.9 ± 0.2	2.6 ± 0.7	
	36:5	0.2 ± 0.1	0.2 ± 0.1	0.1 ± 0.2	
	38:2	0.3 ± 0.2	0.2 ± 0.1	nd	
	38:3	0.4 ± 0.2	0.5 ± 0.2	0.2 ± 0.1	
	38:4	1.0 ± 0.2	1.4 ± 0.2	1.1 ± 0.4	
	38:5	0.6 ± 0.2	0.8 ± 0.2	0.5 ± 0.3	
	38:6	0.2 ± 0.1	0.2 ± 0.1	0.1 ± 0.1	
	40:5	nd	0.0 ± 0.1	nd	
	40:6	nd	0.2 ± 0.1	nd	

Table A.4.4. Multiple comparison of the means from table A.4.3. for PE and PC species. Statistical significance was assessed according to the Student's t-test. * $p < 0.05$; ** $p < 0.01$. (n = 4 for healthy and adenoma, and n = 3 for carcinoma)

		Apical vs Basal	Apical vs AD	Apical vs Carcinoma	Basal vs AD	Basal vs Carcinoma	AD vs Carcinoma
PE	34:0			*			
	34:1	*					
	36:2			**		**	*
	36:3				**	*	
	38:2		**	*	*	*	
	38:3			*		*	
	38:4	*		**		**	
	38:6			*			
	40:4	*		**		*	*
	40:5			**		**	*
PC	32:0	*			**		
	32:1				*		
	34:0				**		
	34:1		*		**		
	34:3		*	-	**	-	-
	36:0	*					
	36:1	*					
	36:2		*				
	36:3		*		**		

Table A.4.5. Average lipid composition of clusters established by *k-means* analysis in healthy, adenomatous and carcinomatous lamina propria. Values are expressed as mean ± SEM (n=4 for healthy and adenoma and n=3 for carcinoma). In the case of PC (positive ion mode) no central cluster was established and no carcinoma was measured. nd: not detected.

Lipid Specie		Apical	Central	Basal	Adenoma	Carcinoma
PI	34:1	1.2 ± 0.2	2.3 ± 0.1	3.5 ± 0.5	3.8 ± 1.6	2.4 ± 0.5
	34:2	0.3 ± 0.1	0.9 ± 0.1	1.6 ± 0.3	1.4 ± 0.6	0.8 ± 0.3
	36:1	2.3 ± 0.3	3.4 ± 0.3	5.7 ± 1.9	4.2 ± 1.4	2.8 ± 0.9
	36:2	4.1 ± 0.4	6.0 ± 0.6	11.1 ± 3.0	6.5 ± 1.3	4.3 ± 0.7
	36:3	0.7 ± 0.1	1.2 ± 0.1	2.2 ± 0.4	1.3 ± 0.3	1.1 ± 0.5
	36:4	2.1 ± 0.2	2.2 ± 0,2	2.3 ± 0.1	2.8 ± 0.1	2.8 ± 0.1
	38:3	13.2 ± 1.7	11.6 ± 1.9	8.7 ± 2.0	11.4 ± 0.6	10.5 ± 1.5
	38:4	68.0 ± 1.9	63.0 ± 1.4	53.4 ± 4.7	55.1 ± 5.7	61.5 ± 4.2
	38:5	3.4 ± 0.2	3.8 ± 0.3	3.7 ± 0.3	4.7 ± 0.9	4.7 ± 0.8
	40:4	1.4 ± 0.1	1.0 ± 0.3	1.1 ± 0.2	1.1 ± 0.4	1.8 ± 0.3
	40:5	1.8 ± 0.5	2.6 ± 0.8	3.6 ± 1.2	4.8 ± 1.3	5.0 ± 1.6
	40:6	1.4 ± 0.5	1.9 ± 0.6	3.1 ± 1.0	2.8 ± 0.6	2.3 ± 0.5
PE	34:0	5.0 ± 0.2	4.9 ± 0.2	4.5 ± 0.2	6.4 ± 0.7	6.2 ± 0.7
	34:1	2.6 ± 0.3	3.5 ± 0.3	3.7 ± 0.6	4.4 ± 0.2	4.4 ± 1.1
	34:2	0.3 ± 0.2	0.6 ± 0.3	1.2 ± 0.4	0.8 ± 0.1	0.8 ± 0.4
	36:1	16.2 ± 0.7	18.7 ± 0.9	20.9 ± 1.9	19.7 ± 1.7	18.8 ± 1.4
	36:2	12.2 ± 1.0	14.6 ± 1.3	19.6 ± 2.4	12.8 ± 0.4	10.7 ± 1.5
	36:3	1.6 ± 0.3	2.4 ± 0.1	3.1 ± 0.9	2.0 ± 0.2	1.7 ± 0.7
	36:4	2.8 ± 0.2	2.2 ± 0.2	1.5 ± 0.4	2.4 ± 0.3	2.1 ± 0.2
	38:1	1.0 ± 0.4	1.6 ± 0.3	1.8 ± 0.3	1.7 ± 0.1	1.6 ± 0.8
	38:2	5.6 ± 0.2	6.9 ± 0.3	8.7 ± 0.6	5.3 ± 0.3	5.2 ± 0.6
	38:3	4.5 ± 0.4	5.1 ± 0.3	5.5 ± 0.3	5.1 ± 0.2	4.3 ± 0.9
	38:4	30.3 ± 1.0	24.8 ± 0.2	19.0 ± 1.5	23.8 ± 1.6	25.0 ± 4.1
	38:5	6.2 ± 0.4	4.6 ± 0.4	3.1 ± 0.6	4.8 ± 0.7	3.9 ± 0.5
	38:6	0.2 ± 0.2	0.2 ± 0.2	0.1 ± 0.1	0.4 ± 0.2	0.9 ± 0.1
	40:3	nd	0.1 ± 0.1	0.2 ± 0.2	nd	0.4 ± 0.2
	40:4	6.3 ± 0.1	5.8 ± 0.1	4.7 ± 0.6	5.6 ± 0.2	7.3 ± 1.2
	40:5	5.1 ± 0.3	3.9 ± 0.3	2.4 ± 0.4	4.4 ± 0.4	4.5 ± 0.4
	40:6	nd	nd	nd	0.5 ± 0.5	2.3 ± 0.4
PE-ether	P 34:1	6.3 ± 0.5	7.2 ± 0.3	7.8 ± 0.4	6.4 ± 0.4	6.9 ± 0.9
	P 34:2	nd	1.0 ± 0.2	1.4 ± 0.3	0.7 ± 0.3	1.2 ± 0.5
	P 36:1	3.4 ± 0.6	4.0 ± 0.2	4.0 ± 0.3	3.4 ± 0.5	3.1 ± 0.5
	P 36:2	3.4 ± 0.6	3.4 ± 0.3	4.2 ± 0.6	3.3 ± 0.3	2.9 ± 0.6
	P 36:3	nd	0.7 ± 0.3	1.4 ± 0.4	1.1 ± 0.2	1.6 ± 0.7
	P 36:4	18.6 ± 1.2	20.4 ± 0.7	21.2 ± 1.6	22.7 ± 1.0	24.0 ± 2.5
	P 38:4	28.4 ± 2.2	28.8 ± 1.7	29.5 ± 3.0	26.5 ± 0.7	25.3 ± 1.4
	P 38:5	13.1 ± 1.4	13.4 ± 1.2	12.3 ± 1.2	13.1 ± 1.1	12.1 ± 0.3
	P 38:6	6.5 ± 0.7	5.1 ± 0.5	4.1 ± 0.6	6.6 ± 0.7	6.7 ± 1.2
	P 40:4	7.6 ± 0.3	6.1 ± 0.4	5.4 ± 0.8	5.7 ± 0.3	5.9 ± 1.1
	P 40:5	5.8 ± 0.6	4.3 ± 0.6	3.6 ± 0.8	4.6 ± 0.3	5.4 ± 0.6

	P 40:6	6.2 ± 0.5	4.5 ± 0.4	2.8 ± 1.2	5.8 ± 0.6	5.0 ± 1.0
PC	30:0	0.1 ± 0.1	nd	0.1 ± 0.1	0.1 ± 0.1	-
	32:0	12.9 ± 0.9		11.7 ± 1.1	11.3 ± 2.9	
	32:1	1.6 ± 0.1		1.8 ± 0.1	1.7 ± 0.2	
	34:0	2.4 ± 0.3		2.4 ± 0.3	3.4 ± 0.5	
	34:1	26.9 ± 0.6		29.7 ± 1.1	37.3 ± 3.8	
	34:2	11.0 ± 1.6		13.4 ± 1.4	12.0 ± 0.8	
	34:3	0.8 ± 0.2		0.9 ± 0.1	0.6 ± 0.2	
	36:0	0.3 ± 0.1		0.3 ± 0.1	0.2 ± 0.1	
	36:1	3.8 ± 0.3		4.9 ± 0.2	4.5 ± 0.6	
	36:2	10.3 ± 0.6		12.6 ± 0.2	11.1 ± 1.4	
	36:3	5.8 ± 0.3		6.3 ± 0.3	5.5 ± 0.5	
	36:4	11.5 ± 1.4		6.7 ± 0.6	6.8 ± 2.4	
	36:5	0.7 ± 0.1		0.4 ± 0.1	0.2 ± 0.2	
	38:2	0.1 ± 0.1		0.1 ± 0.1	nd	
	38:3	0.7 ± 0.4		0.7 ± 0.4	0.3 ± 0.2	
	38:4	6.4 ± 0.7		5.3 ± 0.5	3.1 ± 1.0	
	38:5	3.8 ± 0.8		2.1 ± 0.5	1.8 ± 0.8	
	38:6	0.8 ± 0.2		0.4 ± 0.1	0.2 ± 0.2	
	40:5	0.1 ± 0.1		0.1 ± 0.1	nd	
	40:6	0.1 ± 0.1		0.1 ± 0.1	nd	

Table A.4.6. Multiple comparison from the values in the table A.4.5. Only species statistically different are shown. Statistical significance was assessed according to the Student's t-test. * $p < 0.05$; ** $p < 0.01$; *** $p < 0.005$. (n = 4 for healthy and adenoma, and n = 3 for carcinoma)

		Apical vs Basal	Apical vs Cetral	Apical vs AD	Basal vs AD	Central vs AD
PE-ether	P 34:1	*			*	
	P 34:2	*				
	P 36:1					*
	P 36:3	*		*		
	P 36:4	*		**		
	P 38:6	*			*	
	P 40:4	*	*	***		
	P 40:5	*		*		
	P 40:6	*	*		*	
PC	32:1	**				
	34:1	*		*		
	36:1	*				
	36:2	**				
	36:4	*				
	36:5	**		**		
	38:2			**	*	
	38:4			*		
	38:5			*		
	38:6			*		
	40:5			**	**	
	40:6			**	*	

Appendix Chapter 5

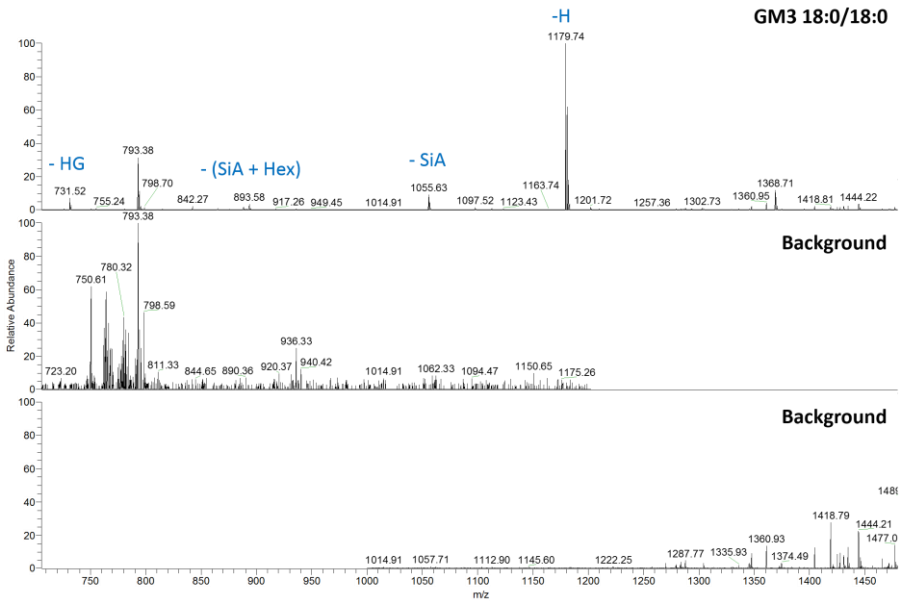

Fig A.5.1. Spectrum obtained for the ganglioside standard used for the ionization characterization in negative ion-mode by MADI-IMS. The major adduct for this type of sphingolipid is the loss of a proton, but it can undergo more fragmentation resulting in the formation of LacCer, lossing a Sialic Acid (-SiA), HexCer, (-SiA+Hex) or the respective Cer (-Head group, HG).

Table A.5.1. Final lipid identification of the negative ion mode mass channels using the prompt ionizations detected in lipid standards and eliminating the redundant peaks (Prompt ionizations and matrix adducts). In Yellow, mass channels with both PC and PE species. For the assignment of these peaks MS/MS and MS^3 was performed. For those peaks with two assignment, if one of them is much more abundant, it is marked in green.

m/z	Lipid ID	m/z teor	Error ppm
581.3108	[Lyso-PI_O-18:2 - H]-	581.309175	-2.795414
599.3209	[Lyso-PI_18:0 - H]-	599.31974	-1.935528
659.5143	[SM_d32:1 - CH3]-	659.513365	-1.417712
673.5304	[SM_d33:1 - CH3]-	673.529015	-2.056333
685.5326	[SM_d34:2 - CH3]-	685.529015	-5.229538
687.5454	[SM_d34:1 - CH3]-	687.544665	-1.069021
698.5154	[PE_O-34:3 - H]- / [PE_P-34:2 - H]-	698.51249	-4.165996
700.5293	[PE_O-34:2 - H]- / [PE_P-34:1 - H]-	700.52814	-1.655894
701.5606	[SM_d35:1 - CH3]-	701.560315	-0.406237
713.5637	[SM_d36:2 - CH3]-	713.560315	-4.743818

714.5124	[PE_34:2 - H]-	714.507405	-6.990830
715.582	[SM_d36:1 - CH3]-	715.575965	-8.433766
716.5306	[PE_34:1 - H]-	716.523055	-10.530017
718.5429	[PC_32:0 - CH3]-	718.53933	-4.968413
722.5195	[PE_O-36:5 - H]- / [PE_P-36:4 - H]-	722.51249	-9.702254
726.5444	[PE_O-36:3 - H]- / [PE_P-36:2 - H]-	726.54379	-0.839592
	[PC_O-34:3 - CH3]- / [PC_P-34:2 - CH3]-	726.544415	0.020646
728.5247	[PE_35:2 - H]-	728.523055	-2.257993
738.5105	[PE_36:4 - H]-	738.507405	-4.190886
740.5248	[PE_36:3 - H]-	740.523055	-2.356443
742.5423	[PC_34:2 - CH3]-	742.53933	-3.999788
	[PE_36:2 - H]-	742.538705	-4.841498
743.611	[SM_d38:1 - CH3]-	743.607265	-5.022813
744.5576	[PC_34:1 - CH3]-	744.55498	-3.518881
	[PE_36:1 - H]-	744.554355	-4.358312
746.517	[PE_O-38:7 - H]- / [PE_P-38:6 - H]-	746.51249	-6.041426
747.5196	[PG_34:1 - H]-	747.517655	-2.601945
748.5326	[PE_O-38:6 - H]- / [PE_P-38:5 - H]-	748.52814	-5.958360
750.5491	[PE_O-38:5 - H]- / [PE_P-38:4 - H]-	750.54379	-7.074870
758.5717	[PC_35:1 - CH3]-	758.57063	-1.410548
764.5279	[PE_38:5 - H]-	764.523055	-6.337284
766.5451	[PE_38:4 - H]-	766.538705	-8.342697
768.5557	[PC_36:3 - CH3]-	768.55498	-0.936823
768.5557	[PE_38:3 - H]-	768.554355	-1.750039
769.6265	[SM_d40:2 - CH3]-	769.622915	-4.658125
770.573	[PC_36:2 - CH3]-	770.57063	-3.075643
771.5198	[PG_36:3 - H]-	771.517655	-2.780235
771.6413	[SM_d40:1 - CH3]-	771.638565	-3.544406
772.59	[PC_36:1 - CH3]-	772.58628	-4.814996
773.539	[PG_36:2 - H]-	773.533305	-7.362320
774.4846	[PC_32:1 + ?1]-	774.476455	-10.516782
774.5482	[PE_O-40:7 - H]- / [PE_P-40:6 - H]-	774.54379	-5.693674
775.5529	[PG_36:1 - H]-	775.548955	-5.086720
776.5644	[PC_O-38:6 - CH3]- / [PC_P-38:5 - CH3]-	776.560065	-5.582311
	[PE_O-40:6 - H]- / [PE_P-40:5 - H]-	776.55944	-6.387148
778.5804	[PC_O-38:5 - CH3]- / [PC_P-38:4 - CH3]-	778.575715	-6.017398
	[PE_O-40:5 - H]- / [PE_P-40:4 - H]-	778.57509	-6.820151

785.6589	[SM_d41:1 - CH3]-	785.654215	-5.963183
786.5335	[PS_36:2 - H]-	786.528605	-6.223550
788.5466	[PS_36:1 - H]-	788.544255	-2.973834
792.5599	[PC_38:5 - CH3]-	792.55498	-6.207771
	[PE_40:5 - H]-	792.554355	-6.996366
794.5733	[PC_38:4 - CH3]-	794.57063	-3.360305
	[PE_40:4 - H]-	794.570005	-4.146897
795.641	[SM_d42:3 - CH3]-	795.638615	-2.997592
797.661	[SM_d42:2 - CH3]-	797.654215	-8.506192
799.6742	[SM_d42:1 - CH3]-	799.669865	-5.420987
808.5156	[PS_38:5 - H]-	808.512955	-3.271438
810.531	[PS_38:4 - H]-	810.528605	-2.954862
833.5225	[PI_34:2 - H]-	833.518105	-5.272831
835.5361	[PI_34:1 - H]-	835.533755	-2.806589
857.5205	[PI_36:4 - H]-	857.518105	-2.792944
859.536	[PI_36:3 - H]-	859.533755	-2.611881
861.5565	[PI_36:2 - H]-	861.549405	-8.235163
863.5691	[PI_36:1 - H]-	863.565055	-4.684071
871.5363	[PI_37:4 - H]-	871.533755	-2.920139
883.5421	[PI_38:5 - H]-	883.533755	-9.445027
885.55	[PI_38:4 - H]-	885.549405	-0.671899
887.5558	[PI_38:3 - H]-	887.565055	10.427405
909.5406	[PI_40:6 - H]-	909.549405	9.680618
913.5894	[PI_40:4 - H]-	913.580705	-9.517495

Table A.5.2. MS/MS and MS^3 was performed for mass channels with a preliminary assignment of PC and PE in order to confirm the final ID. This, FA information of those species is also retrieved from the spectra. Again, m/z in yellow means that both subclass of GP are present in that peak, while those ID that are marked in green are if one of those is in higher abundance. Figure A.5.2 shows an example for the identification of PC or PE, as well as the fatty acid chains.

m/z	Lipid ID	FA chains
698.5154	[PE_O-34:3 - H]- / [PE_P-34:2 - H]-	P-16:0/18:2 or O-16:1/18:2
700.5293	[PE_O-34:2 - H]- / [PE_P-34:1 - H]-	P-16:0/18:1 or O-16:1/18:1
714.5124	[PE_34:2 - H]-	16:0/18:2
716.5306	[PE_34:1 - H]-	16:0/18:1
718.5429	[PC_32:0 - CH3]-	16:0/16:0
722.5195	[PE_O-36:5 - H]- / [PE_P-36:4 - H]-	P-16:0/20:4 or O-16:1/20:4
726.5444	[PE_O-36:3 - H]- / [PE_P-36:2 - H]-	P-18:0/18:2 or O-18:1/18:2 P-18:1/18:1 or O-18:2/18:1
	[PC_O-34:3 - CH3]- / [PC_P-34:2 - CH3]-	P-16:0/18:2 or O-16:1/18:2 P-18:0/16:2 or O-18:1/16:2
728.5247	[PE_35:2 - H]-	17:1/18:1 & 17:0/18:2
738.5105	[PE_36:4 - H]-	16:0/20:4 16:1/20:3 18:2/18:2
740.5248	[PE_36:3 - H]-	18:1/18:2
742.5423	[PC_34:2 - CH3]-	16:0/18:2 16:1/18:1
	[PE_36:2 - H]-	18:0/18:2 18:1/18:1
744.5576	[PC_34:1 - CH3]-	16:0/18:1
	[PE_36:1 - H]-	18:0/18:1 18:1/18:0
746.517	[PE_O-38:7 - H]- / [PE_P-38:6 - H]-	P-16:0/22:6 or O-16:1/22:6
748.5326	[PE_O-38:6 - H]- / [PE_P-38:5 - H]-	P-16:0/22:5 or O-16:1/22:5 P-18:1/20:4 or O-18:2/20:4
750.5491	[PE_O-38:5 - H]- / [PE_P-38:4 - H]-	P-16:0/22:4 or O-16:1/22:4 P-18:0/20:4 or O-18:1/20:5
758.5717	[PC_35:1 - CH3]-	19:1/16:0
764.5279	[PE_38:5 - H]-	18:1/20:4
766.5451	[PE_38:4 - H]-	18:0/20:4
768.5557	[PC_36:3 - CH3]-	18:1/18:2 16:0/20:3
768.5557	[PE_38:3 - H]-	18:0/20:3
770.573	[PC_36:2 - CH3]-	18:0/18:2 18:1/18:1
772.59	[PC_36:1 - CH3]-	18:0/18:1 18:1/18:0
774.5482	[PE_O-40:7 - H]- / [PE_P-40:6 - H]-	P-18:0/22:6 or O-18:1/22:6 P-18:1/22:5 or O-18:2/22:5
776.5644	[PC_O-38:6 - CH3]- / [PC_P-38:5 - CH3]-	P-16:0/22:5 or O-16:1/22:5 P-18:1/20:4 or O-18:2/20:4

778.5804	[PE_O-40:6 - H]- / [PE_P-40:5 - H]-	P-18:0/22:5 or O-18:1/22:5 P-16:0/24:5 or O-16:1/24:5 P-20:1/20:4 or O-20:2/20:4
	[PC_O-38:5 - CH3]- / [PC_P-38:4 - CH3]-	P-18:0/20:4 or O-18:1/20:4
	[PE_O-40:5 - H]- / [PE_P-40:4 - H]-	P-18:0/22:4 or O-18:1/22:4 P-16:0/24:4 or O-16:1/24:4 P-20:0/20:4 or O-20:1/20:4
	[PC_38:5 - CH3]-	16:0/22:5 18:1/20:4 18:0/20:5
792.5599	[PE_40:5 - H]-	18:0/22:5 20:1/20:4 20:0/20:5 18:1/22:4
	[PC_38:4 - CH3]-	18:0/20:4 16:0/22:4
794.5733	[PE_40:4 - H]-	18:0/22:4

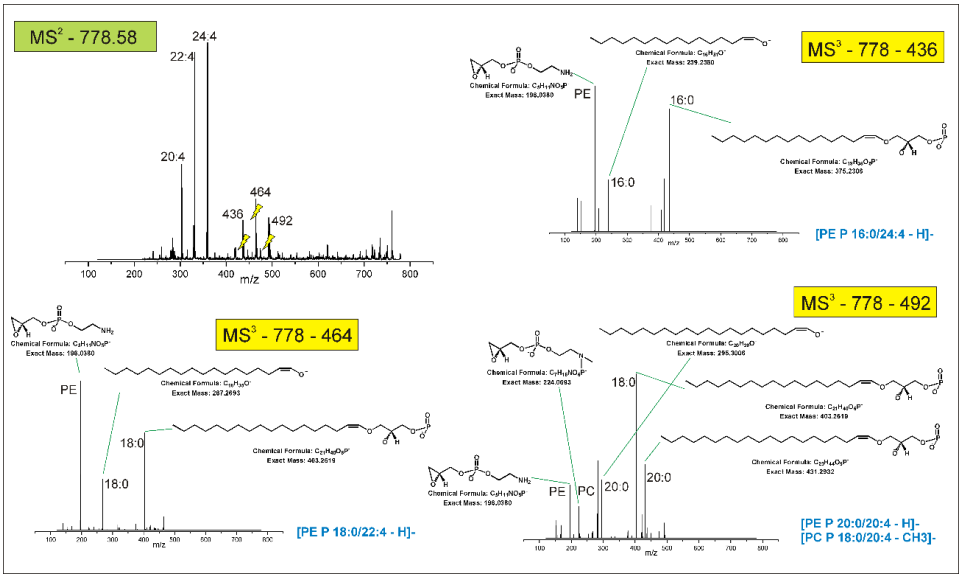

Fig. A.5.2. Example of the MS/MS and MS^3 assignation for m/z = 778.58 Da over the tissue in negative ion-mode. In green MS/MS spectrum of the precursor ion showing the identified fatty acid chains (20:4, 22:4 and 24:4) and in yellow the the three MS^3 spectra from the three unidentified peaks at the MS/MS (mark with lightnings). Those peaks correspond to the loss of the fatty acid chains. However, they could come from, both, PC and PE species. In blue the final lipid identification.

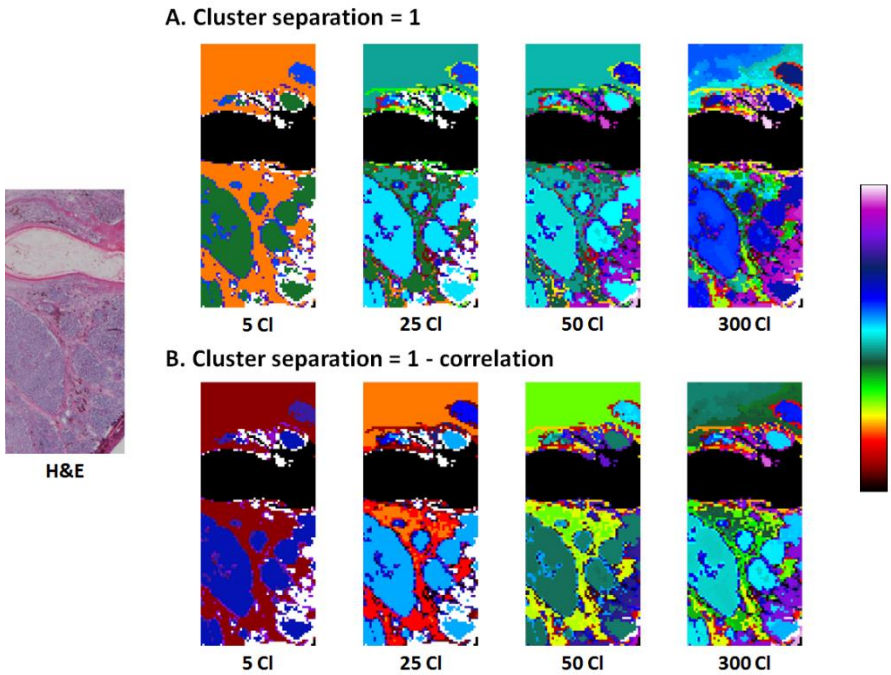

Fig A.5.3. DHCA-RC analysis for another primary melanoma as other example of variability within tissue. **A** - Cluster separation 1. **B** - Separation between cluster 1-correlation colored with a colorbar.

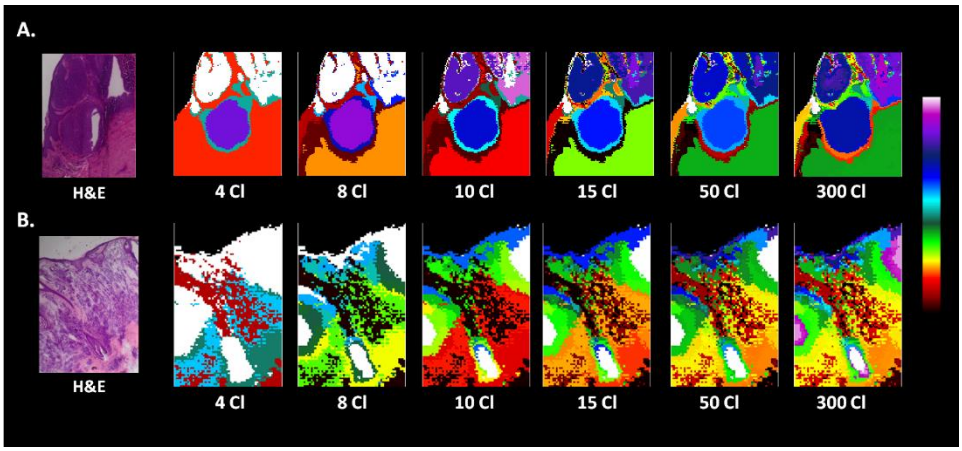

Fig A.5.4. DHCA-RC analysis only with peaks selected after an exhaustive lipid assignment individually over **A** - Primary melanoma (Mel203) and **B** – Nevus (G01). The segmentation maps are visualize in a colorbar with a cluster separation of 1-correlation between them.

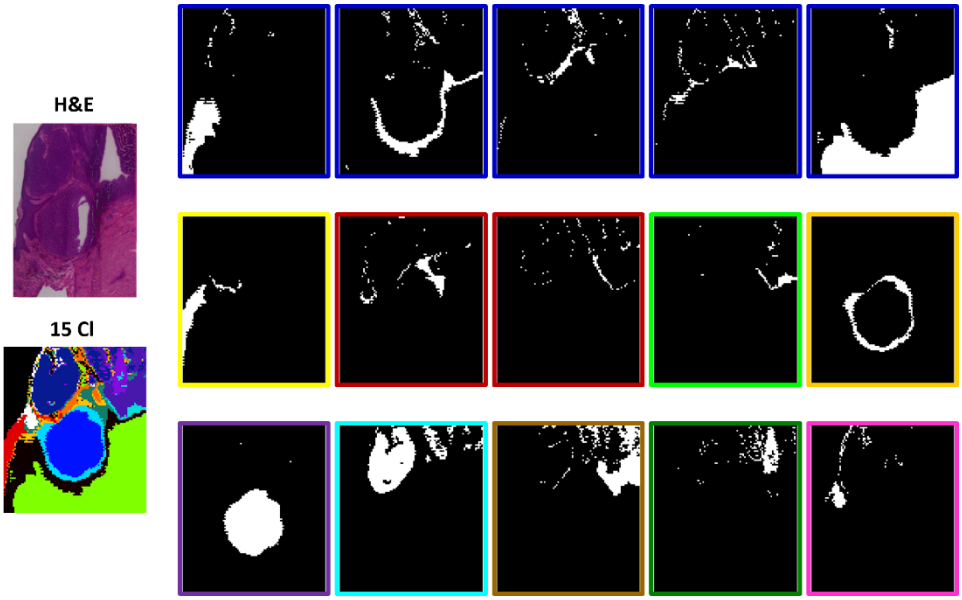

Fig A.5.5. Clusters from the segmentation level 15 for the primary melanoma used as example. Clusters that correlate after the correlation analysis from Figure 5.11, are colored with the same colors as in the correlation matrix for visualization.

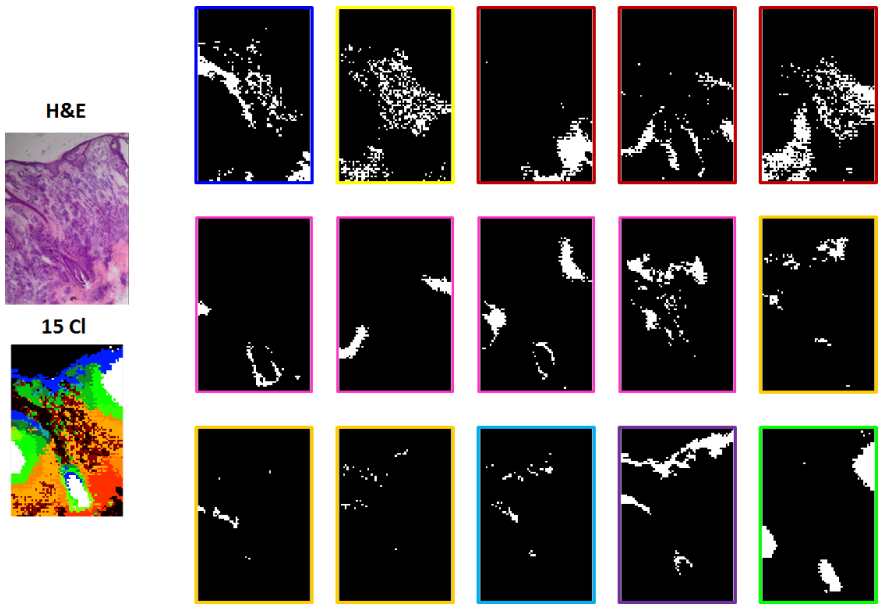

Fig A.5.6. Clusters from the segmentation level 15 for the nevi section used as example. Clusters that correlate after the correlation analysis from Figure 5.11 are colored with the same color as in the correlation matrix from Figure 5.11 for visualization.

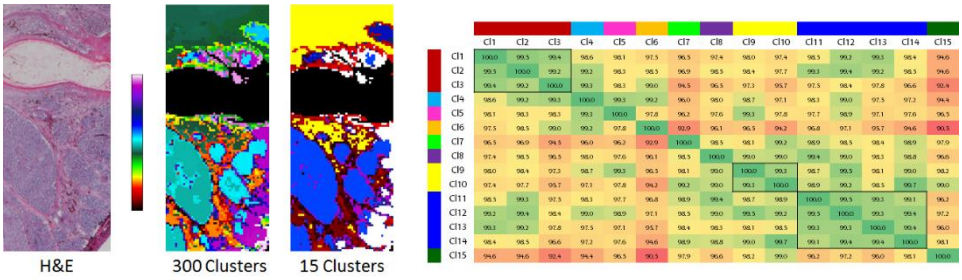

Fig A.5.7. Correlation matrix for the melanoma from Figure A.5.3 (Mel7). The clustering shown here is performing the algorithm only with the peaks selected after the assignation. Taking into account all the parameters established, 9 clusters has been selected for further analysis.

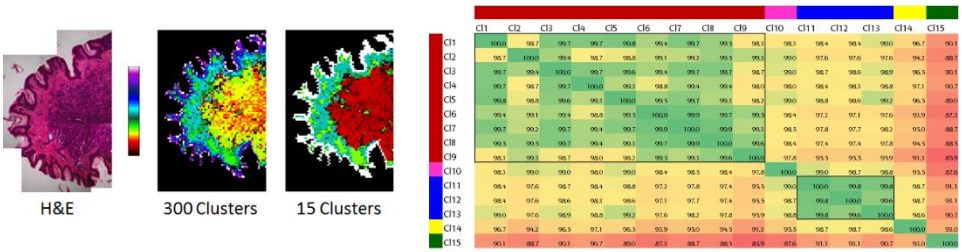

Fig A.5.8. Correlation matrix for a nevi section (N95). The clustering shown here was carried out only with the peaks selected after the assignation. Taking into account all the parameters established in the main manuscript, 5 clusters has been selected for further analysis. Clustering images are visualize with 1-correlation between clusters

Table A.5.3. Summary of the patient samples randomly assigned for each data set, as well as the number of clusters selected for each patient following the guidelines described in the section "Unraveling tumor heterogeneity".

Training set				Validation set			
Nevus	n° cluster	Primary Melanoma	n° cluster	Nevus	n° cluster	Primary Melanoma	n° cluster
C01	6	Mel3	5	C02	7	Mel2	6
G01	8	Mel4	7	G02	6	Mel8	6
G03	6	Mel5	7	G05B	7	Mel9	7
G05A	7	Mel6	6	N82	5	Mel209	9
G05C	8	Mel7	9			Mel211	8
N109	6	Mel10	8				
N30	5	Mel201	6				
N92	6	Mel203	10				
N95	5	Mel204	7				
N97	4	Mel206	5				
		Mel207	7				
		Mel208	3				

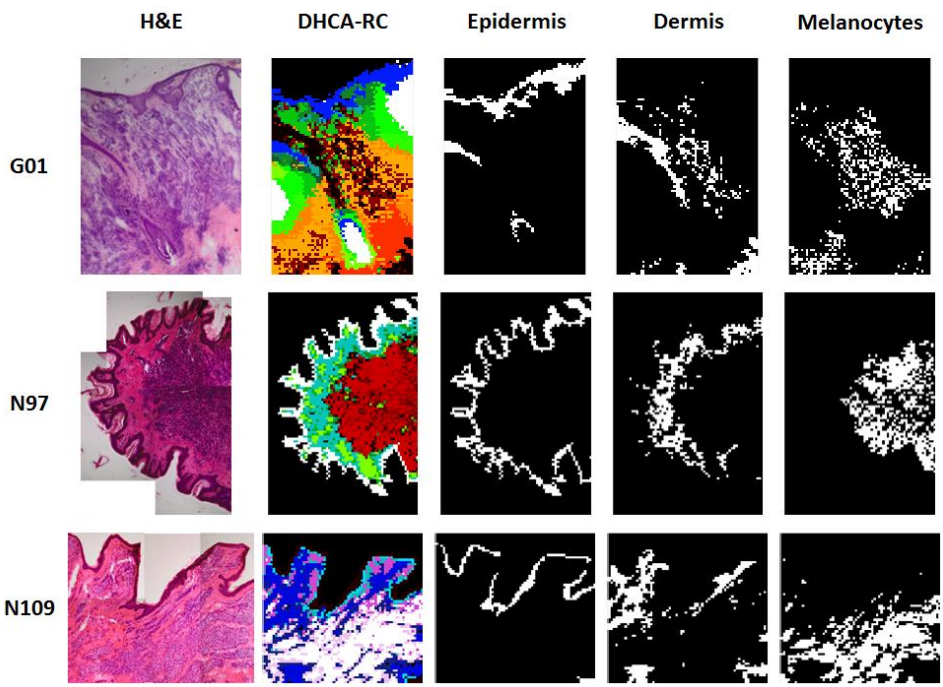

Fig A.5.9. Comparison between the optical images of three nevus and the divisive hierarchical clustering. After the trends observed in the PCA from Figure 5.13.A, clusters were assigned to epidermis, dermis and melanocytes and extracted their spectra for further comparative analysis.

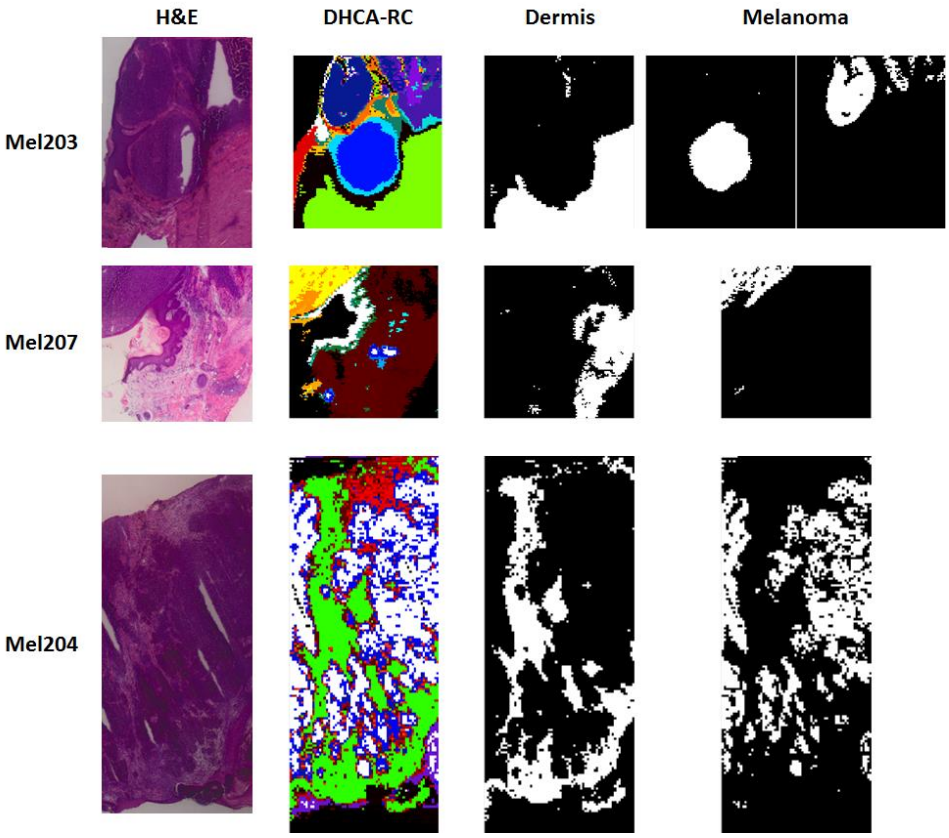

Fig A.5.10. Comparison between the optical images of three primary melanoma and the divisive hierarchical clustering. After the trends observed in the PCA from Figure 5.14.A, clusters were assigned to melanoma and melanoma related stroma and extracted their spectra for further comparative analysis. When more than one melanoma cluster were recognized, they were all selected in order to analyze possible differences within malignant melanocytes, if there were.

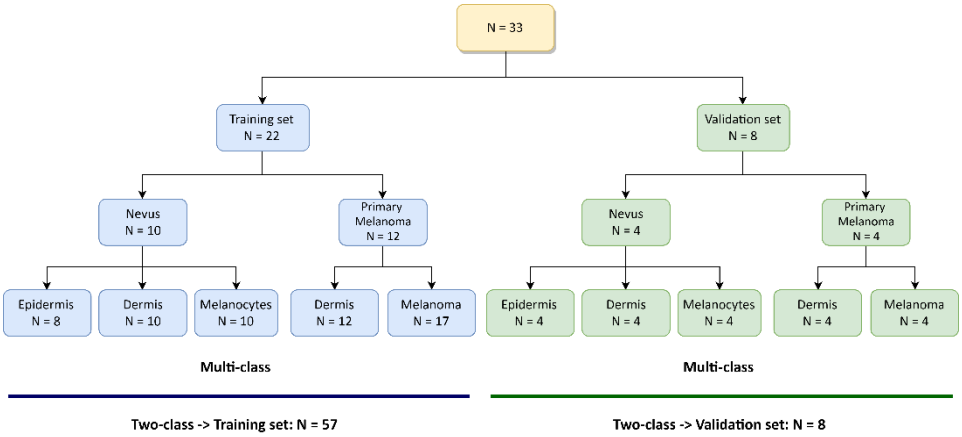

Fig A.5.11. Schematic diagram of final sample distribution. For multiple-class classification tissue types within samples were considered. For binary classification, all tissue types were grouped into nevus and primary melanoma, substantially increasing the sample size with respect to the five-class model.

A.

Method	CA	AUC	F1	Precision	Recall
Logistic Regression	96.5%	0.996	0.966	0.970	0.965
Naive Bayes	94.7%	0.995	0.947	0.955	0.947
Random Forest	94.7%	0.988	0.948	0.954	0.947
SVM	96.5%	1.000	0.965	0.967	0.965

B.

Method	CA	AUC	F1	Precision	Recall
Logistic Regression	100.0%	1.000	1.000	1.000	1.000
Naive Bayes	100.0%	1.000	1.000	1.000	1.000
Random Forest	98.2%	1.000	0.982	0.983	0.982
SVM	100.0%	1.000	1.000	1.000	1.000

Fig A.5.12. Internal 10-fold cross-validation results with the training dataset for five-class classification (**A**) and binary model (**B**). All models yielded an overall accuracy of 90-100%, as well as sensitivity (recall).

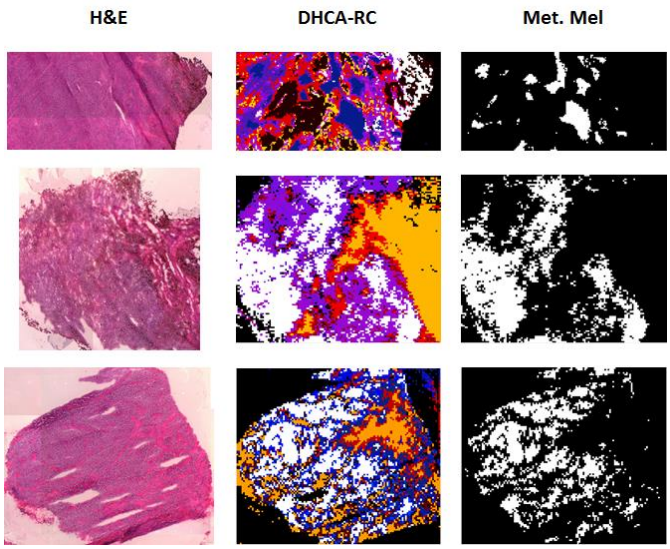

Fig A.5.13. Comparison between the optical images of three metastatic melanoma with H&E staining and the divisive hierarchical clustering. With a histology directed approach, metastatic melanoma cluster were selected and compared to benign melanocytes and primary melanoma.

Appendix Chapter 6

Table A.6.1. Cell lines and primary cells used for the optimization of the protocol for membrane microarray-based technology combined to mass spectrometry

Melanocytes		Melanomas	
Type	**Cell**	**Type**	**Cell line**
Primary culture of melanocytic cells	N1	**Primary Melanoma**	MEL-HO
	N3		A375
	N4		G-361
	N5		Sk-Mel-28
	N6		Sk-Mel-31
	N7		ME4405
	N8	**Metastasis in lymph nodules (MMGL)**	RPMI-7951
	N9		Hs294T
Melanocytic cell lines	HEM-DP		A2058
	HEM-MP		Sk-Mel-3
	HEM-LP		Colo-800
		Subcutaneous metástasis (MMSN)	HT144
		Skin metastasis	WM-266-4
			Sk-Mel-2
		Brain metastasis	VMM1

		HEM-MP	SKMEL-3	WM-266	SKMEL31	Nevus 1	Nevus 4	Nevus 7	HEM-MP
		HEM-DP	SKMEL-3	WM-266	SKMEL31	Nevus 2	Nevus 5	Nevus 8	HEM-DP
		HEM-LP	SKMEL-3	WM-266	SKMEL31	Nevus 3	Nevus 6	Nevus 9	HEM-LP
A375	Hs294T	RPMI	A2058	SKMEL28	ME4405	HEM-MP	HEM-MP	VMM1	SKMEL-2
A375	Hs294T	RPMI	A2058	SKMEL28	ME4405	HEM-MP	HEM-MP	VMM1	SKMEL-2
A375	Hs294T	RPMI	A2058	SKMEL28	ME4405	HEM-MP	HEM-MP	VMM1	SKMEL-2
						MEL-HO	G361	COLO80	HT144
						MEL-HO	G361	COLO80	HT144
						MEL-HO	G361	COLO80	HT144

Fig. A.6.1. Scheme of the membrane microarray designed with melanoma cell lines. Light green are commercial melanocytes with different pigmentation (light, medium and dark). Dark green are melanocytes extracted and cultured from human nevi. Blue are commercial primary melanoma and red and white are cell lines with high metastatic potential. Light red represent metastatic melanoma in lymph nodes (named MMGL in this thesis), white color represents subcutaneous metastasis (MMSN) and dark red represent metastatic melanoma in other location, skin and brain. Due to the small number of sample for MMSN and others, these were removed from the statistical analysis.

Appendix Chapter 7

Table A.7.1. Statistical analysis of the lipid fingerprints of lung biopsies from healthy mucosa, healthy smoker (FUM), COPD and lung cancer. One-way ANOVA and multiple testing correction. The table shows the p-values for Levene's test to determine the homogeneity (H_0 = groups have equivalent variance) to choose the post hoc method (Bonferroni if Leven's p >0.05 and Games-Howell if Levene's p<0.05).

Lipid Species	Levene's test	One-way ANOVA	Post hoc					
	p-value	p-value	Healhty vs FUM	Healhty vs COPD	Healhty vs Cancer	FUM vs COPD	FUM vs Cancer	COPD vs Cancer
Lyso-PI 18:0	0.040	0.076						
Lyso-PI 20:4	0.010	0.617						
Lyso-PI P-18:1	0.090	0.003	1.000	1.000	0.007	1.000	0.011	0.015
PE 32:0	0.050	0.260						
PE 34:0	0.279	0.877						
PE 34:1	0.129	0.124						
PE 34:2	0.032	0.012	0.232	0.788	0.244	0.300	0.121	0.185
PE 35:1	0.064	0.031	1.000	0.299	0.046	0.959	0.158	1.000
PE 35:2	0.019	0.000	0.749	0.090	0.027	0.209	0.038	0.098
PE 36:1	0.223	0.015	0.374	0.142	0.015	1.000	0.303	1.000
PE 36:2	0.160	0.032	0.908	1.000	0.322	0.414	0.034	1.000
PE 36:3	0.591	0.079						
PE 36:4	0.166	0.329						
PE 37:1	0.526	0.001	0.147	0.054	0.001	1.000	0.022	0.156
PE 37:2	0.078	0.010	1.000	0.173	0.013	0.783	0.053	1.000
PE 37:3	0.006	0.018	0.673	0.215	0.215	0.065	0.065	
PE 37:4	0.007	0.007	0.229	0.768	0.768	0.025	0.025	
PE 38:1	0.553	0.208						
PE 38:2	0.405	0.023	0.364	0.118	0.029	1.000	0.671	1.000
PE 38:3	0.009	0.250						
PE 38:4	0.356	0.551						
PE 38:5	0.396	0.745						
PE 38:6	0.747	0.137						
PE 39:2	0.011	0.011	0.498	0.051	0.051	0.407	0.407	
PE 39:4	0.006	0.001	0.848	0.265	0.003	1.000	0.097	0.052
PE 40:3	0.136	0.814						
PE 40:4	0.147	0.856						
PE 40:5	0.476	0.730						
PE 40:6	0.744	0.844						

PE 42:5	0.010	0.048	0.470	0.111	0.111	0.768	0.768	
PE P-34:1	0.278	0.112						
PE P-34:2	0.009	0.280						
PE P-36:1	0.226	0.137						
PE P-36:2	0.107	0.110						
PE P-36:3	0.164	0.496						
PE P-36:4	0.102	0.019	0.681	1.000	0.267	1.000	0.023	0.106
PE P-38:4	0.199	0.025	1.000	1.000	0.134	1.000	0.039	0.099
PE P-38:5	0.020	0.328						
PE P-38:6	0.756	0.531						
PE P-40:4	0.144	0.500						
PE P-40:5	0.026	0.816						
PE P-40:6	0.334	0.570						
PG 34:1	0.004	0.029			0.290		0.290	0.290
PG 36:2	0.898	0.906						
PG 44:9	0.229	0.018	1.000	0.997	0.038	0.949	0.036	0.599
PI 32:0	0.017	0.899						
PI 34:1	0.010	0.982						
PI 34:2	0.098	0.777						
PI 36:1	0.028	0.936						
PI 36:2	0.234	0.807						
PI 36:3	0.152	0.546						
PI 36:4	0.205	0.156						
PI 38:1	0.017	0.432						
PI 38:4	0.018	0.011	0.968	0.295	0.166	0.301	0.170	0.383
PI 38:5	0.056	0.073						
PI 38:6	0.085	0.763						
PI 40:4	0.259	0.889						
PI 40:5	0.279	0.409						
PI 40:6	0.086	0.087						
PS 36:1	0.006	0.042	0.438	0.496	0.918	0.427	0.572	0.580
PS 36:2	0.082	0.658						
PS 38:2	0.010	0.000	0.015	0.015	0.015			
PS 38:3	0.018	0.581						
PS 38:4	0.230	0.984						
PS 40:2	0.000	0.007	0.014	0.758	0.014	0.787		0.787
SM d32:1	0.070	0.011	1.000	1.000	0.067	1.000	0.026	0.028
SM d33:1	0.075	0.126						
SM d33:2	0.279	0.473						

SM d34:1	0.366	0.910						
SM d34:2	0.221	0.063						
SM d35:1	0.355	0.623						
SM d36:1	0.400	0.346						
SM d38:1	0.011	0.245						
SM d40:2	0.230	0.402						
SM d41:1	0.211	0.227						
SM d42:2	0.089	0.306						
SM d42:3	0.235	0.447						
Sulfatide d34:3	0.653	0.016	1.000	1.000	0.024	1.000	0.057	0.128
Sulfatide d36:3	0.575	0.321						
Sulfatide d43:3	0.161	0.000	0.641	0.041	0.000	0.427	0.001	0.021
Sulfatide d43:4	0.004	0.001	0.538	0.334	0.002	0.138	0.064	0.787
Sulfatide d45:4	0.025	0.062						
Sulfatide d45:5	0.080	0.000	1.000	0.000	0.000	0.001	0.001	1.000
Sulfatide d45:6	0.146	0.017	1.000	1.000	0.057	1.000	0.034	0.064

Abbreviations / Laburdurak

	English	Euskera
AA	Arachidonic Acid	Azido arakidonikoa
AD	Adenoma	Adenoma
ANOVA	Analysis of variance	Bariantza analisia
AUC	Area under the curve	Kurba azpiko azalera
Cer	Ceramide	Zeramida
CerP	Ceramide-1-phosphate	Zeramida-1-fosfatoa
CL	Cardiolipin	Kardiolipina
COPD	Chronic obstructive pulmonary disease	Biriketao gaixotasun butxatzaile kronikoa
DAN	1,5-Diaminonaphthalene	1,5-Diaminonaftalenoa
DESI	Desorption electrospray ionization	Elektrospray bidezko desortzio ionizazioa
DHA	Docosahexanoic acid	Azido dokosahexanoikoa
DHCA	Divisive hierarchical clustering algorithm	Klustering hierarkiko zatitzailearen algortimoa
DHCA-RC	Divisive hierarchical clustering algorithm with RankCompete	Klustering hierarkiko zatitzailearen algortimoa RankCompeterekin
DUFA	Diunsaturated fatty acid	Gantz-azido diinsaturatuak
EL	Epithelial layer	Epitelioa
ESI	Electrospray ionization	Elektrospray bidezko ionizazioa
FA/GA	Fatty acids	Gantz-azidoak
FT-ICR	Fourier ransform ion cyclotron resonance	Fourier-en eraldaketa erabiliz ziklotroiaren bitartez erresonantzia ionikoko analizadorea
FWHM	Full width at half maximum	Zabalera altura maximoaren erdia
GC-MS	Gas chromatography-mass spectrometry	Gas-Kromatografia/masa-espektrometria
GL	Glycerolipids	Glizerolipidoak
GP	Glycerophospholipids	Glizerofosfolipidoak
H&E	Hematoxylin & Eosin	Hematoxilina eta eosina
HexCer	Cerebrosides	Zerebrosidoak
IF	Immunofluorescence technique	Immunofluoreszentzia teknika
IHC	Immunohistochemistry	Immunhistokimika
IMS	Imaging mass spectrometry	Masa-espektrometria bidezko irudikapena
ITH	Intratumor heterogeneity	Tumore barneko heterogeneotasuna
LAESI	Laser ablation electrospray ionization	Laser bidezko elektrospray bidezko ionizazioa
LC-MS	Liquid chromatography-mass spectrometry	Likido-kromatografia/masa-espektrometria
LDI	Laser desorption ionization	Laser bidezko desortzio ionizazioa
LP	Lamina propria	Lamina propia
m/z	mass-to-charge ratio	masa-karga erlazioa
MALDI	Matrix assisted laser desorption ionization	Matrizeak lagundutako laser bidezko desortzio ionizazioa
MBT	2-Mercaptobenzothiazoe	2-merkaptobezotiazola

MM	Muscularis mucosae	Muskularis mukosa
MMGL	Metastatic melanoma in lymph nodes	Nodulu linfatikoko melanoma metastatikoa
MMSN	Subcutaneous metastatic melanoma	Azalpeko melanoma metastatikoa
MS	Mass spectrometry	Masa-espektrometria
MUFA	Monounsaturated fatty acid	Gantz-azido monoinsaturatuak
PA	Glycerophosphates / Phosphatidic acid	Glizerofosfatoa / Azido fosfatidikoa
PC	Glycerophosphocholine	Glizerofosfokolina / Fosfatidilkolina
PCA	Principal component analysis	Osagai nagusien analisia
PE	Glycerophosphoethanolamine	Glizerofosfoetanolamina / Fosfatidiletanolamina
PE-Cer	Ceramide phosphoethanolamine	Zermida fosfatidiletanolamina
PG	Glycerophoshoglycerol	Glizerofosfoglizerola / Fosfatidilglizerola
PI	Glycerophosphoinositol	Glizerofosfoinositola / Fosfatidilinositola
PK	Polyketides	Poliketidoak
PR	Prenols	Prenolak
PS	Glycerophosphoserine	Glizerofosfoserina / Fosfatidilserina
PUFA	Poyunsaturated fatty acid	Gantz-azido poliasegabeak
RI	Relative intensity	Intentsitate erlatiboa
ROC	Receiver-operating characteristic	Hargailuaren funtzionamenduko ezaugarria
ROI	Region of interest	Zona interesgarriak
S.E.M	Standard error of the mean	Bataz bestekoaren errore estandarra
s/n	signal-to-noise	seinalea/zarata erlazioa
SEM	Scanning electrom microscope	Ekorketazko mikroskipio elektronikoa
SFT	Sulfatides	Sulfatidoak
SIMS	Secondary ion mass spectrometry	Bigarren mailako ioien masa-espektrometria
SL	Saccharolipids	Sakarolipidoak
SM	Sphingomyelin	Esfingomielina
SP	Sphingolipids	Esingolipidoak
SPF	Simple peak findings	*Simple peak findings*
ST	Sterols	Esterolak
SVM	Support Vector Machine	Euskarri bektoredun makina
TIC	Total ion current	Ioien koronte totala
TOF	Time-of-flight	Hegaldi-denbora